Spectral Induced Polarisation for an enhanced pore-space characterisation and analysis of dissolution processes of carbonate rocks

Doctoral thesis

to be awarded the degree

Doctor rerum naturalium
- Dr. rer. nat. -

submitted by
Sarah Hupfer
from Leipzig

approved by
the Faculty of Energy and Economic Sciences,
Clausthal University of Technology

Date of oral examination
25.10.2019

Dean:	Prof. B. Lehmann	- TU Clausthal
Chairperson of the Board of Examiners:	Prof. H.-J. Gursky	- TU Clausthal
Supervising tutor:	Prof. A. Weller	- TU Clausthal
Reviewer:	Prof. S. Kruschwitz	- TU Berlin

Abstract

Sarah Hupfer, Leibniz Institute for Applied Geophysics, PhD thesis, 2019

Spectral Induced Polarisation for an enhanced pore-space characterisation and analysis of dissolution processes of carbonate rocks

Keywords: complex electrical conductivity, spectral induced polarisation, petrophysics, carbonate rocks, dissolution processes, subrosion

Subrosion due to the subsurface leaching of soluble rocks, e.g. carbonates, is a global phenomenon that results in surface depressions and sinkholes. Fundamental research on dissolution processes of carbonates is necessary to better understand subrosion processes, to improve risk assessment and forecasting.

This thesis deals with enhanced pore-space characterisation and analysis of dissolution processes in carbonates using spectral induced polarisation (SIP). SIP is a suitable method to conduct fundamental research to characterise the pore space and to obtain detailed information on rock properties. Systematic laboratory measurements on carbonates are conducted to investigate rock characteristics and their influence on IP responses and their sensitivity to dissolution processes. The core analysis program includes a multi-methodical approach that combines petrophysical, mineralogical and geochemical techniques, e.g. complex conductivity spectra, and data from 2D and 3D imaging techniques, as well as quantities such as porosity, permeability, specific surface area, and nuclear magnetic-resonance decay-time distributions.

First, carbonate sample sets from four different type locations with a broad range of petrophysical parameters are investigated to better understand IP responses and mechanisms in carbonates. Different IP experiments are conducted to investigate the polarisation behaviour of the carbonate samples and the results are compared with the existing knowledge of SIP on sandstones. I show that four different types of polarisation behaviour can be observed in the spectra of the phase shift: (1) a constant phase angle, (2) a continuous increase, (3) a combination of both, and (4) a maximum type. Each carbonate type can be assigned to a characteristic curve type, which is reproducible for the whole sample set. Comparison of SIP with petrophysical parameters shows that it is more challenging to find clear correlations, especially compared to sandstones. However, it is possible to transfer empirical relationships and model assumptions from sandstones to carbonates, e.g. formation factor estimation and permeability prediction.

In the second step, an experimental setup for systematic dissolution under monitoring conditions and an uniquely tailored experimental concept was successfully developed to investigate the impact of dissolution procedures on mineral and pore structure under controlled conditions. Before and after each dissolution step, the core analysis program was carried out to systematically record the changes of pore space. Dissolution processes change distinct petrophysical parameters on different scales. Grain density and porosity increase, whereas the specific surface increases at first and decreases at later stages, depending on contrary scenarios of specific surface variation on pore scale. The pore radii distributions of mercury intrusion porosimetry and μ-CT data reveal an enlargement of the dominant pore radii with increasing dissolution. Changes within the carbonate due to dissolution can be observed by SIP to a certain extent. An increased porosity, a decreased formation factor, and a decreased volume tortuosity leads to an increased real part of electrical conductivity. The shape of the σ''-spectra changes as well. The imaginary part of electrical conductivity increases for higher frequencies due to dissolution processes, which indicates the formation of smaller pores. Contradictory processes of smoothing and roughing of the pore surface leads to both decreased and increased surface tortuosities, which affects the behaviour of the imaginary part of conductivity during dissolution. In summary, the volume conductivity increases more strongly than the surface conductivity. Due to small, dissolution-induced changes of the rock parameters, data interpretation is challenging. Hence, further research regarding dissolution processes of carbonates is required.

This work demonstrates the potential of enhanced pore-space characterisation and analysis of dissolution processes of carbonate rocks using SIP.

Zusammenfassung

Sarah Hupfer, Leibniz-Institut für Angewandte Geophysik, Doktorarbeit 2019

Spectral Induced Polarisation for an enhanced pore-space characterisation and analysis of solution processes of carbonate rocks

Stichworte: komplexe elektrische Leitfähigkeit, spektrale induzierte Polarisation, Gesteinsphysik, Karbonatgestein, Lösungsprozesse, Subrosion

Subrosion, d.h. die unterirdische Auslaugung von leicht löslichen Gesteinen wie z.B. Karbonat, ist eine weltweit auftretende Erscheinung, die letztlich zu subrosionsbedingten Erdfällen und Senken führt. Grundlagenforschung im Bereich von Lösungsprozessen an Karbonaten ist erforderlich für ein besseres Prozessverständnis dieser Ereignisse, um die Risikoeinschätzung sowie die Vorhersagemöglichkeiten zu verbessern.

Diese Dissertation befasst sich mit der erweiterten Porenraumcharakterisierung und Auswertung mittels Spektraler induzierter Polarisation (SIP) von Lösungsprozessen in Karbonaten. SIP ist eine etablierte Methode für die Durchführung von Grundlagenforschung auf Porenskala im Bereich der Porenraumcharakterisierung und Bestimmung von Gesteinseigenschaften. Systematische Labormessungen an Karbonaten werden durchgeführt, um Gesteinscharakteristika und deren Einfluss auf die IP-Parameter als auch ihre Sensitivität auf Lösungsprozesse zu untersuchen. Die gesteinsspezifischen Untersuchungen umfassen ein multimethodisches Herangehen, welches petrophysikalische, mineralogische und geochemische Verfahren kombiniert, u.a. Spektren der komplexen elektrischen Leitfähigkeit und Daten von 2D und 3D Bildgebungsverfahren als auch Messgrößen wie Porosität, Permeabilität, spezifische Oberfläche und Verteilungen der Nuklear-Magnetischer Resonanz Relaxationszeiten.

Zuerst werden für ein besseres Verständnis der IP-Parameter sowie Polarisationsmechanismen in Karbonaten Probensätze vier verschiedener Typlokationen mit einer großen Variation ihrer petrophysikalischen Eigenschaften untersucht. Zur Untersuchung des Polarisationsverhaltens der Karbonatproben werden verschiedene IP-Experimente durchgeführt und die Ergebnisse mit den vorhandenen Erkenntnissen über Sandsteine verglichen. Vier verschiedene Typen des Polarisationsverhalten können im Phasenspektrum ermittelt werden: (1) ein konstanter Phasenwinkel, (2) ein kontinuierlicher Phasenanstieg, (3) eine Kombinaten aus beiden sowie (4) ein Maximumtyp. Die explizite Zuordnung eines Karbonattyps zu einem charakteristischen Kurventyp ist übertragbar für den gesamten Probensatz. Der Vergleich von IP-Parametern mit petrophysikalischen Daten zeigt, dass es anspruchsvoller ist klare Korrelationen zwischen den Parametern festzustellen, vor allem im Vergleich zu Sandsteinen. Die Übertragbarkeit von empirischen Beziehungen und Modellannahmen, wie z.B. Formationsfaktorabschätzung und Permeabilitätsvorhersage, ist dennoch realisierbar.

Im zweiten Schritt wurde ein Messplatz für systematische Lösungen sowie ein maßgeschneidertes experimentelles Konzept erfolgreich konzipiert und angewendet, um den Einfluss von Lösungsprozessen auf Mineral- und Porenstrukturen unter kontrollierten Laborbedingungen zu untersuchen. Zur systematischen Erfassung der Änderungen im Porenraum wurden vor und nach jeder Lösung gesteinsspezifische Untersuchen vorgenommen. Der Lösungsprozess beeinflusst verschiedene petrophysikalische Parameter mit unterschiedlicher Ausprägung. Während die Korndichte und Porosität zunehmen, erhöht sich zunächst die spezifische Oberfläche und verringert sich in späteren Stufen. Die Porenradienverteilungen aus Quecksilberporosimetrie und μ-CT Daten weisen auf eine Vergrößerung des dominanten Porenradius mit zunehmenden Lösungstufen hin. Die durch die Lösungsprozesse hervorgerufenen Änderungen in den Karbonaten lassen sich bis zu einem gewissen Grad mit SIP beobachten. Der Anstieg im Realteil der elektrischen Leitfähigkeit ergibt sich aus der zunehmenden Porosität sowie dem abnehmenden Formationsfaktor und der abnehmenden Volumentortuosität. Die Form der σ''-Spektren ändert sich ebenfalls, da bei höheren Frequenzen der Imaginärteil der elektrischen Leitfähigkeit zunimmt, was auf die Entstehung kleinerer Poren hindeutet. Die gegensätzlichen Prozesse Glättung und Aufrauung der Porenoberflächen haben eine Abnahme bzw. Zunahme der Oberflächentortuosität zur Folge, was dementsprechend das Verhalten des Imaginärteils der elektrischen Leitfähigkeit beeinflusst. Insgesamt nimmt die Volumenleitfähigkeit stärker zu als die Oberflächenleitfähigkeit. Aufgrund der durch die Lösungsprozesse verursachten kleinen Änderungen der Gesteinsparameter ist die Dateninterpretation herausfordernd. Daher ist weitere Forschung im Bereich von Lösungsprozessen an Karbonaten erforderlich.

Diese Dissertation verdeutlicht das Potential von SIP zur erweiterten Porenraumcharakterisierung sowie Auswertung von Lösungsprozessen von Karbonaten.

Contents

1 Introduction

1.1 Motivation

Subrosion processes and their consequences are worldwide phenomena and constitute an enormous hazard risk (Waltham et al., 2005; Gutiérrez et al., 2014; Sahu & Lokhande, 2015). Subrosion is defined as a circulation of unsaturated water (e.g. ground- and meteoric water) with soluble rocks (e.g. rock salt, anhydrite, gypsum and limestone), which leads to leaching of these rocks and causes an enlargement of the pore space, crack growth, and cavity formation (Smyth, 1913; Martinez et al., 1998; Galloway et al., 1999; Yechieli et al., 2003). Subrosion structures, such as karst, sinkholes and depressions, occur as a final result of mass movement and subsurface cavities (Gutiérrez et al., 2008; Kaufmann, 2014). The sudden collapse of an underground cavity is an unpredictable, but inevitable consequence of the subrosion processes (Rawal et al., 2015), sometimes with catastrophic impacts (Bezuidenhout & Enslin, 1970; Waltham et al., 2005; Gutiérrez et al., 2009; Ford & Williams, 2013). Especially, the occurrence in urban areas can cause

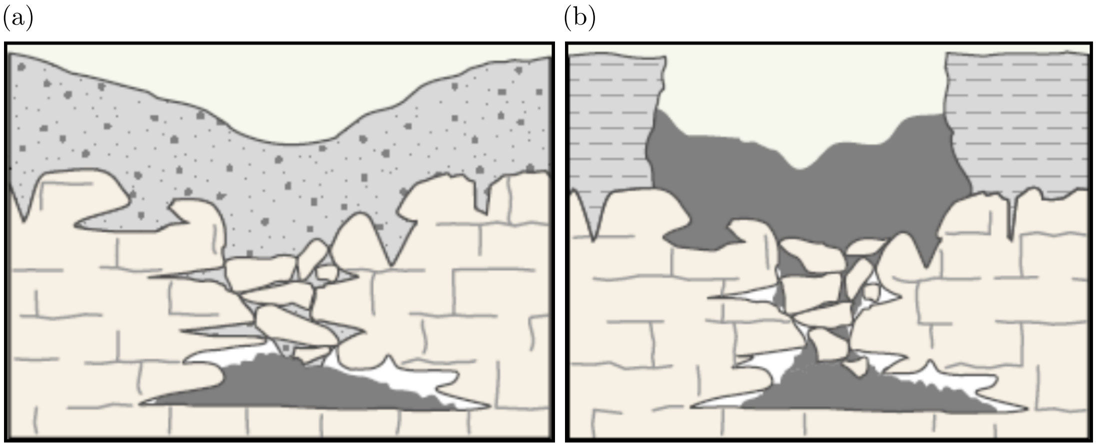

Figure 1.1: Two types of cover sinkholes (after Tihansky, 1999). The dissolution of soluble rocks generates a small cavity at first. a) If the cavity is covered by soft sediments, the overlying sediments continuously settles into the void and generates a surface depression. b) If the cavity is covered by solid rocks, the void increases over time and forms a structural arch. The cavity migrates upwards by progressive roof collapse and a sudden sinkhole collapse occur as final result.

life-threatening situations and damage to buildings and infrastructure (Waltham, 2002; Brinkmann et al., 2008; Lei et al., 2013). Hence, a better understanding of subrosion processes is necessary in order to improve risk assessment and forecasting. Accordingly, subrosion is a topic of high social relevance. In contrast to other natural hazards, like earthquakes and tsunamis, the current stage of knowledge about subrosion processes and therefore about the ability of predicting such events is insufficient.

Junior research group 'Subrosion' A junior research group 'Subrosion' was established at the Leibniz-Institute for Applied Geophysics (LIAG) with the objective to obtain new insights about subrosion structures and their underlying processes. The complexity of the processes requires an integrated geophysical approach to investigate the fundamentals of subrosion structures, hydraulics mechanics, and dissolution and transport processes. The junior research group uses five methodological approaches on different spatial and temporal scales:

(1) **Petrophysics including Spectral Induced Polarisation (SIP)**
The first work package led to this dissertation and investigated subrosion processes on a pore scale for an enhanced pore-space characterisation and analysis of dissolution processes of carbonate rocks. This is done using SIP, which is a suitable method to conduct fundamental research at the laboratory scale as well as to be applied at the field scale.

Fundamental research is essential to obtain new insights about process understanding, since otherwise only phenomenology is possible. The results of this doctoral thesis supports the other work packages in order to obtain an improved understanding of subrosion processes and their resulting structures as follows:

(2) **Surface deformation and gravimetry**
The second work package uses repeated time-lapse gravity and levelling surveys in order to observe time-dependent subrosion-induced mass changes and to identify local hazard zones. Petrophysical parameters like porosity, density, and information regarding subrosion rates from dissolution experiments can be used as input for gravimetric modelling. The underground model includes the temporal distribution of mass movement and supports the understanding of subrosion processes.

(3) **Near-surface shear wave and borehole reflection seismics**
The third work package uses high-resolution shear-wave reflection- and borehole seismics to image structural features of subrosion structures and

their spatial variability in order to characterise unstable zones with elastic parameters and seismic attributes. The laboratory analysis provides input parameters for correlation of the petrophysical parameters, e.g. elastic moduli, porosity, and permeability, with geological structures and fracture zones, and petrophysical parameters derived from seismic data (Scaling).

(4) **Electromagnetics**
Work package four uses electromagnetic methods, ground penetrating georadar (GPR) and electrical resistivity measurements to characterise karst structures, sinkholes and disaggregation zones. The findings of the laboratory analysis can be used to correlate water content, permeability, porosity and the results from the dissolution experiments with spatial distribution of electrical conductivity. Scaling of the results can lead to identification of fluid pathways and subrosion zones.

(5) **Numerical modelling**
Work package five utilise numerical modelling to simulate the collapse mechanisms associated with sinkhole occurrence. A better understanding of the dissolution processes on pore scale, regarding pore structure changes and involved rock components, supports the modelling of cavity formation and changes of rock parameters such as for example porosity and permeability. The dissolution processes can be simulated on pore or field scale until rock failure, including the simulation of hazard scenarios as sinkhole formation from fracture generation to unstable zones.

Figure 1.2 presents a schematic overview, how the laboratory results of this work have to be planned to be implemented into the other studies. Important input quantities are petrophysical parameters - especially the electrical conductivity - as well as their changes during induced dissolution experiments. The upscaling of IP data from the laboratory to the field scale will lead to challenges regarding the interpretation of the results, because the data error increases significantly. Nevertheless, scaling of the results from core samples to field scale supports the understanding of the subrosion process and sinkhole formation across scales. Finally, the overall aim is to develop a reliable sinkhole monitoring and forecasting system on the basis of the combined results of the integrated geophysical approach.

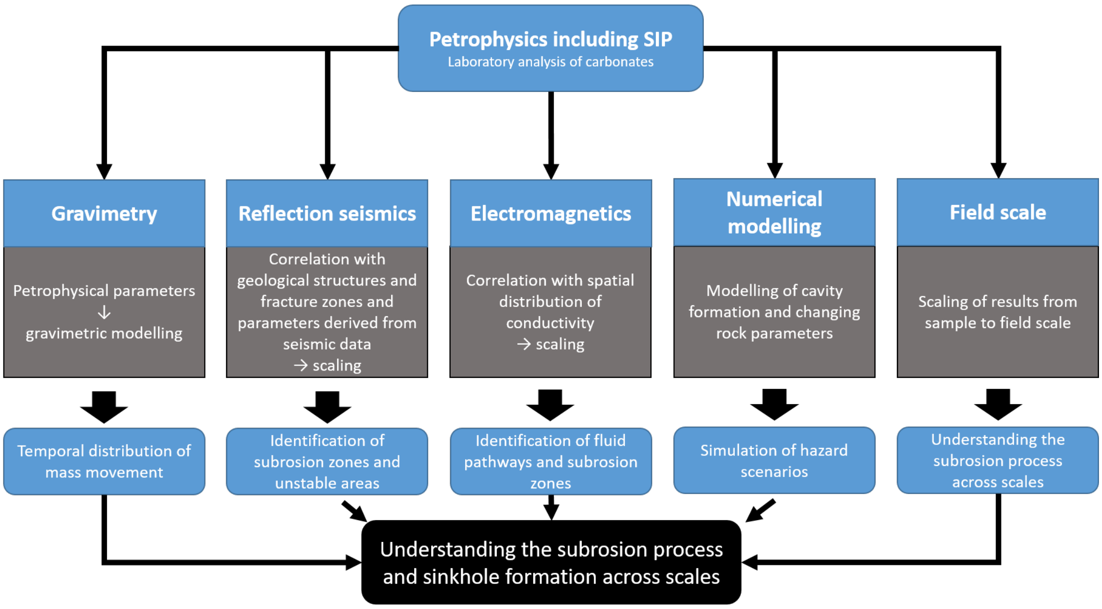

Figure 1.2: Recommended workflow of research group 'Subrosion' showing how the laboratory results of this work have to be planned to be implemented into the other studies.

1.2 State of the art

Methodical subrosion research

Currently, research on subrosion processes and their resulting structures is conducted by a variety of methods, including subsurface as well as near surface geophysical applications. A comprehensive overview is given by Gutiérrez (2016). Series of studies have focused upon the understanding and imaging of subrosion structures and are reviewed in Waltham et al. (2005). Monitoring the development of sinkholes and surface deformation is done by airborne and satellite images (Cooper & Waltham, 1999; Alexander et al., 2013), e.g. pinpointing masked sinkholes by old images (Festa et al., 2012). Additional methods are airborne photogrammetry (Dou et al., 2015; Al-Halbouni et al., 2017), airborne LiDAR (Light Detecting And Ranging) (Miao et al., 2013), and InSAR (Synthetic Aperture Radar Interferometry) (Atzori et al., 2015). The airborn methods provide information about subsidence rates, sinkhole activities, and ground deformation. The data are used to analyse spatial and temporal evolution patterns. For small-scale studies and local investigations ground-based geodetic methods are more suitable, e.g. ground-based LiDAR (Benito-Calvo et al., 2018) and InSAR (Intrieri et al., 2015), as well as high-precision levelling (Desir et al., 2018). To forecast karst collapse by detection of changes in physical properties and geometrical features, subsurface methods as geophysical surveys are applied. Voids, fluid paths, and aquifers can be identified by ERT (eletrical resistivity tomography) and GPR

(Gómez-Ortiz & Martín-Crespo, 2012; Carbonel et al., 2014; Miensopust et al., 2015). Furthermore, GPR is a valuable tool to image near-surface structures in a few meters depth (Rodriguez et al., 2014). Other geophysical methods are electromagnetics (Frumkin et al., 2011) and micromagnetics (Rybakov et al., 2005). Gravimetry is used to detect subrosion-induced mass-movement (Patterson et al., 1995; Tuckwell et al., 2008; Kobe et al., 2019). Information on physical rock parameters can be obtained by borehole logging. (McDonnell et al., 2007; Song et al., 2012). Imaging of sinkholes and karst structures and the determination of seismic velocities can be obtained by P-wave reflection (Sargent & Goulty, 2009) and refraction seismics (Higuera-Díaz et al., 2007), S-wave seismics (Wadas et al., 2016, 2017), and borehole seismics. Joint geophysical approaches are used for multidisciplinary field studies (Tuckwell et al., 2008; Kaufmann et al., 2018). For describing the collapse mechanisms and underground stress distributions, numerical modelling is a feasible method (Augarde et al., 2003; Al-Halbouni et al., 2018; Kaufmann et al., 2018).

SIP in general and on carbonates

Induced polarisation (IP) is a geophysical method that measures the low-frequency electrical properties of rocks and soil material. Originally, IP was developed for detection of mineral deposits and became popular in the middle of the 20th century (Van Voorhis et al., 1973; Pelton et al., 1978), e.g. differentiation between electrolytical and metallic conductors (Bleil, 1953). During the last 30 years, IP has been extensively used in hydrogeological and environmental studies (Vanhala & Peltoniemi, 1992; Börner et al., 1993; Kemna et al., 2012; Revil et al., 2012a) with major interest on flow and transport properties, fluid content and fluid chemistry. For a theoretical description of the complex electrical conductivity in porous media different models are developed (Dias, 2000). A common theory is the membrane polarisation model (Marshall & Madden, 1959; Bücker & Hördt, 2013a; Hördt et al., 2017) explaining polarisation by calculation of ion dynamics in the pore-space electrolyte in the presence of pore constriction with the pore length as the characteristic scale. Further mechanistic polarisation models are based on the polarisation of the electrical double layer surrounding the mineral grains implying that the controlling parameter is the grain size or the grain size distribution (Leroy et al., 2008; Revil & Florsch, 2010).

SIP is commonly used for investigating electric rock properties of sandstones and sandy materials on the laboratory scale. Several studies have discussed the connection between intrinsic structural characteristics and the resulting spectral

IP signature, in order to prove the general applicability of the method. IP has been proposed as a potential method for permeability estimation by Börner et al. (1996); Slater & Lesmes (2002); Weller et al. (2010a); Revil & Florsch (2010); Zisser et al. (2010); Weller et al. (2015a); Robinson et al. (2018). The specific surface is frequently used to characterise the transport properties of porous media and the influence on IP parameters is well established (Börner et al., 1996; Weller et al., 2010b; Revil, 2012). Several studies investigated the influencing factors of the IP parameters with focus on fluid chemistry (Vaudelet et al., 2011), saturation (Ullrich & Slater, 2004; Jougnot et al., 2010; Breede et al., 2012), temperature (Binley et al., 2010; Zisser et al., 2010; Martinez et al., 2012; Bairlein et al., 2016), salinity (Vinegar & Waxman, 1984; Lesmes & Frye, 2001; Slater & Glaser, 2003; Weller et al., 2011) multiple fluid phases (Cassiani et al., 2009; Schmutz et al., 2010; Revil et al., 2011), pressure (Zisser & Nover, 2009), grain size distributions (Revil & Florsch, 2010), pore size distributions (Florsch et al., 2014; Revil et al., 2014; Zhang et al., 2017), pH-value (Skold et al., 2011; Hördt et al., 2016), and the effect of micobiological processes (Atekwana & Slater, 2009). The lithological properties of the rock affect the IP response and a yet unsolved and a highly controversial subject is which parameter and length scale control the imaginary part of conductivity of a porous medium (Revil, 2014; Weller et al., 2014; Volkmann & Klitzsch, 2016; Kruschwitz et al., 2016).

So far, complex electrical behaviour of sandstones, building materials and sandy materials are studied intensively (Titov et al., 2010; Kruschwitz et al., 2010; Weller et al., 2015b), while IP variations in carbonates have rarely been investigated in previous research. The first lab study was conducted by Wu et al. (2010) to quantify the IP response of calcite precipitation with a glass beads experiment. The calcite precipitation produces a characteristic IP signature, which is directly related to the volume fraction and the grain size. Only a few other working groups have focussed on research concerning IP characteristics of carbonates. A field study of Johansson et al. (2016) used time domain-induced polarisation to image the upper surface of the Cretaceous limestone and has explained the observed variations in Cole-Cole parameters. Norbisrath et al. (2017) investigated dolomites with regards to relationships between kHz-frequency complex electrical resistivity spectra and pressure, petrophysical properties and pore structure. They also combined their results with digital image analysis on thin sections. They concluded that complex resistivity spectra are directly linked to the carbonate pore structure. A study of Müller-Huber et al. (2018) interpreted SIP measurements on mud-dominated and grain-dominated carbonate rocks in combination with magnetic resonance (NMR) and mercury intrusion (MIP) measurements with focus on the correlation of characteristic SIP parameter with pore geometrical data.

1.3 Research questions and chapter description

It is of high research interest to study carbonate rock characteristics and their influence on IP responses systematically. A better understanding of the IP responses and mechanisms in carbonates in order to investigate and identify the causes of variations (e.g. IP signal, petrophysics, mechanistics) is necessary. The existing knowledge about SIP on sandstones and sandy materials will be applied to carbonate rocks. It is well known, that the IP response is dependent on pore geometry and transferred to carbonates, possibly by fossils, texture or changes caused by carbonate dissolution and precipitation processes in the rock.

The remarks in the introduction are leading to various hypotheses and thus to scientific questions, which may be answered in a systematic study on complex electrical conductivity behaviour of carbonates:

- Do carbonate rocks have polarisation effects?
- How can the causes of polarisation behaviour be determined?
- Is it possible to transfer empirical relationships and model assumptions from sandstones to carbonates?

The objectives include (1) the extension of the carbonate data base related to SIP, (2) comparing the results with existing relationships and the better understood polarisation of sandstones, and (3) the improving of the SIP data processing for a better correlation and prediction of petrophysical parameters from SIP as well as (4) the understanding of polarisation phenomena of carbonates.

The second part deals with dissolution experiments on carbonates. It includes (1) a systematic modification of the pore space (2) with measuring the change of the petropyhsical parameters and (3) the quantification of the influence on the IP effect in order to determine subrosion sensitive parameters. To achieve this, an experimental setup for systematic dissolution under monitoring condition and an individual adopted measuring concept will be developed and a suitable acid will be chosen for the treatment of the samples. Hence, the following scientific questions arise:

- Does the experimental setup work for systematic dissolution under monitoring conditions?
- Is the chosen acid suitable for the systematic manipulation of the pore space?
- Which quantitative changes are observed in the pore space?
- Are there other advantages of SIP?
- What is the potential influence of pore geometric effects on IP derived parameters or what is the influence of the dissolution process on the IP Effect?

First, this doctoral thesis introduced to the scientific topic in chapter 1. Next, chapter 2 provides the principles of complex electrical conductivity to introduce the physical fundamentals, conductivity mechanisms, induced polarisation as well as common model assumptions for analysing the IP response. Chapter 3 introduces the used petrophysical, mineralogical and geochemical methods. The method SIP and the dissolution experiment are described in detail. Necessary information about basic petrophysical properties and mineralogical composition of the investigated carbonate samples are given in chapter 4 as well as a general description of carbonates. Chapter 5 presents the results, which are divided into combined rock evaluation, methodical investigation of carbonate rocks and the dissolution experiment. Chapter 6 discusses the results of the systematic investigation of the complex electrical conductivity on carbonates and dissolution experiment with regard to subrosion. Chapter 7 concludes and summarises the key findings of this thesis and takes a brief look onto future work.

2 Principles of complex electrical conductivity

2.1 Physical fundamentals

The electric conductivity and dielectric polarisation belong to the fundamental physical rock properties and describe how charges are transported. The physical fundamentals of the electromagnetic phenomena are expressed by the Maxwell's equations (Maxwell, 1865). These laws include the Gauss's law, the Maxwell-Faraday equation, and the Amperès's circuit law with the Maxwell's addition. The total current density $\mathbf{J_t}$ is an additive term of two components: (1) the electric current density $\mathbf{J_c}$, which results from the transport of charges, and (2) the displacement current density $\mathbf{J_d}$, which only occurs when the applied field varies with time. According to that the Amperè's circuit law can be written as:

$$\nabla \times \mathbf{H} = \mathbf{J_t} = \mathbf{J_c} + \mathbf{J_d}, \tag{2.1}$$

where

$$\mathbf{J_d} = \frac{\partial \mathbf{D}}{\partial t}. \tag{2.2}$$

H is the magnetic field intensity and **D** the electric displacement. In a homogeneous isotropic media, the variables of the electromagnetic theory are connected through the constitutive relations (Nabighian, 1988):

$$\mathbf{J_c} = \sigma^* \cdot \mathbf{E} \tag{2.3}$$

and

$$\mathbf{D} = \epsilon^* \cdot \mathbf{E}, \tag{2.4}$$

with **E** being the electric field intensity. The electrical conductivity of a material describes after Equation 2.3 the transport process of charges, which is also known as Ohm's law. The dielectric polarisation represents the process of charge accumulation (see Eq. 2.4) (Glover, 2015). The quantity σ^* is the electrical conductivity and ϵ^* the dielectric permittivity. Both quantities are frequency dependent and in general written as complex quantities (Schön, 2004):

$$\sigma^*(\omega) = \sigma'(\omega) + i\sigma''(\omega) \tag{2.5}$$

and

$$\epsilon^*(\omega) = \epsilon'(\omega) + i\epsilon''(\omega), \tag{2.6}$$

where $i = \sqrt{-1}$. The angular frequency ω is related to the technical frequency f by $\omega = 2\pi f$. The quantities $\sigma'(\omega)$ and $\epsilon'(\omega)$ are the real parts and $\sigma''(\omega)$ and the $\epsilon''(\omega)$ are imaginary parts of the complex quantities. If we consider a time-dependent electrical field and regarding the constitutive relations (Eq. 2.3 and 2.4) $\mathbf{E} = \mathbf{E_0}e^{i\omega t}$, the Amperès's circuit law (Eq. 2.1) must be written in frequency domain as follows:

$$\begin{aligned} \mathbf{J_t}(\omega) &= \sigma^*(\omega) \cdot \mathbf{E}(\omega) + i\omega\epsilon^*(\omega) \cdot \mathbf{E}(\omega) \\ &= [\sigma^*(\omega) + i\omega\epsilon^*(\omega)] \cdot \mathbf{E}(\omega) \end{aligned} \tag{2.7}$$

Induced Polarisation considers low-frequency measurements. In this frequency range the quasi-static approximation $|\sigma| >> |i\omega\epsilon|$ is valid, if $f < 10^5\,\text{Hz}$. Under this condition the displacement current density can be neglected. Besides the notation using the real and imaginary part σ' and σ'', the complex electrical conductivity can be presented by magnitude $|\sigma^*|$ and phase angle φ:

$$\sigma^*(\omega) = |\sigma^*|e^{i\varphi} \tag{2.8}$$

with

$$|\sigma^*| = \sqrt{(\sigma')^2 + (\sigma'')^2} \tag{2.9}$$

and

$$\tan(\varphi) = \frac{\sigma''}{\sigma'}. \tag{2.10}$$

Whereas the real part σ' represents the ohmic conduction, the imaginary part or quadrature conductivity component σ'' includes all polarisation phenomena. The complex conductivity is related to complex resistivity ρ^* by the reciprocal.

2.2 Conductivity mechanisms

The electrical conductivity is the most important physical property to determine the propagation behaviour of the electromagnetic field in a medium (Knödel et al., 2013). Porous media consist of the three components: grains, pores and interfaces between those two that characterised by different electrical conductivity mechanisms. Hence, the total conductivity of rocks is described by the conductivity of the matrix σ_m, the electrolytic conductivity σ_el and the conductivity between bulk and pore space filling σ_surf. The conductivity σ of a rock is a function of fluid conductivity, porosity, saturation and the texture of the material (Glover, 2015; Guéguen & Palciauskas, 1994). The electrical conductivity is a highly dynamical physical material property with a range over 25 orders of magnitude (Knödel et al., 2013).

2.2.1 Matrix conductivity

The matrix conductivity of most silicates, sulfates and carbonates is negligible (10^{-14} - $10^{-10}\,\mathrm{S{\cdot}m^{-1}}$) (Knödel et al., 2013), so that the solid rock matrix can be considered as insulator. Only for ore-bearing rocks (e.g., sulfides or graphites), electronic conduction or metallic conduction as a special form of the matrix conductivity has to be taken into account. The electronic conduction is caused by charge transport of free electrons in the solid rock matrix. The electronic conductivity has a significant effect if present.

2.2.2 Electrolytic conductivity

In general, the pore space is filled with pore fluids which contain dissolved ions. Their movement through the pore space is the cause of the electrolytic conductivity. As this is a purely ohmic conduction mechanism, it is frequency independent and described by the real part of the conductivity. Because σ_m is negligible in comparison with σ_el, the electric conduction of a rock is directly proportional to the electric conductivity of the pore water σ_w. Obviously increasing ion concentration in the pore fluid, thus a higher amount charge carriers, leads to an increase of σ_w as well as σ_el (Telford et al., 1990). The Archie law for a clay-free and ore-free, fully saturated medium is valid (Archie, 1942):

$$F = \frac{\sigma_\mathrm{w}}{\sigma_\mathrm{el}} = \frac{a}{\Phi^m m}, \tag{2.11}$$

where F is the resistivity formation factor, which was originally defined as the ratio between fluid conductivity σ_w and the conductivity of the fully saturated sample σ_el. Φ is the porosity, m the cementation exponent and a a proportional factor. The empirically determined parameters m and a are controlled by the pore-space geometry (constrictivity, tortuosity) (Schön, 2004). The exponent m varies from 1.3 for unconsolidated sands to 2.0 for consolidated sandstones (Rubin

& Hubbard, 2006). A derivation of cementation exponents using a cross plot of the formation factor versus porosity is proposed by Schön (2004). For chalky limestones, the estimated m is between 1.7 - 1.8, whereas crystalline and granular carbonates lead to $m = 1.8 - 2$ and carbonates with vugs to cementation exponents above 2.

If the clay-free rock is only partly saturated, the conduction is affected by a reduction of the fluid saturation S_w. This dependence is described by an extension of the original Archie law (Archie, 1942):

$$\sigma_\mathrm{el} = \frac{\Phi^m}{a} \sigma_\mathrm{w} S_\mathrm{w}^{\,n}, \tag{2.12}$$

where S_w is the saturation with the associated saturation exponent n. It should be keep in mind that Archie's laws are originally empirical and only valid for so-called clean rocks (Glover, 2015).

2.2.3 Surface conductivity

An additional conduction mechanism occurs at the interface between mineral surface and pore fluid (Revil & Glover, 1997). The interaction of pore fluid and solid rock matrix causes the surface conductivity σ_surf. This surface conduction mechanism results from a current flow along the area of the grain surface. This contribution to the total conductivity has to be considered in the Archie equation (Eq. 2.11). The extension is made by assuming a parallel arrangement of σ_surf and σ_el (Rink & Schopper, 1974):

$$\sigma_0 = \frac{\sigma_\mathrm{w}}{F} + \sigma_\mathrm{surf} \tag{2.13}$$

and

$$\sigma'' = \sigma''_\mathrm{surf}. \tag{2.14}$$

The strength of the surface conductivity is controlled by pore surface properties, e.g. the connectivity of the surface conduction pathways, the characteristic pore size of a rock and the solution chemistry (Waxman & Smits, 1968). The surface conductivity is dominant at low pore fluid salinities and for rocks containing a significant fraction of clay (Glover, 2015). The described interface is regarded as an electric double layer (EDL). The EDL is important for the polarisation behaviour of a rock and responsible for the membrane polarisation and Stern-layer polarisation.

Electrical double layer

An electrical double layer arises along a mineral surface. The grain surface develops a negative surface charge when in contact with an electrolyte forming an electrical potential (Lesmes & Frye, 2001). Hence, positively charged ions from the electrolyte are attracted and accumulated on the mineral surface. This fixed layer of adsorbed cations is called Stern layer (Stern, 1924). Due to a shielding effect of the Stern layer, the concentration of anions is zero. Next to the Stern layer is the diffuse layer, which is a zone of higher ion mobility. The layer is characterised by an exponentially decreasing cation concentration with increasing distance from the grain surface, whereas the anion concentration increases simultaneously (Grahame, 1947). The diffuse layer gets thinner for an increasing fluid conductivity, i.e. salinity (Glover, 2015). Next to the diffuse layer follows the free electrolyte, in which anions and cations are not influenced by the electrical potential of the grain surface. The concentration of anions and cations is the same and the ions are able to move freely.

2.3 Induced polarisation

Induced Polarisation (IP) is a current-stimulated electrical phenomena, which results from the frequency dependency of the complex electrical conductivity of rocks (Schön, 2004). The IP-effect can be observed as delayed voltage response (Ward, 1990), because the earth material behaves like a capacitor. While transmitting current, energy will be stored in a polarisable medium, which is observable as a transient voltage after shut off the current (Knödel et al., 2013). Frequency effects can be measured in time domain referred to as TDIP (Time Domain Induced Polarisation) or in frequency domain referred to as SIP (Spectral Induced Polarisation). Both domains measure the same polarisation effects and can be, in theory, transformed into each other by Fourier transformation (Schön, 2004). The assumption for a correct transformation from time to frequency domain is an infinite measurement time.

The time-domain effect is shown in Figure 2.1. The IP-effect can be observed after an abrupt interruption of the primary current. The voltage does not drop off to zero instantaneously, but decreases suddenly from the value U_1 to a residual value U_2 (Lowrie, 2007). Afterwards the voltage decays asymptotically and continuously to zero. The decay time may last seconds or even minutes (Telford et al., 1990). Conversely, when a constant current is switched on, a similar observation is made.

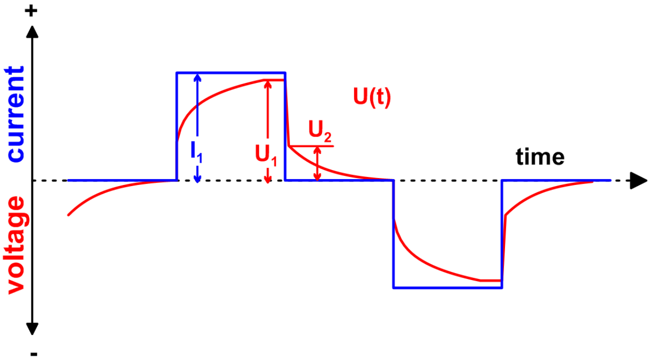

Figure 2.1: Schematical description of the time variation of a typical inducing current signal and the corresponding voltage signal over a polarisable underground. The current signal has a box-like appearance and the voltage signal $U(t)$ shows a charge and a discharge curve.

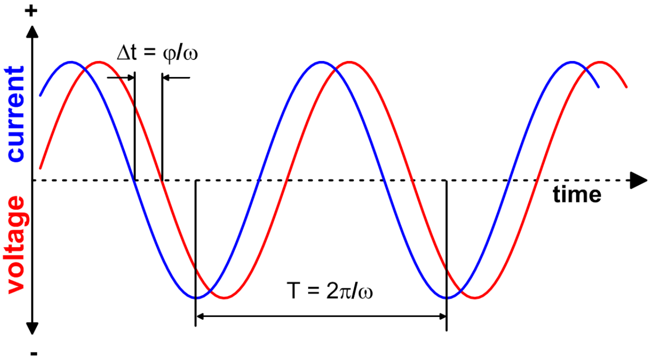

Figure 2.2: Schematical description of a typical injecting current signal and the corresponding voltage signal over a polarisable underground. The inducing current is an alternating current for a defined frequency ($f = T^{-1}$) and the voltage signal shows a time shift Δt towards the current signal.

The potential increases abruptly to a certain value U_2 and increases slowly within a similar time interval to the direct current (DC) amplitude U_1.

In the frequency domain the injecting current is an alternating current instead of a constant current. The amplitudes of the measured voltage respective the electrical conductivity are considered for various frequencies. Figure 2.2 shows the behaviour of both signals for one frequency. The induced polarisation phenomenon results in frequency domain in a phase shift between the injecting current signal and the corresponding voltage signal plus an increase of the conductivity (Knödel et al., 2013). The IP-effect causes higher voltages for lower frequencies, because the time for building up the full voltage is reduced for high frequencies (Militzer & Weber, 1985).

Induced polarisation is a method, which was originally developed for ore exploration, prospection and characterisation of mineral deposits (Bleil, 1953; Van Voorhis et al., 1973; Pelton et al., 1978; Seigel et al., 2007). Because of the strong polarisation effects of ores (Bleil, 1953), this method, besides and as extension of the conventional classic direct current geoelectrical method, was predestined to distinguish between electrolytic and metallic conductors. Currently IP is a well-established geophysical exploration method (Kemna et al., 2012). Near-surface investigations in relatively low-polarisable, sedimentary environments have gained increasing importance in research in the last three decades. Hydrogeological and environmental investigations were made with major focus on flow and transport properties as well as fluid content and chemistry. After Schön (2004) polarisation effects are influenced by type, volume fraction and distribution of electronic conducting material and clay minerals, size and shape of grains and pores as well as type and salinity of the electrolyte in the pore channels. Further important factors are water saturation, temperature, porosity and permeability.

Polarisation mechanisms

The applying of an electrical field generates an imbalance with regard to the electric charge. The ions of the fluid aim to rearrange to a new state of equilibrium. Various electrochemical processes are the reasons, why this compensation movement is delayed or the charge exchange is inhibited. This processes could be the interaction between ions and electrons, properties of the mineral interface, cation-exchange processes, pore constrictivity and further effects, which depend on the rock properties and their interaction (Schön, 2004). Many fundamental studies deal with polarisation in porous solid rocks and in unconsolidated materials. At frequencies below 1 MHz five different main mechanism control the polarisation behaviour (Kemna et al., 2012): (1) Maxwell-Wagner polarisation (Lesmes & Frye, 2001), (2) Stern layer polarisation (Leroy et al., 2008), (3) diffuse layer polarisation (Dukhin, 1991), (4) membrane polarisation (Titov et al., 2002), and (5) electrode polarisation (Wong, 1979). The polarisation mechanism types (2) to (5) belong to low frequencies effects, while the Maxwell-Wagner Polarisation (Maxwell, 1865; Wagner, 1914; Bruggeman, 1935; Hanai, 1960) becomes relevant for higher frequencies (above 1 kHz). High-frequency polarisation effects can be explained by atomic oder molecular structures, the low-frequency mechanisms are related to the electromigration of ions and depends on the various conductivity mechanism. Electrode reactions between metal mineral grains and electrolytes as well as differences of the ion mobility in rocks are important phenomena, which contribute to the induced polarisation (Telford et al., 1990). Two typical polarisation mechanism are described below.

Electrode polarisation

Electrode polarisation occurs in ore bearing rocks and is based on the different mobilities of ions and electrons. The change of the conductivity mechanisms from electrolytic to electronic conduction (mineral-electrolyte interface) produces a polarisation effect. A schematic sketch of the electrode polarisation is shown in

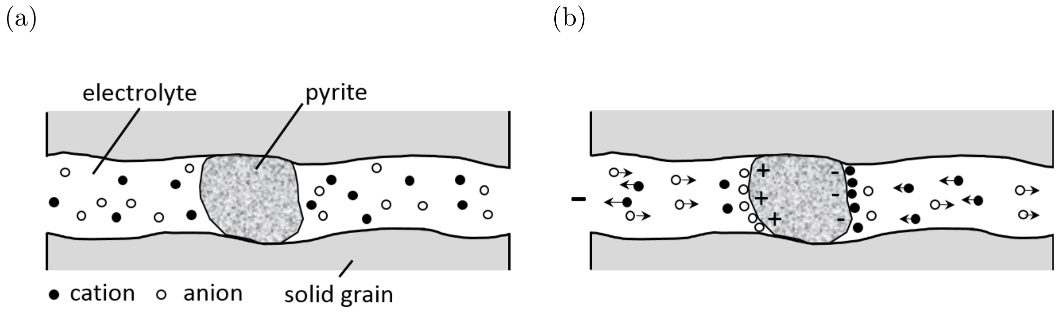

Figure 2.3: A simplified model of the electrode polarisation mechanism. It shows a pyrite bearing rock with an pore path with ionic solution. a) Distribution of ions within the pore fluid without an external electrical field. b) Accumulation of ions at the grain-fluid interface after applying an external electrical field (modified after Telford et al., 1990).

Figure 2.3. After applying an external electrical field, cations and anions move in opposite directions. At the interface between fluid and ore mineral no charge exchange is possible, because of the different conduction mechanisms (Schön, 2004). The electrons in the metallic grain have a higher velocity than the ions in the fluid (Lowrie, 2007). Charges of opposite sign accumulate on facing surfaces of the ore mineral, which blocks the pore space. This produces an overvoltage after the external current is switched on. After turning off the external current, the residual voltage decays slowly and the ions return to an uniform distribution again (Lowrie, 2007).

Membrane polarisation

The membrane polarisation effect is one magnitude lower than that of the electrode polarisation. It belongs to the electrolyte-interface polarisation, which is caused by the different abilities of ions to move through the pore space (Lowrie, 2007) as e.g. ion mobilities and diffusion processes (Schön, 2004). Membrane polarisation occurs in non-mineralised rocks with clay particles (Fig. 2.4) as well as in clay-free rocks (Fig. 2.5). Figure 2.4 shows membrane polarisation of a porous rock containing clay. The clay particle blocks the pore path of the ionic flow through the pore solution (Schön, 2004). An accumulation of cations takes place at the negative charged surface of clay minerals and forms a cloud of cations. If an external electrical field is applied, the barrier of cations prevent the anions to pass through this area and an ion-selective membrane is formed. Hence, there are zones with a surplus of anions respective cations on one side of the membrane and a lack of corresponding ions on the other side. If the external electrical field is switched off, the ions return into equilibrium state.

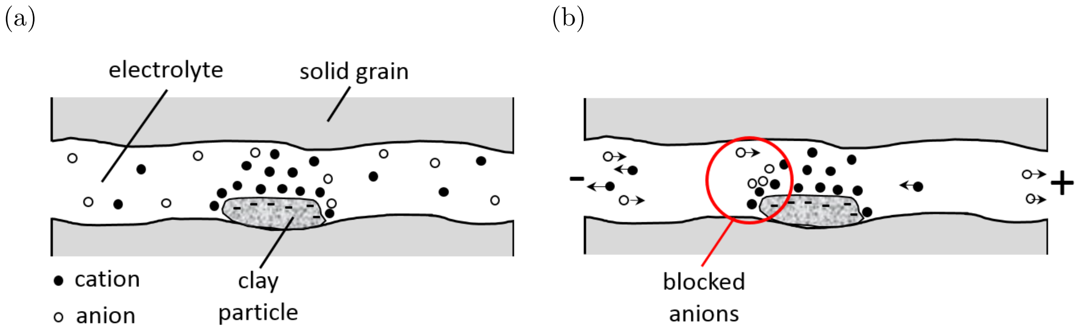

Figure 2.4: A simplified model of the membrane polarisation mechanism in a clay-bearing rock with an ionic solution. a) Distribution of ions within the pore fluid without an external electrical field and accumulation of cations at the clay surface. b) Blockade of the anions movement due to the cloud of cations after applying an external electrical field (modified after Schön, 2004).

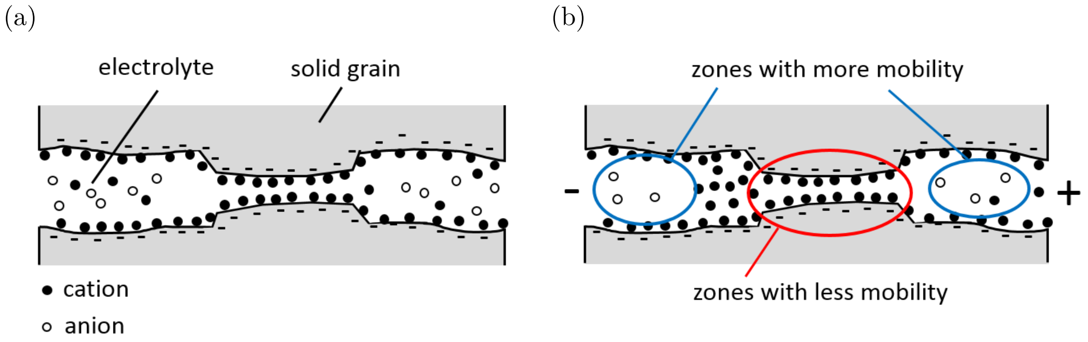

Figure 2.5: A simplified model of the membrane polarisation mechanism because of pore constrictivity. It shows a pore system of narrow and wide pores with ionic solution. a) Distribution of ions in the pore system without an external electrical field. b) Appearance of zones with more and less mobility after applying an external electrical field (modified after Schön, 2004).

Polarisation also depends on pore constrictivity. For example, narrow pores lead to stronger polarisation effects compared to large/wide pores. If the diameter of the pore throats is in the range of the thickness of the EDL, cations cannot pass and accumulate in front of the throat. Figure 2.5 shows a pore system made of wide and narrow pores. Zones with less mobility occur at the entrances to narrow pores respective pore throats, reducing the ion mobility and thus affecting the current flow (Knödel et al., 2013). Zones with higher mobility are located in the area of the wide pores, in which the mobility of the ions is not restricted. The entire pore space is composed of these zones. Under the influence of an external electrical field, these zones have a local concentration gradient. Summarizing a surplus or lack of cations respective anions occurs in the transition zone from wide to narrow pores and the other way round (Schön, 2004).

2.4 Models

This chapter explains model assumptions for SIP and the approach for analysing the observations of SIP measurements. The theoretical description of the IP effect and mechanism is challenging and there is a lack of physical understanding the measured response. Mathematical models offer a good fitting to describe the measured spectra but provide no information about the physics behind it. Physical models, which are rarely available for polarisation phenomena are mostly valid only for simplified model cases. Empirical models/relationships between the derived quantities and the IP-parameter are used as well for understanding of polarisation behaviour. The three model types will be explained in more detail in the following.

2.4.1 Mathematical models

A quantitative interpretation is essential for an evaluation of SIP data. For this purpose, mathematical models are used, which are based on empirical relationships or phenomenological models. From these models several SIP parameters can be derived. Numerous models describe the electrical behaviour of the material by an equivalent circuit to characterise the IP data with parametric values. The equivalent circuits are able to reproduce very well the relaxation properties of the material. The problems are that not all spectra can be fitted properly with the same model and it is challenging to find a quantitative solution (Nordsiek & Weller, 2008). Mathematical models are limited, because they offer no mechanistic information for interpretation of IP measurements and no information on physical processes. Hence, analytical models have less predictive power (Revil, 2012), it is method of choice to interpret IP spectra, when only few parameters are available. Over several decades various models were developed, which are described by Dias (2000).

Cole-Cole family

One of the well known and most commonly used phenomenological models is the one presented by Cole & Cole (1941) for permittivity. The approach is equally applicable to IP spectra. The generalised form of the Cole-Cole model uses five independent parameter to describe the spectra with the following model function:

$$Z(\omega) = R_0 \left(1 - m \left(1 - \frac{1}{(1 + (i\omega\tau)^c)^a}\right)\right), \tag{2.15}$$

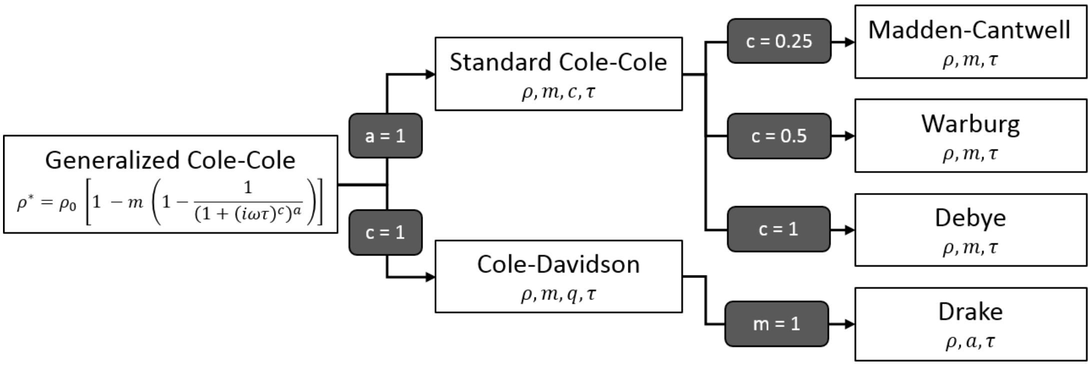

Figure 2.6: The scheme shows selected special cases of the Cole-Cole-family with different degrees of freedom. All models can be found in the comprehensive list of Dias (2000).

where $Z(\omega)$ is the frequency dependent impedance and ω is the angular frequency. The five independent parameters are the chargeability m, the time constant τ of the relaxation process, the DC-resistance R_0 and the two dimensionless exponents a and c, which describe the asymmetry of the phase spectra and the broadness of the relaxation time distribution. The function of the general Cole-Cole model is the base for various number of special case models, which are distinguished from each other only by minor modifications (Fig. 2.6).

If c is 1, the generalised Cole-Cole model is simplified to Cole-Davidson model (Davidson & Cole, 1950). According to this model, the phase spectra have a slope of 1 at the low-frequency side of the phase peak and an arbitrary 1 $(-a)$ at the other side. If a is 1, the resulting model will be symmetrical and referred to as standard Cole-Cole model (Cole & Cole, 1941). This special case was originally formulated to describe the behaviour of dielectric properties and was subsequently adopted by Pelton et al. (1978) to describe complex resistivity spectra. If c is 0.5, the standard Cole-Cole model is called Warburg model after the $(i\omega)^{-0.5}$ behaviour of Warburg impedances (Warburg, 1899). Revil et al. (2014) use this transfer function to determine the pore size or the pore-size distribution on siliciclastic rocks. A special case of the Cole-Cole model is the Debye model for which c is 1 as well. Figure 2.6 shows an overview of several relaxation models of the Cole-Cole family with corresponding resistivity formulation.

A comparison of some of the mentioned models is given by Nordsiek & Weller (2008), who analyse spectra of slag-sand mixtures. Due to the high degree of freedom, the generalised Cole-Cole model offers a high fitting quality of the data, but the correlation towards the petrophysical characteristics is very poor, whereas the Cole-Davidson model provides well correlated parameters, but a bad fitting quality. If more than one peak occurs in the phase spectra, then the results do not fit with the Cole-Cole model. Therefore a combination of several Cole-Cole models is necessary.

Debye decomposition

The simplest relaxation model is the classic Debye model (Debye, 1929). The Debye model describes orientated dipole polarisation, more precisely viscous dielectrics. A polarisation with a single relaxation process can be characterised by a Debye relaxation:

$$\epsilon^* = \epsilon_\infty + \frac{\epsilon_0 - \epsilon_\infty}{1 + (i\omega\tau)}, \tag{2.16}$$

with ϵ_0 and ϵ_∞ being the asymptotes of permittivity at low and high frequency, respectively. The parameter τ denotes the relaxation time of the exponential decay curve which is used to describe the discharge of a capacitor in an electrical circuit. In the Debye decomposition, the general response of complex conductivity is considered as a result of a number of polarisation processes. Each polarisation process corresponds to a Debye model and the measured IP spectra are regarded as a superposition of several Debye models (Nordsiek & Weller, 2008).

Constant phase

If a constant phase angle is observed, instead of a phase peak, the Drake model by Van Voorhis et al. (1973) is applied. The complex electrical resistivity is expressed by

$$\rho^* = \frac{\rho^*}{(1 + i\omega\tau^a)}. \tag{2.17}$$

In conductivity notation, it can be written as

$$\sigma^* = i(\frac{\omega}{\omega_0})^b \sigma_\mathrm{n}, \tag{2.18}$$

where σ_n is the amplitude of the conductivity at the frequency ω_0 and b is the frequency dependency.

Such a constant phase angle behaviour was found, e.g. in copper deposits (Van Voorhis et al., 1973), clayey sandstones (Börner, 1992), gneisses and amphibolites (Börner et al., 1993) and clayey silt and sands (Börner et al., 1996). This model is used for spectra of rocks that are not interpretable with the Cole-Cole model.

2.4.2 Mechanistic models

Mechanistic models describe the physical behaviour on which the IP mechanisms are based on and it allows to identify relationships between the results. Over time, several mechanistic models were developed, but none was able to fully explain the observations. In general, there are two classes of approaches to describe polarisation effects in ore-free rocks: the grain-based models and the pore-based models. The first regard an aggregate enclosed by an electrolytic fluid and the latter regard electrolyte-filled pore space enclosed by rocks. The existing models may be helpful to estimate hydraulic parameters of sediments from SIP data by simulating the electrical impedance depending on the geometrical properties at the pore scale. Both approaches are suited to reproduce experimental results (Volkmann & Klitzsch, 2016). The issue of the characteristic length scale controlling the observed polarisation phenomena is a highly controversially discussed subject.

Grain-based models

The simplest concept based on Schwarz (1962) describes a single mineral grain. The EDL occurs along the mineral surface and the applying of an external electrical field results in a time-dependent displacement of the EDL by a tangential movement of the ions along the surface. One side of the grain has a lack of charge carriers, whereas the other side has a surplus. This charge distribution produces a dipole moment and Stern layer polarisation occurs in case of alternating fields. The time constant τ is related to the grain size radius r by,

$$\tau = \frac{r^2}{2D}, \tag{2.19}$$

with D being the diffusion coefficient of the counterions.

The Stern layer polarisation model is based on the assumption that the Stern layer is discontinuous between the grains (Revil, 2012). The combination of the triple layer model (TLM) of the EDL and the macroscopic model are used by Leroy et al. (2007, 2013) to develop a Stern layer polarisation model, which calculates the complex surface conductivity of a mineral grain. The developed model POLARIS from Revil and co-workers (Revil & Florsch, 2010; Revil, 2012, 2013a,b) allows a parametrisation of the complex electrical conductivity response of clean and shaly sands.

Pore-based models

Membrane polarisation models calculate ion dynamics in the pore-space electrolyte using pore constrictions to explain rock polarisation as shown in Figure 2.5. The basic model idea of membrane polarisation was first described as an one-dimensional model by Marshall & Madden (1959) (Fig. 2.7 a). In this model, the polarisation results only from differences between the ion mobilities along the pore space. An improvement of the basic model was suggested by Titov et al. (2002), which they called short narrow pore (SNP) model. The simplification reduces width and length of the active zones compared to the passive ones ($L_2 \ll L_1$), which is applicable to saturated pure sands. Under the assumption that the diffusion coefficient is equal at both narrow and wide pores, there is a quadratic dependence of the relaxation time τ on the length L_2 of the narrow pores:

$$\tau = \frac{L_2^2}{4D}. \tag{2.20}$$

A numerical approach was developed by Blaschek & Hördt (2009) considering different combination of pores. The 3D simulation of Volkmann & Klitzsch (2010) uses a cylindrical pore model. Contradictory to the findings of Titov et al. (2002), the results of the numerical studies suggest a dependence of the relaxation time on the length of the wide pore and a significant importance of the radius of the narrow pore for the polarisation phenomena. An extension of the one-dimensional model to 2D pores was implemented by Bücker & Hördt (2013a). The model consists of sequences of wide and narrow pores with an EDL including information about ion mobility, pH value and pore sizes (Fig. 2.7 b) to calculate an analytical solution.

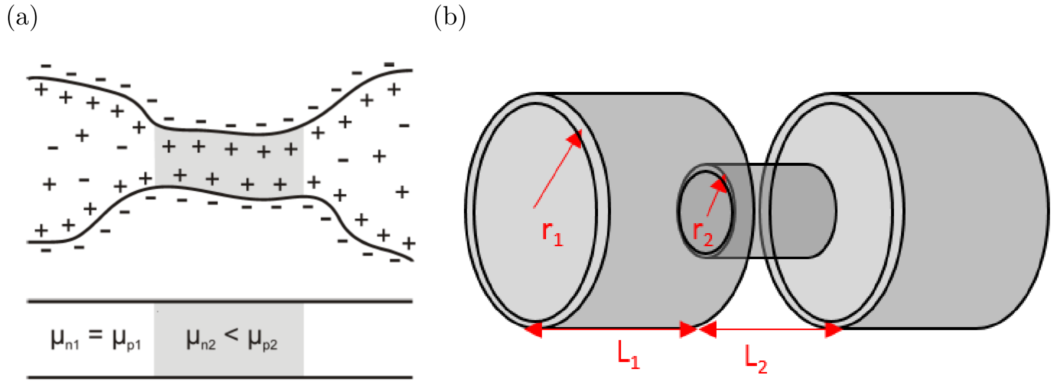

Figure 2.7: a) One-dimensional pore space model published by Bücker & Hördt (2013a) consisting of a sequence of two zones with different lengths ($L_1 > L_2$) and ion mobilities (μ_n and μ_p). b) Sketch of a two-dimensional model based on the membrane polarisation formulation. The narrow and wide pores are characterised by their lengths L and radius r including an electrical double layer (modified after Bücker & Hördt, 2013a).

Bücker & Hördt (2013a,b) derived analytically a new SNP model and the long narrow pore model (LNP). Stebner et al. (2017) extended the two-dimensional model of Bücker & Hördt (2013a) to 3D impedance networks. Connecting different combinations of cylinders to networks allow an approach of a realistic pore space geometry. Another extension of the membrane polarisation model by Hördt et al. (2017) integrates geometrical constraints for the membrane polarisation. It implies that the relaxation in the wide pore (WP) regime is more relevant than in the SNP regime, and the pore length of the WP is likely to control the measured relaxation times.

2.4.3 Empirical models

In addition to above-mentioned recent theoretical findings, an extensive database for a wide range of rock samples has been analysed to verify theoretical and empirical relations. The empirical relationships are used for interpretation of SIP data sets and to improve the understanding of the controls of pore geometry and pore fluid chemistry on induced polarisation measurements. From the relationships between electric and rock properties, rock parameters can be derived from SIP data, e.g. specific surface, permeability, formation factor.

Specific surface area

(Börner et al., 1996) first suggested the critical role of the specific surface area related to the pore volume S_{por} in controlling the magnitude of the IP magnitude. Extensive investigations on sandstones and unconsolidated sediments by Weller et al. (2010b) result in a derivation of a single empirical relationship between the quadrature conductivity σ'' (taken at 1 Hz) and S_{por}:

$$\sigma'' = c_{\text{p}} \cdot S_{\text{por}} \, , \tag{2.21}$$

with c_{p} being the specific polarisability with a value of $c_{\text{p}} \approx 10 \cdot 10^{-12}\,\text{S}$. According to empirical studies, the specific polarisability is only weakly dependent on mineralogy (Weller et al., 2010b; Weller & Slater, 2015). Further investigations and a more extensive database confirm this relationship and assume that S_{por} alone is the appropriate geometric factor controlling σ'' (Weller et al., 2015b). A further relationship was found between S_{por} and the normalised chargeability m_{n} by Weller et al. (2010b):

$$m_{\text{n}} = c_{\text{s}} \cdot S_{\text{por}} \, , \tag{2.22}$$

with c_{s} has a value of $72 \cdot 10^{-12}\,\text{S}$ for sandstones.

Permeability

Complex electrical measurements offer the possibility to predict permeability, because of the good correlation of the measures and the representative geometrical length scales controlling permeability (Binley et al., 2005; Slater, 2007; Weller et al., 2015a). Weller et al. (2015a) proposed an empirical model for permeability prediction based on the PaRiS model of Pape et al. (1987). The new empirical equation uses the linear proportionality between σ'' and S_{por} (Eq. 2.21) to link σ'' and formation factor F to permeability:

$$k_{\sigma''} = \frac{2.66 \cdot 10^{-7}}{\sigma''^{0.66} \cdot F^{5.35}} \, , \tag{2.23}$$

with $k_{\sigma''}$ is given in m^2, F is unitless, and σ'' is given in $\mathrm{mS{\cdot}m^{-1}}$. A second equation uses the relation between m_{n} and S_{por} (Eq. 2.22) for the permeability prediction:

$$k_{m_{\mathrm{n}}} = \frac{8.69 \cdot 10^{-7}}{m_{\mathrm{n}}^{0.79} \cdot F^{5.38}} \, , \tag{2.24}$$

with $k_{m_{\mathrm{n}}}$ is given in m^2, F is unitless, and m_{n} is given in $\mathrm{mS{\cdot}m^{-1}}$.
Both equations are valid for sandstones. A limitation of the permeability prediction is that F must be known.

Formation factor

A reliable formation factor estimation is required and highly relevant for numerous disciplines including hydrogeophysics and geophysical well logging. A method which uses only one single salinity measurement can provide a predicted or corrected formation factor. According to Börner et al. (1996) and Equation 2.13, the corrected formation factor is determined by

$$F_{\mathrm{corr}} = \frac{\sigma_{\mathrm{w}}}{\sigma' - \sigma'_{\mathrm{surf}}} = \frac{\sigma_{\mathrm{w}}}{\sigma' - \frac{\sigma''}{l}} \, , \tag{2.25}$$

whereas the factor l is known from fitting the linear relationship between σ''_{surf} and σ'_{surf}. The factor l is important to improve the petrophysical interpretation by electrical measurements. The ratio of the two surface conductivities components,

$$l = \frac{\sigma''_{\mathrm{surf}}}{\sigma'_{\mathrm{surf}}} \, , \tag{2.26}$$

is nearly independent of salinity for sandstone samples (Börner, 1992).

Fluid salinity

Multi salinity measurements are required to estimate σ'_{surf} and the formation factor. By the linear relation shown in Equation 2.13, a single salinity measurement provide only an apparent formation factor F'. A true formation factor can be determined, if the salinity range extends to high enough salinities ($\sigma_{\mathrm{w}} \cdot F^{-1} \gg \sigma'_{\mathrm{surf}}$), where the following relation is valid (Weller et al., 2013):

$$\sigma' = \frac{1}{F} \cdot \sigma_{\mathrm{w}} \,. \tag{2.27}$$

The true formation factor is used to calculate a salinity-dependent surface conductivity:

$$\sigma'_{\mathrm{surf}}(\sigma_{\mathrm{w}}) = \sigma'(\sigma_{\mathrm{w}}) - \frac{1}{F} \cdot \sigma_{\mathrm{w}} \,. \tag{2.28}$$

If the salinity range is limited, an approximation by fitting the expected asymptotic behaviour of $F'(\sigma_{\mathrm{w}})$ versus σ_{w} provides the true formation factor. Due to F' approach a constant value at high salinities ($F' = F$), the following fit can explain the relation of $F'(\sigma_{\mathrm{w}})$ versus σ_{w} (Weller et al., 2013):

$$F' = \frac{F\sigma_{\mathrm{w}}}{a + \sigma_{\mathrm{w}}} \,, \tag{2.29}$$

with a being a free parameter.

Radii

Several authors have observed relations between the pore size and different types of relaxation (Binley et al., 2005; Scott & Barker, 2003, 2005; Titov et al., 2010). Based on the theory of the polarisation of spherical grains (Eq. 2.19), the pore radius or diameter is considered as a characteristic pore size by Kruschwitz et al. (2010, 2016). The studies consider the dominant pore throat radius r_{dom}, determined by MIP, as a suitable characteristic pore size and controlling parameter of relaxation time. An empirical relation between the relaxation time determined by CC and the dominant pore throat radius predicts a proportionality of $\tau_{\mathrm{CC}} \propto \mathrm{d}_{\mathrm{dom}}^{2.97}$ ($\mathrm{R}^2 = 0.55$), which is valid for building material and sandstones with $d_{\mathrm{dom}} > 4\,\mu\mathrm{m}$ (Kruschwitz et al., 2010). The systematically focused study of Kruschwitz et al. (2016) does not confirm a general τ_{peak} - d_{dom}^2 relationship, but distinguishes between three different relaxation types. Weller et al. (2016) discuss the relation of pore radius and induced polarisation regarding their role in permeability estimation. Between the effective hydraulic radius r_{eff} and the IP relaxation time is no direct relation, because the relating parameter, the diffusion coefficient D, varies and is not constant as assumed.

3 Methods

3.1 Petrophysical Investigations

3.1.1 Triple weighing method

This method is based on Archimedes' principle. A body immersed in a fluid is buoyed upward by a force equal to the weight of the displaced fluid. The triple weighing method provides very precise values for porosity Φ and grain density d_{gr} as long as the used technical equipment is rule-consistent. In total, three different weighings were conducted: (1) a weighing in dry state (m_{dry}), (2) a weighing of the fully saturated sample (m_{sat}), and (3) a weighing of the fully immersed sample (m_{im}). The samples are dried at 150 °C for 24 hours, which ensures that no water remains in the pore space. After the weighing in dry state, the samples are saturated with a fluid of known density. In this work, tap water was used with a density $d_{\mathrm{H_2O}}$ of $0.998\,\mathrm{g\cdot cm^{-3}}$. Prior to the weighing of the fully saturated sample, excess water is removed with a towel. The measurement of the weighing of the fully immersed sample requires a water filled beaker with a tared pan inside, which is connected to a balance. The recorded weights allow the calculation of the bulk volume V_{b}, the pore volume V_{p}, and the grain volume V_{gr} of the sample as shown in Equation 3.1, 3.2 and 3.3:

$$V_{\mathrm{p}} = \frac{m_{sat} - m_{\mathrm{dry}}}{d_{\mathrm{H_2O}}}, \tag{3.1}$$

$$V_{\mathrm{b}} = \frac{m_{\mathrm{sat}} - m_{\mathrm{im}}}{d_{\mathrm{H_2O}}}, \tag{3.2}$$

$$V_{\mathrm{gr}} = \frac{m_{\mathrm{dry}} - m_{\mathrm{im}}}{d_{\mathrm{H_2O}}}. \tag{3.3}$$

The porosity is given by the ratio of V_{p} and V_{b}:

$$\Phi = \frac{V_{\mathrm{p}}}{V_{\mathrm{b}}} = \frac{(m_{\mathrm{sat}} - m_{\mathrm{dry}})}{(m_{\mathrm{sat}} - m_{\mathrm{im}})}. \tag{3.4}$$

The grain density is calculated by using

$$d_{\mathrm{gr}} = \frac{m_{\mathrm{dry}}}{V_{\mathrm{gr}}} = \frac{m_{\mathrm{dry}}}{m_{dry} - m_{\mathrm{im}}} \cdot d_{\mathrm{H_2O}}. \tag{3.5}$$

All measurements follow protocols related to core and special core analysis (SCAL) (RP40, 1998).

3.1.2 Gas pycnometry

Another method to determine the porosity and the grain density of a sample is the gas pycnometry. This method is based on the use of the Boyle-Mariotte-Law (Tipler & Mosca, 2007). It states that the pressure and the volume are inverse proportional under the assumption of a constant temperature and amount of an ideal gas. The Boyle-Mariotte-Law is a special case of the general gas law:

$$p \cdot V_{\mathrm{gas}} = n_{\mathrm{gas}} \cdot R \cdot T, \tag{3.6}$$

where p is the gas pressure, V_{gas} the volume of the gas, n_{gas} is the amount of gas, R the ideal gas constant $[R = 8.314\,\mathrm{J{\cdot}K^{-1}{\cdot}mol^{-1}}]$ and T the temperature.

A measurement with a pycnometer is performed by putting a sample inside a closed chamber, which is flushed with helium gas until the saturation pressure (p_1) is reached. Figure A.1 show a schematic description of the principles of operations. The estimation of an unknown sample-volume is done by the following steps: (1) a calibration of the measurement chamber with a defined test-volume to estimate the volume of the chamber V_{c}, (2) measurement with a dry sample to obtain p_1, (3) enlargement of the volume of the chamber by adding a defined volume V_{add} by opening the valve, (4) measurement of the gas pressure (p_2), which decreases because of the larger volume.

The following equation is obtained after Boyle-Mariotte:

$$p_1(V_{\mathrm{c}} - V_{\mathrm{gr}}) = p_2(V_{\mathrm{c}} - V_{\mathrm{gr}} + V_{\mathrm{add}}), \tag{3.7}$$

where the left hand-side describes the first state and the right hand-side the second state. V_{gr} can be derived from the transformation of Equation 3.7:

$$V_{\mathrm{gr}} = V_{\mathrm{c}} - \frac{V_{\mathrm{add}}}{1 - \frac{p_1}{p_2}}. \tag{3.8}$$

The bulk density d_{gr} can be calculated by the quotient of V_{gr} and m_{dry} as

$$d_{\mathrm{gr}} = \frac{m_{\mathrm{dry}}}{V_{\mathrm{gr}}}. \tag{3.9}$$

The geometrically determined bulk volume V_{geo} of the sample and the pore volume V_{p} as the difference of V_{geo} and V_{gr} were necessary to calculate the porosity:

$$\Phi = \frac{V_{\mathrm{p}}}{V_{\mathrm{geo}}} = \frac{V_{\mathrm{geo}} - V_{\mathrm{gr}}}{V_{\mathrm{geo}}}. \tag{3.10}$$

3.1.3 Steady-state gas permeability

The permeability of a porous medium is the most important hydraulic property. Different factors are controlling the permeability, e.g., pore geometry, bedding, porosity and confining stress (Tiab & Donaldson, 2012). The pore geometry includes grain size, grain orientation, packing, degree of cementation, clay content, grain size distribution and grain sorting. Especially, for carbonates, the permeability is influenced by the degree of mineral alteration, porosity development and fractures. The permeability is described by Darcy's law (Darcy, 1856):

$$k_{\mathrm{a}} = \frac{\eta \cdot Q \cdot l}{A \cdot \Delta p}, \tag{3.11}$$

where k_{a} is the fluid or apparent permeability, η the fluid viscosity, Q the volumetric flow rate ($Q = V \cdot t^{-1}$) and Δp the hydraulic pressure gradient between p_1 and p_2. The sample geometry is given by the cross sectional area A and the length l.

The steady-state permeability measurement is the preferred method for high-permeable rocks, because low-permeable samples would increase the measurement time significantly (Tiab & Donaldson, 2012). The dried plug is installed within a flexible sleeve in a FANCHER-type core holder for the measurement (Fig. A.2). Radial confining stress is applied and an isostatic stress is assumed for the core. This guarantees no gas-flow along the sample boundary. The core has axial ports for the inflow and outflow of the gas. Furthermore, it has a second port for determining the upstream and downstream pressure, as well as their difference (Δp). The volumetric flow rate can be measured at the downstream pressure port with a flow meter. Equation 3.11 is only valid, if the five Darcy conditions are fulfilled. This is the case, if (1) the fluid is incompressible, (2) the flow is laminar, (3) the flow velocity is zero at the capillary wall, (4) the flow is laminar, and (5) there is no chemical reaction between the pore fluid and the rock. If gas as fluid is used, condition (1) and (3) are violated. Firstly, gas is a compressible fluid and this fact results in a dependency of k_{a} on the mean absolute gas pressure p_{mean}.

Secondly, the displacement directly by the capillary wall is non-zero and a slip occurs. Hence, permeability needs to be corrected as proposed by Klinkenberg et al. (1941):

$$k_{\mathrm{kl}} = k_{\mathrm{a}} \cdot (1 + \frac{\alpha}{p_{\mathrm{mean}}})^{-1}, \tag{3.12}$$

where α is the Klinkenberg-factor and k_{kl} is the slip-corrected (Klinkenberg) or gas permeability. Permeability values without the Klinkenberg gas slippage are generally higher than those obtained with correction (Tiab & Donaldson, 2012). The Klinkenberg approach is reasonable for an intermediate flow regime, which ranges from Knudsen numbers 0.01 to 0.1. The dimensionless Knudsen number (Kn) is defined as the ratio of the molecular mean free path against the characteristic length in the flow path.

3.1.4 Gas physisorption

The process of gas physisorption can be measured by the method of Brunauer-Emmet-Teller (BET) (Brunauer et al., 1938), termed after its developers. BET is very precise and delivers reproducible data for the evaluation of the surface area. The BET method is based on the Langmuir theory (Langmuir, 1916), which is a monolayer model isotherm for adsorbed gas onto a solid surface. With the three assumptions, that (1) the gas molecules physically adsorb on a solid infinitely and (2) interact with adjacent layers as well as (3) the Langmuir theory can be adopted to each layer, the resulting BET-equation is:

$$\frac{p/p_0}{n_a(1 - p/p_0)} = \frac{1}{n_{\mathrm{mono}}C} + \frac{C-1}{n_{\mathrm{mono}}C} \cdot \frac{p}{p_0}, \tag{3.13}$$

where $p \cdot p_0^{-1}$ is the ratio of gas pressure in the measuring cell (p), p_0 the pressure in the reference cell, n_{a} the total amount of adsorbate molecules, n_{mono} the monolayer capacity and C the BET parameter.

For the determination of the inner surface, the dried sample is placed inside a sealed cell, which is filled with gas. By immersion of the cell into liquid nitrogen (T = 77 K) the temperature decreases and the movement of the molecules decreases. Thus, more gas molecules can be adsorped at the surface of the sample. That also leads to a decreasing pressure in the measuring cell. By increasing the temperature continuously to 20 °C (room temperature), the gas molecules desorb from the surface. This results in an increasing pressure in the cell.

A BET plot (Fig. A.3) shows the relative pressure versus the left-hand side of Equation 3.13. Equation 3.13 shows a linear relationship between a certain pressure range ($0.05 < p \cdot p_0^{-1} < 0.35$) (Fig. A.3). Therefore, n_{mono} and C can be determined by the slope a and the intercept point b of this relationship (ISO9227, 2010):

$$n_{\mathrm{mono}} = \frac{1}{a+b} \tag{3.14}$$

and

$$C = \frac{b}{a} + 1. \tag{3.15}$$

The expression of the surface area per mass S_{m} is written as follows:

$$S_{\mathrm{m}} = n_{\mathrm{mono}} \cdot N_{\mathrm{A}} \cdot A, \tag{3.16}$$

where N_{A} is the Avogadro constant and A the molecular cross sectional area. The surface area per pore volume S_{por} is written as follows (Schön, 2004):

$$S_{\mathrm{por}} = S_{\mathrm{m}} \cdot d_{\mathrm{gr}} \cdot \frac{(1-\Phi)}{\Phi}, \tag{3.17}$$

where d_{gr} is the grain density and Φ the porosity. Depending on the sample surface, different types of gases are preferred. One of the conventional gases is nitrogen with a detection limit of the surface area per mass down to values of $0.2\,\mathrm{m}^2 \cdot \mathrm{g}^{-1}$. If the surface values are smaller, krypton gas is necessary as adsorption gas. Because of its lower vapor pressure, it is easier to measure a larger pressure change, which allows a better measurement accuracy. Therefore, krypton is more suitable for the determination of lower surface areas and allows to measure surface areas down to $0.05\,\mathrm{m}^2 \cdot \mathrm{g}^{-1}$ or less.

3.1.5 Mercury intrusion porosimetry

Mercury intrusion porosimetry (MIP) is used for the determination of the volumetric distribution and the porosity of pores in the range of between micro ($< 2\,\mathrm{nm}$) and macro pores ($> 50\,\mathrm{nm}$ (Sing, 2001)). The intrusion of mercury (Hg) allows the determination of pore radii up to a minimum size of 2 nm. Mercury has a high surface tension ($\gamma = 0.480\,\mathrm{N{\cdot}m^{-1}}$ at $20\,^{\circ}\mathrm{C}$). Therefore, mercury is incapable to intrude into pores smaller than $100\,\mu\mathrm{m}$ under vacuum condition. Only if an additional pressure is applied, mercury can fill pores below $100\,\mu\mathrm{m}$. MIP is recording capillary pressure curves which are based on the capillary law regarding liquid penetration into small pores. According to Washburn (1921), this can be expressed:

$$r_{\mathrm{p}} = \frac{-2 \cdot \gamma \cdot cos(\theta)}{p_{\mathrm{c}}}, \tag{3.18}$$

with r_{p} is being the radius of pore-throat aperture for a cylindrical pore, γ the surface tension of Hg, θ the contact angle of Hg in air and p_{c} the capillary pressure. The Washburn equation is valid for non-wetting fluids and assuming cylindrical pores. The mercury intrudes stepwise on different pressure levels into an evacuated, cleaned and dried core plug. The mercury volume of each pressure level is recorded until the sample is saturated or the maximum pressure is reached. The pressure values enable the determination of the mean pore radius r_{mean} and the dominant radius r_{dom} by the intrusion data. One problem of this method is that only the radius of the pore-throat aperture can be determined. For pores that are only accessible by a narrow bottleneck, this leads to a determination of distorted pore sizes (Markl, 2008). Another disadvantage is that the process of Hg intrusion is irreversible, because a certain amount of mercury stays in the sample after release of pressure and the sample cannot be used for further investigations. Hence, MIP should be the last step of core analysis.

3.1.6 Nuclear magnetic resonance

The method of nuclear magnetic resonance (NMR) allows an insight in the microscopic and internal structure of porous media without disturbing them. The principle of the measurement is based on the concept of the nuclear spin, one of the basic properties of an atom nucleus. The spin describes the rotation of the nucleus and leads to a magnetic moment of each nucleus (Dunn et al., 2002). Because of its magnetic moment, a hydrogen nucleus (proton) interacts with magnetic fields. If an external static magnetic field $\mathbf{B_0}$ is applied, the protons orient along the magnetic lines and their ensemble of spins lead to a magnetisation. Because the protons have additionally an angular momentum, it causes a tumbling motion around the magnetic lines, called precession. Dependent on the strength of $\mathbf{B_0}$, this precession occurs at the Larmor frequency, which is characteristic for each proton and depends on the strength of the magnetic field.

During a NMR experiment, the observable NMR effect on a sample is reduced to the magnetisation. The magnetisation is not quantifiable, therefore an electromagnetic pulse with the specific Larmor frequency is applied to excite the protons from their equilibrium and manipulate the orientation of the magnetisation. The NMR signal is recorded as a voltage response after the excitation of the sample. One information of the signal is the initial NMR amplitude. A second information is the relaxation time, which describes the needed time of the proton to return to equilibrium after excitation. There are two independent relaxation processes, one perpendicular and one parallel to $\mathbf{B_0}$, which are described by time constants, the longitudinal (T_1) and the transverse (T_2) NMR relaxation time, respectively. Relaxation is caused by interaction of the protons in the fluid with each other (bulk relaxivity) and by interacting with the pore surface (surface relaxivity).

The above-described amplitude of the measured response signal is directly proportional to the water content of the sample. If the sample is fully saturated and has a known volume, the porosity can be determined by relating the signal amplitude at the sample to a water calibration measurement with equal volume. The decay behaviour of the measured response signal permits conclusions, after inverse modelling and further steps, in respect of information about the material properties of the sample, e.g. medium pore radii, surface-to-volume-ratio and permeability (Brownstein & Tarr, 1979; Carman, 1938; Kozeny, 1927). The T_2 relaxation time is related to the pore radius by,

$$T_2 = \frac{r}{2\rho_\mathrm{S}}, \tag{3.19}$$

with ρ_S being the surface relaxivity.

3.1.7 X-ray micro-computed tomography

Micro-Computed Tomography (μ-CT) is an 3D imaging technique, which is suitable for a quantitative and qualitative analysis of rock properties. The mathematical fundamentals of modern image reconstruction goes back to the work of Radon (1917). The μ-CT technique is similar to the medical computed tomography. The sample is located in the ray path of a X-ray source for data acquisition (Fig. A.4). A special detector unit is recorded a single 2D projection, which is in principle an image of the density distribution within the sample. While the sample rotates stepwise around its own axis, the detector produces a several number of single 2D-projections. The 2D-projections can be combined to a 3D data set after reconstruction. The high resolution μ-CT-system enables a focal spot size down to 0.6 μm, which implies a detail detectability of about 0.2 μm (Halisch, 2013). Hence, voxel resolutions of 1.25 μm to 2.0 μm could be achieved. The μ-CT analysis enables investigations about the interior structures, different types of porosity, pore space interconnectivity, and the mineralogical components of rocks (Halisch, 2013). The insights of a high-resolution μ-CT imaging allow a characterisation of the pore space of porous rocks, a quantitative or qualitative determination of characteristic mineral phases and structural composition as well as a segmentation of images regarding the granular structure, the cementation and the pore space for a qualitative analysis.

The digital image analysis is individually focused on the selected sample. A general workflow is shown as an example in Figure 3.1. Pre-imaging includes all settings before the record of the 2D-projections (Imaging). The next step is the reconstruction of the 2D-projections to a 3D data set. The data is imported and the volume of interest is selected for the post-processing. A list of scanned and used volume is in the appendix (Tab. B.18). Filtering is an individual process for each sample with no 'set rules'. During this study, Gaussian, median, non-local mean filters (Buades et al., 2005) or a combination of them turned out to be appropriate to reduce image noise and artefacts in order to increase information value (Ohser & Schladitz, 2009). The Gaussian filter is a classical denoiser, but leads to a blurring (mineral) phase edges. The median filter removes image noise without blurring the phase edge and the grey-value distribution, but with blurring the interior pore. The non-local mean filter is in principle a combination of both and showed the best results. Nevertheless, applying an additional second filter leads sample-dependent to better results. A comparison of a representative unfiltered and filtered 2D-slice is shown in Figure 3.2 a and b. During the pore segmentation stage, the watershed algorithm (Ohser & Schladitz, 2009) computes the separating points in the main pore network. Afterwards the main pore net work is separated into individual pores. The separated pores obtain a random ID number (labelling) and the pore geometry is analysed (label analysis). Figure 3.2 c shows the pore network after segmentation and Figure 3.2 d the same pore network after separation and labelling of the pores has been performed.

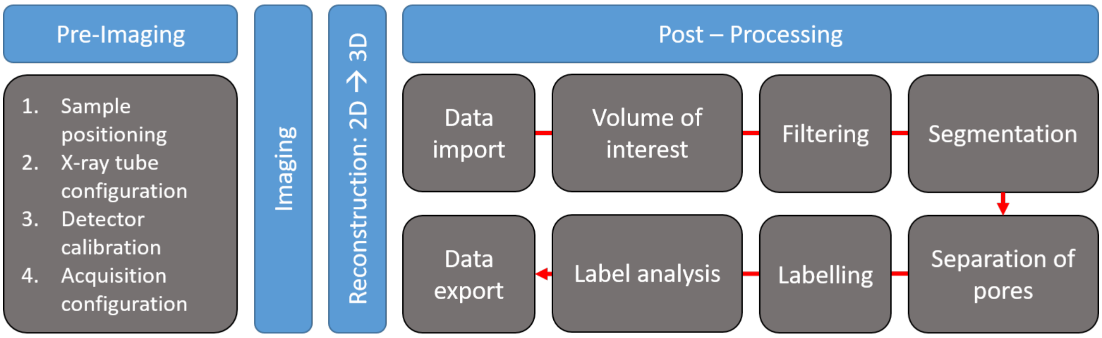

Figure 3.1: Exemplified workflow of data image analysis.

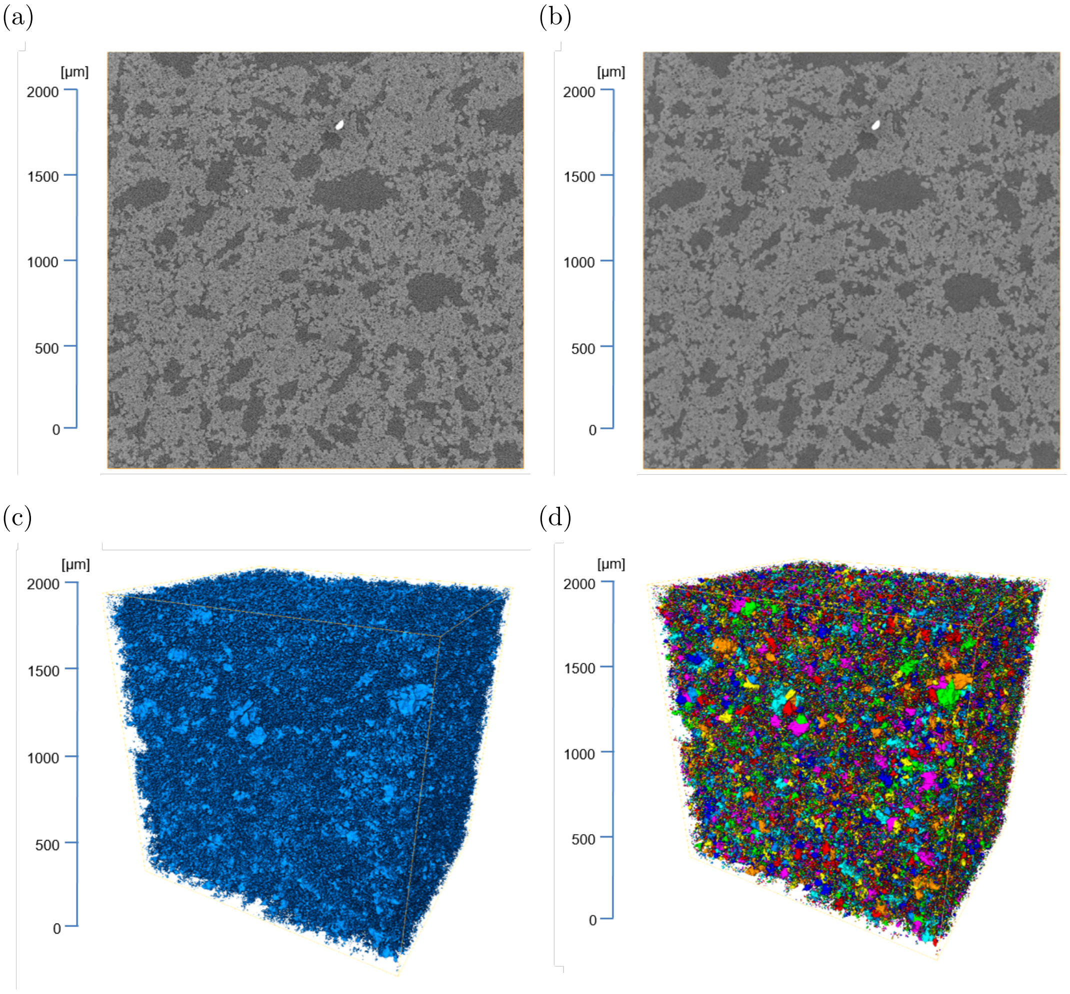

Figure 3.2: Representation of different post-processing steps during digital image analysis. a) Unfiltered 2D slice of the μ-CT data. b) The same 2D slice after filtering. c) 3D cube of the pore network after pore segmentation. d) 3D cube of the pore network after labeling.

3.2 Mineralogical and Geochemical Investigations

3.2.1 Environmental scanning electron microscopy

Environmental scanning electron microscopy (ESEM) is primary optimised for images. This classical mineralogical method allows to visualise surface structures up to a size of 100 nm (100000x magnification) with simple electrons optics (Markl, 2008). ESEM takes advantage of the interaction between the electrons and the surface of the material. The measurement requires a freshly prepared fractured surface of a dried sample. The material is shot by electrons in an evacuated chamber (low-vacuum mode, 0.6 mbar). A silicon detector absorbs back-scattered electrons from the sample or rather emitted electrons by the sample itself (secondary electrons). The beam of stimulating electron scans the area of interest by moving over the sample applying a voltage. A computer recomposes the single points to an image. The main difference of the ESEM towards the conventional SEM is the avoidance of special sample preparation (e.g. gold cover), no need of a hard vacuum and a specialised electron detectors. The used device is additional equipped with an energy dispersive X-ray spectrometer (EDX). EDX is especially used for a fast chemical identification of materials or for qualitative analyses. The element concentration is measured by detecting arising X-rays after being shot by a high energy beam. A typical EDX spectrum shows the intensity of the most important X-ray lines of the detected elements plotted against their energy. The EDX is able to measure only the surface of the sample and is incapable to detect elements below the surface.

3.2.2 X-ray fluorescence spectroscopy

X-ray fluorescence spectroscopy (XRF) is a qualitative and quantitative analysis of major and trace elements. This method works in a similar way like the micro probe of the EDX. The sample material is bombarded with high energy X-rays instead of electrons. Thus, the tightly held inner electrons are expelled. This emitted radiation consists of a characteristic radiation and a deceleration radiation. The characteristic radiation can be used to identify the element from which it is emitted because this radiation is a defining feature and occurs in high intensities only in small, sharply limited wavelength ranges. One advantage of this method is, that larger samples can be used, which is important for overall analysis (Markl, 2008).

3.2.3 X-ray diffraction

X-ray diffraction (XRD) is based on the principle of reflection and diffraction on crystal lattices. A primary use of this technique is the investigation of lattice structures to identify and characterise mineral compositions with the help of these structures. The Bragg's law is the basis of this method (Bragg & Bragg, 1913):

$$n \cdot \lambda = 2 \cdot l \cdot \sin(\theta), \tag{3.20}$$

with n being a positive integer, λ the wavelength, l the inter-atomic distance between the lattice planes, and θ the incident angle. The l-values are absolute characteristics for each mineral. Thus, measuring of the distance between the lattice planes is sufficient to determine the lattice structure. The available device is a PANalytical MPD Pro and requires 1 g to 2 g powdered material for an analysis.

3.2.4 Carbon and sulphur analysis

Carbon and sulphur analysis is part of the organic geochemistry. The instrument LECO CS 230 is used as carbon-sulphur-analyser to get the values for total carbon content c_{ges}, organic carbon content c_{org} and total sulphur content S_{ges}. For this purpose, the samples were burned in a high frequency furnace at 2000 °C. The resulting sulfur dioxide and carbon dioxide are analysed by infra-red detection. The carbon monoxide has to be catalytically oxidised to carbon dioxide. Untreated samples are necessary for the determination of c_{ges} and S_{ges}, whereas the determination of c_{org} requires decarbonised samples. The elimination is achieved by treatment with 10 % hydrochloride acid at a temperature of 80 °C before burning.

3.2.5 Cation exchange capacity

The Cation exchange capacity (CEC) is one of the basic properties of clay minerals and describes the amount of exchangeable cations. The method is occasional very elaborate and disadvantageous mineral compositions of the samples can lead to unsatisfactory and less meaningful results. A precise, fast and reproducible method for the determination of CEC is the Cu(II)-Triethylenetetramine-technique after Meier & Kahr (1999). This technique is based on the straightforward principle of the photo-metrical determination of atomic absorption spectroscopy. The Cu(II)-Triethylenetetramine-solution is added to the sample material. The natural absorbed cations are equivalently replaced by Cu(II) complex-ions and the solution is decolourised. The linear relationship between the discolouration and the decrease of Cu(II) complex-ions provides the CEC-values for the material.

3.3 Spectral induced polarisation

3.3.1 Core holder

A modular core holder has been developed during this work for laboratory measurements. Currently, there are no unified standards and technical requirements for core holders used for IP measurements. Because of the noise additive nature of SIP measurements, a core holder should satisfy different requirements to enable high precision SIP data acquisition. Known instrumental influences are the electromagnetic coupling effects between connection wires in particular. These effects cause frequency-dependent errors for higher frequencies, in most cases above 100 Hz. Furthermore, core holder effects exist like, coupling of the sample-electrode system, self-polarisation effects, leakage currents along the sample boundary and evaporation. These effects influence the quality of the SIP data. The listed challenges require a construction made of non-polarisable and brine-resistant material, including non-polarisable potential and non-oxidizing current electrodes. In addition, the core holder needs practical requirements such as simple handling, low-maintenance, compact design and the ability to fit different sample sizes without drastic changes.

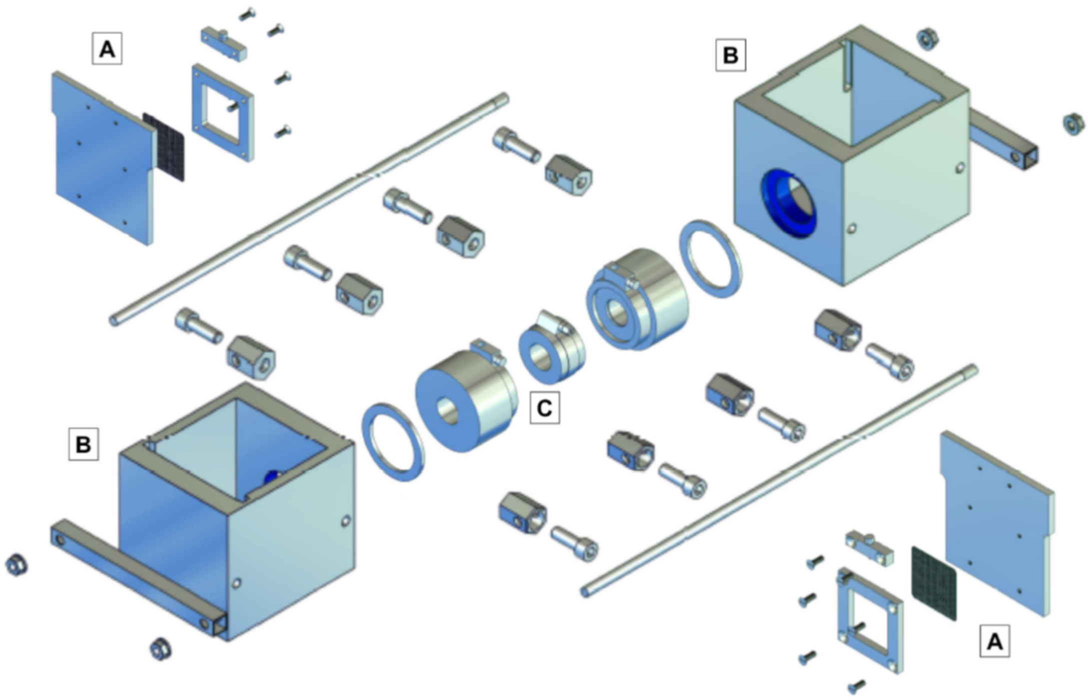

Figure 3.3: Schematic exploded view of the core holder for SIP measurements. a) Current electrode holder with platinum net electrodes. b) Electrolyte reservoir tanks. c) Core sleeve with the potential electrode adapters for silver chloride ring-electrodes. (Halisch et al., 2017)

Figure 3.3 shows the conceptual design of the developed SIP core holder in an exploded view. The used three main modules are the current electrodes (A), the electrolyte reservoir (B), and the core sleeve with the potential electrode adapters (C). The current electrodes consist of a 8 x 8 cm platinum net (Fig. 3.4 b), which has a net aperture of 125 μm. This arrangement guarantees a highly uniform current density along the sample holder. The platinum net is fixed on acrylic glass plate and can be connected to the current generator with a socket plug. The current electrodes are functionally interchangeable within the reservoir tanks. The reservoir tanks have a capacity of 1.5 l per reservoir and are constructed in light-weight design of transparent perspex (Fig. 3.4 a). The tanks have a functional clamping system consisting of rail ways, which enables to have a flexible electrode distance depending on the sample size. In addition, an exact cover for each tank protects the saturation fluid from evaporation. The third main module includes the potential electrodes and the core holder by itself. The two adapters for the potential electrodes are silver made ring electrodes (99.9 % purity; diameter 0.4 mm) (Fig. 3.4 c). This electrode type provides optimal signal-to-noise ratio as well as the optimum coupling to the core and saturating fluid. The silver wire should be chlorinated as a prevention of polarisation effects on the electrode surface. The adapter is dipped into hydrochloride acid. The process can be described by the following chemical equations:

$$\text{Oxidation:}\;\; 2\mathrm{Ag} + 2\mathrm{HCl} \Rightarrow 2\mathrm{AgCl} + 2\mathrm{H}^+ + 2e^-; \tag{3.21}$$

$$\text{Reduction:}\;\; 2\mathrm{H}^+ + 2e^- \Rightarrow \mathrm{H}_2;$$

$$\text{Total:}\;\; 2\mathrm{Ag} + 2\mathrm{HCl} \Rightarrow 2\mathrm{AgCl} + \mathrm{H}_2.$$

The chloride layer lasts several measurements and has to be renewed at times. The adapters exist for several plug sizes and match samples with diameters of 20 mm, 25 mm and 30 mm as well as lengths from 30 mm to 80 mm. The core is enclosed by a chemical inert rubber sleeve (Fig. 3.4 d), which is compressed by a hose clamp. Thus, the rubber narrowly fits to the sample surface and inhibits leakage currents at the core boundary. The current version of the measuring cell was presented on an international conference (Halisch et al., 2017) and will be patented in 2019.

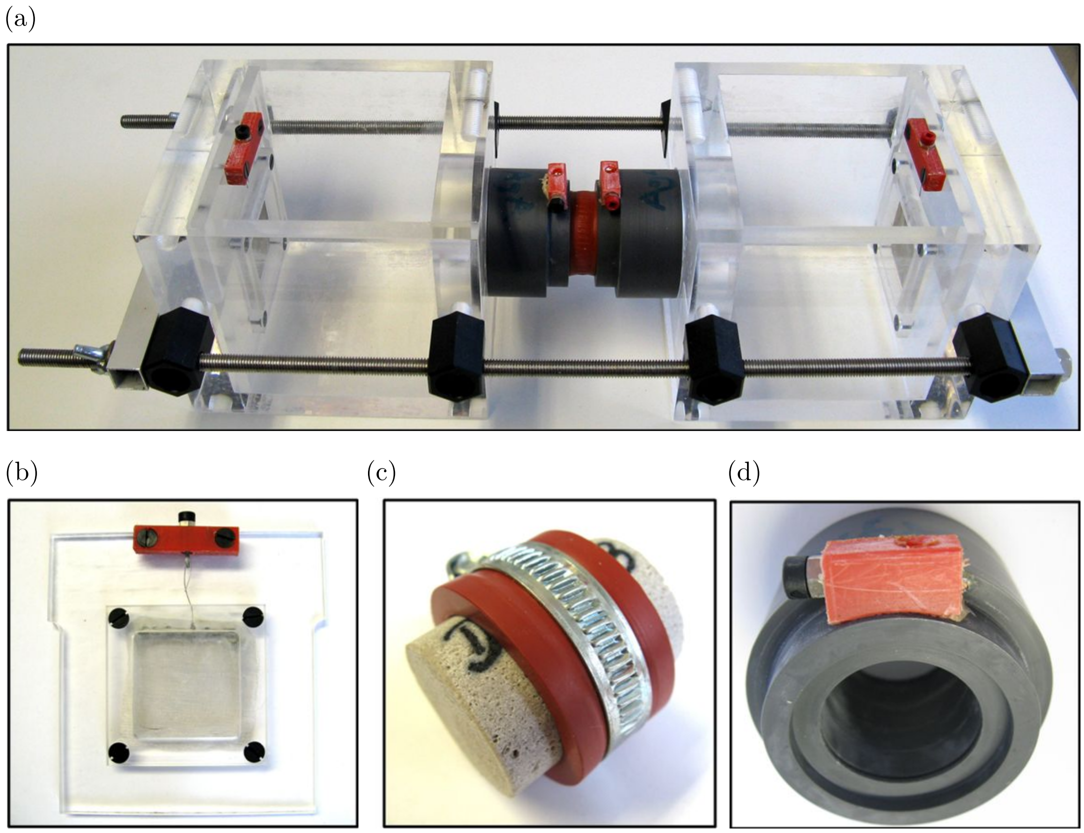

Figure 3.4: Photos of the main modules of the core holder. a) Total measuring cell. b) Current electrode. c) Potential electrode. d) Core holder sleeve with core.

3.3.2 Instrument

A classical four point measurement with a shunt resistor was used for impedance measurements. Three different instruments were used for the data acquisition: SIP-Quad (Radic & Halisch, 2017), SIP-Fuchs 3 and ZEL-SIP04-V02 (Zimmermann et al., 2008b), whereby the SIP-Quad performed the main part of the measurements. The advantage of the SIP-Quad is the wide frequency range of about 9.5 decades and the simultaneous measurements on four core holders. The measurement concept provides two electrodes for current transmission (current electrodes) and two electrodes for the voltage measurement (potential electrodes). One channel is necessary for each pair of electrodes. Thus, eight channels are used for four core holders (Fig. 3.5). All channels are decoupled from each other. Upstream current or potential probes decide whether a channel is for measuring current or voltage. These probes are directly connected to the core holder. The integrated electronic prevents the impact of interference signals and systematic measuring errors over the measurement lines. The implemented real-time DFT (Discrete Fourier Transformation) increases the measuring process. The SIP-Fuchs 3 is a kind of a prototype of the SIP-Quad with a lower frequency range (seven decades) and only one channel for laboratory measurements. The instrument is suited for both field and laboratory measurements. Therefore, it consists of a base unit and several remote units. Both devices are manufactured by *Radic Research*. The ZEL-SIP04-V02 is a high-accuracy impedance spectrometer built by *Forschungszentrum Jülich* (Zimmermann et al., 2008b). It covers a frequency range from 1 mHz to 45 kHz and provides the possibility of measuring two sample simultaneously.

3.3.3 SIP measurement

SIP measurements follow a defined protocol, which is identical for all measurements. This procedure guarantees the reproducibility and comparability of the data sets. The samples are dried at 150 °C in a drying cabinet to ensure that the pores are water-free. The saturation with calciumchlorid ($CaCl_2$) takes place under vacuum in a desiccator. A $CaCl_2$ brine as pore fluid reduced the chance of interactions between the carbonate ($CaCO_3$) and the saturation fluid, because both constituents have the same chemical milieu. After saturation the samples are stored in a closed box until a chemical balance is attained. Changes of the fluid conductivity can be used as a proxy, whether the equilibrium between pore fluid and sample is reached. If the changes of the conductivity are significant, the fluid must be diluted with distilled water and the sample is observed furthermore. A discrepancy of less than 5 % from the initial value states a balance at the electrical double layer. It is assumed that there are no noticeable solution processes at the

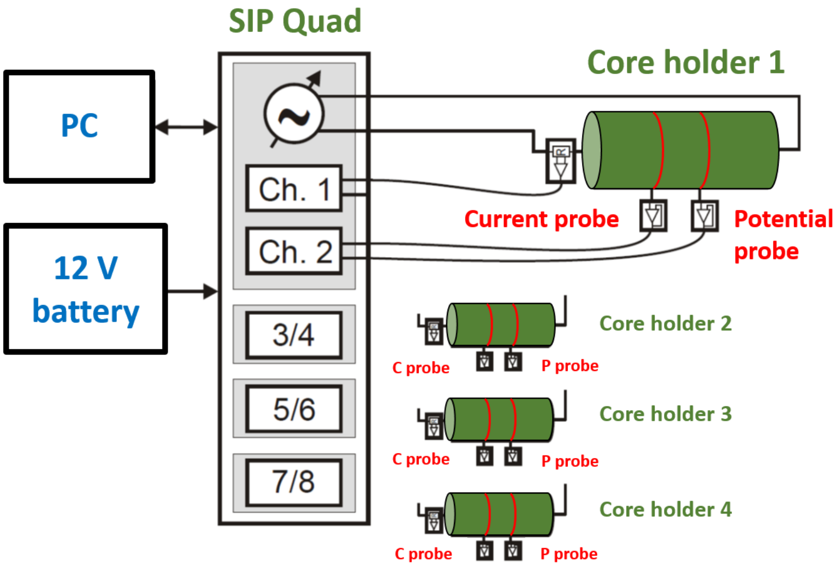

Figure 3.5: Block diagram of the SIP-Quad device after Radic & Halisch (2017).

boundaries and the ion concentration is balanced between the fluids outside and inside the sample. The installation of the saturated sample in the core holder follows and the measurement cell is placed in a climate chamber at a constant temperature of 20 °C overnight. This ensures that the fluid reaches the same temperature. The SIP-measurement itself takes place as well in a climate chamber. In addition, the casing of the climatic chamber shields the SIP-measurement from electromagnetic noise sources. A frequency range of 1 mHz to 60 kHz was used for most of the measurements, but the graphical presentation takes place mainly over 5 frequency decades between 2 mHz and 100 Hz. Resistivity and phase shift values are recorded for each frequency. In general three data sets on three different days are recorded to ensure the reproducibility of a single measurement series. Conductivity, temperature and pH values of the fluid inside the two tanks are recorded after each measurement to monitor changes. A standard measurement requires a saturation fluid with a conductivity of $100\,\mathrm{mS{\cdot}m^{-1}}$. Specific measurements as the multi-salinity measurements vary the pore fluid conductivity in certain steps from $5\,\mathrm{mS{\cdot}m^{-1}}$ to $1600\,\mathrm{mS{\cdot}m^{-1}}$.

Analysis

One way of determination of the parameter τ and m is described in subsection 2.4.1. A simpler approach to determine the time constant τ is to use the peak frequency f_{peak}, i. e. the frequency where the maximum phase shift is observed,

$$\tau_{\mathrm{peak}} = \frac{1}{2\pi f_{\mathrm{peak}}} \,, \tag{3.22}$$

and for m to use the relative difference between low and high frequency resistivity amplitude

$$m_{\mathrm{s}} = \frac{\rho_{f_{\mathrm{min}}} - \rho_{f_{\mathrm{max}}}}{\rho_{f_{\mathrm{min}}}} \,. \tag{3.23}$$

$\rho_{f_{\mathrm{min}}}$ is the resistivity value of the minimum frequency and $\rho_{f_{\mathrm{max}}}$ is the resistivity value of the maximum frequency. The latter values can be used as starting values for the Cole-Cole fit.

Normalised IP parameter as the normalised relaxation time τ_n (Slater et al., 2005) and the normalised chargeability m_{n} (Lesmes & Frye, 2001) can be calculated by multiplication of the original parameters and σ_0:

$$m_{\mathrm{n}} = m \cdot \sigma_0 \,. \tag{3.24}$$

$$\tau_{\mathrm{n}} = \tau \cdot \sigma_0 \,. \tag{3.25}$$

3.4 Dissolution experiment

This chapter focuses on the controlled dissolution of carbonate samples. For this purpose, a new experimental setup was designed enabling systematic dissolution steps under monitoring conditions. The main aim is to quantify the impact of dissolution processes on the IP-effect. The pore space is systematically consciously manipulated and the variations are recorded. The measurements of the complex electrical conductivity are conducted in combination with classical petrophysical measurements. Additionally, imaging techniques (ESEM, μ-CT) are used to visualise and quantify subsequent variation of the dissolution steps.

Laboratory conditions

Experimental setup

The dissolution treatment procedure requires a specific new experimental setup to enable acidizing and cleaning of carbonate samples at variable flow rates with different fluids under monitoring conditions. Hence, a new device has been designed and constructed for this purpose (Fig. 3.6 and A.5). The sample is placed in a highly durable silica-rubber sleeve inside of a core holder, a so-called Fancher-type cell. The sleeve is compressed at very low overburden pressures (12 bar) to fit tight with the sample surface and to inhibit creeping flow alongside the sample. The device consists of four independent fluid reservoir tanks. One fresh water and one acid-water fluid reservoir are located at the inflow side respectively and

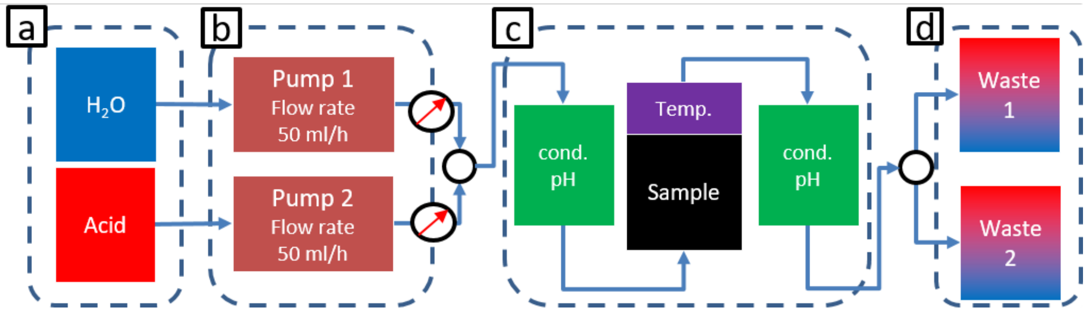

Figure 3.6: Schematic view of a custom built device for the dissolution treatment procedure. a) Inflow fluid reservoir tanks for water and acid. b) High-precision piston pumps for each fluid, including pressure measurement at the core holder inflow. c) Core holder with a temprature sensor inside a furnace for sample saturation and cleaning, including pH-value and fluid conductivity monitoring at both, inflow and outflow side. d) Outflow waste fluid reservoir tanks.

two tanks for the residual fluids are at the outflow side. The fluids are pushed trough the sample by two high precision piston pumps for each fluid, which allow variable flow rates in the range of 0.001 to 999 ml·h^{-1} at a maximum inflow pressure of 40 bar. The monitoring of fluid conductivity and pH-value of the inflowing and outflowing fluid takes place permanently during the experiment. Other continuously measured parameters are the pressure at sensors between pumps and sample and the temperature directly at the outflow of the sample.

Acid

Carbonate samples are treated with a solution of the acid Acidgen$^{\mathrm{TM}}$FG3 of the company Cleansorb Solution. This type of acid is a temperature activated type and allows a homogeneous dissolution of carbonate throughout the whole pore space. A previous investigation demonstrated the homogeneous dissolution of carbonate samples under quite easy to handle laboratory conditions (Kjøller et al., 2016). The general chemical reactions can be formulated as:

$$\text{Stage 1:} \quad \mathrm{Acidgen^{TM}FG3} + \mathrm{H_2O} \Rightarrow \mathrm{2HCOOH}; \tag{3.26}$$

$$\text{Stage 2:} \quad \mathrm{2HCOOH} + \mathrm{CaCO_3} \Leftrightarrow \mathrm{Ca(HCOO)_2} + \mathrm{CO_2} + \mathrm{H_2O}.$$

Stage 1 describes the creation of the water-acid-mixture and stage 2 the dissolution procedure after saturating the sample with the solution. The acid combined with water forms a formic acid solution. The reaction of the formic acid solution with the carbonate leads to water, gaseous CO_2 and calcium-formate as reaction products. The calcium-formate is totally dissolved in the water because of its high solubility (160 g·l^{-1}).

General dissolution procedure

The principle workflow of the procedure is shown in Figure 3.7. The investigation starts with a basic characterisation of the carbonate sample by a general core analysis program (N2 adsorption, TWM, steady-state gas permeability, NMR, μ-CT, ESEM) including SIP measurements of the untreated sample. Next is the dissolution of the initially water saturated sample (tap water conductivity 50 mS·m^{-1}). Each sample is flushed with 10 pore volumes (PV) of a 5 vol-% acid solution at flow rates of 40 ml·h^{-1} to 50 ml·h^{-1}. After 5 PV the plug is turned around and is flowed through from the other side to prevent trapping effects. The flushing is monitored by the electrical conductivity measurement of the inflow and outflow fluid and is completed once the electrical conductivity at the outflow

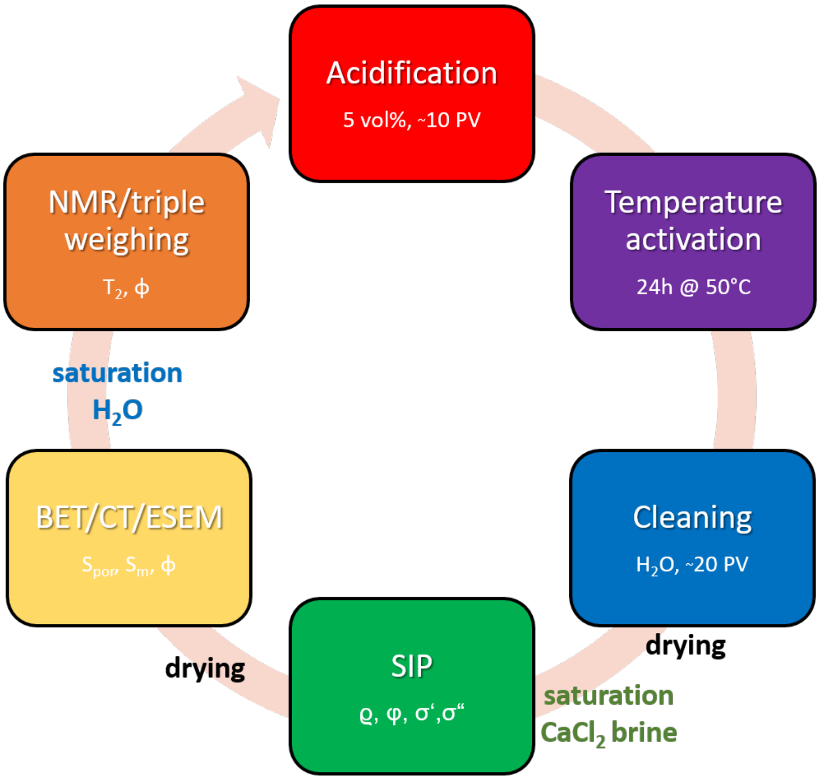

Figure 3.7: Principle sketch of the workflow that is used for the laboratory measurements and dissolution procedures on the carbonate samples.

reaches a steady state. The temperature activation of the chemical reaction follows in a furnace by increasing the temperature to 50 °C for a shut-in period of 24 hours. Afterwards, the sample is flushed with fresh water until the conductivity of the outflowing fluid achieves the same level of the water conductivity as measured at the inflow. The amount of fresh water for cleaning is estimated with 20 PV (10 PV in each direction). SIP and core analysis (CAL) measurements follow these steps in order to quantify the effects of acid treatment. SIP measurements were conducted at a constant temperature of 20 °C using a $CaCl_2^-$ solution with a constant conductivity of 100 $mS{\cdot}m^{-1}$ as pore fluid. Due to the expense, μ-CT, MIP and ESEM images are not part of each treatment cycle and only conducted on selected samples. This workflow is repeated as previously described.

Side track investigation of the induced dissolution process

In addition to the systematic general dissolution procedures (section 3.4), μ-CT and MIP measurements are carried out on one plug as a systematic side track investigation for the dissolution experiment. The reasons for this side track investigation are, that either the method requires a fragment of the plug (μ-CT), or the procedure is irreversible and the sample is destroyed after the measurement (MIP). Additionally, the results will help to support the overall interpretation and

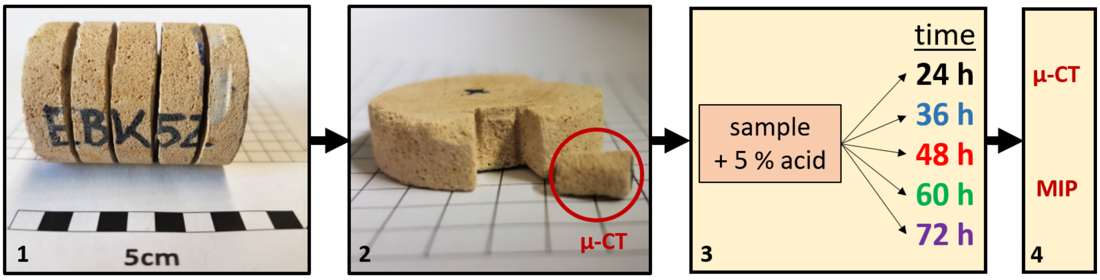

Figure 3.8: Principle workflow of the side track investigation of the induced dissolution. (1) Cutting the plug into five slices. (2) Sub-sampling for μ-CT imaging. (3) Acidification for different time intervals. (4) Final investigations by μ-CT and MIP.

understanding of the dissolution process. For this purpose, a plug was divided into five slices and a sub-sample from each slice was cut out for the 3D imaging. First, the specimens were imaged in untreated state. In the next step, the slices and the according sub-samples were treated by the same 5 vol-% acid, but with different durations of dissolution. The time periods are 24 h, 36 h, 48 h, 60 h, and 72 h. After the treatment, the μ-CT imaging is repeated for each of the specimens. The residual part of the slice is used for MIP measurements. Figure 3.8 shows the principle workflow of the side track investigation.

4 Sample material

4.1 Carbonates in general

Carbonates are classified as sedimentary rocks, which are composed primarily of carbonate minerals. Generally, carbonates are divided in two major types: limestones consisting of calcite or aragonite ($CaCO_3$) and dolostones consisting of dolomite ($CaMg(CO_3)_2$) (Siever et al., 2004). Carbonates are biochemical in nature and are formed and deposited in situ in near-shore lagoons, platforms organic build ups, and shelf margin shoals to slope and basinal settings. Warm, shallow, clear marine water in low latitudes is a good indicator for carbonate deposits. Lime secreting animals, plants and bacteria exist and form carbonate rocks with shells and secretion and in addition lead to chemical precipitation of calcium carbonates or calcium-magnesium carbonates (Tiab & Donaldson, 2012). The diagenesis contains six major processes including cementation, microbial micritisation, neomorphism, dissolution, compaction and dolomitisation (Tucker & Wright, 1990) and takes place in three major diagenetic environments containing marine, near-surface meteoric and burial environments. The three major components of a carbonate rock are grains (allochems), the matrix (micrite) and cementation (sparite) (Folk, 1962).

The simple mineralogy of carbonates rocks contrasts the complexity of the petrography and the chemistry (Tucker & Wright, 1990). Because of their large range of origin, carbonates highly vary in composition and have a wide property range. The textures can be described depositionally (similar to siliclastic sediments), by the growth of the organism or by production of chemical precipitation. Carbonates are characterised by a great diversity of grain sizes and porosities. Sandstones indicate intergranular porosity, whereas carbonates show an irregular porosity referred to type and distribution (e.g. intercrystalline, mouldic, fracture, channel, vuggy porosity) (Tucker & Wright, 1990). Most porosity in limestones is diagenetic (secondary porosity), whereas sandstones have mostly a primary porosity. Additionally, the carbonate pore system itself is more complex as well as the pore size distribution, compared to sandstones.

A systematic study was conducted that includes four different carbonate types: Indiana Limestone (ILS), Silurian Dolomite (DOL), Lueders (LK) and Edwards Brown Carbonate (EBK), which were classified as biogenous sediments. All used samples are clay-poor carbonates. Despite of the regional problem of karstification and subrosion, carbonates from Lower Saxony are not considered. The regional carbonates of the jurassic are heterogeneous and very tight and thus they are not suitable for a systematic study and characterisation. In choosing samples, it is important, that the samples of each carbonate type show a broad range of the petrophysical parameters covering a wide spectrum. There are 50 plugs of each carbonate type to have a sufficient number of identical or rather comparable samples. I used cylindrical plugs with a length of 40 mm and a diameter of 30 mm. Since the micro structure of carbonates differs from sandstones, a micro scale investigation was performed in order to give an insight into the micro structure and composition of the investigated rock types. The core analysis was carried out on the entire sample, except μ-CT and the MIP measurements. While μ-CT requires a sample size of $< (5 \mathrm{x} 2)$ mm, MIP is an irreversible process for which half a plug was used. XRF, XRD, CEC and carbon analysis were carried out on the other half, making the sample useless for further core analysis.

The selection of the carbonate type, which is used for the dissolution experiment, takes place according to specified criteria. Firstly, sufficiently high porosity of the sample is required to ensure an adequate amount of the acid fluid inside of the sample. This guarantees, that the chemical reaction causes significant changes before the chemical equilibrium is obtained and the dissolution stops. Secondly, a high permeability is advantageous, because the experimental setup is based on flow through or, more precisely, flow rates. Thirdly, the phase spectra of the IP measurement should have a characteristic shape (e.g. maximum type) to facilitate the observability and quantification of changes due to the dissolution. In view of these criteria, the Edwards Brown Carbonate has been selected, which is described more in detail in section 4.2.

4.2 Edwards Brown Carbonate (EBK)

The Edwards Brown Carbonate originates from a quarry in Texas/USA and belongs to the Edwards limestone group of the Edwards Plateau, which also includes the Edwards White and Edwards Yellow Carbonates. The deposition of the carbonate sediments took place in mostly shallow marine water and tidal environments during the early Cretaceous (Maclay & Small, 1984).

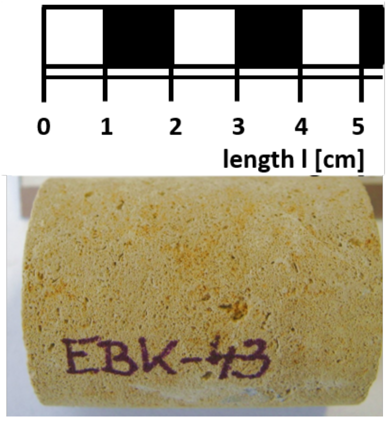

Figure 4.1: Plug of an EBK sample used for petrophysical analysis.

The EBK (see in Figure 4.1) can be described as a yellow beige, highly porous sparite, which is obviously diagenetically overprinted. Indicators of dissolution and precipitation are visible as well as intraclasts. Additionally, an intense reaction with hydrogen chloride (HCl) is observable. The samples are heterogeneous and the whole set of samples shows different proportions of matrix and parts with recrystallisation. The recrystallisation of rocks in this formation is mainly caused by dedolomitisation. It describes the replacement of magnesium with calcite caused by freshwater flushing (Maclay & Small, 1984).

4.2.1 Mineralogical and geochemical characterisation

Representative ESEM-images of the EBK are shown in Figure 4.2. The fine-grained matrix of the EBK consists of idiomorphic rhombohedral-shaped crystals with diameters between 10 μm and 20 μm. Some of them show cavities inside (Fig. 4.2 a). Cementation is observable on the crystal surfaces, but does not occur in larger pores (Fig. 4.2 b). The EDX suggests a dolomite as seen in the quantification result in Figure A.6. Dolomite ($MgCa(CO_3)_2$) has an amount of 90 wt% according to EDX analysis. The composition of $CaMg(CO_3)_2$ is a sign for a dolostone. A negligible amount of kaolinite ($Al_4[(OH)_8[Si_4O_{10}])$ was identified in some samples (Fig. A.7), which is of minor importance.

The results of the EDX has been confirmed by the XRF and XRD analysis as well as by the determination of the carbon and sulphur content. One third of a plug from several samples was analysed. Figure 4.3 shows the average chemical composition of the EBK consisting of 90 % $CaMg(CO_3)_2$, 7.5 % SiO_2 and 2 % clay minerals, inter alia Al_2O_3. Aluminium oxide is an indication of kaolinite. The complete list of major and trace elements is given in the appendix (Tab. B.5). The carbon and sulphur analysis indicates a total carbon content of 11.5 % to 12 %.

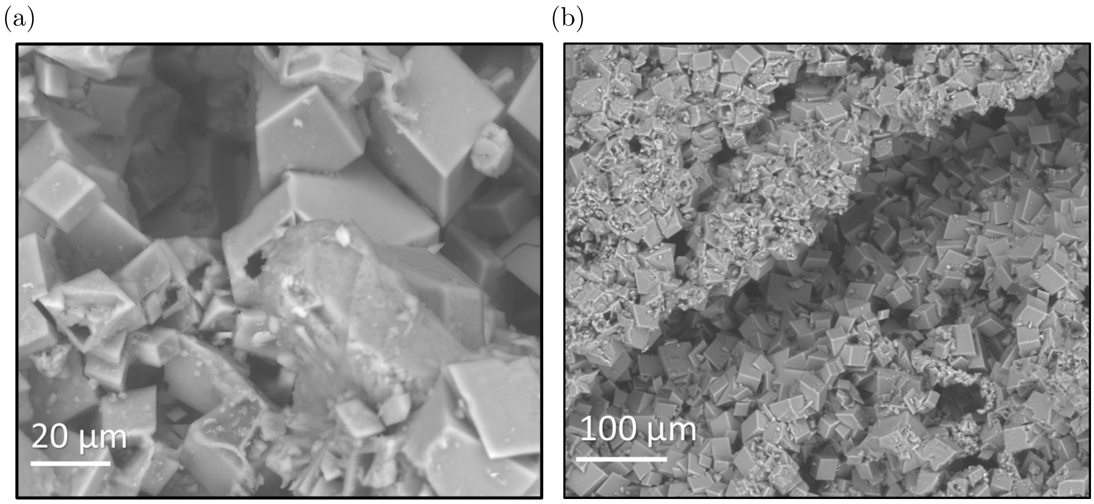

Figure 4.2: ESEM-images of the Edwards Brown Carbonate showing a) dolomitic crystals with cavities and b) the fine-grained matrix consisting of dolomitic crystals.

The sulphur content is even less ($< 0.1\,\%$) and may originate from traces of pyrite. According to X-ray diffraction, the detected major and minor components are calcite, dolomite and ankerite ($CaFe[CO_3]_2$) as shown in Tab. B.9. The identified trace minerals are calcite, quartz, kaolinite, whereby calcite is either major/minor or trace mineral (Tab. B.9).

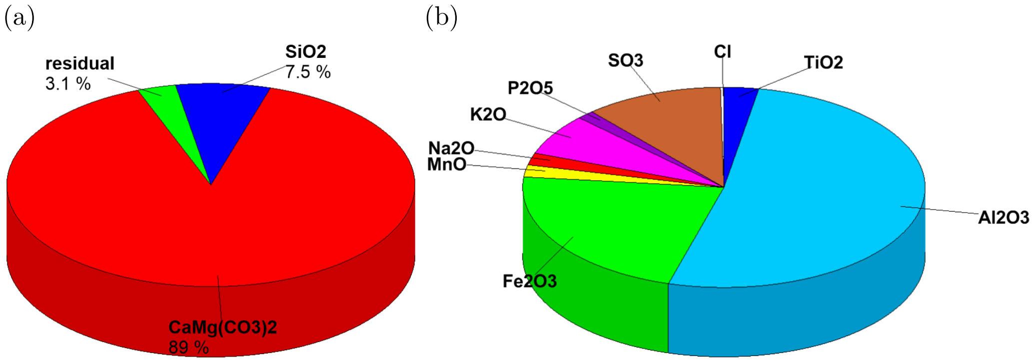

Figure 4.3: Average composition of the minerals in the Edwards Brown Carbonates. a) Major components are dolomite ($CaMg(CO_3)_2$; 89 %) and quartz (SiO_2; 7.5 %). The remaining components comprises 3.1 %. b) Minor components are 3.1 % of all components in total. Clays (1.9 %) include the minerals aluminium oxide (Al_2O_3), manganese oxide (MnO), potassium oxide (K_2O) and sodium oxide (Na_2O). Significant minerals are iron(III) oxide (Fe_2O_3), aluminium oxide (Al_2O_3) and sulphur trioxide (SO_3)

4.2.2 Petrophysical characterisation

The general core analysis program for density, porosity, permeability, surface area and NMR T_2 decay time is conducted for the whole sample set of EBK, whereas MIP and μ-CT measurements were performed only on selected samples, because

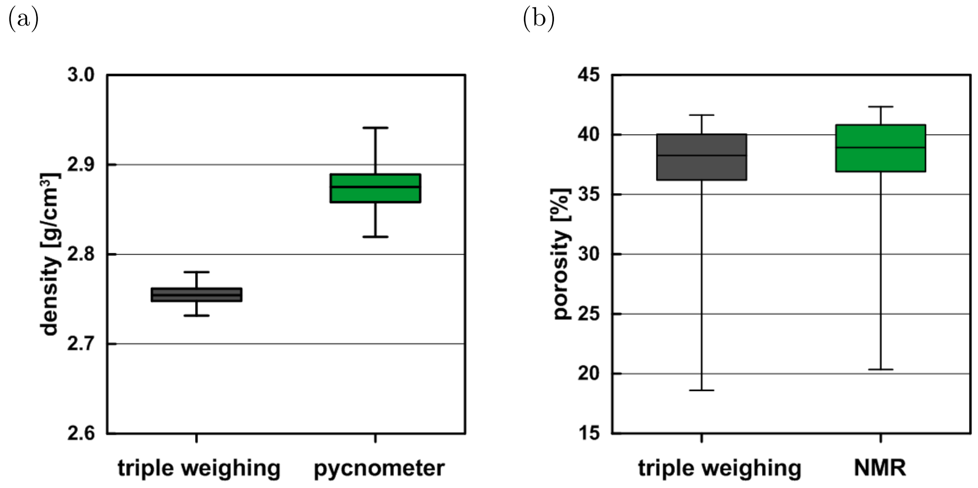

Figure 4.4: Results of the petrophysical characterisation of the EBK are shown in box-and-whisker plots. a) Comparison of the density values measured by triple weighing and by using a pycnometer. b) Comparison of the porosity values determined by triple weighing and NMR measurements.

the sample is useless for further investigations afterwards. Figure 4.4 a shows the comparison between densities derived from the triple weighing method (TWM) and by the pycnometer measurements. The density ranges from $2.73\,\mathrm{g}\cdot\mathrm{cm}^{-3}$ to $2.78\,\mathrm{g}\cdot\mathrm{cm}^{-3}$, whereas the pycnometer density is higher with a range between $2.82\,\mathrm{g}\cdot\mathrm{cm}^{-3}$ to $2.94\,\mathrm{g}\cdot\mathrm{cm}^{-3}$. The gap between both methods can be explained by the use of different fluids to detect the volume of the sample. Water is used by TWM whereas helium is used by the pycnometer measurements, which results in a systematic deviation of the density. This observation is made exclusively for carbonates and not known for sandstones. Literature values for major components calcite are between $2.70\,\mathrm{g}\cdot\mathrm{cm}^{-3}$ and $2.74\,\mathrm{g}\cdot\mathrm{cm}^{-3}$ and for dolomite between $2.86\,\mathrm{g}\cdot\mathrm{cm}^{-3}$ and $2.95\,\mathrm{g}\cdot\mathrm{cm}^{-3}$ (Schön, 2004). The sample set indicates a low scattering of the densities, regardless of the method. A complete list of the density measurements is part of the appendix (Tab. B.1).

The EBK is characterised by high porosities (Fig. 4.4 b) which were determined by NMR and TWM. The NMR porosity is slightly higher compared to the TWM. The majority of the samples shows porosities of about 37 %. However, the porosity is significantly reduced to 18.6 % (TWM) and 20.4 % (NMR) for some plugs. The samples with lower porosities have more parts with recrystallisation structures or, more precisely, cemented areas, standing for zones with less pore space. In the following, all correlations are plotted with the porosity values of the triple weighing method.

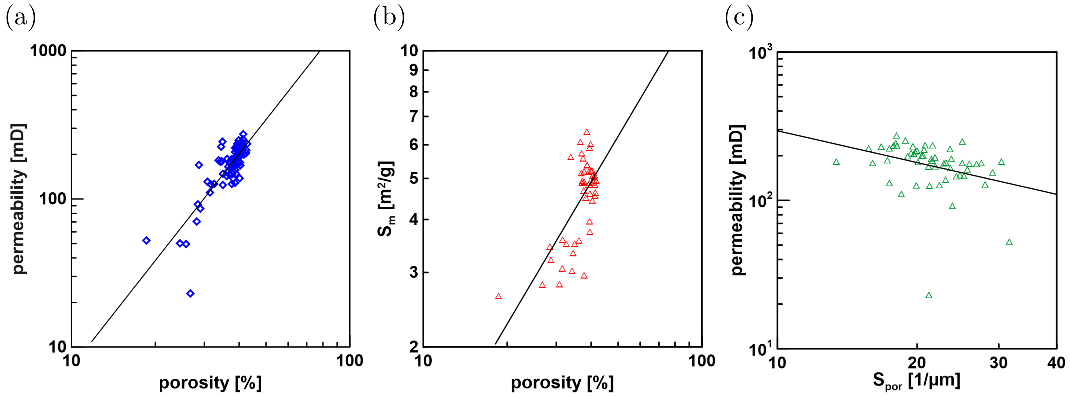

Figure 4.5: Crossplots of the pore-space properties of the EBK samples. a) Permeability in relation to porosity values. b) S_m in relation to porosity values. c) Permeability in relation to S_por values.

Furthermore, a moderate permeability is characteristic for the EBK (Fig. 5.1 b) with an average of 200 mD, whereas the minimum is at 27 mD and the maximum is at 291 mD. A positive correlation appears between the porosity and permeability according to Figure 4.5 a. The relation can be described by $k = 0.03 \cdot \Phi^{2.39}$, $R^2 = 0.68$. R-squared (R^2) is the coefficient of determination evaluating the quality of a fit in a range of 0 to 1. The dependence of permeability on porosity for sandstones is obvious, but it is not comparable in the same way for carbonates, because of their higher number of porosity types.

Surface areas have been derived from 7-point BET adsorption measurements for each sample as shown in Figure 5.1 c and d. The surface related to the mass (S_m) is directly determined and the surface area related to the pore volume (S_por) is calculated by Equation 3.17. The average of S_por is 21.6 $\mu\mathrm{m}^{-1}$, but the range varies between 13.4 $\mu\mathrm{m}^{-1}$ to 31.6 $\mu\mathrm{m}^{-1}$. The derived values of S_m differs from 2.6 $\mathrm{m}^2 \cdot \mathrm{g}^{-1}$ to 6.4 $\mathrm{m}^2 \cdot \mathrm{g}^{-1}$ with an average of 4.6 $\mathrm{m}^2 \cdot \mathrm{g}^{-1}$. The cross plot in Figure 4.5 b shows no relationship between the porosity and S_m ($R^2 = 0.48$). Samples with a porosity of about 40 % cover the complete range of S_m. This can also be applied for the relationship between S_por and permeability as shown in Figure 4.5 c: no significant trend between both parameters is observable ($R^2 = 0.10$).

NMR measurements provide, next to the porosity, information about pore size distribution and effective porosity. Figure 4.6 shows three exemplary pore radius distributions of the EBK including the average percentage of effective porosity of all NMR investigations related to the empirical cut off values. A comparison of the red with the blue spectra in Figure 4.6 shows that different porosities influence the T_2 decay time spectra and thus, the pore radius distribution. The part of the bimodal T_2 distribution relating to cut off times higher than 33 ms (as indication for free movable water) corresponds to large pores and interconnected pore space. Accordingly, approximately 75 % of the effective porosity results from large pores. The cut off times of the distribution between 4 ms and 33 ms are related to capillary water, which equals medium sized pores. The medium sized pores contribute 25 % to the effective porosity. For cut off times < 4 ms, the NMR signal is related to clay bound water and therefore small pores. Decay time spectra of the EBK shows that 0.5 % of the effective porosity is related to small pores. In average, the calculated median radius of the pores r_{50} is 35.6 μm using 100 μm·s^{-1} as surface relaxivity and Equation 3.19. The surface relaxivity results from the plot of the μ-CT and NMR results as seen in Figure 4.8. Since the NMR method and μCT data are both sensitive to the pore body radius, the surface relaxivity has been chosen so that a good agreement between both curves in the overlapping range of pore body radii is reached.

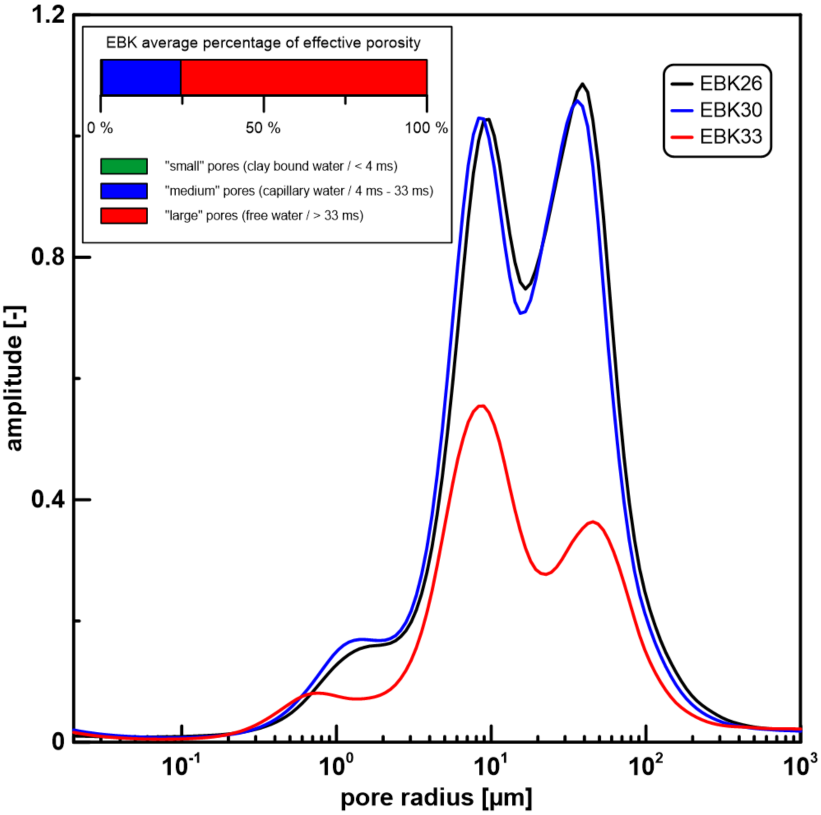

Figure 4.6: Exemplary pore radius distributions from NMR measurements using $\rho_S = 100\,\mu\text{m}{\cdot}s^{-1}$ for three samples and average percentage of effective porosity for the EBK samples.

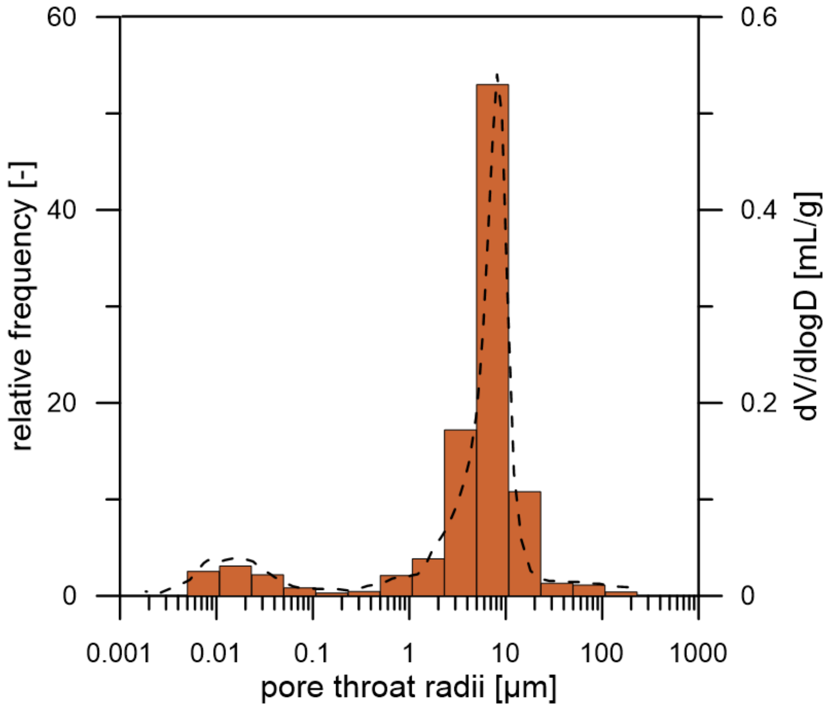

Figure 4.7: Representative pore throat distributions derived from mercury injection experiments for the EBK samples.

The results from capillary pressure experiments differ from NMR observations. The pore throat radii distribution indicates a range of $r_{\mathrm{dom}} = 6\,\mu\mathrm{m}$ - $8\,\mu\mathrm{m}$ (Fig. 4.7). However, the main pore throat size is determined in between of 3 to 20 μm. The differences are due to the fact that NMR is more sensitive to the pore body and MIP is sensitive to the pore throats.

The μ-CT measurements provide also a pore radius distribution after digital image analysis. Figure 4.8 shows the combination of the pore radius distribution determined by MIP (black), μ-CT (green) and NMR (blue). For clarity, the pore volume distribution is plotted for all methods and the area below the curves corresponds to the porosity. The number of grid points between the decades is ten for each method to ensure a better comparability. The MIP curve corresponds to the narrow pores, whereas the μ-CT curve correlates to the wide pores. The pore geometry of the EBK can be described as more heterogeneous with larger pore aspect ratios (≈ 8). The two relaxation peaks of the NMR measurement can be attributed to both the narrow or the wide pore.

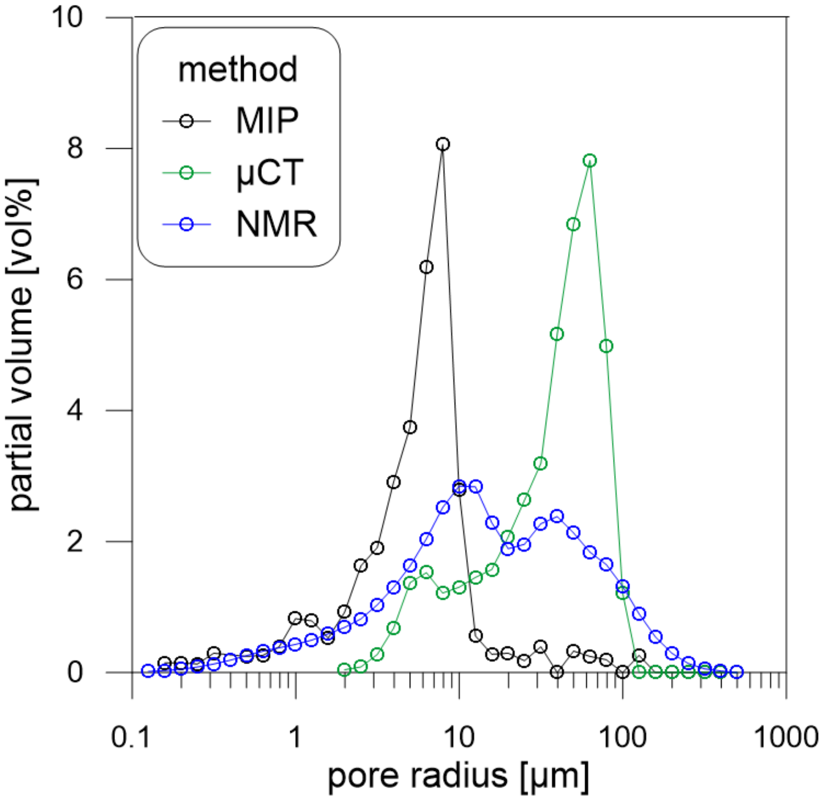

Figure 4.8: Pore radius distribution from MIP, μ-CT and NMR data using $\rho_S = 100\,\mu\text{m}\cdot s^{-1}$ for the EBK.

4.3 Lueders Carbonate (LK)

The Lueders carbonate or limestone is part of the Lueders formation, which is associated to the Permian. The formation is named after the eponymous Lueders Basin near Abilene, Texas. The rock is characterised by a macroscopically homogeneous and isotropic structure (Heard & Griggs, 1972). Teufel & Clark (1981) have described this carbonate as greyish-tan, fine-grained limestone. The limestone is composed of calcium carbonate in the form of micrite, diagenetically altered organic particles, fossil fragments and sparry calcite cement.

The first rock description of the Lueders samples, as shown in Figure 4.9, widely confirms these literature descriptions. The sample is a white to light grey low porous micritic biosparite. The rock is massive and contains dissolution pores (secondary porosity). Molluscs with sizes of 0.25 mm to 1 mm are visible. Furthermore, a very intense reaction with hydrogen chloride (HCl) is observable.

Figure 4.9: Plug of a LK sample used for petrophysical analysis.

4.3.1 Mineralogical and geochemical characterisation

Representative ESEM-images of the LK are shown in Figure 4.10. The LK has a very fine crystalline calcium carbonate matrix with small recrystallisation structures and with a wide range of grain sizes (Fig. 4.10 a). The EDX proposes an almost pure calcite as seen in the quantification results in Figure A.8. Calcium carbonate ($CaCO_3$) has an amount of 92 wt% according to EDX analysis. The samples contain also a small amount of iron hydroxide ($Fe_2(OH)_3$), which can be seen as a white-coloured material in Figure 4.10 b. The results of the EDX analysis are shown in Figure A.9.

The results of the EDX can be confirmed by the XRF analysis, XRD analysis, and the determination of the carbon and sulphur content. Figure 4.11 shows the average chemical composition of the LK consisting of 90 % $CaCO_3$, 6.7 % SiO_2

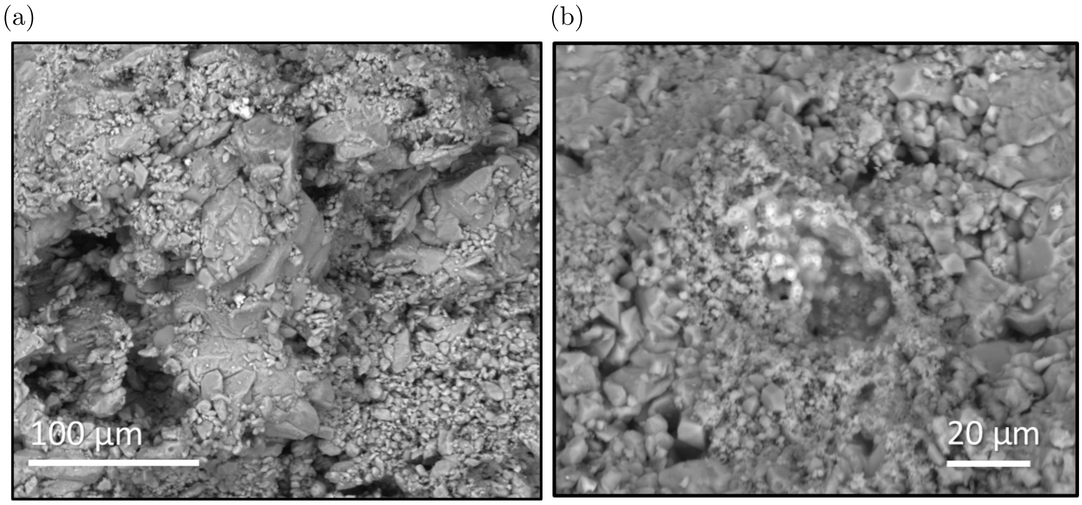

Figure 4.10: Exemplary ESEM-images of the Lueders carbonate. a) Overview of the matrix of the LK and the wide range of grain sizes. b) Shot of probably a piece of illite covered by white-coloured iron hydroxide.

and less than 1 % clay minerals, i.a. Al_2O_3. The complete list of major and trace elements is given in the appendix (Tab. B.7). The carbon and sulphur analysis indicates a total amount of carbon of 11.1 % to 11.5 %, whereby the organic carbon proportion is less than 0.1 %. The sulphur content is even less (< 0.1 %). X-ray diffraction is used to analyse the mineral composition of the LK. The detected major and minor component is calcite as shown in Tab. B.9. Quartz is identified as trace mineral (Tab. B.9).

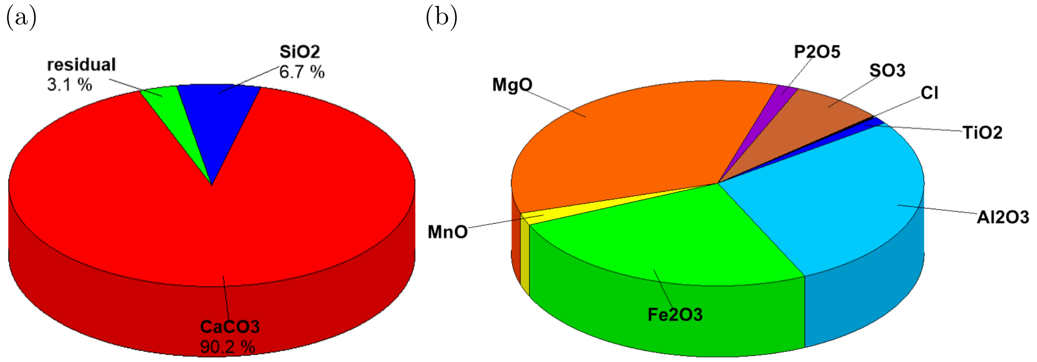

Figure 4.11: Average composition of the minerals in the Lueders carbonate. a) Major components are calcite ($CaCO_3$; 90.2 %) and quartz (SiO_2; 6.7 %). The remaining components comprise 3.1 %. b) Minor components are 3.1,% of all components in total. Clays (1 %) include the minerals aluminium oxide (Al_2O_3), manganese oxide (MnO), potassium oxide (K_2O) and sodium oxide (Na_2O). Significant minerals are iron(III) oxide (Fe_2O_3), aluminium oxide (Al_2O_3) and sulphur trioxide (SO_3)

4.3.2 Petrophysical characterisation

The general core analysis program for density, porosity, permeability, surface area, NMR T_2 is conducted for the whole sample set of EBK, whereas MIP and μ-CT measurements took place only on selected samples. The comparison of the densities derived from the triple weighing method (TWM) and by the pycnometer measurements is shown in Figure 4.12 a. The grain density derived from TWM ranges from 2.68 g·cm^{-3} to 2.71 g·cm^{-3}, whereas grain density values of the pycnometer are in a higher range of 2.74 g·cm^{-3} to 2.80 g·cm^{-3}. The values are identified to be in a realistic range for carbonates consisting of more than 90 % calcite ($\rho_{\text{calcite}} = 2.70$ g·cm^{-3} - 2.74 g·cm^{-3} (Schön, 2004)). A complete list of the grain density measurements is part of the appendix (Tab. B.2).

The LK is characterised by porosities of around 10 % to 20 % (Fig. 4.12 b). The porosities are determined by NMR and TWM. Both methods display almost identical results, whereby the porosity values of the NMR measurements are

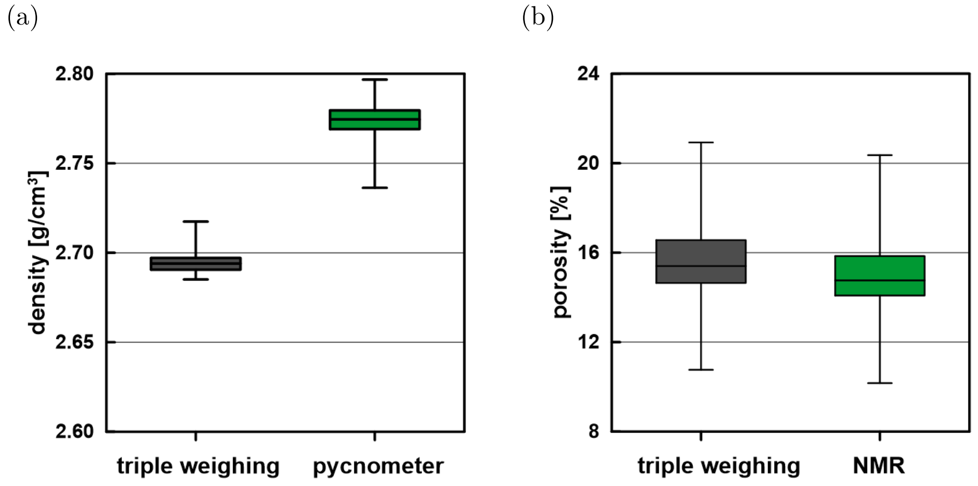

Figure 4.12: Results of the petrophysical characterisation of the Lueders carbonate are shown in box-and-whisker plots. a) Comparison of the density values measured by triple weighing and by using a pycnometer. b) Comparison of the porosity values determined by triple weighing and NMR measurements.

slightly lower. The samples have a mean value of about 15 %. In the following, all correlations are plotted with the porosity values of the triple weighing method.

A further characteristic of the LK is its small permeability k in comparison to the EBK (Fig. 5.1 b). The minimum is at $k = 0.07$ mD and the maximum is $k = 4.4$ mD. The porosity values correlate with the permeability values as seen in Figure 4.13 a. The permeability increases with increasing porosities. Porosity and permeability show a good correlation ($k = 5.8 \cdot 10^{-8} \cdot \Phi^{5.76}$, $R^2 = 0.77$), which is a general indication of rock sample homogeneity.

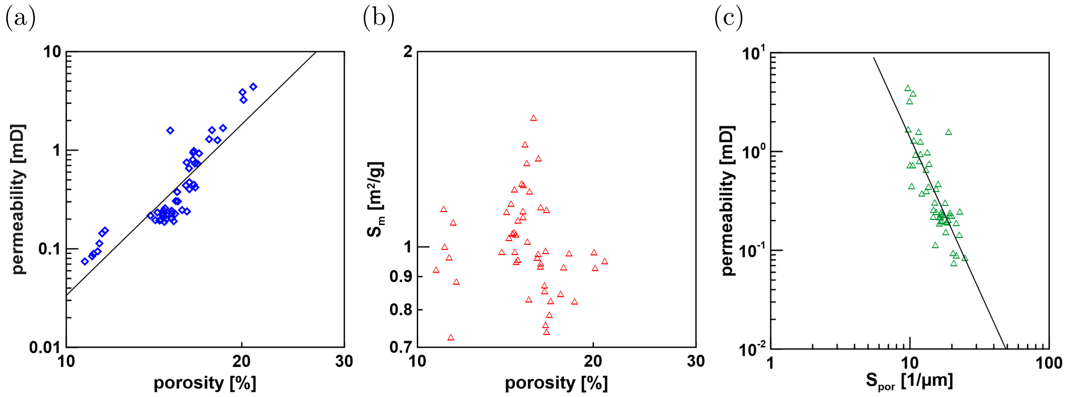

Figure 4.13: Crossplots of the pore-space properties of the LK samples. a) Permeability in relation to porosity values. b) S_m in relation to porosity values. c) Permeability in relation to S_por values.

The surface related to the mass (S_m) is directly determined and the surface area related to the pore volume (S_por) is calculated by the means of S_m and the measured porosities and densities of the TWM. The results are shown in Figure 5.1 c and d. The average value of S_por is at 15.6 μm^{-1} and in total the values have a broader range from 9.7 μm^{-1} to 24.7 μm^{-1}. The derived values of S_m vary from 0.73 m^2·g^{-1} to 1.58 m^2·g^{-1} with an average value of 1.03 m^2·g^{-1}. The cross plot of porosity and S_m (Fig. 4.13 b) shows no relationship ($R^2 = 0.010$). A negative trend is observed for the relationship of permeability and S_por (Fig. 4.13 c); if the surface increases the permeability decreases: $k = 1.77 \cdot 10^3 \cdot S_\mathrm{por}^{-3.1}$, $R^2 = 0.66$.

Figure 4.14 shows four exemplary pore radius distributions of the LK including the average percentage of effective porosity of all NMR investigations related to the empirical cut off values. The LK samples have a high number of large pores (approximately 52 % in average) and medium range pores (capillary bound water; approximately 47 % in average). The residual 1 % of the effective porosity is related to clay bound water, i.e. small pores. In average, the calculated median radius of the pores r_{50} is 5.6 μm using 45 μm·s^{-1} as surface relaxivity. The surface relaxivity results from the plot of the μ-CT and NMR results as seen in Figure 4.16.

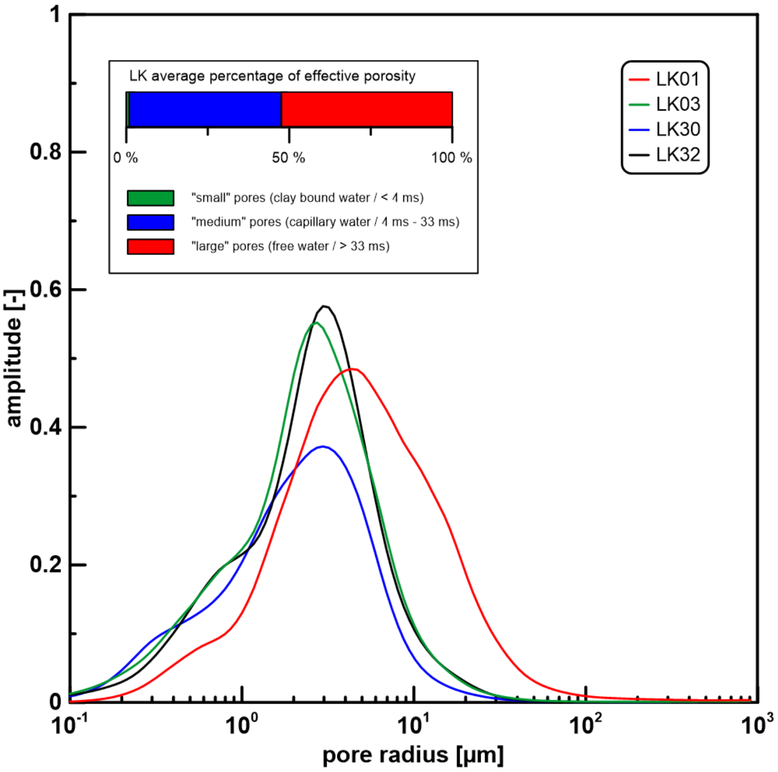

Figure 4.14: Exemplary pore radius distribution from NMR data using $\rho_\mathrm{S} = 45\,\mu\mathrm{m}\cdot s^{-1}$ of four samples and average percentage of effective porosity of the LK samples.

The capillary pressure experiments of the LK show a dominant pore radius ($r_{dom} = 0.6\,\mu m$), which is one magnitude smaller in comparison to the EBK (Fig. 4.15). More than 80 % of the pore throats radii are in the range of $0.05\,\mu m$ to $0.5\,\mu m$.

A common representation of the results of the pore radius distribution determined by MIP (black), μ-CT (green) and NMR (blue) is given in Figure 4.8. The pore geometry of the LK can be described as more heterogeneous with larger pore aspect ratios (> 30). One relaxation peak of the NMR measurement can be attributed the wide pore. The other one of the bimodal distribution does not support the narrow pores of the MIP data. It is a possible solution that NMR is more affected by the larger pores.

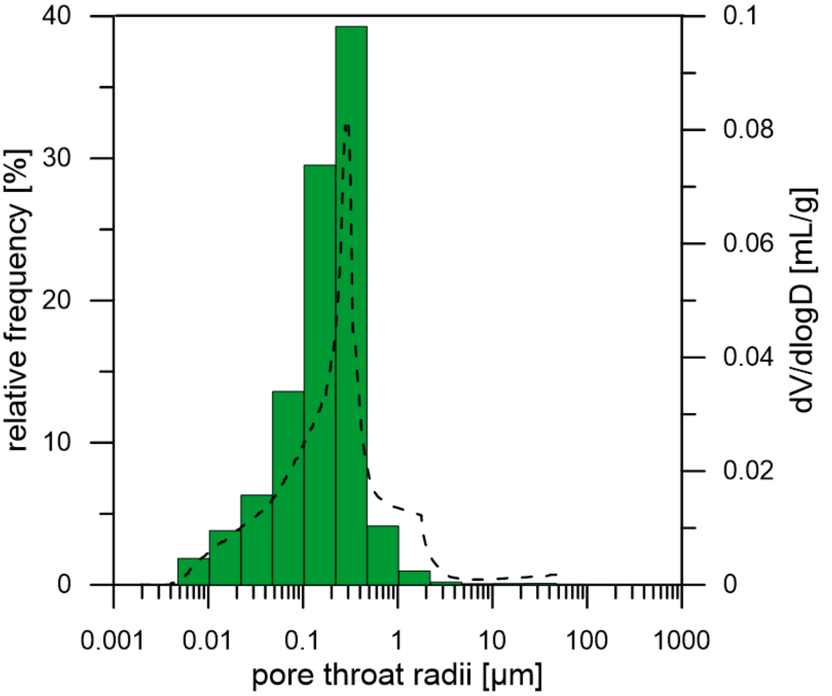

Figure 4.15: Representative pore throat distribution derived from mercury injection experiments on the LK samples.

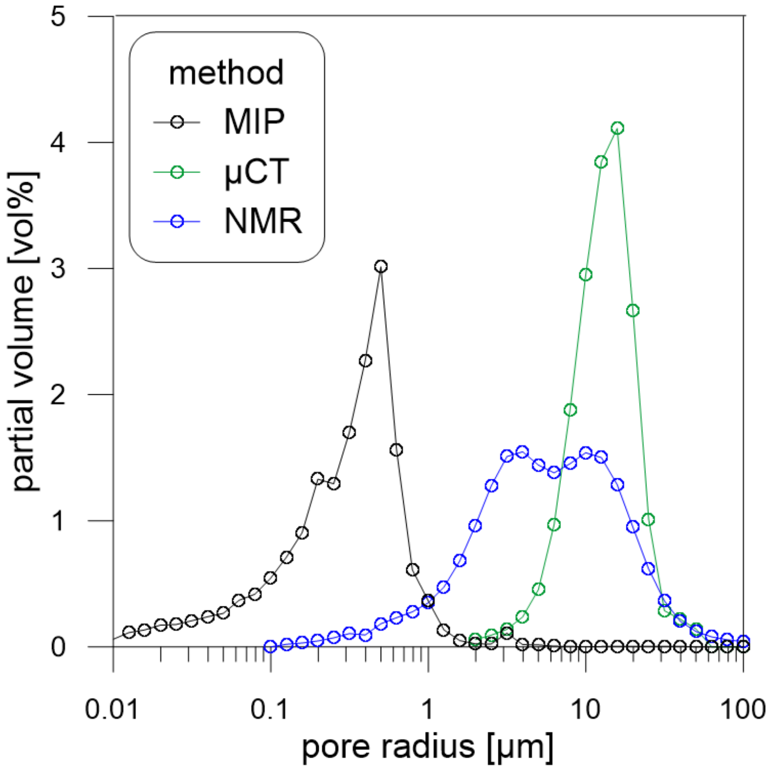

Figure 4.16: Pore radius distribution from MIP, μ-CT and NMR data using $\rho_S = 45\,\mu\text{m}\cdot s^{-1}$ for the LK.

4.4 Indiana Limestone (ILS)

The Indiana limestone or formerly called Salem limestone is part of the Salem formation, which is associated with the middle Mississippian. The ILS is located in the U.S. states Illinois, Indiana, Kentucky, and Missouri and is primarily quarried near Bedford (Indiana). Ji et al. (2012) have classified this limestone as a calcite-cemented grainstone with fossil fragments. The main fossils are bryozoans, echinoderms, and endothyra (Carr et al., 1966). Besides fossils, other allochems are ooids and peloids, which are all frequently coated with concentric layers of calcite (Ji et al., 2012).

The first description of the Indiana limestone samples as shown in Figure 4.17 widely confirms these results. The limestone is a porous ooid-leading bioclastite with needle-shaped fossils (sponges, echinoderms) and shell fragments (molluscs, gastropods). The ILS is a homogeneous grainstone of uniform texture and grade. Additionally, an intense reaction with hydrogen chloride (HCl) is observable.

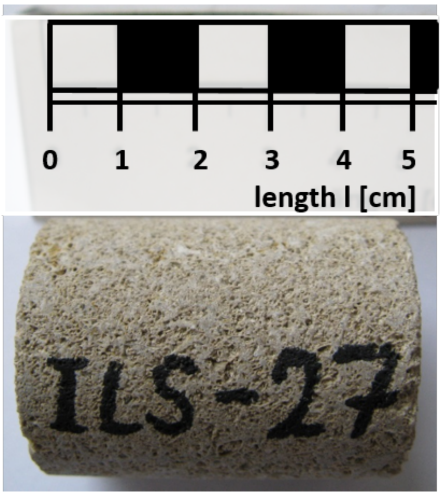

Figure 4.17: A plug of an ILS sample used for petrophysical analysis.

4.4.1 Mineralogical and geochemical characterisation

Exemplary ESEM-images of the Indiana limestone are shown in Figure 4.18. The ILS contains almost exclusively calcium carbonate (Fig. 4.18 a). The calcium carbonate exists as recrystallisation structures and partly with sharp-edged fractured surfaces. Aggregates with calcite shells are visible, which recrystallise towards the pore (Fig. 4.18 b). The EDX suggests calcite as shown in the quantification result in Figure A.10. Calcium carbonate ($CaCO_3$) has an amount of 91.1 wt% according to EDX analysis.

The average chemical composition of the ILS is determined using the XRF analysis and confirmed the results of the EDX. The Indiana limestone consists of 98 % $CaCO_3$, 0.6 % SiO_2 and less than 0.1 % clay minerals, i.a. Al_2O_3 (Fig. 4.19). The

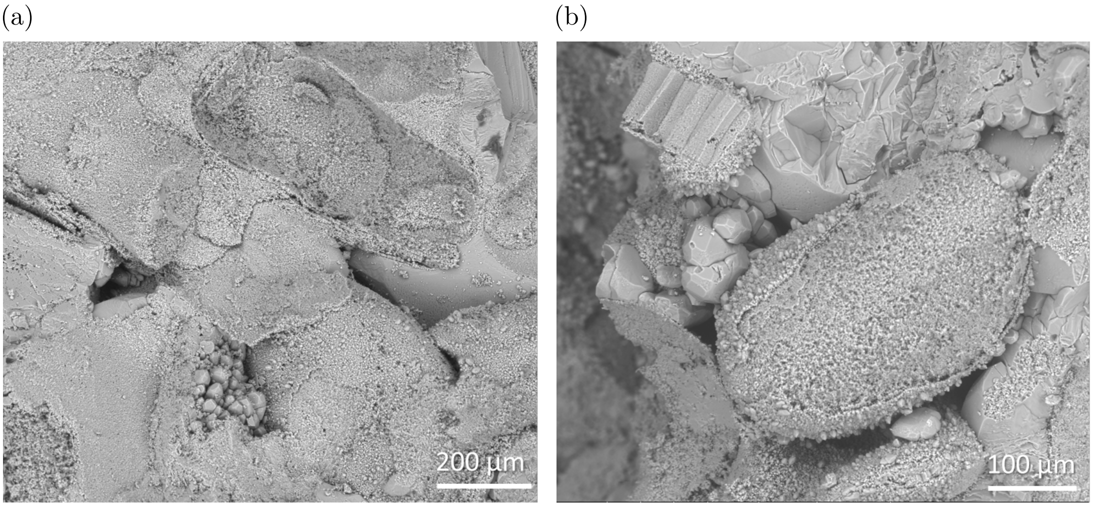

Figure 4.18: Exemplary ESEM-images of the Indiana limestone. a) Overview of the almost calcitic matrix of the ILS. b) Shot of an aggregate with calcite shells.

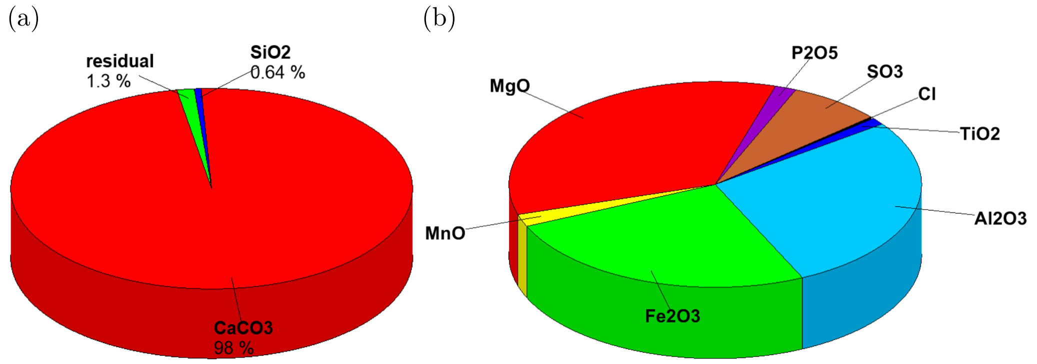

Figure 4.19: Average composition of the minerals in the Indiana limestone. a) Major components are calcite ($CaCO_3$; 98.0 %) and quartz (SiO_2; 0.64 %). The remaining components comprise 1.34 %. b) Minor components are 1.34,% of all components in total. Clays (0.10 %) include the minerals aluminium oxide (Al_2O_3), manganese oxide (MnO), potassium oxide (K_2O) and sodium oxide (Na_2O). Significant minerals are iron(III) oxide (Fe_2O_3), aluminium oxide (Al_2O_3) and sulphur trioxide (SO_3).

complete list of major and trace elements is given in the appendix (Tab. B.6). The CO analysis reveals a carbon content of 11.9 % to 12.1 %. According to XRD analysis, the ILS consists of calcite as major component and contains traces of quartz (Tab. B.9).

4.4.2 Petrophysical characterisation

The general core analysis program for permeability, density, surface area, porosity, permeability, NMR T_2 is applied for the whole sample set of ILS, whereas μ-CT measurements and MICP is conducted only on selected samples. The density is measured by triple weighing method and by pycnometer as shown in Figure 4.20 a. The TWM provides a mean value of $2.68\,\mathrm{g{\cdot}cm^{-3}}$ with barely scattering. The values of the pycnometer measurement are slightly higher and vary from $2.67\,\mathrm{g{\cdot}cm^{-3}}$ to $2.72\,\mathrm{g{\cdot}cm^{-3}}$. Literature values of the major element calcite from $2.70\,\mathrm{g{\cdot}cm^{-3}}$ to $2.74\,\mathrm{g{\cdot}cm^{-3}}$ (Schön, 2004) indicate that both methods provide appropriate results. A complete list of the density values is part of the appendix (Tab. B.3).

The porosity is determined by triple weighing method and by NMR measurements as shown in Figure 4.20 b. The mean value of the porosity is about 18 % for both methods. The TWM porosity values cover a range from 14.2 % to 19.9 % (Tab. B.3), whereas the scattering of the NMR porosity is slightly lower (15.3 % to 19 %). In the following, all correlations are plotted with the porosity values determined by TWM.

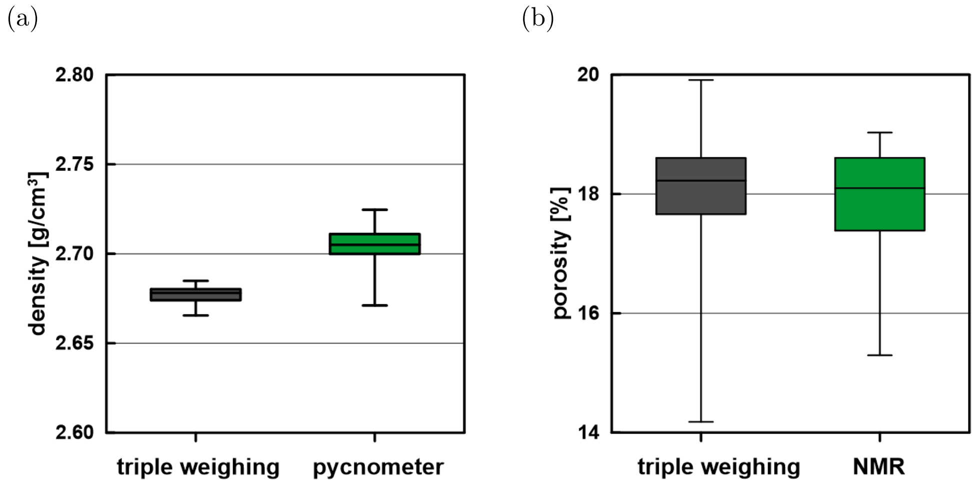

Figure 4.20: Results of the petrophysical characterisation of the Indiana limestone are shown in box-and-whisker plots. a) Comparison of the density values measured by triple weighing and by using a pycnometer. b) Comparison of the porosity values determined by triple weighing and NMR measurements.

Another characteristic of the ILS is its moderate permeability as shown in Figure 5.1 b. The scattering within the sample set is low and the permeability values range from 125 mD to 308 mD. The correlation between porosity and permeability is displayed in Figure 4.21 a. The permeability increases with increasing porosity despite of some outliers. The trend reveals the following fit: $k = 0.55 \cdot \Phi^{2.02}$, $R^2 = 0.33$.

The surfaces are given in relation to the mass S_m and to the pore volume S_por as shown in Figure 5.1 c and d. The S_por values range from 2.7 μm^{-1} to 5.7 μm^{-1} with a mean value of 3.9 μm^{-1}. The determined S_m-values range from 0.25 m^2·g^{-1} to 0.53 m^2·g^{-1}. If considering the cross plots of S_m and the petrophysical parameters porosity and permeability, no clear trends are observable and power laws provide poor adaptions ($\mathrm{R}^2 < 0.12$) as shown in Figure 4.21 b and c.

Four exemplary pore radius distributions of the ILS are shown in Figure 4.22. The amount of free movable water is similar to the LK (approximately 58 % in average). However, the amount of capillary bound water is reduced to 28 % in average, whereas the amount of clay bound water, related to small pores, has increased to approximately 14 % in average. In average, the calculated median radius of the pores r_{50} is 12.2 μm using 70 μm·s^{-1} as surface relaxivity. The surface relaxivity results from the plot of the μ-CT and NMR results as seen in Figure 4.24.

The capillary pressure experiments show bimodal pore throat radii distribution (Fig. 4.23). The dominant pore radius is located at 20 μm and the second peak at

0.3 μm.

A joint representation of the results of the pore radius distribution determined by MIP (black), μ-CT (green) and NMR (blue) is shown in Figure 4.24. The pore geometry of ILS can be described as more heterogeneous with larger pore aspect

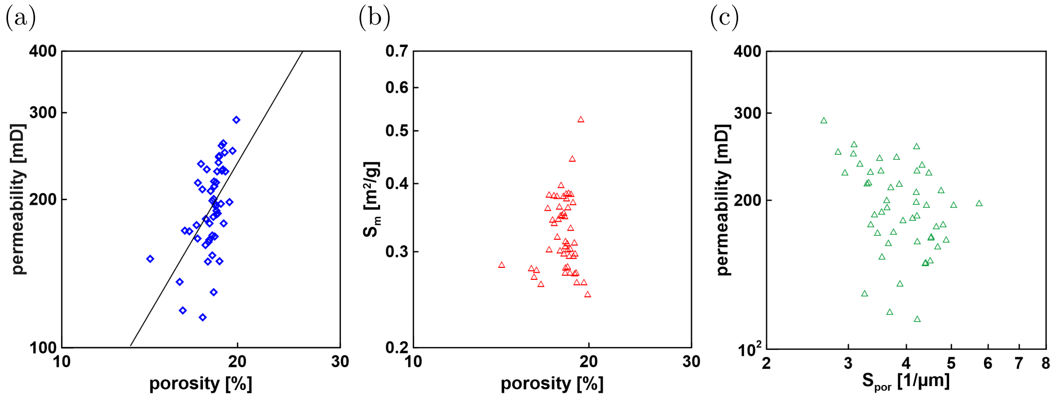

Figure 4.21: Crossplots of the pore-space properties of the ILS samples. a) Permeability in relation to porosity values. b) S_m in relation to porosity values. c) Permeability in relation to S_por values.

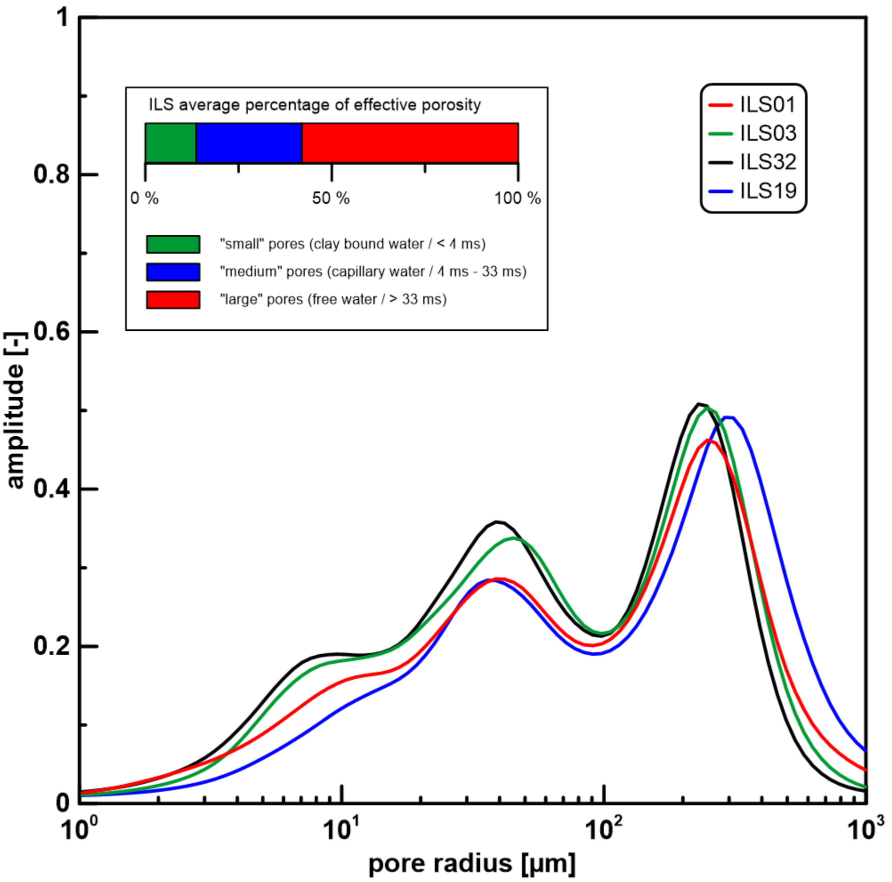

Figure 4.22: Exemplary pore radius distribution from NMR data using 70 μm·s^{-1} for four samples and average percentage of effective porosity for the ILS samples.

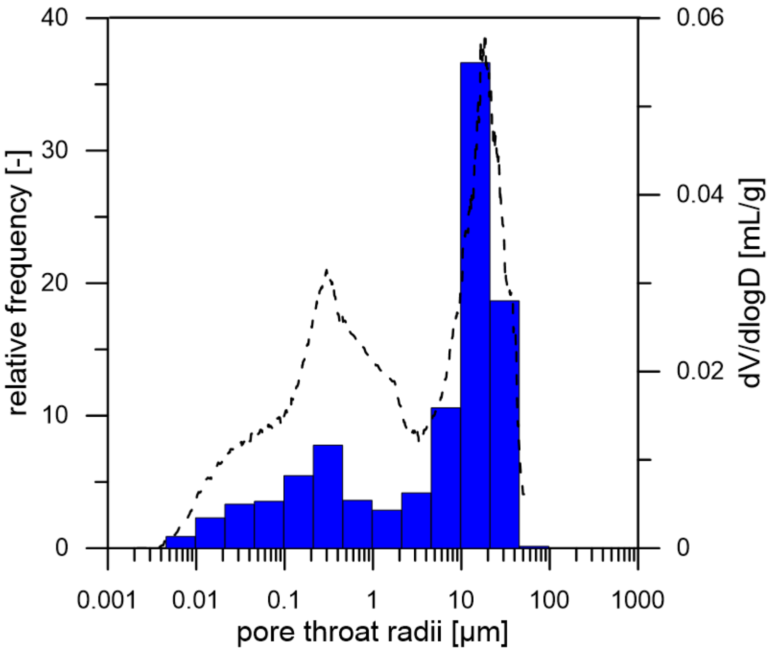

Figure 4.23: Representative pore throat distribution derived from mercury injection experiments of the ILS samples.

ratios (≈ 8). One relaxation peak of the NMR measurement can be attributed the wide pore and the other one fits the narrow pores of the MIP data.

4.5 Silurian dolomite (DOL)

The Silurian dolomite (DOL) originates from a quarry in Thornton (Illinois/USA) and is associated with the Silurian. The dolomite belongs to the formation Racine Dolomite, which is part of the Silurian system. The reef facies of this formation consists mainly of dolomite (Mikulic et al., 1999). The general character of the DOL in the reefs is described as high-purity dolomite, grey and vuggy (Willman, 1973).

The first description of the Silurian Dolomite samples as seen in Figure 4.25 confirms this character. The dolomite is a porous sparite with a white to light greyish colour. The DOL is an inhomogeneous rock with spherical pores, which contain recrystallisation structures. Additionally, a weak but longer-lasting reaction with hydrogen chloride (HCl) is observable.

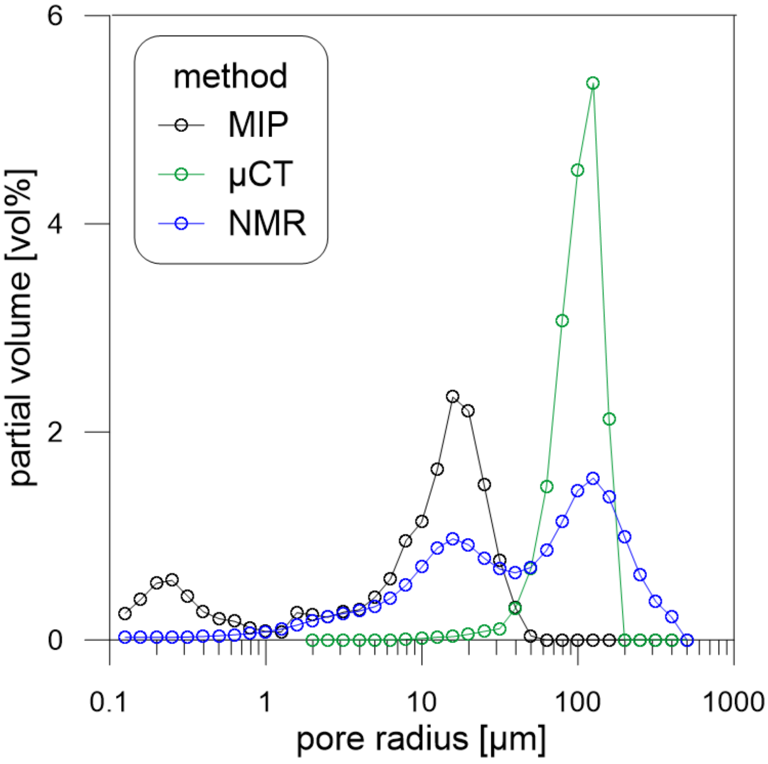

Figure 4.24: Pore radius distribution from MIP, μ-CT and NMR measurements for the ILS.

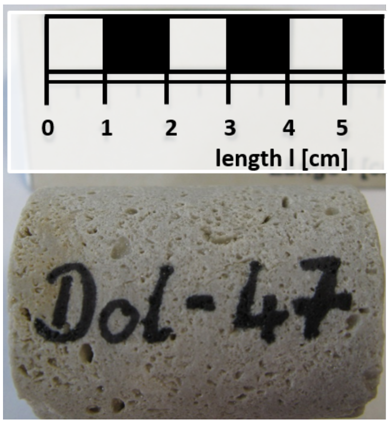

Figure 4.25: A photography of one plug of the DOL samples.

4.5.1 Mineralogical and geochemical characterisation

The DOL carbonate consists of large idiomorphic crystals with some dissolution structures (Fig. 4.26). The crystals have a size of almost 100 μm and are embedded in the matrix. The EDX suggests a dolomite as shown in the quantification result in Figure A.11. Dolomite ($MgCa(CO_3)_2$) has an amount of 88.5 wt% according to EDX analysis. The high composition of $CaMg(CO_3)_2$ is a hint for a dolostone.

The average chemical composition of the DOL is determined using the XRF analysis and confirmed the results of the EDX. The Silurian Dolomite of 99 % $CaCO_3$, 0.7 % SiO_2 and less than 0.14 % clay minerals, i.a. Al_2O_3 (Fig. 4.19). The complete list of major and trace elements is given in the appendix (Tab. B.8). The CO analysis reveals a carbon content of 11.9 % to 12.1 %. According to XRD analysis, the DOL consists of dolomite as major component and contains no traces of other components (Tab. B.9).

4.5.2 Petrophysical characterisation

The general core analysis program for permeability, density, surface area, porosity, permeability, NMR T_2 is applied to the whole samples of DOL, whereas μ-CT measurements and MICP is conducted only on selected samples. The average values of grain density for the Silurian Dolomite vary between 2.79 g·cm^{-3} and 2.83 g·cm^{-3} for the TWM and between 2.80 g·cm^{-3} and 2.87 g·cm^{-3} derived from

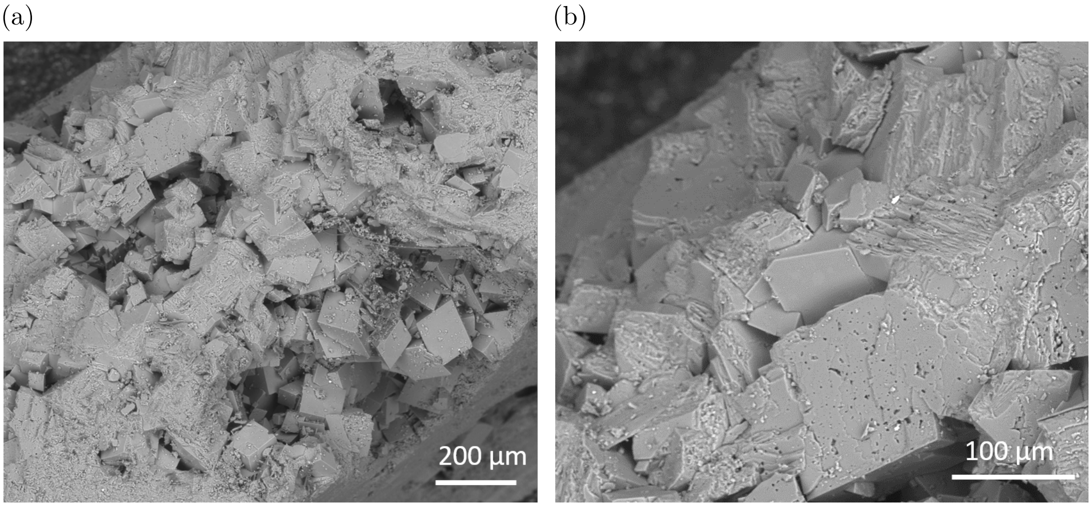

Figure 4.26: Exemplary ESEM-images of the Silurian Dolomite. a) Overview of the almost dolomitic idiomorphic crystals of the DOL. b) Shot of a dissolution structures on the crystal surfaces.

pycnometer (Fig. 4.28 a). A comparison of these values with published literature density values of the major components calcite ($2.70\,\mathrm{g\cdot cm^{-3}}$ - $2.74\,\mathrm{g\cdot cm^{-3}}$) and dolomite ($2.86\,\mathrm{g\cdot cm^{-3}}$ - $2.95\,\mathrm{g\cdot cm^{-3}}$) (Schön, 2004) shows, that a the grain density indicates also a dolomite. A complete list of the grain density measurements is part of the appendix (Tab. B.4).

The DOL is characterised by porosities of 7 % to 18 %, derived from TWM. The porosities derived from NMR data are in the same range, but with a lower maximum ($\Phi = 14.5\,\%$). The mean value of both methods is about 11 %. The permeability of the DOL covers four orders of magnitude (from 0.2 mD to 280 mD, Fig. 5.1 d). The majority of samples show permeability values in the range of 10 mD to 100 mD. The permeability is directly related to the porosity as shown in Figure 4.29 a. The porosity-permeability relation can be described by a power law ($k = 4 \cdot 10^{-6} \cdot \Phi^{6.27}$, $R^2 = 0.80$). As shown in Figure 5.1 c, the values of S_{por} range from $0.08\,\mu\mathrm{m}^{-1}$ to $12.7\,\mu\mathrm{m}^{-1}$. The values of S_{m} are very small and vary between $0.005\,\mathrm{m^2\cdot g^{-1}}$ and $0.14\,\mathrm{m^2\cdot g^{-1}}$ (5.1 d). The cross plots of S_{por} and the other two parameter Φ and k display large scattering without any kind of trend in both ($\mathrm{R}^2 < 0.05$)(Fig. 4.29 b, c).

Four exemplary pore radius distributions are shown in Figure 4.30. The differences between the distributions can be explained with the heterogeneity of the DOL samples. The amount of large pores is about 70 %, in average. The residual effective porosity is almost similar divided into medium range (capillary bound water, approximately 13 %) and small pores (capillary bound water, approximately

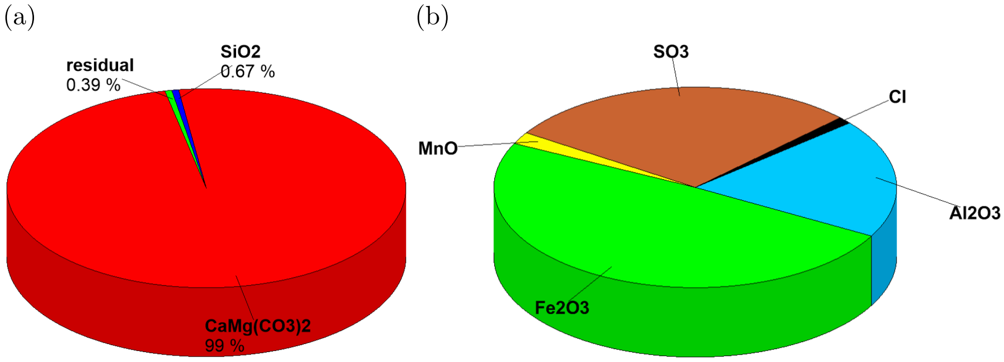

Figure 4.27: Average composition of the minerals in the Silurian Dolomite. a) Major components are dolomite ($CaMg(CO_3)_2$; 98.94 %) and quartz (SiO_2; 0.67 %). The remaining components comprise 0.39 %. b) Minor components are 0.39 % of all components in total. Clays (0.14 %) include the minerals aluminium oxide (Al_2O_3), manganese oxide (MnO), potassium oxide (K_2O) and sodium oxide (Na_2O). Significant minerals are iron(III) oxide (Fe_2O_3), aluminium oxide (Al_2O_3) and sulphur trioxide (SO_3).

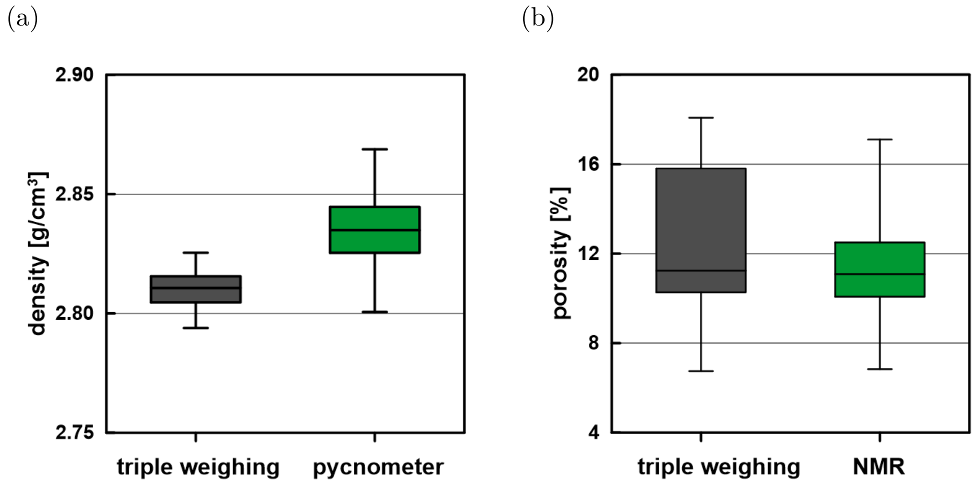

Figure 4.28: Results of the petrophysical characterisation of DOL are shown in box-and-whisker plots. a) Comparison of the density values measured by triple weighing and by using a pycnometer. b) Comparison of the porosity values determined by triple weighing and NMR measurements.

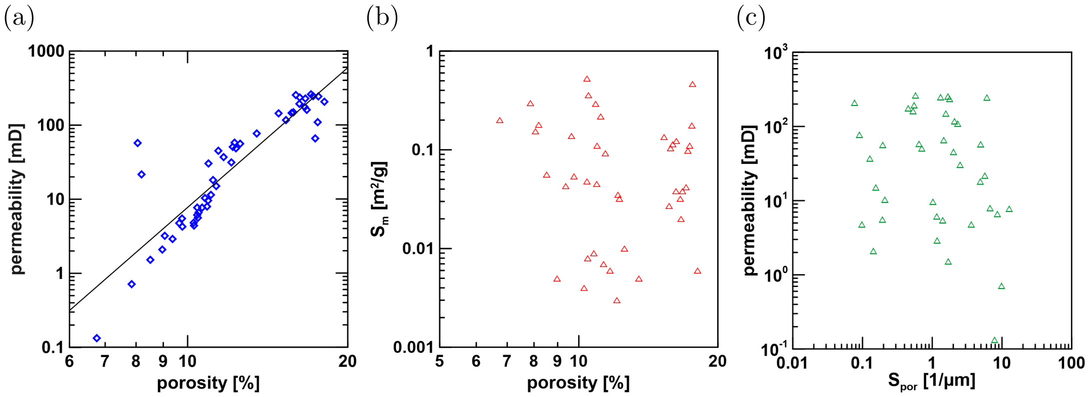

Figure 4.29: Crossplots of the pore-space properties of the whole DOL samples. a) Permeability in relation to porosity values. b) S_{m} in relation to porosity values. c) Permeability in relation to S_{por} values.

16.5 %). In average, the calculated median radius of the pores r_{50} is 25.0 μm using 25 μm·s^{-1} as surface relaxivity. The surface relaxivity results from the plot of the μ-CT and NMR results as seen in Figure 4.32. The capillary pressure experiments indicate a dominant pore radius of 8 μm as shown in the exemplified pore throat radii distribution (Fig. 4.31). The main pore throat size is located in a range of 2 to 50 μm.

A joint representation of the results of the pore radius distribution of the DOL determined by MIP (black), μ-CT (green) and NMR (blue) is shown in Figure 4.32. The pore geometry of DOL can be described as more heterogeneous with larger pore aspect ratios ($\approx$ 20). One relaxation peak of the NMR measurement can be

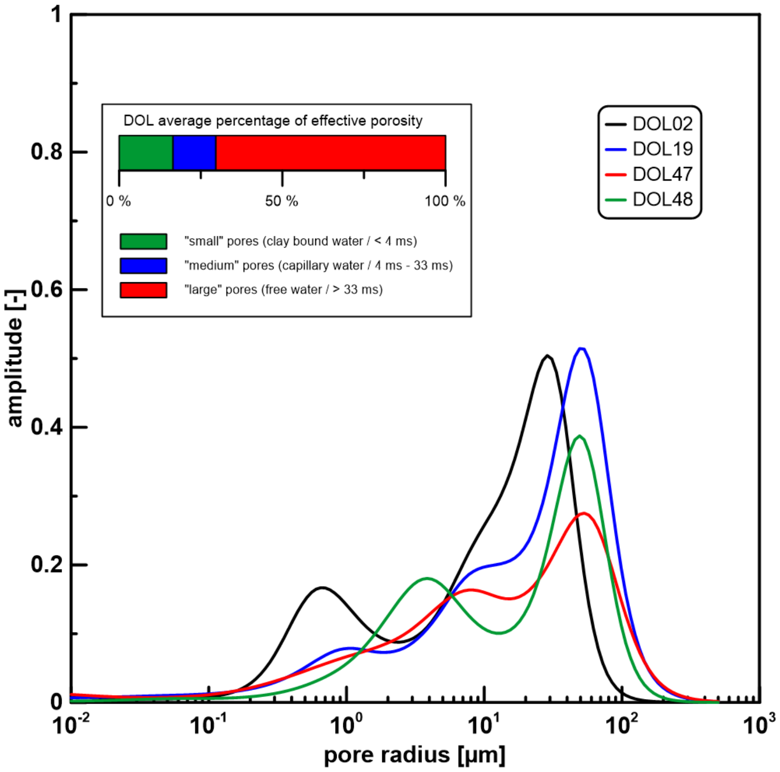

Figure 4.30: Exemplary pore radius distribution from NMR data using 25 μm·s^{-1} for four samples and average percentage of effective porosity for the DOL samples.

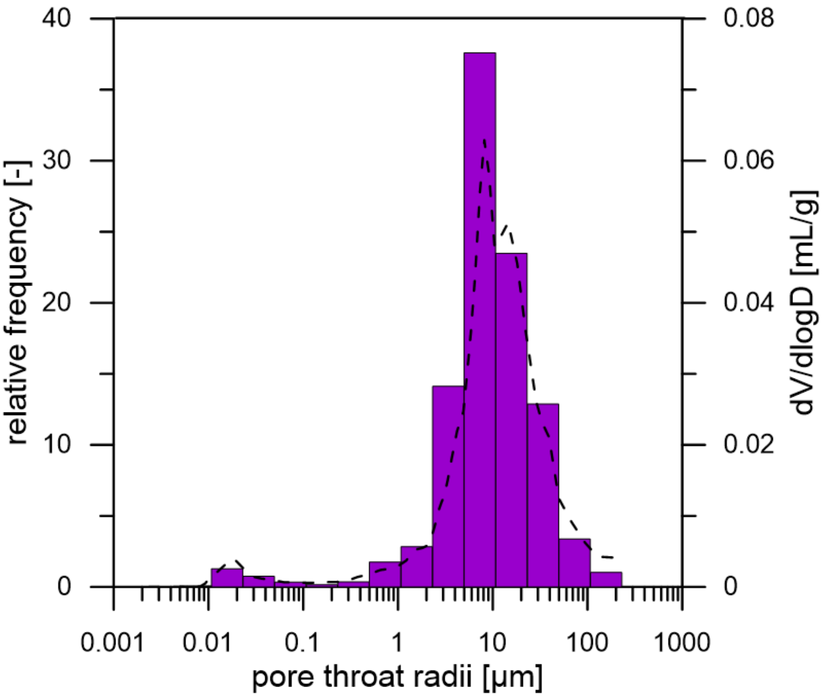

Figure 4.31: Exemplary representative pore throat distribution derived from mercury injection experiments for the DOL samples.

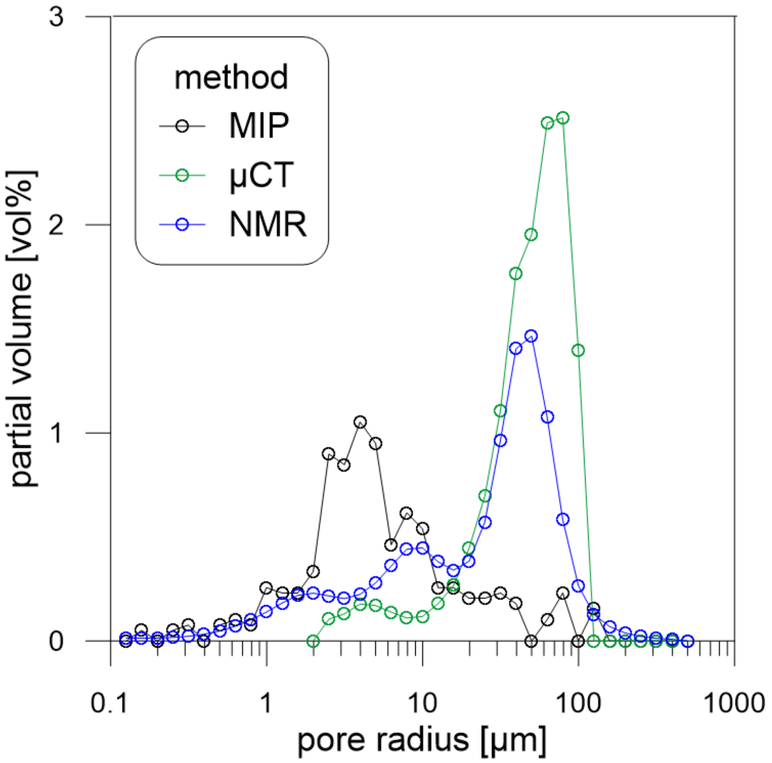

Figure 4.32: Pore radius distribution from MIP, μ-CT and NMR data using 25 μm·s^{-1} for the DOL.

attributed the wide pores and the other one fits the narrow pores of the MIP data.

5 Results

This chapter is divided into three parts. First, a combined rock evaluation will be given, which sum up and compare the single characterisations of different carbonate types to identify common features and differences (section 5.1). Second, the results of the methodical investigation of the complex electrical conductivity of carbonates is presented by IP spectra, relationships between IP parameter and petrophysical parameter as well as determination of the formation factor and permeability prediction using IP data (section 5.2). Third, the experimental procedure of the dissolution experiment is described followed by the characterisation of the structural changes and the evaluation of the change of the IP parameter due to dissolution (section 5.3).

5.1 Combined rock evaluation

A comparison of the petropyhsical parameters of the different carbonate types is shown in Figure 5.1. The majority of LK, DOL, and ILS samples show porosities between 10 % and 20 %, whereas the average porosity of the EBK is twice as high as the other types (Fig. 5.1 a). EBK and ILS are characterised by high permeabilities, whereas LK is less permeable as displayed in Figure 5.1 b. The permeability of DOL covers several orders of magnitude from low to high. In Figure 5.1 c the surfaces related to pore volume show similar high surface values for EBK and LK, whereas the ones of ILS and DOL are significantly smaller. However, the DOL surfaces show high variations from $0.01\,\mu\mathrm{m}^{-1}$ to $10\,\mu\mathrm{m}^{-1}$. The values in the lower part reach the limits of measuring accuracy. Similar observations can be made regarding the surface related to the mass (Fig. 5.1 d). EBK has the largest surface values, followed by LK and ILS. DOL shows a high scattering of very low S_m values. The majority of the sample set has surfaces smaller than the detection limit of nitrogen ($S_\mathrm{m} < 0.2\,\mathrm{m}^2/\mathrm{g}$). Therefore, krypton as adsorption gas is required to improve the measurement accuracy. Nevertheless, the surface sizes reach the resolution limit and thus are less reliable.

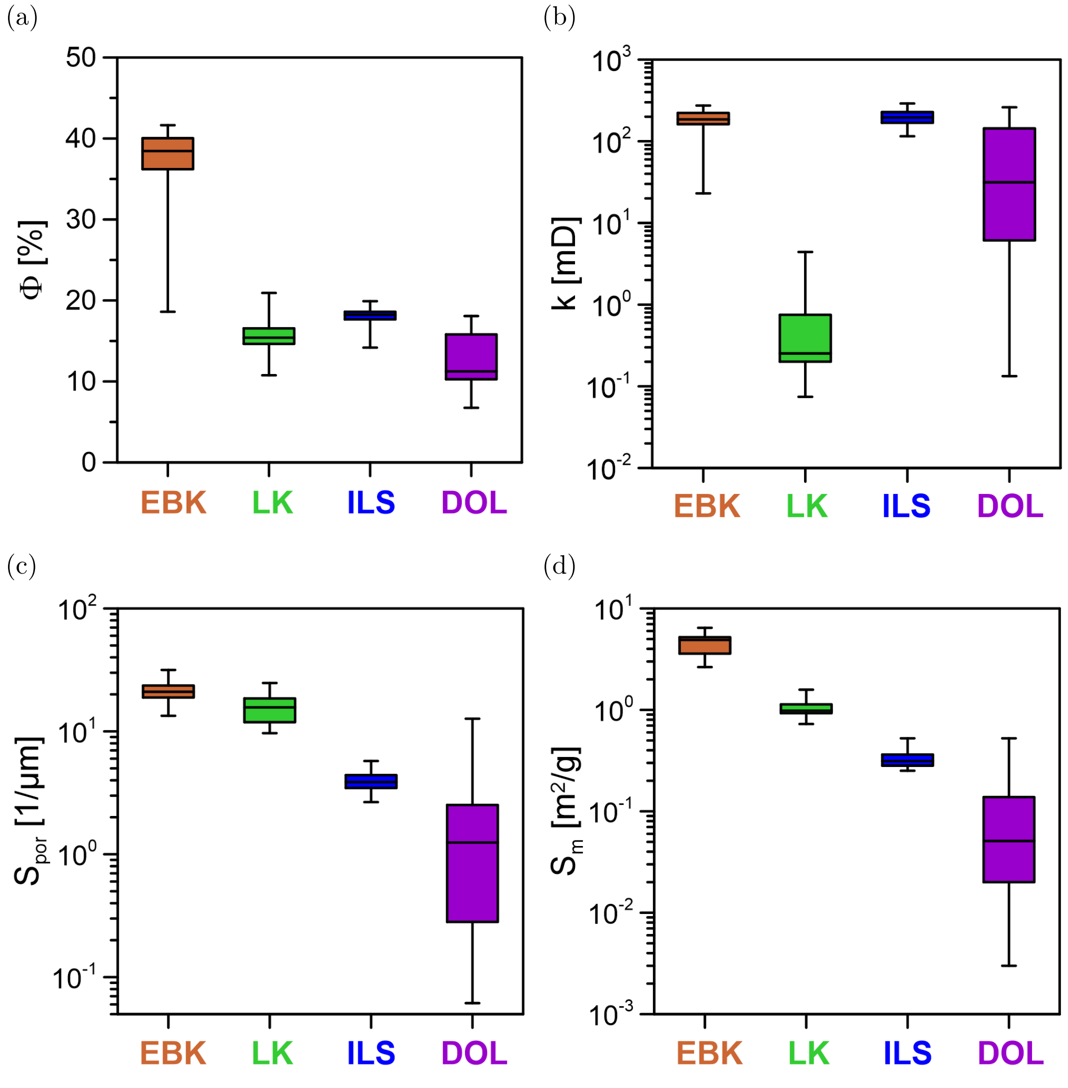

Figure 5.1: Comparison of the petrophysical parameters a) porosity, b) permeability, c) S_{por} and d) S_{m}.

Figure 5.2 a shows a positive correlation between permeabilities and porosities of the different samples. The data can be divided into two clusters with EBK and LK in cluster 1 and ILS and DOL in cluster 2. A power law fit for cluster 1 (solid red line) leads to $k_{\mathrm{EBK/LK}} = 5.8 \cdot 10^{-9}\Phi^{6.7}, R^2 = 0.96$, whereas cluster 2 (dashed red line) can be fitted by $k_{\mathrm{ILS/DOL}} = 4.13 \cdot 10^{-5}\Phi^{5.3}, R^2 = 0.78$. The shift between the two regression lines can be explained by the different grain sizes: EBK has crystals smaller than 20 μm, LK has a very fine crystalline matrix, whereas the crystals of DOL are five times larger than those of EBK, and the ILS is identified as packstone. A fine grained rock type is less permeable in comparison to a medium or coarse grained rock type with the same porosity.

No best-fit can be drawn for specific surface against porosity, which is shown in Figure 5.2 b for each carbonate type. ILS, LK and the EBK are clustered, whereas the DOL scatters over two orders of magnitude of surface values independent of the porosity.

The relation between permeability and S_{por} shows two clusters of EBK and ILS and a wide distribution of the DOL samples (Fig. 5.2 c). ILS and EBK have the same permeability range but different average valuesof S_{por}, whereas LK and EBK have similar surfaces but different permeabilities. A clear trend is only visible for the LK: with decreasing permeability the surface increases. The sample set can be fitted by $k_{\mathrm{LK}} = 1.8 \cdot 10^4 S_{\mathrm{por}}^{-3.1}, R^2 = 0.65$.

Figure 5.2 d shows the relationship between the formation factor and permeability. A correlation of LK and EBK can be described by $k_{\mathrm{EBK/LK}} = 7.7 \cdot 10^{-6} F^{-4.3}, R^2 = 0.79$ including 25 samples (red solid line). DOL can be fitted by $k_{\mathrm{DOL}} = 8.9 \cdot 10^{-5} F^{-3}, R^2 = 0.97$ (red dashed line) including five samples.

For comparison purposes, μ-CT images of each sample are shown in Figure 5.3. The EBK is characterised by a high amount of very small pores as well as very large pores (> 200 μm) (Fig. 5.3 a). Idiomorphic crystals are visible in the μ-CT-image of the EBK sample, which appear with a rhombohedral shape. The connected porosity is 40.8 % compared to the total porosity of 43.6 %. The LK has no amount of pores larger than 50 μm and a connected porosity of 19.9% compared to the total porosity of 21.3 % (Fig. 5.3 b). The ILS is characterised by aggregates surrounded by shells (Fig. 5.3 c), as observed as well in the ESEM images (Fig. 4.18). The pore space is composed of large pores ($> 100\,\mu m$) and significant smaller pores ($< 25\,\mu m$). The connected porosity is 8.06 % in comparison to the total porosity

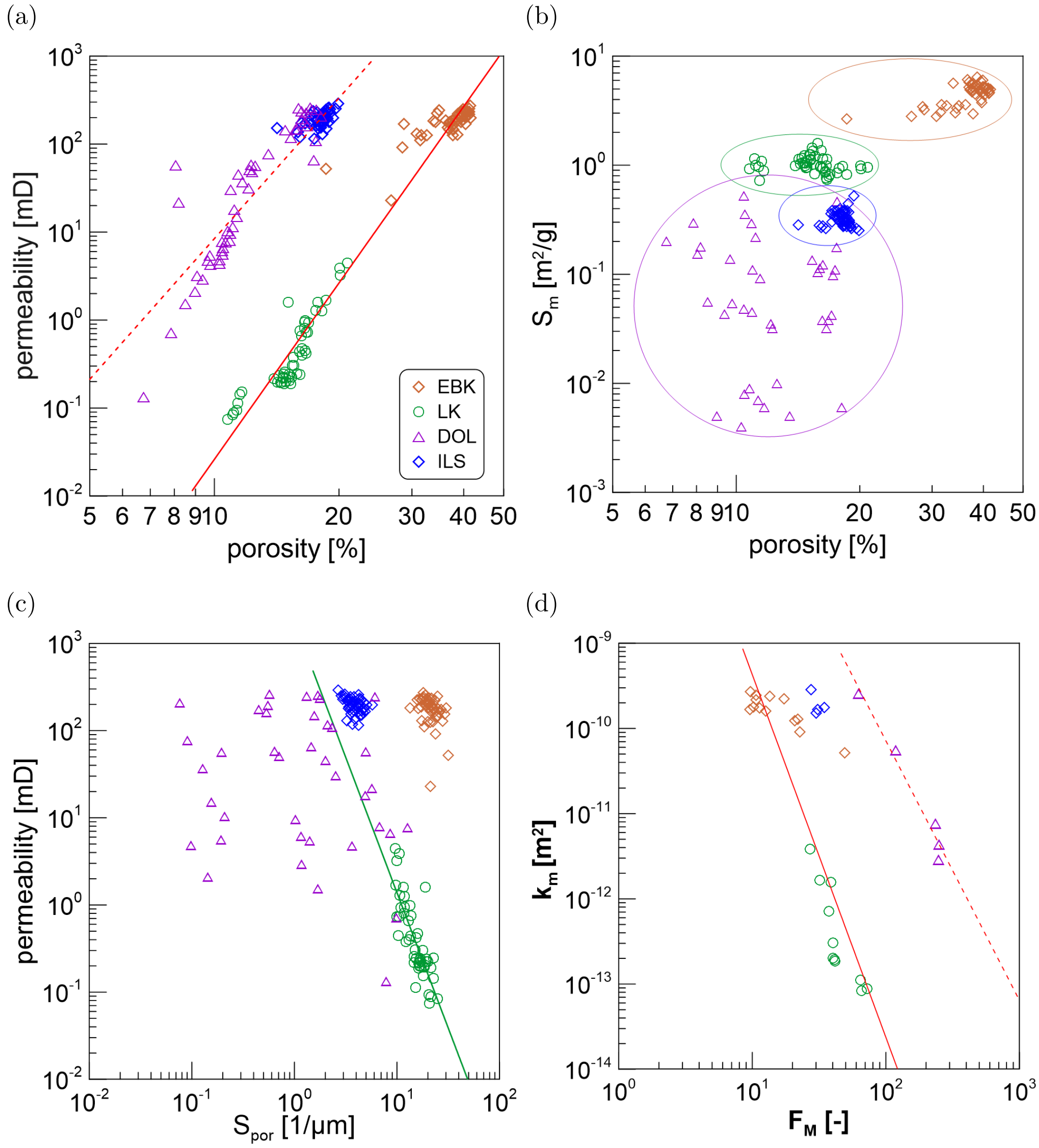

Figure 5.2: Relationships between the measured petrophysical parameters porosity Φ, permeability k, surface related to mass S_m, surface related to pore volume S_por and formation factor F in double logarithmic plots.
a) Relationship between porosity and permeability for the carbonate samples. The red solid line shows the best linear fit on the samples EBK and LK. The red dashed line indicates the results of a power law fitting including DOL and ILS. b) Relationship between porosity and specific surface S_m for the carbonate samples. c) Relationship between permeability and specific surface S_por for the carbonate samples. The green solid line indicates the results of a power law fitting including only LK. d) Relationship between formation factor and permeability for the carbonate samples. The red solid line indicates the results of a power law fitting including 25 samples of EBK and LK. The dashed red line indicates a fitting line for DOL including 5 samples.

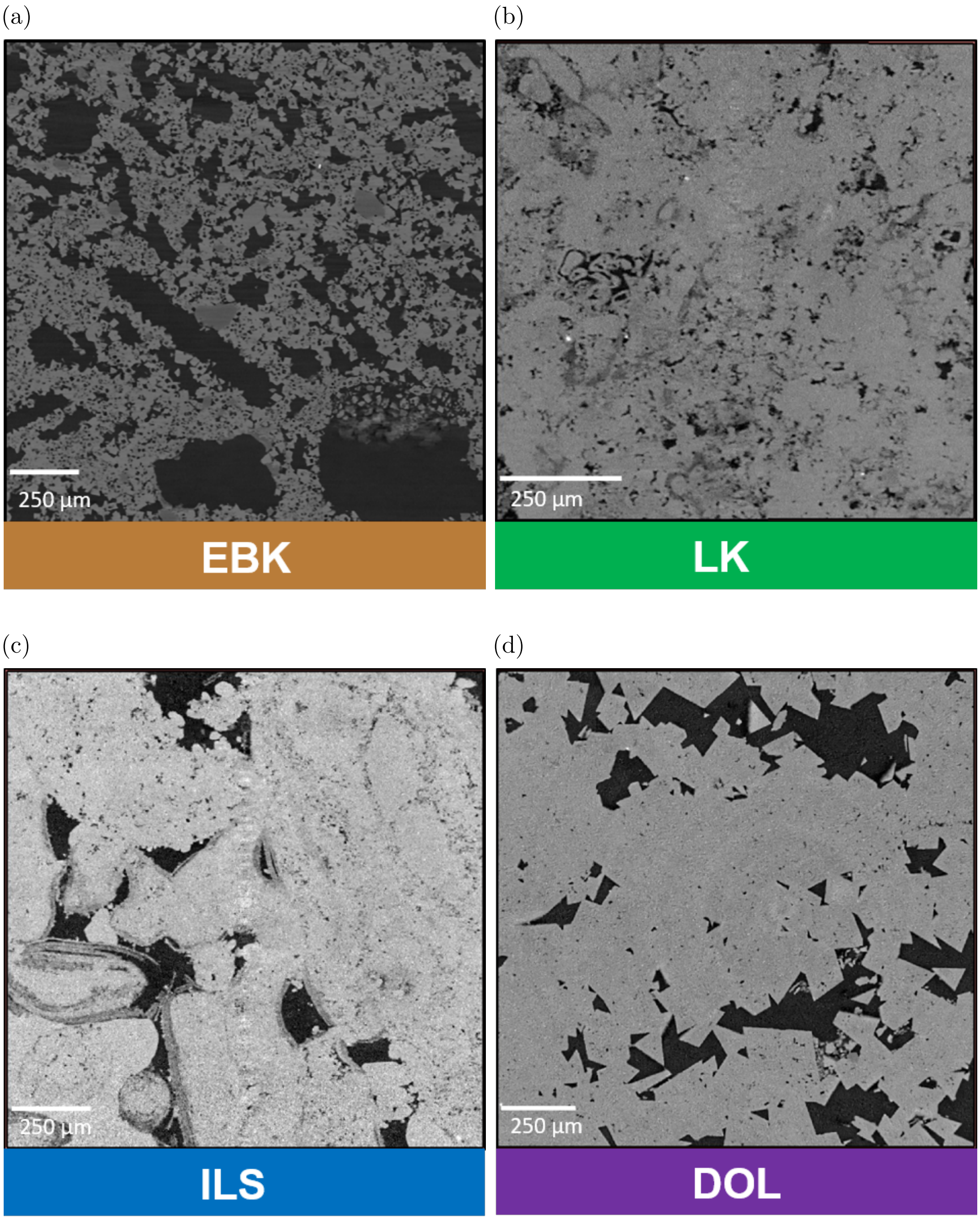

Figure 5.3: 2D μ-CT images (1000^2 pixel @ 2 μm voxel resolution). Pores are presented in black and the matrix parts are presented in shades of grey. Representative slices for a) EBK, b) LK, c) ILS, and d) DOL.

of 11.1 %, The μ-CT image of the DOL shows idiomorphic rhombohedral crystals, which are approximately ten times larger than the ones of the EBK (Fig. 5.3 d). The quantification of the pore space is comparable to the ILS. The amount of very large pores ($> 100\,\mu m$) is high, but the pore space is also characterised by smaller pores ($< 50\,\mu m$). The total porosity amounts 15.2 %, whereas the connected porosity is 13.8 %. The visualisation of the pore network of connected and unconnected pores is shown in the appendices (Fig. A.12).

A comparison of the pore radius distribution of the four different carbonates is shown in Figure 5.4 according to the used methods NMR, MIP and μ-CT. The pore volume distribution is plotted with 10 grid points between the decades. The corresponding Table 5.1 lists the dominant and mean pore radius as well as the effective pore radius, which is calculated by

$$r_{\text{eff}} = \sqrt{8Fk}, \tag{5.1}$$

with F being the formation factor, and k the permeability. The dominant pore radius of LK (green) is the smallest, followed by EBK (brown), DOL (purple) and ILS (blue) regardless of the method used for determination. The mean pore radius of LK is also the smallest, but the following order differs from the dominant pore radius. It is due the fact, whether the distribution is unimodal or bimodal.

Table 5.2 gives a review about different features of the characterisation determined from imaging and mineralogical investigation of the four carbonate types. Table 5.3 gives a review about different criteria of the petrophysical characterisation for the different carbonate types. The criteria are evaluated according to the suitability

Table 5.1: Pore radius (in μm) determined by different methods for the four investigated carbonate samples as well as the used surface relaxivity (in $\mu m s^{-1}$) to calculate from NMR data the pore radii.

		EBK	LK	ILS	DOL
surface relaxivity		100	45	70	25
pore radius					
	r_{eff}	3.8	0.5	7.1	3.4
NMR	r_{50}	35.6	5.6	34.7	25.0
	r_{dom}	39.7	4.0	125.6	50.0
μ-CT	r_{dom}	62.9	15.8	125.6	79.2
MIP	r_{dom}	7.8	0.6	19.3	8.0
	r_{50}	5.7	0.6	2.5	10.8

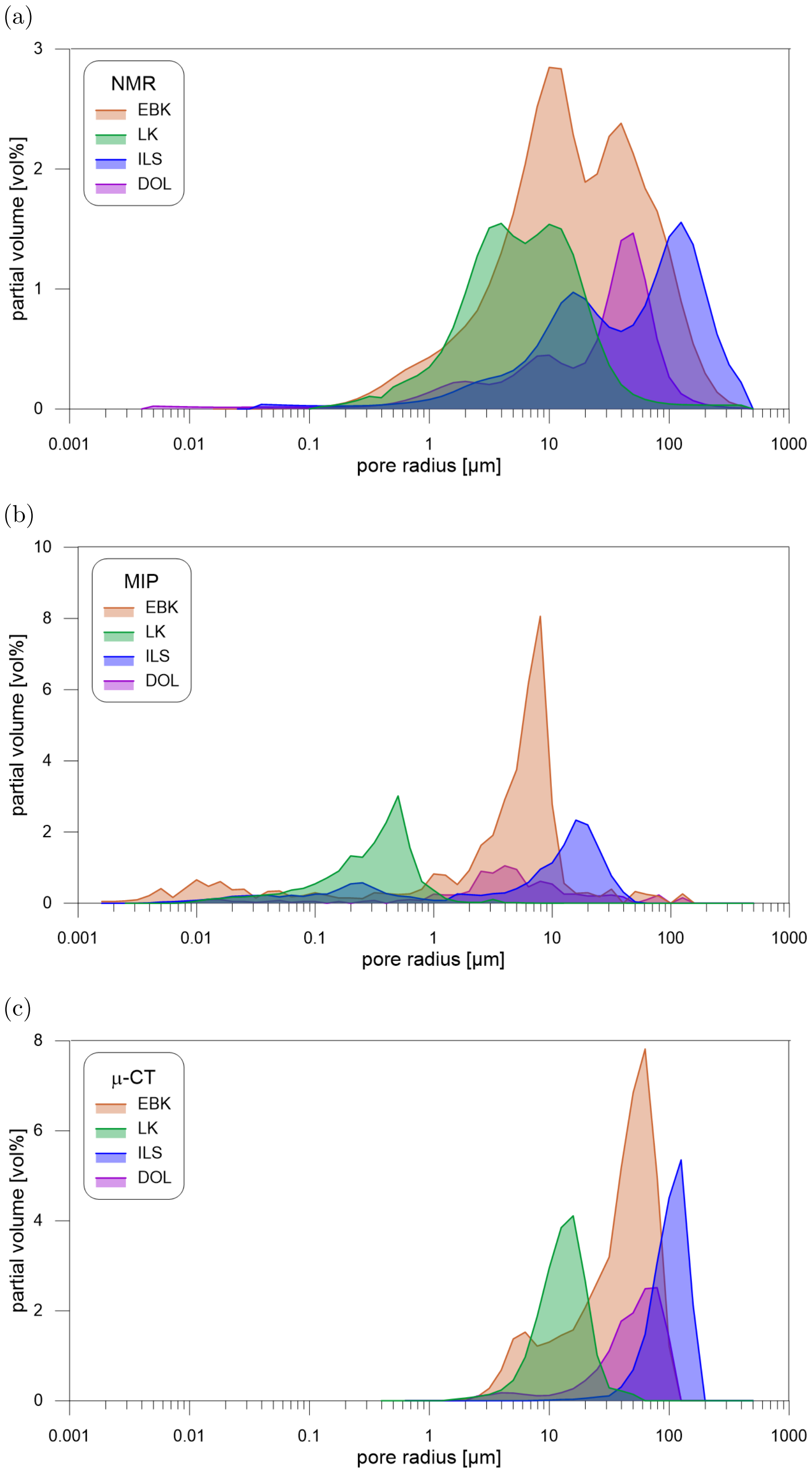

Figure 5.4: Comparison of the pore radii distribution of the carbonate samples determined by NMR, MIP or μ-CT. Pore radius distribution using a) NMR as method, b) MIP as method, and c) μ-CT as method.

for a SIP measurement or rather the expected IP effect. A higher porosity is favourable as well as a high permeability and a high specific surface. The EBK is most suitable considering porosity, permeability and specific surface as criteria.

Table 5.2: Summarised features of the four carbonate types, which are determined by imaging procedures and mineralogical investigations.

		feature	EBK	LK	ILS	DOL
Imaging	(1)	amount of connected pore space	93 %	93 %	86 %	73 %
	(2)	pore size distribution (μ-CT)	bimodal	unimodal (small pores)	unimodal (large pores)	bimodal
	(3)	grain size	very fine to fine crystalline		medium to coarse	
	(4)	fossils	-	✓	✓	-
	(5)	recrystallisation	✓	✓	✓	✓
Mineralogy	(1)	carbonate	dolomite	calcite	calcite	dolomite
	(2)	SiO_2	7.50 %	6.70 %	0.64 %	0.67 %
	(3)	clay	1.90 %	1.00 %	0.10 %	0.14 %

Table 5.3: Evaluation of the carbonate rocks by different criteria with regard to SIP.

criteria	EBK	LK	ILS	DOL
Φ	++	+	+	+
k	++	-	++	+
S_{por}	++	+	o	−

5.2 SIP on carbonates

5.2.1 IP-Spectra of carbonates

In the following, the measured IP spectra in a frequency range from 2 mHz to 100 Hz of the four selected carbonate types are presented. The complete data list of all measured spectra is part of the appendix (Tab. B.10, Tab. B.11, Tab. B.12, Tab. B.13). Each carbonate type is represented by four selected samples. The figures of IP spectra show resistivity and phase spectra as well as the spectra of real and quadrature conductivity, whereby ρ and φ can be converted to σ' and σ'' by Equations 2.8, 2.9, and 2.10.

Edwards Brown Carbonate The spectra of the samples EBK09 (blue), EBK10 (red), EBK11 (green), and EBK13 (black) are shown in Figure 5.5. The resistivity amplitudes (Fig. 5.5 a) range between 40 Ωm and 60 Ωm. Note, that EBK samples with significantly lower porosity as the majority of the samples (cf. Fig. 4.4 b) show resistivities up to 150 Ωm. A phase maximum (Fig. 5.5 b) appears in the phase spectrum for all EBK samples. The four displayed samples show the peak at the same frequency of 0.2 Hz. Considering all measured spectra of the EBK, the peak frequency varies slightly between 0.08 Hz and 0.32 Hz. The maximum phase shift ($\varphi_{\max}$) varies from sample to sample and ranges from 15 mrad to 37 mrad. The real part of conductivity (Fig. 5.5 c) qualitatively shows the reverse behaviour of the resistivity and the quadrature conductivity (Fig. 5.5 d) displays a similar behaviour like the phase spectra. The conductivity of the four samples ranges from 17 mS·m^{-1} to 24 mS·m^{-1}. The peak frequency of the σ'' spectra is the same, as observed in the phase spectra. In case of these four samples, the maximum values of σ'' range from 0.35 mS·m^{-1} to 0.8 mS·m^{-1}. The minimum is noted for the EBK12 at 0.1 mS·m^{-1}.

Lueders Carbonate Figure 5.6 shows the spectra of the representative samples LK09 (blue), LK13 (red), LK38 (green), and LK40 (black). According to the resistivity spectrum (Fig. 5.6 a), the largest resistivity with ∼ 250 Ωm appears for sample LK40 and the minimum resistivity with ∼ 80 Ωm for the samples LK09 and LK13. All measured LK samples of this study range from 60 Ωm to 340 Ωm. The phase spectra (Fig. 5.6 b) show no clear peak for all samples. LK40 has a maximum phase shift of 17 mrad at a frequency of 0.8 Hz and LK13 also at 0.8 Hz ($\varphi_{\max} = 9$ mrad). The phase characteristic of LK is a combination of constant phase behaviour or slight slope at higher frequencies and a constant slope at lower frequencies. In the range of 1 Hz, a visible change takes place in the slope of

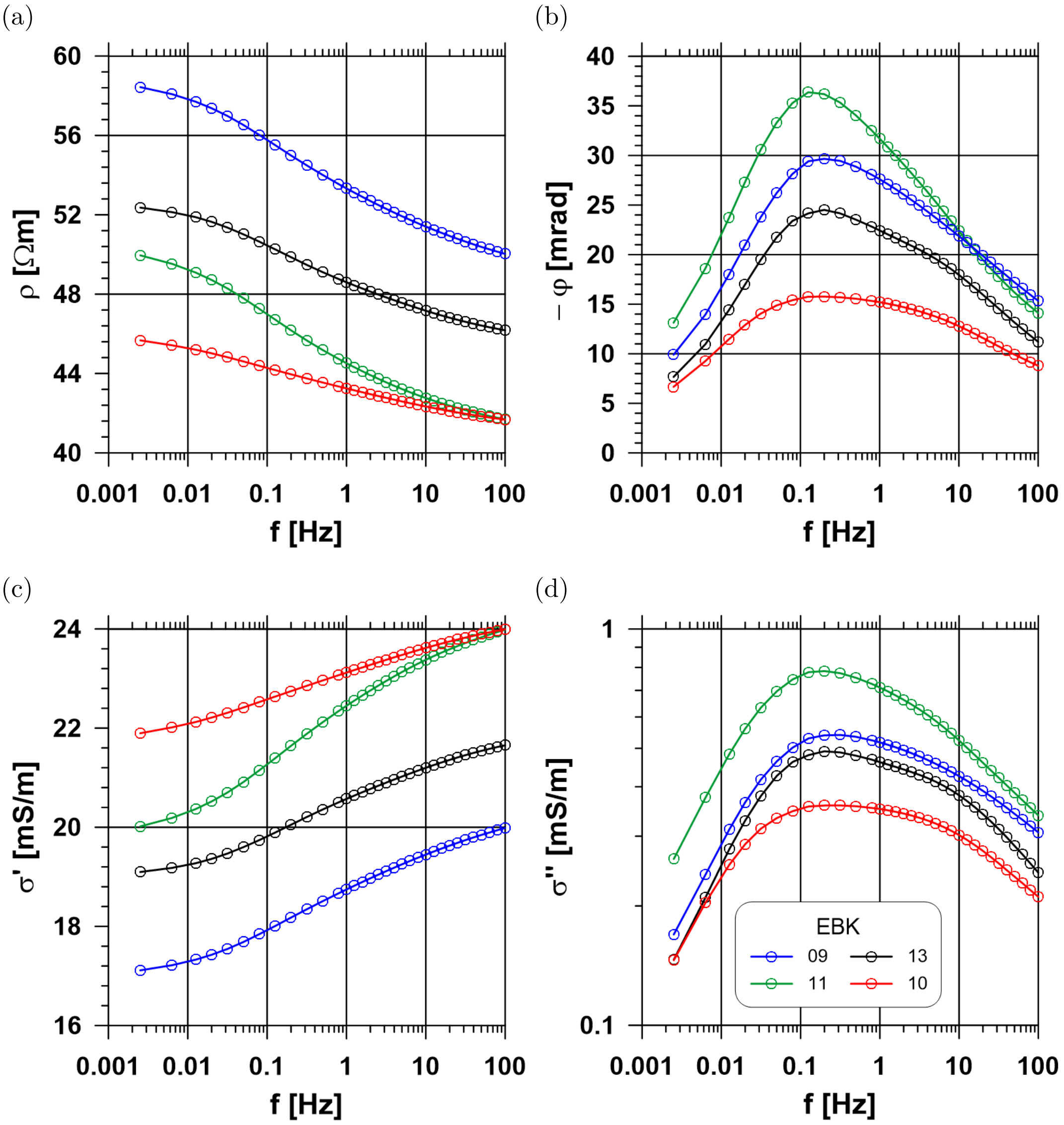

Figure 5.5: Spectra of four selected EBK samples saturated by a $CaCl_2$-solution with a conductivity of 100 mS·m^{-1} and measured at a temperature of 20 °C: a) Resistivity amplitude, b) phase, c) real part of conductivity, and d) quadrature conductivity.

the phase spectra. The spectrum of real part of conductivity shows the reverse order of the samples in a range from 4 mS·m^{-1} to 12 mS·m^{-1} in comparison to the resistivity. The observations made for the phase spectra are the same for the quadrature conductivity and the behaviour of the σ'' curve changes in a frequency range of 0.1 Hz to 1 Hz. The four spectra have σ''-values from 0.01 mS·m^{-1} to $\sim$0.1 mS·m^{-1}.

Indiana Limestone Representative spectral datasets obtained for ILS01, ILS02, ILS03, and ILS50 are displayed in Figure 5.7. The resistivities (Fig. 5.7 a) show nearly constant values over the complete frequency range and the values of the measured samples range from 200 Ωm to 325 Ωm. The phase spectra (Fig. 5.7 b) show very small phase shifts close to 0.5 mrad, which corresponds to the limit of resolution. Due to the scaling, the curves have a slightly constant slope, but the phase shifts change only about 1 mrad over five frequency decades. Because of the very small phase shifts, it is not possible to give a reliable statement regarding the phase behaviour. Because of the very small phase shift, it is challenging to measure a reproducible series for the same sample. The real part of conductivity (Fig. 5.7 c) displays low values between 3 mS·m^{-1} and 5 mS·m^{-1}. The spectra of the quadrature conductivity (Fig. 5.7 d) confirm the observations made for the phase spectra; a constant σ'' behaviour and very small values ($\sigma'' = 0.0006$ mS·m^{-1} - 0.005 mS·m^{-1}).

Silurian Dolomite The spectra of the samples DOL45, DOL46, DOL49, and DOL50 are displayed in Figure 5.8. Concerning the resistivities (Fig. 5.8 a), almost constant values can be observed for each sample. The resistivity values vary from around 500 Ωm to 750 Ωm. The phase shifts (Fig. 5.8 b) of all DOL samples are characterised by a slope. The phase shift is decreasing from about 4 mrad at a frequency of 100 Hz to around 1 mrad at 2 mHz. The real part of conductivity (Fig. 5.8 c) displays very low conductivity values between 1 mS·m^{-1} and 2 mS·m^{-1}. The same behaviour, as observed for the phase spectra, is also identified for the quadrature conductivity (Fig. 5.8 d); with decreasing frequencies, σ'' is decreasing as well. The values of σ'' vary between 0.01 mS·m^{-1} and 0.001 mS·m^{-1} over the displayed frequency range.

Comparison A comparison of the four carbonate types is shown in Figure 5.9. The Silurian Dolomite displays the largest resistivity values (Fig. 5.9 a), followed by the Indiana limestone. The smallest resistivities are identified for the Lueders carbonate and the Edwards Brown Carbonate. This observation is transferable

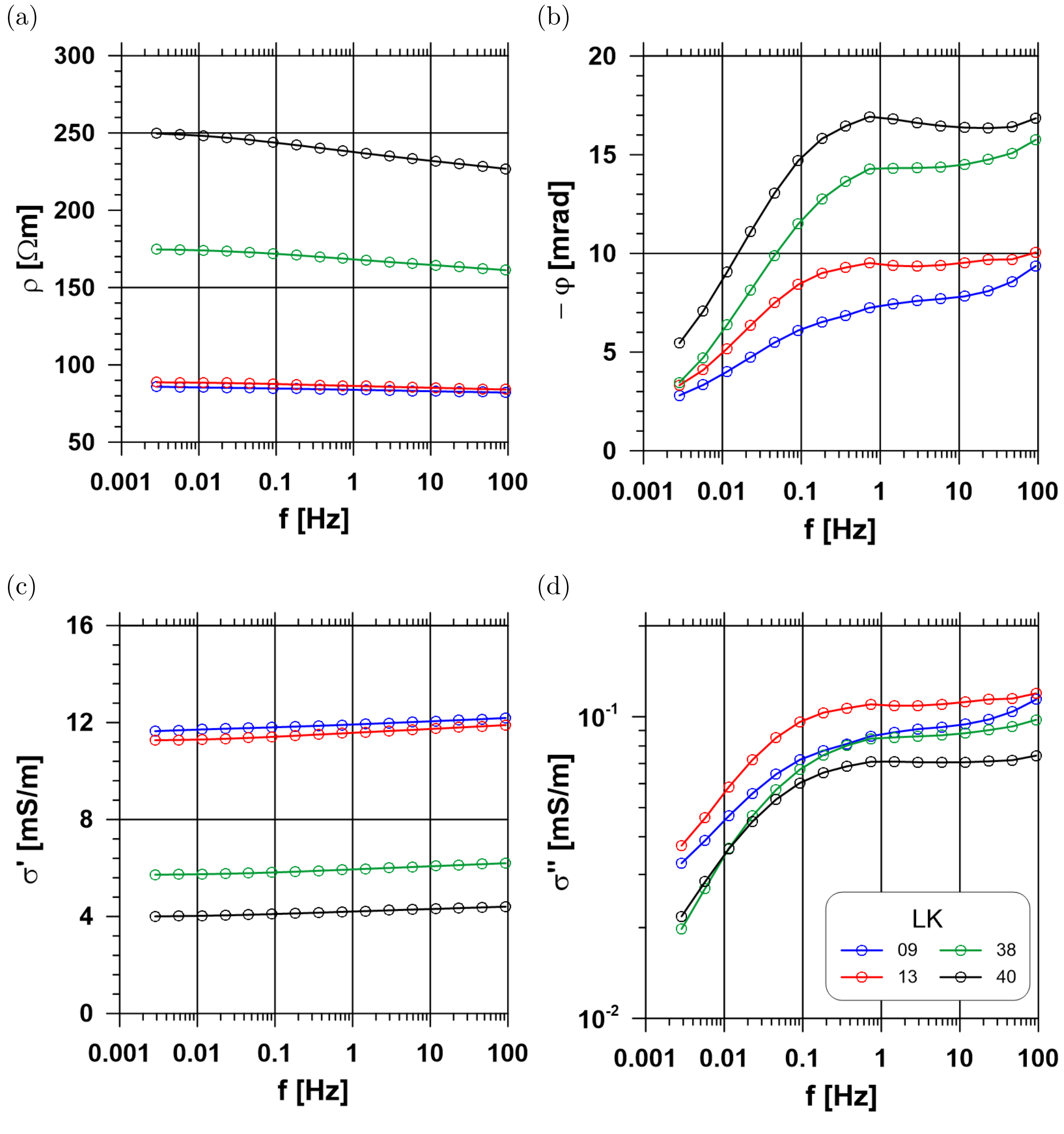

Figure 5.6: Spectra of four selected LK samples saturated by a $CaCl_2$-solution with a conductivity of 100 mS·m^{-1} and measured at a temperature of 20 °C: a) Resistivity amplitude, b) phase, c) real part of conductivity, and d) quadrature conductivity.

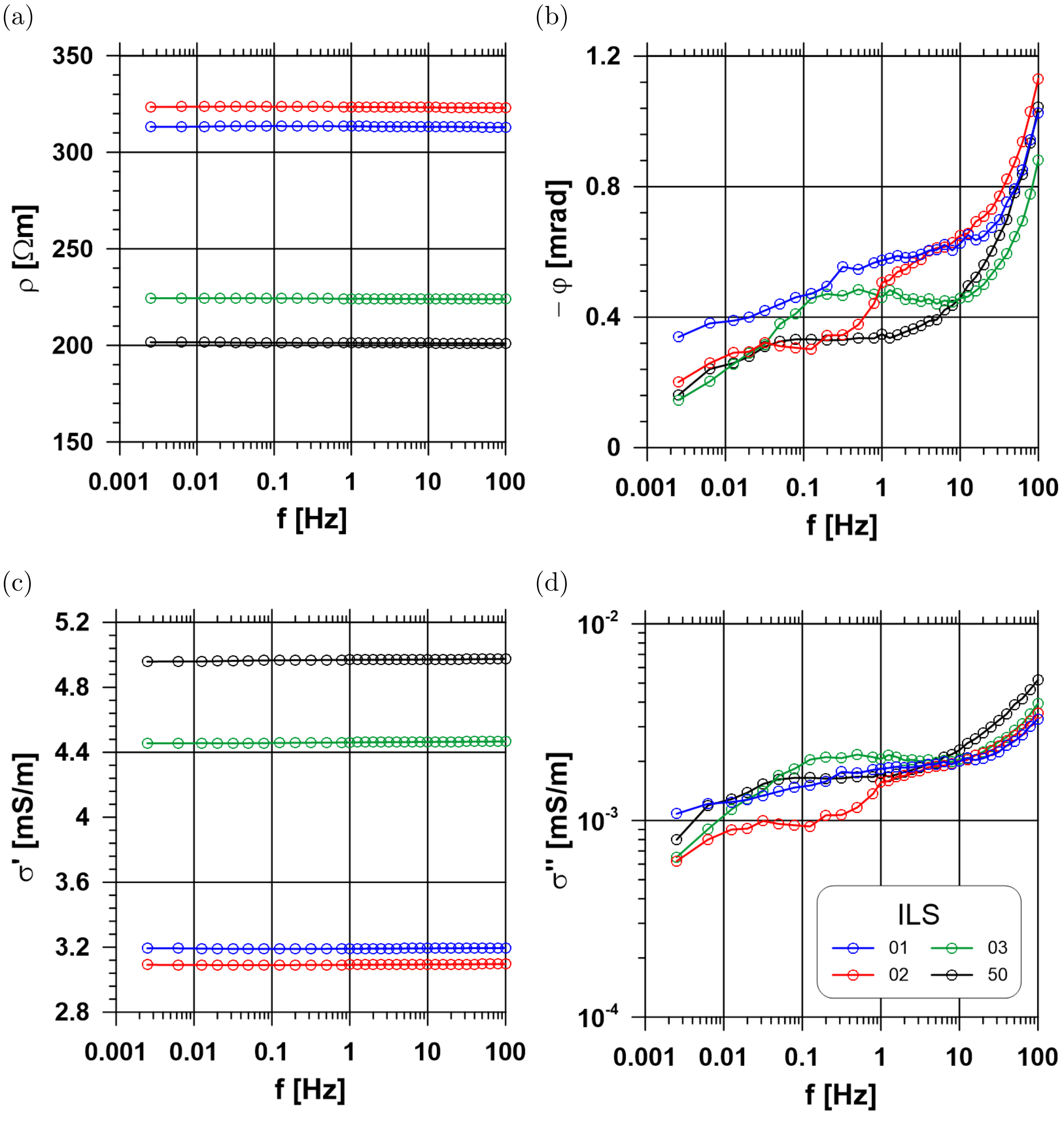

Figure 5.7: Spectra of four selected ILS samples saturated by a $CaCl_2$-solution with a conductivity of $100\,\mathrm{mS \cdot m^{-1}}$ and measured at a temperature of 20 °C: a) Resistivity amplitude, b) phase, c) real part of conductivity, and d) quadrature conductivity.

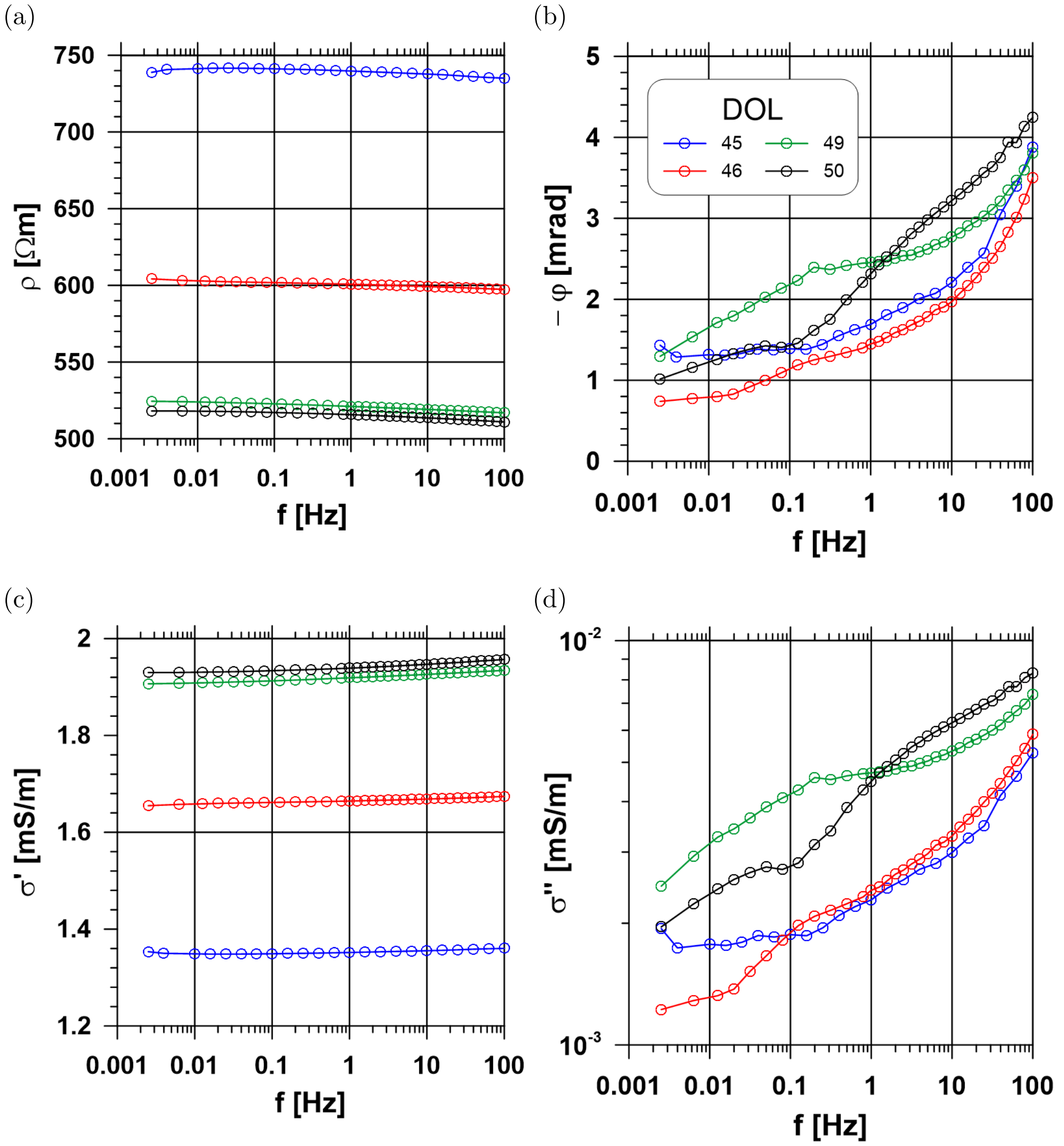

Figure 5.8: Spectra of four selected DOL samples saturated by a $CaCl_2$-solution with a conductivity of 100 mS·m^{-1} and measured at a temperature of 20 °C: a) Resistivity amplitude, b) phase, c) real part of conductivity, and d) quadrature conductivity.

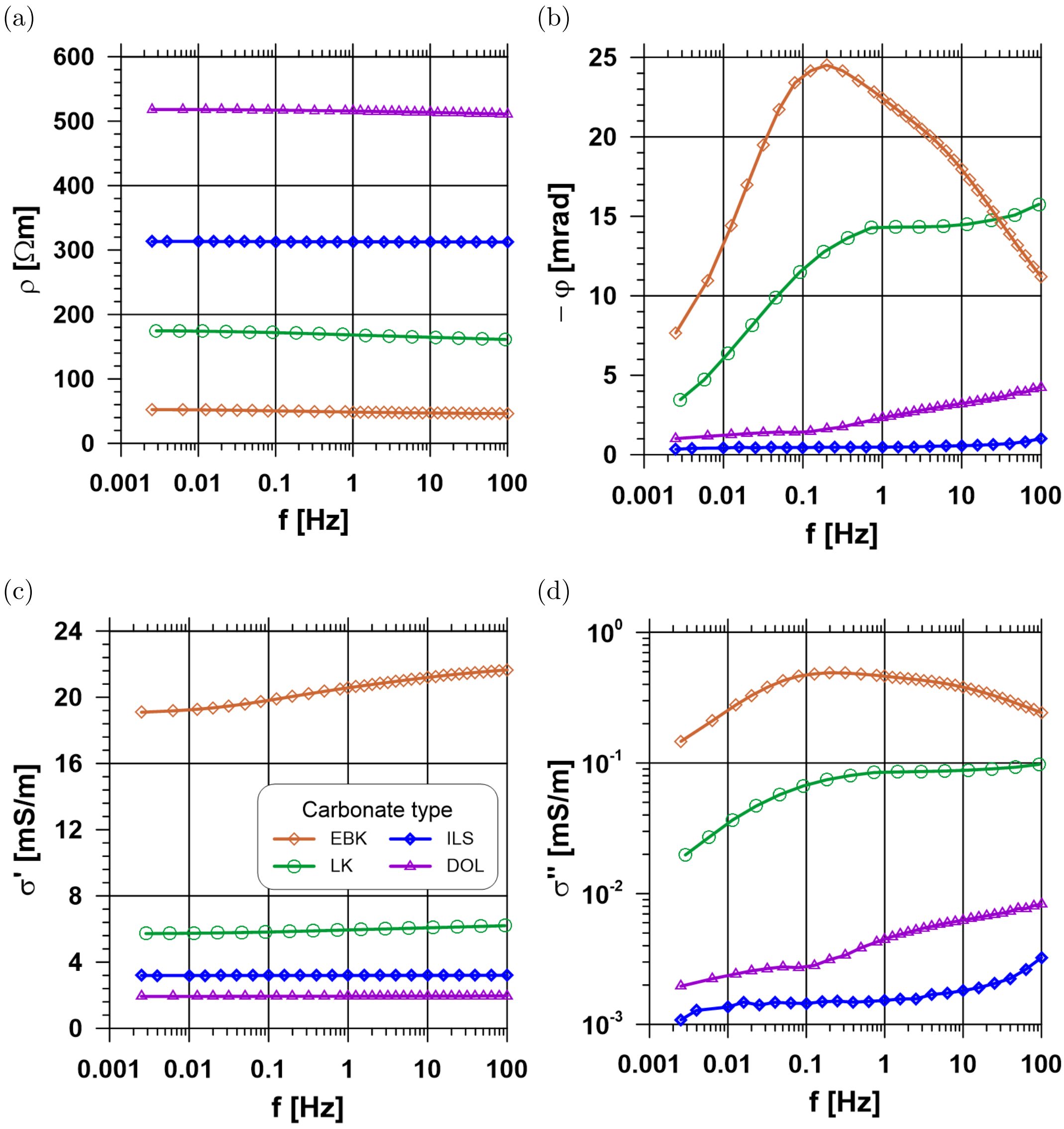

Figure 5.9: Examples of four results of the SIP measurements of the carbonate sample. The carbonates are saturated with a $CaCl_2$-solution with a conductivity of $100\,\mathrm{mS{\cdot}m^{-1}}$ and measured at a temperature of 20 °C: a) Resistivity amplitude, b) phase, c) real part of conductivity, and d) quadrature conductivity.

to the majority of the sample sets. With respect to the frequency dependence, four different types of polarisation behaviour were observed in the spectra of the phase shift as well as of the quadrature conductivity (Fig. 5.9 b and d); a constant phase angle (ILS), continuous increase (DOL), a combination of both (LK) and a maximum type (EBK). Each behaviour can be assigned to the specific carbonate type and is reproducible for the whole sample set. The real part of conductivity spectra shows the reverse order of the resistivity spectra (Fig. 5.9 c). The highest values for the quadrature conductivity can be observed for EBK (Fig. 5.9 d). The values of LK are one magnitude lower. The quadrature conductivity is again one magnitude lower for ILS and DOL. ILS shows the smallest σ''-values. The different phase behaviour of the carbonate types and possible causes are discussed in section 6.1.1.

5.2.2 Empirical relationships of SIP-derived parameters

Petrophysical parameter

In the following, the complex conductivity is related to different petrophysical parameters (Φ, k, S_{por}, S_{m}). The real (σ') and imaginary part (σ'') of the electrical conductivity at a frequency of $\sim$1 Hz were used here, which is a common convention in petrophysics and allows a comparison with other studies. The complete lists of the petrophysical parameters and IP parameters is part of the appendix (Tab. B.10, Tab. B.11, Tab. B.12, Tab. B.13).

Porosity The dependence of the real part of conductivity σ' on the porosity Φ is shown in Figure 5.10 a. The conductivity increases with increasing porosity of the carbonates. A clear trend is given by EBK and LK. The other two carbonate types show a greater scattering, but fit well with the general trend. The correlation can be described by $\sigma' = 1.6 \cdot 10^{-3}\Phi^{1.93}, R^2 = 0.9$. The cross plot of Φ and σ'' (Fig. 5.10 b) shows a clustering of the carbonates into two types. The carbonates with lower polarisation effects (DOL/ILS) show no correlation or trend, whereas EBK sustains the positive correlation between Φ and σ'' very well. The relationship can be describe by $\sigma''_{\mathrm{EBK}} = 1.2 \cdot 10^{-4}\Phi^{2.18}, R^2 = 0.75$ and is sustained equally by LK, while LK itself shows no clear dependence.

Permeability The dependence of the real part of conductivity on the permeability is shown in Figure 5.10 c. When considering only EBK and LK, a slight increase of the conductivity with increasing permeability is visible. This dependence is a result of the relation between porosity and permeability as well as the correlation

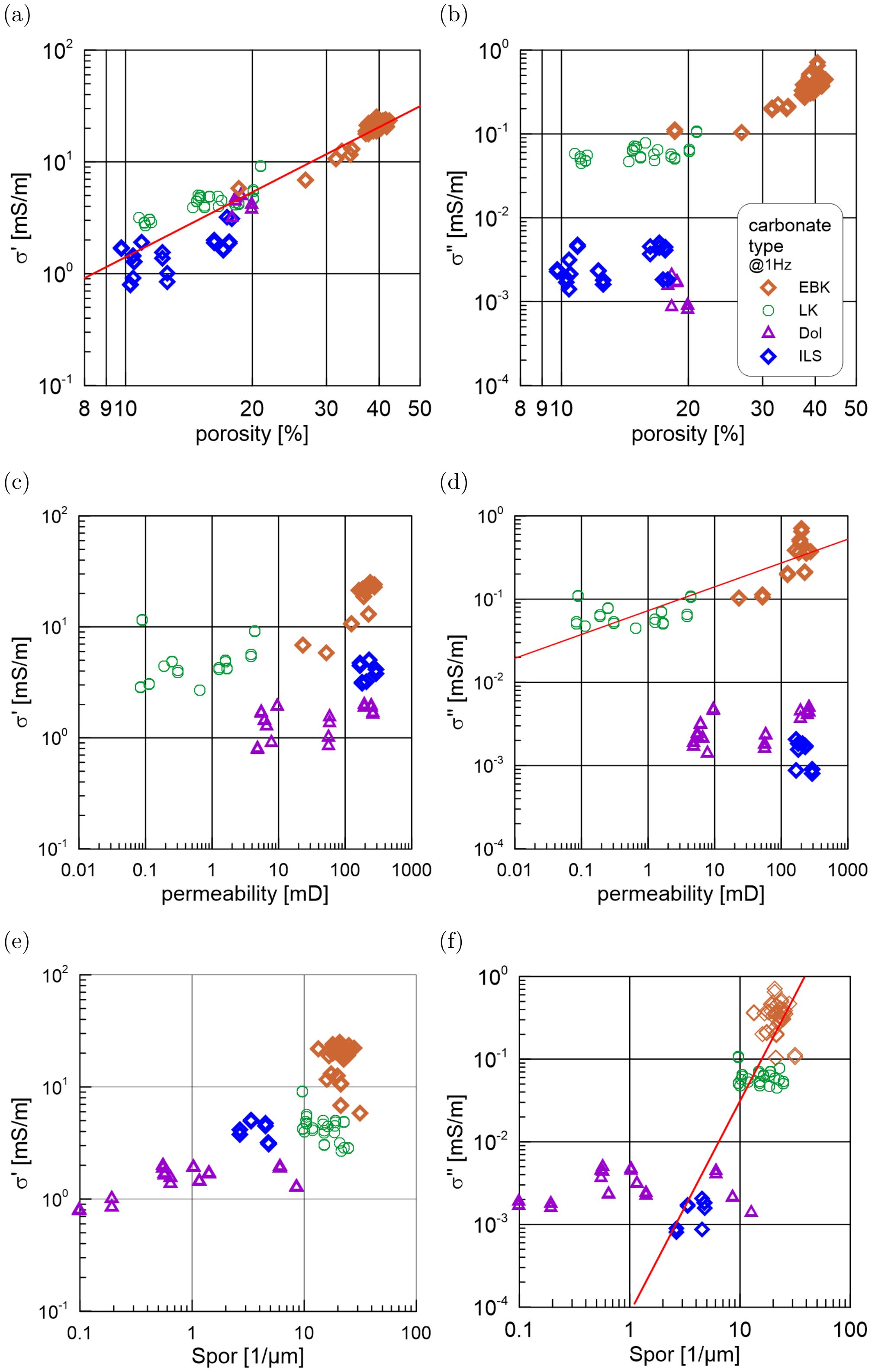

Figure 5.10: Cross plots of the petrophysical parameters porosity Φ, permeability k and surface related to the pore volume S_{por} and the real part of the conductivity σ' and the quadrature conductivity σ''. Red solid lines display the data fit. a) Variation of σ' with porosity. b) Variation of σ'' with porosity. c) Variation of σ' with permeability. d) Variation of σ'' with permeability. e) Variation of σ' with S_{por}. f) Variation of σ'' with S_{por}.

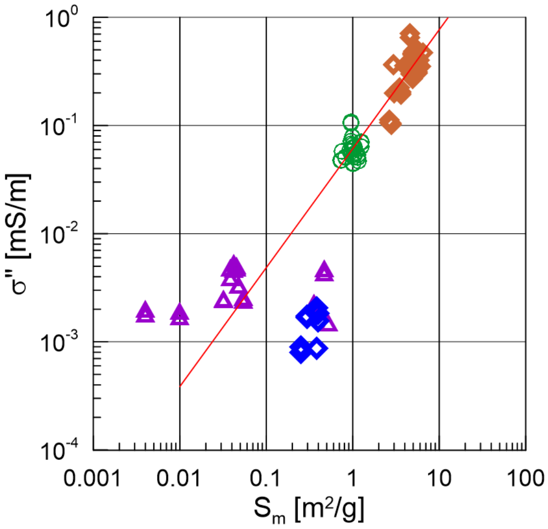

Figure 5.11: The correlation between S_{m} and σ''. The red solid line displays the data fit of the LK and EBK sample set.

of porosity and real part of conductivity, as shown in the Figures 5.2 a and 5.10 a. Considering all four carbonate types, no trend is observable. The relation between permeability and quadrature conductivity is displayed in Figure 5.10 d. Regarding σ'', the carbonates are divided into two clusters (as described for the porosity dependence). The two carbonate types with higher polarisation effects (EBK/LK) show a strong relationship between permeability and quadrature conductivity describable by the following fit: $k_{\mathrm{EBK/LK}} = 3745 \cdot \sigma''^{3}, R^2 = 0.85$. The carbonate types with lower polarisation effects (DOL/ILS) behave differently and do not show a dependence on permeability.

Specific surface The cross plot of S_{por} and σ' is displayed in Figure 5.10 e and indicates that with increasing surface the conductivity increases as well. Nevertheless, no trend is visible of any of the carbonate types. The Silurian Dolomite shows similar conductivity values over two decades of surface values. The other three carbonate types show a clustering and do not follow a significant trend. A similar observation is made for the relationship of S_{por} and σ'' according to Figure 5.10 f. The DOL shows similar quadrature conductivities over two decades of surface values whereas the other three carbonate types form three cluster. A correlation of the three clusters is given by $\sigma'' = 8.15 \cdot 10^5 \cdot S_{\mathrm{por}}^{2.6}, R^2 = 0.74$, but no trend is observable within one carbonate type. Considering the specific surface related to the mass, a better correlation is found including EBK and LK (Fig 5.11). The linear relationship is given by $\sigma''_{\mathrm{EBK/LK}} = 0.075 \cdot S_{\mathrm{m}}, R^2 = 0.92$.

Multi salinity measurement

In addition to the standard measurements with a constant fluid conductivity of 100 mS·m^{-1}, multi salinity measurements with a gradually increasing fluid conductivity were carried out. Considering the previously shown results of the IP-spectra, the EBK type was chosen due to the peak behaviour and the highest phase shift. Starting with a low calcium chloride concentration, the samples were saturated with fluid conductivities between 25 mS·m^{-1} and 1600 mS·m^{-1}. The fluid conductivity was doubled after each step.

IP spectra The resulting spectra of one EBK sample are shown in Figure 5.12. The resistivity spectra show almost parallel curves, which are equally spaced due to the doubling of the calcium chloride concentration (Fig. 5.12 a). The spectra of the different fluid conductivities are sorted as expected: the highest fluid conductivity shows the smallest resistivity. The variation of the phase shift spectra is shown in Figure 5.12 b. Three main observations can be made: (1) decrease of the phase shift with increasing fluid conductivity, (2) no shift of the peak frequency with varying calcium chloride concentration, and (3) no visible maximum phase shift at the two highest fluid conductivities because of the low phase shift. The observation of the resistivity spectra is transferable to the real part of conductivity spectra (Fig. 5.12 c), which shows the reverse order of the resistivity spectra. The observations of the phase spectra can not be fully adopted to the quadrature conductivity spectra, which is shown in Figure 5.12 d. The peak frequency does not change with varying calcium chloride concentration, as well as the two highest fluid conductivities also show no clear phase peaks. Until a fluid conductivity of 400 mS·m^{-1} is reached, an increase of σ'' with increasing fluid conductivity can be observed, but the two highest concentrations overlap the previous measurements and does not follow the sequence. An additional observation, which is only visible for the quadrature conductivity spectra is that the three highest concentrations show a significant increase of the quadrature conductivity in the frequency range of 1 to 100 Hz. A second peak becomes visible in the σ'' spectra.

Complex electrical conductivity The relationships σ' vs. σ_w and σ'' vs. σ_w at a given frequency are displayed in Figure 5.13. Two cases are considered: $\sigma''(\sim 1\,\mathrm{Hz})$ and $\sigma''(f_\mathrm{peak})$, with $f_\mathrm{peak} = 0.2\,\mathrm{Hz}$. The real part of conductivity shows an expected linear relationship with σ_w (Fig. 5.13 a and b). This linear relationship provides an approach to determine a formation factor, because the slope is the inverse of the formation factor, as mentioned in Equation 2.13. It can be assumed, that, if the fluid conductivity is zero, σ' is equivalent to σ'_surf.

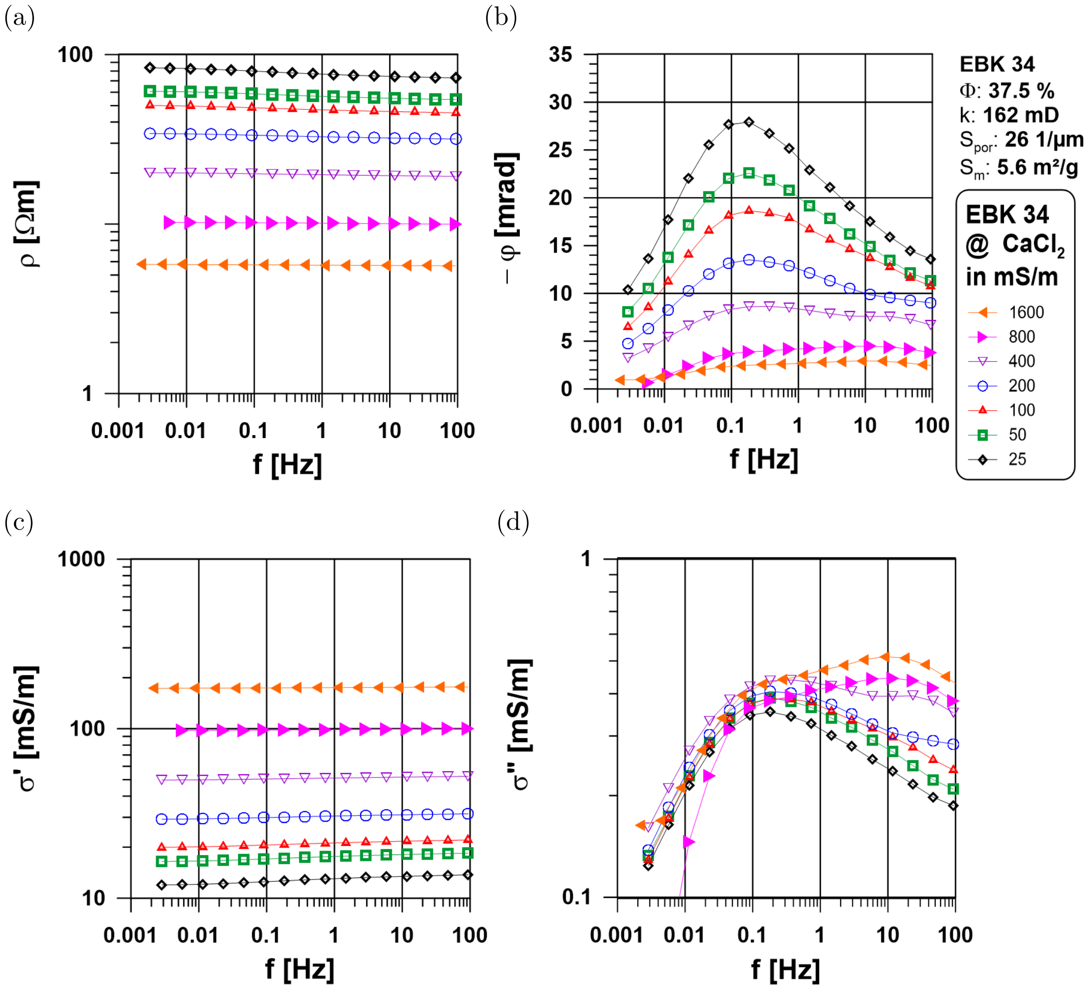

Figure 5.12: Multi salinity measurements of for the exemplary EBK34 sample in a fluid conductivity range of 25 mS·m^{-1} to 1600 mS·m^{-1}. a) Variation in resistivity spectra with fluid conductivity. b) Variation in phase spectra with fluid conductivity. c) Variation in real part of conductivity spectra with fluid conductivity. d) Variation in quadrature conductivity spectra with fluid conductivity.

The determination of the formation factor and σ'_{surf} produces similar values for both frequencies with $R^2 > 0.998$. The cross plot of $\sigma'(\sim 1\,\mathrm{Hz})$ and σ_{w} provides $\mathrm{F} = 9.72$ and $\sigma'_{\mathrm{surf}} = 11.23\,\mathrm{mS{\cdot}m^{-1}}$, which corresponds to the results of the cross plot of $\sigma'(f_{\mathrm{peak}})$ and σ_{w} yielding $\mathrm{F} = 9.65$ and $\sigma'_{\mathrm{surf}} = 11.10\,\mathrm{mS{\cdot}m^{-1}}$. Considering the quadrature conductivity as a function of the fluid conductivity, an increase of σ'' with increasing σ_{w} can be observed ($\sigma'' = 0.2 \cdot \sigma_{\mathrm{w}}^{0.1}$). An asymptotic solution with a threshold value was expected, but this behaviour is not clearly visible in both cases. Figure 5.13 c shows that $\sigma''(\sim 1\,\mathrm{Hz})$ increases further, because of the formation of a second maximum starting at a fluid conductivity of $400\,\mathrm{mS{\cdot}m^{-1}}$ in a the frequency range of 1 Hz to 100 Hz. For the dependency of $\sigma''(f_{\mathrm{peak}})$ and σ_{w} no continuous increase can be observed (Fig. 5.13 d). The two highest fluid conductivities show a second σ'' peak at higher frequencies, which influences the peak at $f = 0.2\,\mathrm{Hz}$. In order to ensure the comparability, $\sigma''(f_{\mathrm{peak}})$ for the fluid conductivities of $800\,\mathrm{mS{\cdot}m^{-1}}$ and $1600\,\mathrm{mS{\cdot}m^{-1}}$ is chosen at the same f_{peak} as the other fluid conductivities. A complete list of the parameters used for description of the salinity influence is part of the appendix (Tab. B.14).

Chargeability and time constant The IP parameter chargeability m and time constant τ were determined by Debye decomposition (DD) and Cole-Cole (CC) fit. Figure 5.14 shows the variation of chargeability with fluid conductivity. The EBK sample shows a strong decrease of m with increasing salinity. The chargeability derived by DD has slightly lower values than m derived by CC. A negative logarithmic function fits the relationship between m and σ_{w} with $R^2 = 0.99$ (DD) and $R^2 = 0.95$ (CC). The normalised chargeability in variation with salinity is shown in a double logarithmic plot (Fig. 5.14 b). The increase of the normalised chargeability with increasing fluid conductivity can be described by power laws: $m_{\mathrm{n}}\,(\mathrm{DD}) = 0.4{\cdot}\sigma_{\mathrm{w}}^{0.16}$ and $m_{\mathrm{n}}\,(\mathrm{CC}) = 0.4{\cdot}\sigma_{w}^{0.20}$. The normalised chargeability derived by DD is slightly lower than m_{n} determined by CC.

For the dependency of time constant on salinity, a constant behaviour was expected since the peak frequency does not change with salinity. Figure 5.14 c shows that τ_{CC} remains unaffected by different pore water salinities. The CC values are similar but show a scattering and no clear constant behaviour. The time constants derived by DD are lower and show a slight decrease with increasing salinity, except of the value of the highest salinity. It has to be mentioned that the CC fit and the calculation according to Equation 3.22 provides only outliers for conductivities higher $400\,\mathrm{mS{\cdot}m^{-1}}$, because the curves, shown in Figures 5.12 b and d, are no symmetrical CC-curves. The outliers are not shown here. Because τ is nearly independent of the pore fluid conductivity, the normalised time constant displays a linear dependence on the salinity, as can be seen in Figure 5.14 d. The increase of τ_n with rising salinity can be described by a power law. The best fit is achieved by τ_n calculated by DD: $\tau_\mathrm{n}(\mathrm{DD}) = 0.4 \cdot \sigma_\mathrm{w}^{0.5}, R^2 = 0.88$. A complete list of the DD and CC parameters used for description of the salinity influence is part of the appendix (Tab. B.15). Table 5.4 sums up the observations of the multi salinity measurements.

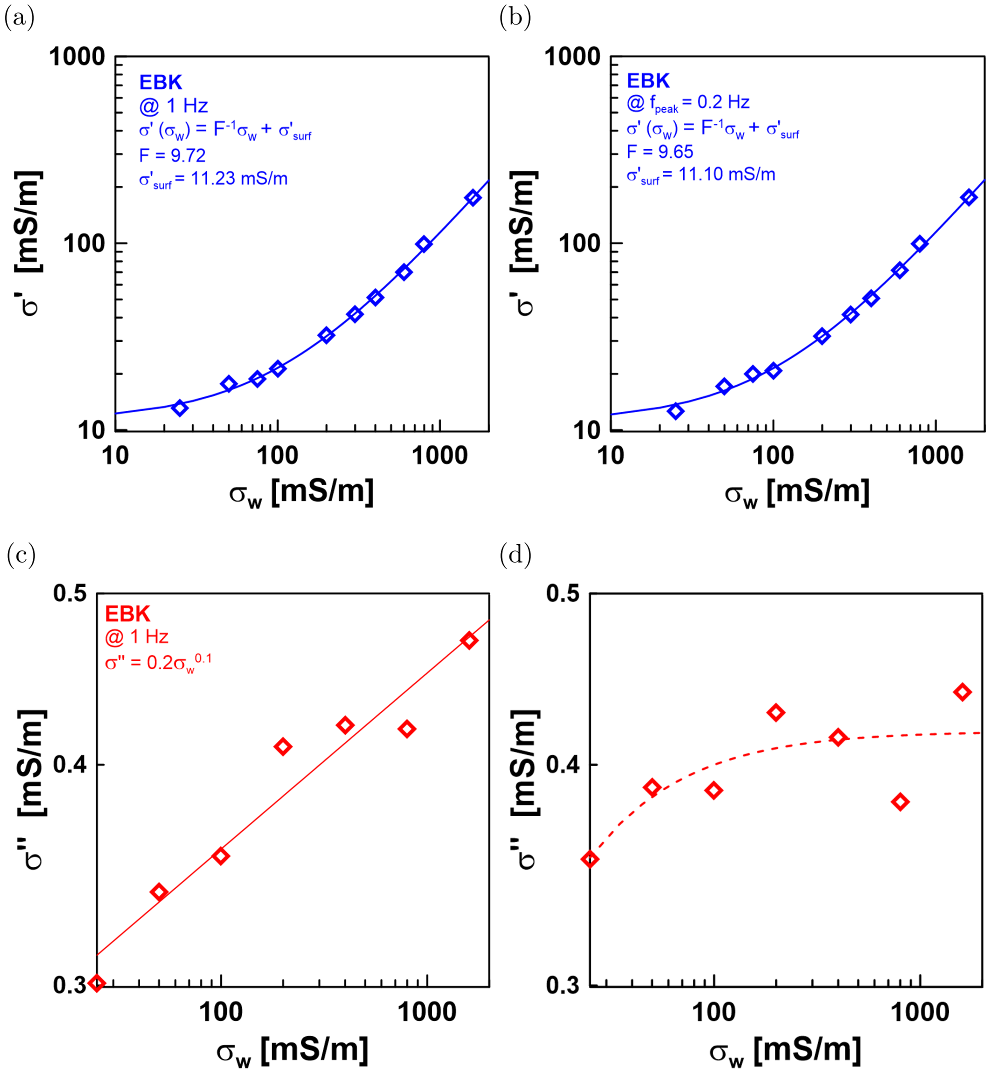

Figure 5.13: Multi salinity results of the complex electrical conductivity in a fluid conductivity range of 25 mS·m^{-1} to 1600 mS·m^{-1} for the exemplary EBK34 sample. Variation in real part of conductivity spectra a) at a frequency of 1 Hz and b) at f_peak spectra conductivity as well as in quadrature conductivity spectra c) at a frequency of 1 Hz and d) at f_peak with fluid conductivity.

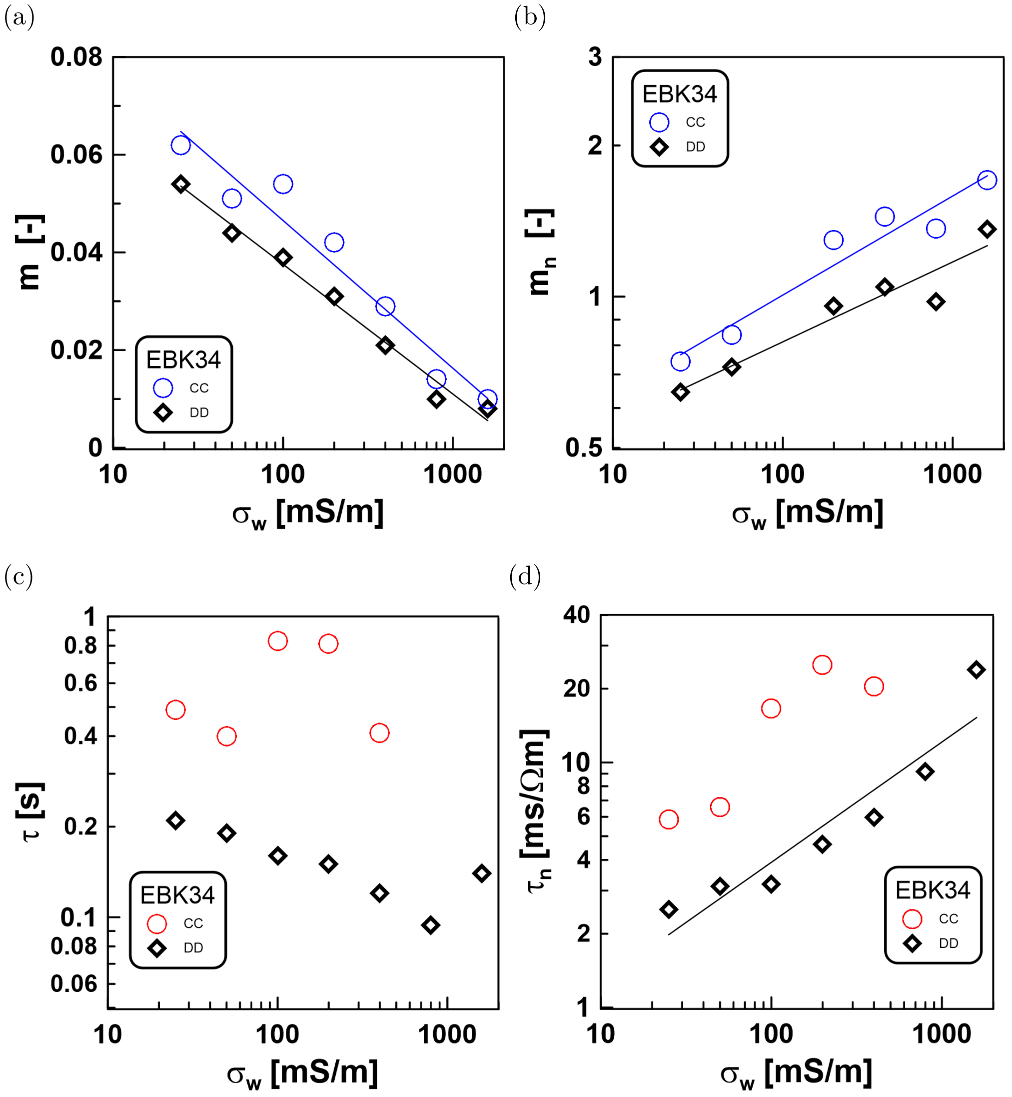

Figure 5.14: Multi salinity results of the chargeability and time constant derived by Debye decomposition and Cole-Cole model in a fluid conductivity range of 25 mS·m^{-1} to 1600 mS·m^{-1} for the exemplary EBK34 sample. Solid lines display the data fit. Variation a) in chargeability, b) in normalised chargeability, c) in time constant, and d) in normalised time constant with fluid conductivity.

Table 5.4: Variation of IP parameter with increasing fluid salinity.

EBK	ρ	φ	σ'	σ''	f_{peak}	m	m_n	τ	τ_n
$\sigma_w\uparrow$	↓	↓	↑	↑	-	↓	↑	-	↑

Estimation of the formation factor

The formation factor can be determined by different approaches. Five of which and the corresponding equations are listed below:

(1) $\mathbf{F_M}$ with $F = \frac{\sigma_\mathrm{w}}{\sigma_0}$ at high salinities (Eq. 2.11),

(2) $\mathbf{F_{Arch}}$ with $F = \frac{1}{\Phi^m}$ (Eq. 2.11),

(3) σ' vs. σ_w with $\sigma' = \frac{1}{\mathbf{F_1}} \cdot \sigma_\mathrm{w}$,

(4) F' vs. σ_w with $F' = \frac{\mathbf{F_2} \cdot \sigma_\mathrm{w}}{a + \sigma_\mathrm{w}}$, and

(5) using IP data with $\mathbf{F_{corr}} = \frac{\sigma_w}{\sigma' - \sigma''/l}$ (Eq. 2.25 and Eq. 2.26).

The first item indicates the method to determine the formation factor with a single salinity measurement provided that σ_w is high enough. Archie's Law is used to calculate F from a known porosity and cementation exponent. On the next three items, the determination of the formation factor is based on SIP measurements. One approach to determine F using SIP measurements is to vary the salinity of the pore fluid. The items three and four require multi salinity measurements, which are described in 5.2.2. The last item describes the determination of the formation factor using a single IP measurement.

(1) $\mathbf{F}_\mathrm{M}$ Originally, the formation factor was defined as the ratio between σ_w and the electrical conductivity σ_0 of a fully-saturated porous rock on the condition that electrical conductivity is purely ionic and the pore fluid is the only conducting medium (Eq. 2.11). The salinity σ_w is set to $12\,\mathrm{S{\cdot}m^{-1}}$ to fulfil the condition of Equation 2.11. The directly measured formation factor is highly reliable. A complete list of the directly measured formation factors is part of the appendix (Tab. B.16 and Tab. B.17).

(2) $\mathbf{F}_\mathrm{Arch}$ The calculation of F by using Archie's law (Eq. 2.11) requires a known interconnected porosity and cementation exponent. The porosity is given by triple weighing method but m is unknown. Literature suggests values for carbonate rocks from 1.7 - 1.8 (chalky limestones) to 1.8 - 2.0 (crystalline and granular carbonates) to 2.1 - 2.6 (carbonates with vugs) (Schön, 2004). The parameter m of carbonates depends on the porosity type.The crossplot of Φ and the directly measured F_M is a possibility to determine m for each carbonate type (Fig. 5.15 a). The negative correlations (solid lines) provide a characteristic exponent for each carbonate type: $m_\mathrm{EBK} = 2.37$, $m_\mathrm{LK} = 1.94$, $m_\mathrm{DOL} = 2.38$, and $m_\mathrm{ILS} = 2.03$. The coefficient of

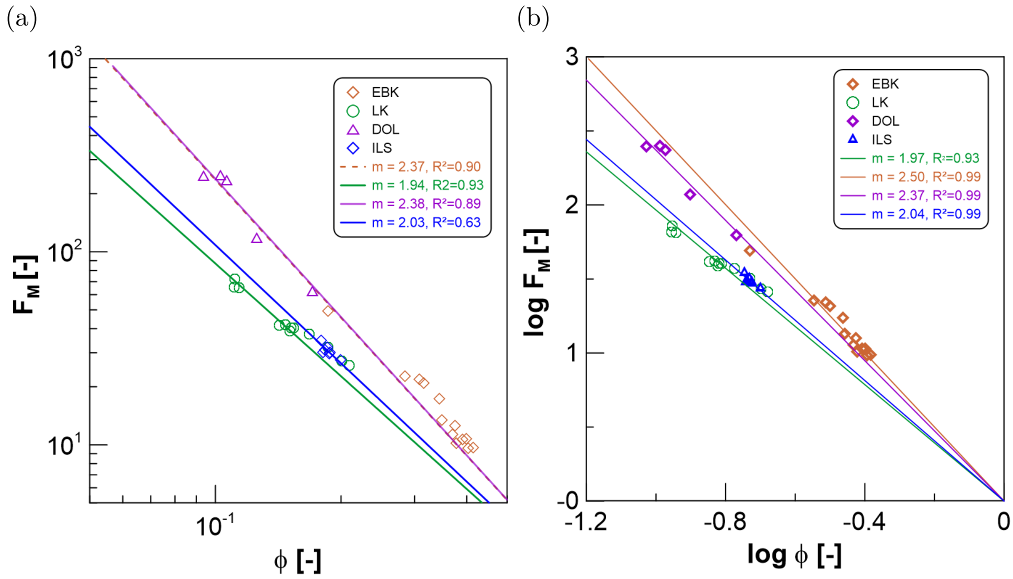

Figure 5.15: a) Formation factor F_M is plotted against porosity for the studied carbonates yielding the exponent for each sample type. b) Logarithmic plot of formation factor F_M and porosity for the studied carbonates yielding the exponent m for each sample type.

determination R^2 is about 0.9 for EBK, LK, and DOL. The correlation of ILS shows a lower $R^2 =$ 0.63. It has to be mentioned that DOL includes only five samples and ILS only seven, while the correlations of EBK and LK contain 13 and 12 data points. A disadvantage of this method is the stronger weighting of higher F-values. An alternative method is the use the log values of F_M and Φ (Fig. 5.15 b). The slopes (solid lines) of each carbonate type provide m: $m_\mathrm{EBK} = 2.50$, $m_\mathrm{LK} = 1.97$, $m_\mathrm{DOL} = 2.37$, $m_\mathrm{ILS} = 2.04$.

The comparison of F_M and F_Arch shows a good consistency with an average deviation on a logarithmic scale of $d = 0.0382$ for the first method and $d = 0.0378$ for the second method (Fig. 5.16). The second approach to determine the parameter m provides better results for F_Arch in comparison to F_M. The determined values of m offers the opportunity to calculate F_Arch for the whole sample set. A complete list of F_Arch is part of the appendix (Tab. B.16 and Tab. B.17).

(3) $\mathbf{F_1}$ and (4) $\mathbf{F_2}$ Figure 5.13 a shows, that F_1 is given as $F_1 = 9.65$ by the inverse slope of the linear relationship. The apparent formation factor F' is calculated for each salinity step by $F' = \sigma_\mathrm{w} \cdot \sigma'^{-1}$ at a frequency of around 1 Hz. Figure 5.17 shows that the salinity data results by Equation 2.29 in $F_2 = 9.70$, which is almost the same value as F_1.

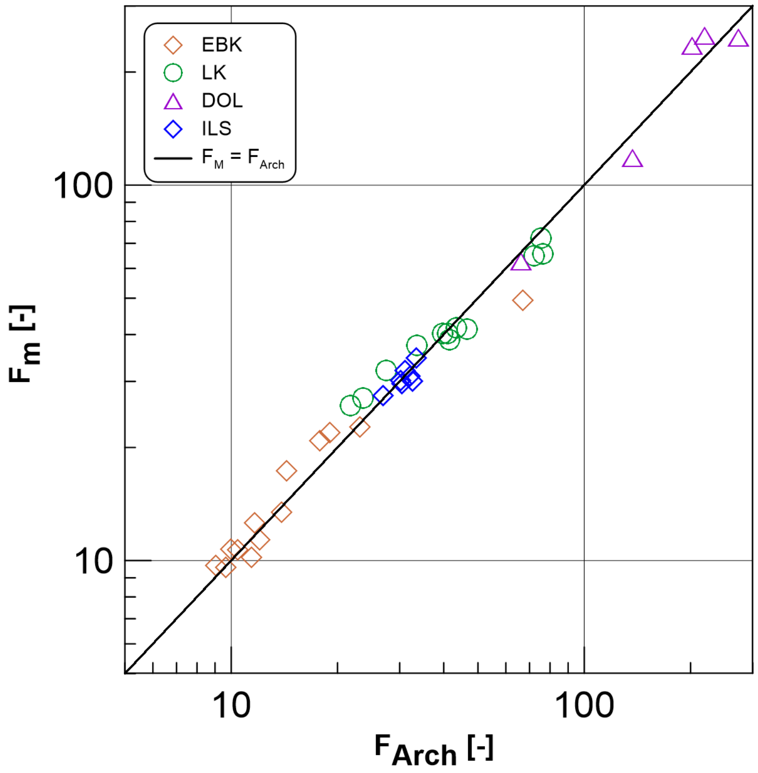

Figure 5.16: Crossplot of F_{Arch} (determined by Figure 5.15 b) versus F_{M}. Average deviation between F_{Arch} and F_{M} is 0.0378 on logarithmic scale.

(5) F$_{\mathrm{corr}}$ The relationship between σ'_{surf} and σ'' is basic for a reliable prediction of formation factors of carbonate rocks (Fig. 5.18). The parameter σ'_{surf} is determined by Equation 2.28 using F_{M} as formation factor. The two carbonate types with higher polarisation effects (EBK/LK) follow the trend very well, while the DOL and ILS exhibit larger deviations from the determined trend. Thus, the observations show clearly that the surface conductivity controls quadrature conductivity as well as the polarisation mechanism. The ratio of the two surface conductivities corresponds to the factor l (Eq. 2.26), which can explain the data (red solid line). The factor l for the studied carbonates is 0.0291 with a R-squared of 0.96. Considering only EBK and LK samples, the factor of $l = 0.0293$ ($R^2 = 0.99$) is almost the same. The predicted formation factor F_{corr} is determined by Eq. 2.25 using only a single salinity measurement.

Figure 5.19 shows the results of the calculated F_{corr} in relation to the porosity Φ. A fit (solid black line) provides a cementation exponent of 2.02 for the studied carbonates. The comparison of F_{M} and F_{corr} shows a good consistency with an average deviation of $d = 0.096$ on logarithmic scale, which corresponds to an error of ±25 % (Fig. 5.20). The determined l offers the opportunity to calculate F_{corr} for the whole sample set (Tab. B.16 and Tab. B.17).

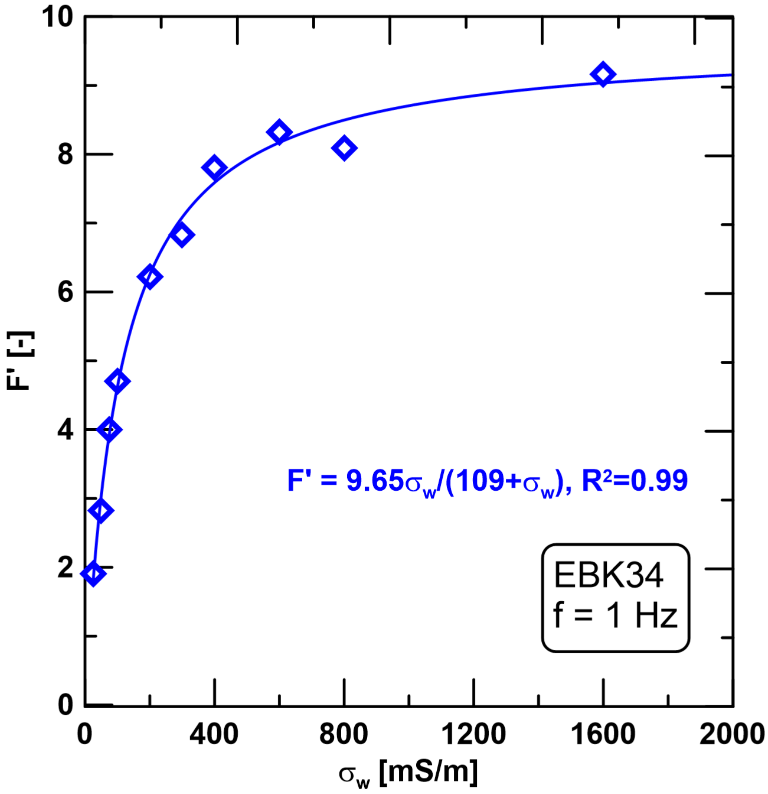

Figure 5.17: Procedure to estimate the true formation factor F_2 from multi salinity measurement of the real part of conductivity. F_2 is given by the high-salinity asymptote.

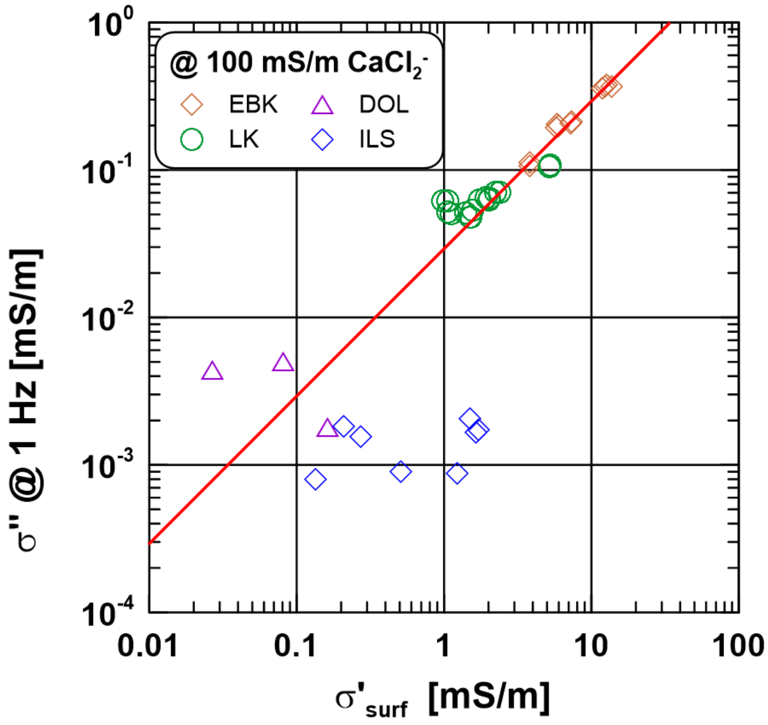

Figure 5.18: Crossplot between σ'' (at 1 Hz) and σ'_{surf} for the investigated samples. The red solid line displays the data fit including 36 measured samples.

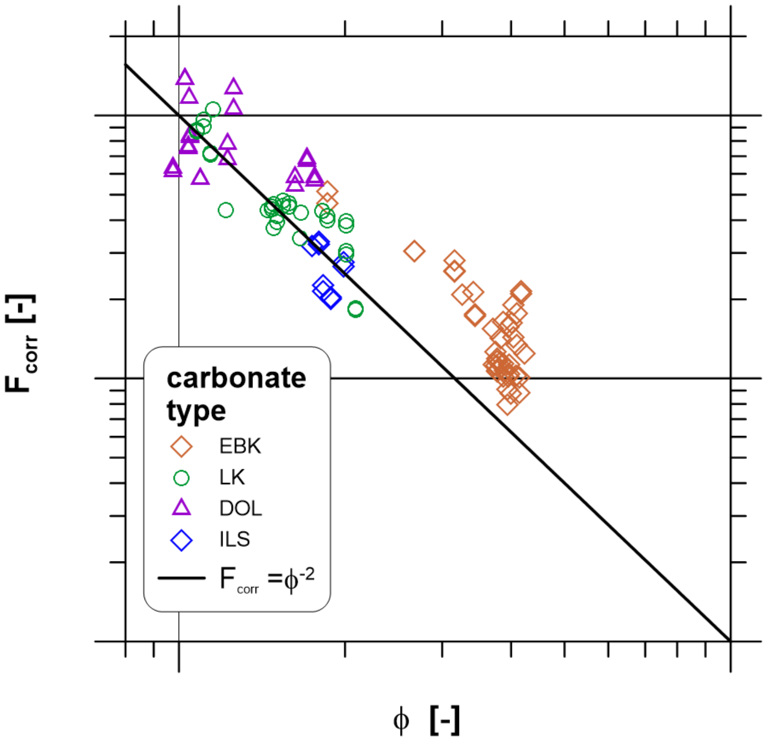

Figure 5.19: Formation factor F_{corr} is plotted against porosity for the studied carbonates.

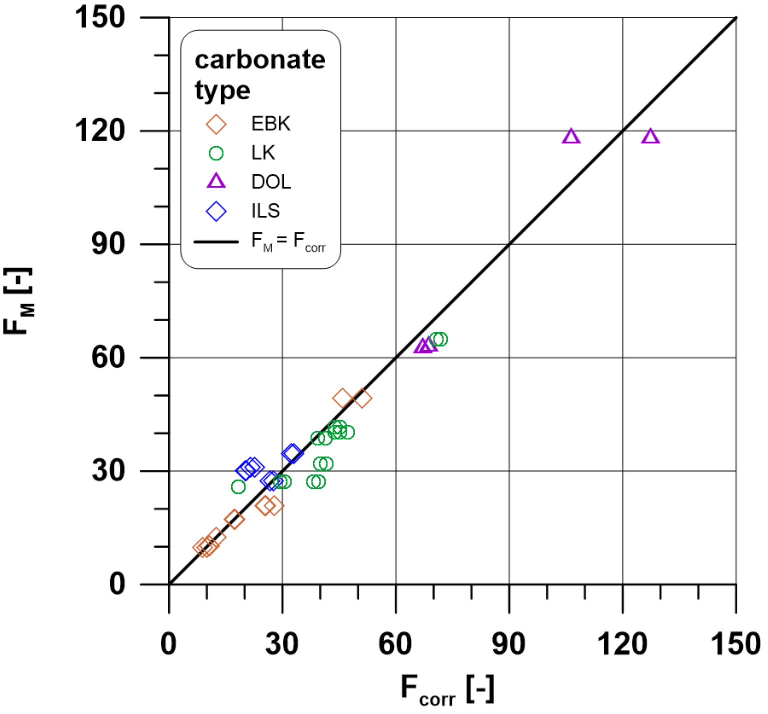

Figure 5.20: Crossplot of F_{corr} versus F_{M}. Average deviation between F_{corr} and F_{M} is 0.096 on logarithmic scale.

Table 5.5 summarises the formation factors of sample EBK34 and two additional samples obtained by five different approaches. The comparison shows that the different approaches provide similar formation factors. The formation factors F_1 and F_2, determined by multi salinity measurements, are very close to each other. Due to the determination on different salinities, F_1 and F_2 can be considered as the most reliable ones. Concurrently, the multi salinity approach is time consuming and impracticable for field measurements. Comparing to F_1, and F_2, the formation factors F_{M}, F_{Arch} and F_{corr} are slightly overestimated.

Table 5.5: Formation factor of three EBL samples obtained by different approaches.

sample	F_1 σ' vs. σ_w	F_2 F' vs. σ_w	F_{M}	F_{Arch}	F_{corr}
EBK34	9.65	9.72	12.6	11.64	12.58
EBK01	9.35	9.15	11.69	9.65	13.40
EBK02	9.36	9.19	11.46	9.18	13.00

Permeability prediction

The negative correlation of F_{M} and k_{m} is already shown in Figure 5.2 d. Figure 5.21 a displays the same cross plot using F_{corr} instead of F_{M}. For F_{corr}, the double amount of data points is available. The correlation of all carbonates is given by the following power law:

$$k_{\mathrm{F}} = 3.21 \cdot 10^{-8} \cdot F_{\mathrm{corr}}^{-2.1}, \tag{5.2}$$

with $\mathrm{R}^2 = 0.37$. Considering only the sample types EBK and LK, the coefficient of determination increases to $\mathrm{R}^2 = 0.74$ and the power law reads as follows:

$$k_{\mathrm{F}} = 1.43 \cdot 10^{-6} \cdot F_{\mathrm{corr}}^{-3.6}. \tag{5.3}$$

Figure 5.21 b shows the relationship of σ'' at a given frequency of around 1 Hz and k_{m} and indicate no correlation considering the four carbonate types in total. Nevertheless, a positive correlation can be observed for EBK and LK given by

$$k_{\sigma''} = 3.7 \cdot 10^{-9} \cdot \sigma''^{3}, \tag{5.4}$$

with $\mathrm{R}^2 = 0.85$.

The relationships between the formation factor and permeability and quadrature conductivity and permeability, as shown in Figure 5.21, are the basis of the following k prediction. The following equation combines the three parameter k, σ'' and F_{corr}:

$$k_{\mathrm{F}\sigma''} = \frac{a}{F^b \cdot \sigma''^c}, \tag{5.5}$$

with k in m^2, σ'' in mS·m^{-1}, and F as unitless. The equation is linearised and becomes a vector-matrix problem. The adaptation is performed through a least squares estimation between the matrix and the vector using firstly all data points and secondly only data points of EBK and LK. For comparison purposes, DOL and ILS are excluded for a second adaptation because both carbonate types deviate by a greater amount of correlations with IP parameter. The linear regression provides the following parameters for all carbonates: $a = 3.2 \cdot 10^{-7}$, $b = 3.5$, and $c = 0.72$. Figure 5.22 displays the comparison of the measured and the predicted permeabilities k_{F} and $k_{\mathrm{F}\sigma''}$ considering all studied carbonates. The following average deviations on logarithmic scale are provided by the cross plot: $d_{\mathrm{F}} = 0.67$ and $d_{\mathrm{F}\sigma''} = 0.63$. Considering only EBK and LK, the average deviation changes as follows: $d_{\mathrm{F}} = 0.58$ and $d_{\mathrm{F}\sigma''} = 0.44$.

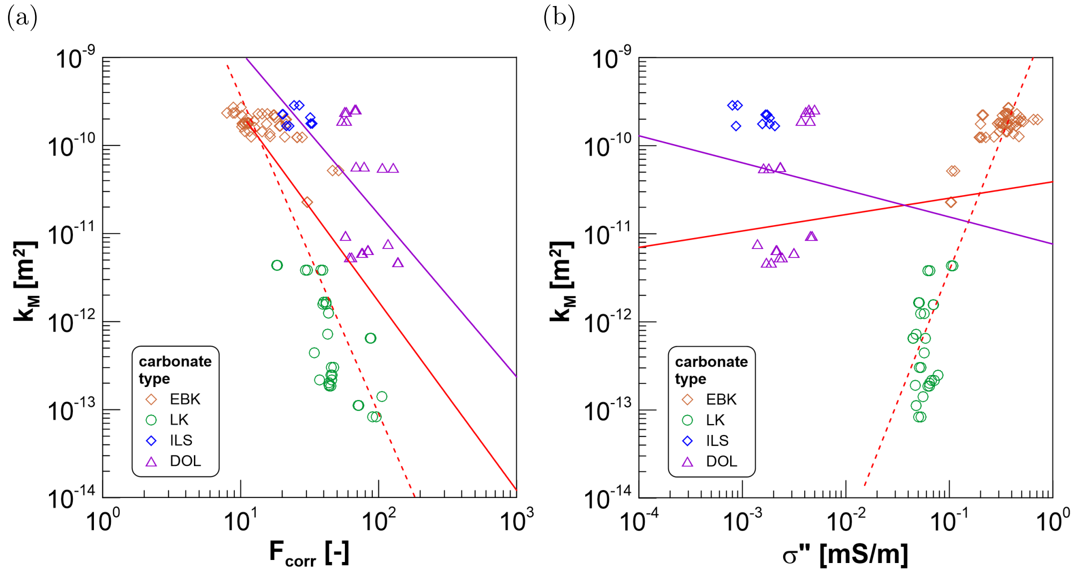

Figure 5.21: Relationships between permeability and the predicted formation factor as well as the quadrature conductivity. The red solid line indicates the results of a power law fitting including 112 data points of all carbonates, whereas the dashed red line includes only data points (81) of EBK and LK and the purple solid line includes only data points (21) of ILS and DOL. a) Relationship between the F_{corr} and k for the carbonate samples. b) Relationship between the σ'' and k for the carbonate samples.

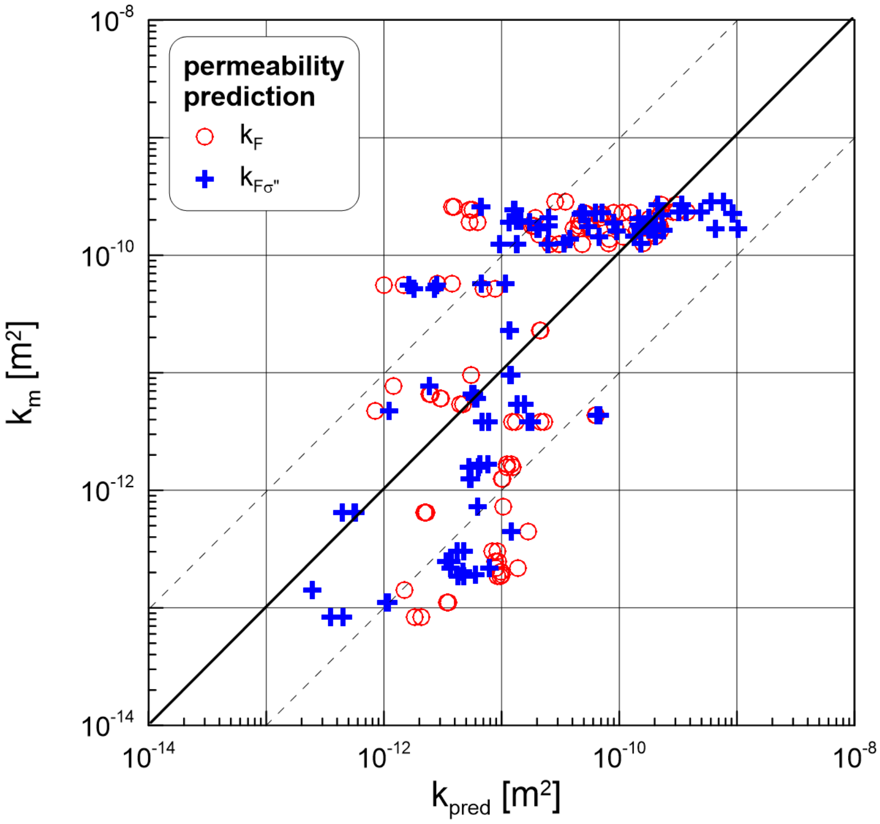

Figure 5.22: Permeability calculated from equation 5.2 (red circles), and 5.5 (blues crosses) versus measured permeability of 106 carbonate samples. The two dashed lines on either side of the diagonal indicate a deviation of one order of magnitude from the measured permeability value.

5.3 Dissolution experiment

In this chapter, the results of the dissolution experiment will be given in three parts. The first part describes the experimental procedure itself regarding functionality and first valuation of the acid solution. The second part characterises the structural changes triggered by the acid solution: (1) imaging methods are used to visualise and quantify the changes caused by dissolution and (2) the structural changes are recorded systematically by petrophysical methods to characterise the pore space. The last part describes how IP parameters change during dissolution processes. The selection of the carbonate type, which is used for the dissolution experiment, takes place according to specified criteria. The EBK is considered suitable because of its high porosity ($\sim 37\,\%$) and moderate permeability ($\sim 200\,\mathrm{mD}$) as well as its significant IP effect.

5.3.1 Experiment

The experimental setup has been specially designed and constructed for this study. The practical testing and usage provides findings about functionality and the behaviour of the acid solution during dissolution procedures. The general workflow is described in section 3.4. Figure 5.23 shows representative monitoring results of the acidifying and flushing phase.Note, that the data of the outflow is recorded time-delayed to the actual process at the sample because the fluid is transported towards two in-a-row located container to measure conductivity and pH value, as seen in Figure 3.6. The transport includes a volume of around 2.5 ml fluid and the containers contain each 11 ml fluid. The time shift depends on the flow rate.

Acidifying phase Figure 5.23 a shows the monitoring of the acidifying phase. A conductivity of $200\,\mathrm{mS{\cdot}m^{-1}}$ was measured for the inflowing acid. Due to the time dependency of the acid-water-mixture, the conductivity of the acid (σ_{acid}) varies between the acidification procedures. The conductivity increases with increasing endurance of the acid-water mixture. The outflow conductivity increases abruptly after breakthrough of the acid solution. During the acidification procedure, the flow direction is changed in order to prevent trapping effects. The short-time stopping of the pistons is visible as a drop of the outflow conductivity. The acidification procedure continues until the outflow conductivity reaches steady state. Obviously, the outflow conductivity is higher than the inflow conductivity. The pH value of the acid solution is about 3 for the inflow fluid and increases to 6 for the outflow fluid.

Flushing phase The inflow conductivity of flushing water is about 50 mS·m^{-1}, which is the typical tap water conductivity in the region of Hanover. The conductivity of the outflow fluid decreases, starting from 1000 mS·m^{-1}, until the conductivity of the inflow is reached. The original assumption of an amount of 10 pore volumes of fresh water for cleaning is modified based on of the monitoring results. The cleaning procedure takes longer than the dissolution process and the amount of fresh water is about 40 pore volumes. The pH value of fresh water is about 8 for the inflow fluid. The value of the outflow fluid increases from a start value of 6 to about 7. The flow direction is also changed during the cleaning as for the acidifying phase.

Geochemical analysis A geochemical analysis of the used acid solution is carried out as well as an analysis of the outflowing fluid during acidifying and flushing. The analysis includes a number of qualitative and quantitative specifications, which provide an overview about quality and composition of the mixture. An overview of the time of sample extraction during the experiment is given in Figure A.14. In total, seven samples of the outflow fluid were analysed during the acidifying procedure and six samples are analysed during the flushing of the carbonate sample. The amount of the three main components calcium, magnesium, and formate is displayed for the extraction times (Fig. A.15).

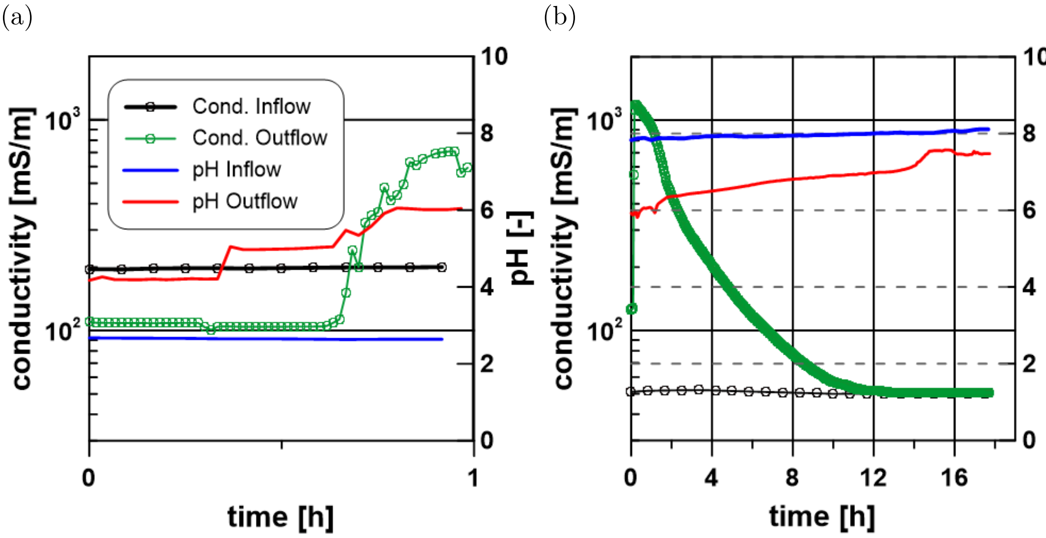

Figure 5.23: Monitoring of the conductivity and pH value at inflow and outflow. a) Monitoring results of the acidifying phase. b) Monitoring results of the flushing phase.

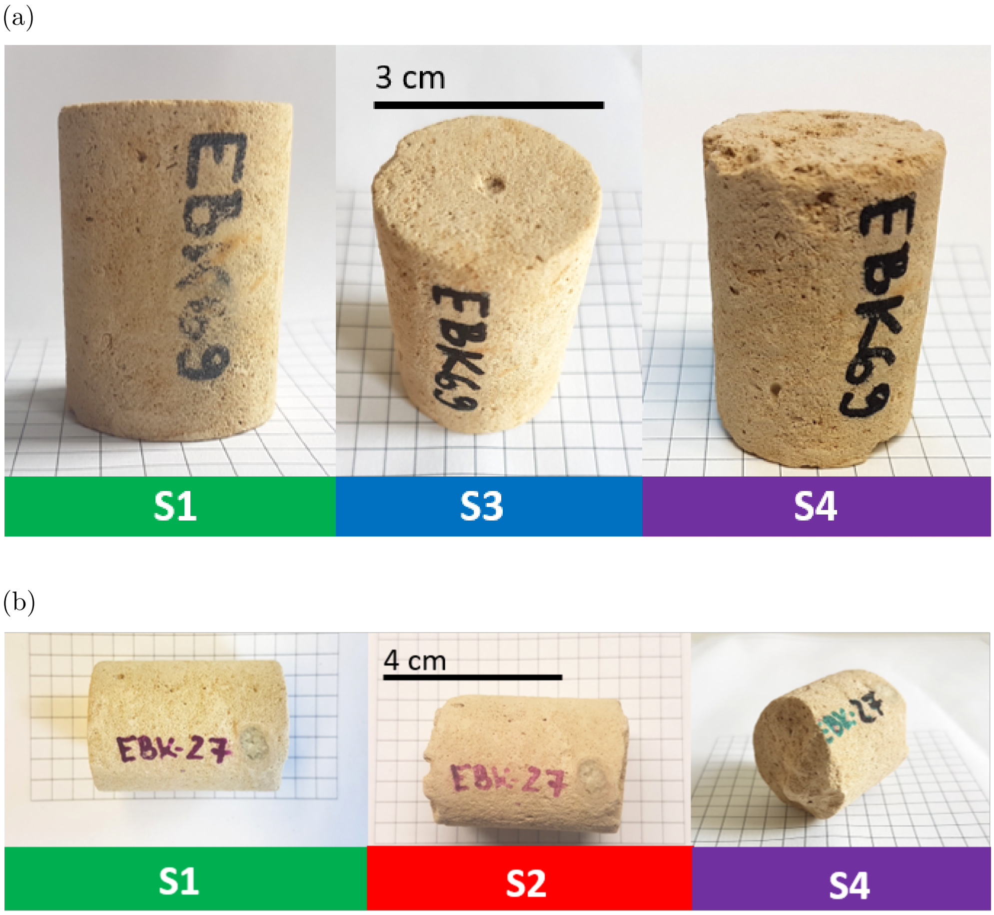

Figure 5.24: Alteration of the treated EBK samples. a) The plug keeps its cylindrical shape during dissolution steps one (S1, green), three (S3, blue), and four (S4, purple). b) The plug shows a significant mass loss during dissolution steps one (S1, green) and two (S2, red) as well as during two (S2, red) and four (S4, purple).

5.3.2 Structural changes

Imaging

A quantitative description of the alteration process can be given by imaging. Figure 5.24 shows the plugs during the dissolution steps. The surface of the plugs shows a significant alteration after the treatment. It is affected by chemical solution, which leads to corrosion. In Figure 5.24 a, the plug keeps its cylindrical shape after several treatment steps. Only the last dissolution step (S4) shows a mass loss at the base of the cylindrical plug. The bases of the cylindrical plugs are highly affected by dissolution, as shown for the sample in Figure 5.24 b.

ESEM images On the basis of the ESEM images, important observations concerning the dissolution process can be made. The comparison of the images in Figure 5.25 a and b reveals a significant alteration of the carbonate. The ESEM

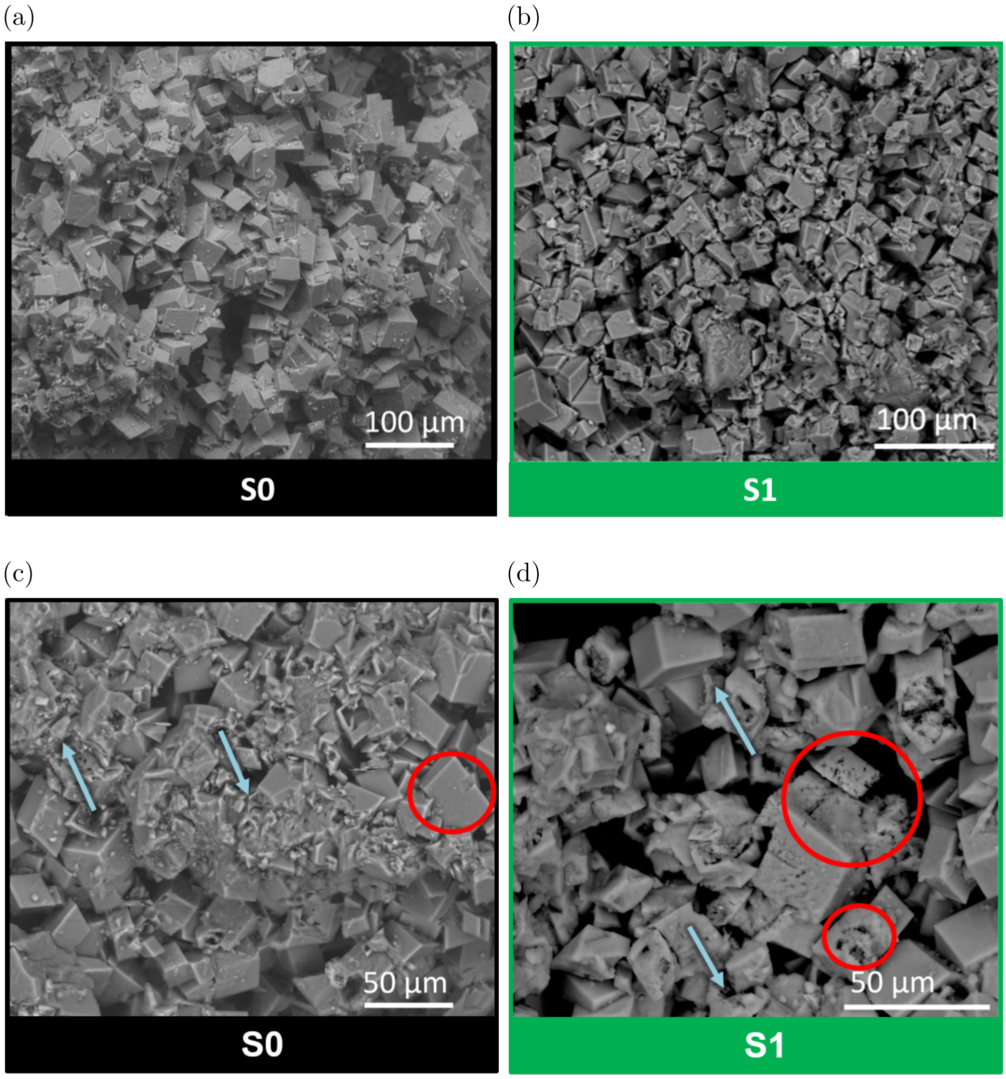

Figure 5.25: Comparison of ESEM images of the Edwards Brown carbonate before and after dissolution. a) Image of an untreated sample. b) Image of a sample after the first dissolution step. c) Image of an untreated sample with marked spots: carbonate cement (blue arrows) and smooth crystal surfaces (red circle). d) Image of a sample after the first dissolution step with marked spots: missing carbonate cement (blue arrows) and corroded crystal surfaces (red circles).

images suggest a homogeneous dissolution process. A closer examination shows that the dissolution takes place at two different locations within the samples (Figure 5.25 c and d): Firstly, the carbonate cement between the idiomorphic crystals seems to be preferably dissolved by the acid solution (indicated by blue arrows). Secondly, the surfaces of the idiomorphic crystals are affected by a continuous, but slower dissolution process (highlighted by red circles). The above described dissolution results in holes at the surface and at the edges of the crystals. As explained in section 4.2.1, some of the crystals show interior cavities and in combination with the holes triggered by dissolution, they can lead to the generation of new pathways (between two holes) or dead ends (one hole). Additional geochemical analyses have shown that the idiomorphic crystals consist of dolomite ($CaMg(CO_3)_2$) and the cement consists of calcite ($CaCO_3$). This results in a higher solubility of the cement as for the crystals itself, because dolomite is more acid-proof than calcite. Firstly, the formic acid solves the calcite and at a later time, the dolomite is etched. This also explains the increasing mechanical instability of the sample material after each dissolution step. An additional evidence of the preferred dissolution of pure $CaCO_3$ cement is given by Figure 5.26. The ESEM image shows dissolved and flushed out *mud* after dissolution of the sample. The mud mainly consists of single dolomite crystals, and the carbonate cement is missing.

Petrophysics

The petrophysical core analysis includes measurements of the density, porosity, surface area and T_2 time distributions on all samples as well as MIP and

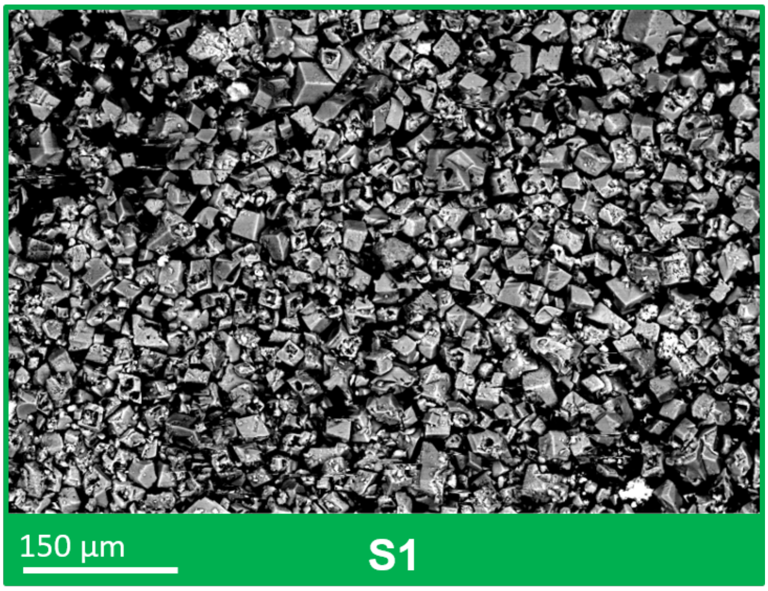

Figure 5.26: ESEM image of dissolved and flushed out *mud* after acidification of the sample.

μ-CT on selected samples. Figures 5.27 a - 5.30 a show the absolute values of the petrophysical parameters density, porosity, surface area related to the mass, and surface area related to the pore volume summarised in a box-and-whisker plot for each treatment step. Each step contains the same amount of samples to ensure the comparability throughout the steps. Accordingly, the samples have to be measured in the steps S0, S1, S2, and S3 to be included. Figures 5.27 b - 5.30 b display the relative changes of the petrophysical parameters in percent, which are less error-prone in comparison to the absolute values.

Density Figure 5.27 a shows the change of the grain density with increasing dissolution steps for 15 samples. A constant density and no impact by acidification was expected, but a slight increase is observed. The median value of the untreated samples is $d_{S0} = 2.776\,\mathrm{g{\cdot}cm^{-3}}$ and increases to $d_{S1} = 2.800\,\mathrm{g{\cdot}cm^{-3}}$, $d_{S2} = 2.804\,\mathrm{g{\cdot}cm^{-3}}$ and up to $d_{S3} = 2.811\,\mathrm{g{\cdot}cm^{-3}}$ after the third dissolution step. Figure 5.27 b displays the percentage change of the density between different dissolution steps. The majority of the samples ($> 75\,\%$) is always in the area greater than zero for each considered constellation, which indicates an increase in density. The positive percentage change increases with each additional dissolution step: the increase from step 0 (S0, black) to step 1 (S1, green) is about 1 % for a set of 24 samples and increases up to 1.5 % considering the percentage change from S0 to S3 (blue) for a set of 16 samples. A comparison of the percentage change between two consecutive dissolution steps indicates that the first dissolution step (S0 - S1, green) causes the highest percentage change (1 %), whereas the following steps cause a percentage change of the density of 0.4 % (S1 - S2, orange) and 0.14 % (S2 - S3, pink).

Porosity Figure 5.28 b displays the change of the absolute porosity values with increasing dissolution steps for 15 EBK samples. A significant increase of the porosity after dissolution is observed. The median value of the porosity increases from $\Phi_{S0} = 38.97\,\%$ of the untreated samples (black) to $\Phi_{S1} = 39.46\,\%$ (S1, green), to $\Phi_{S2} = 40.46\,\%$ (S2, red), and to $\Phi_{S3} = 41.41\,\%$ (S3, blue). Three dissolution steps correspond to an increase of about 2.5 %. The relative percentage change of the porosity between different dissolution steps is displayed in Figure 5.28 b. The majority of the sample set shows a positive percentage change of the porosity. The positive percentage change increases with each additional dissolution step: the increase is about 2.5 % from S0 to S1 (green) including 22 samples, about 4.5 % from S0 to S2 (red) including 20 samples, and about 5.2 % from S0 to S3 (red) including 15 samples. A comparison of the percentage change of two consecutive

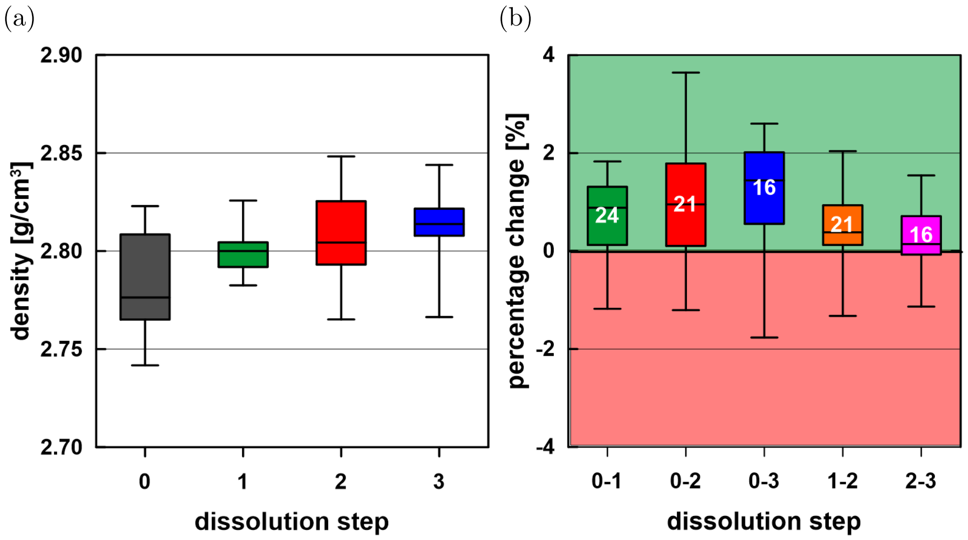

Figure 5.27: Results of the density data of three dissolution steps are shown in box-and-whisker plots. a) Comparison of the absolute density including 15 samples. b) Comparison of the relative percentage change of the density between different dissolution steps. The white coloured number refers to the number of included samples.

dissolution steps shows the same observation as for the density: the first step triggers the highest percentage change (2.5 %) compared to the following steps with percentage change of 1.6 % (orange) and 1.8 % (pink). Figure 5.29 displays the absolute change of the porosity depending on the strength of the acid. An acid solution of 5 vol-% causes a change of 0.45 % per dissolution step (seven steps measured). An acid solution of only 2.5 vol-% causes a change of 0.35 % per dissolution step and an acid solution of 10 vol-% causes a change of 0.58 %, but both cases include less measured dissolution steps with 3 and 2 dissolution steps, respectively.

Surface area related to the mass Figure 5.30 a shows the change of S_m for the different dissolution steps including a set of 10 samples. After the first dissolution step, the median S_m increases from $S_\mathrm{m\,S0} = 5.095\,\mathrm{m}^2{\cdot}\mathrm{g}^{-1}$ to $S_\mathrm{m\,S1} = 5.333\,\mathrm{m}^2{\cdot}\mathrm{g}^{-1}$. In the following dissolution steps, a decrease of S_m can be observed. Median S_m decreases to $S_\mathrm{m\,S2} = 5.331\,\mathrm{m}^2{\cdot}\mathrm{g}^{-1}$ at S2 and to $S_\mathrm{m\,S3} = 5.103\,\mathrm{m}^2{\cdot}\mathrm{g}^{-1}$ at S3. The relative percentage change of S_m between different dissolution steps is displayed in Figure 5.30 b. The first dissolution (S0 - S1, green) shows the highest positive percentage change with a median value of 7.4 %. The first two dissolution steps (S0 - S2) and the first three dissolution steps (S0 - S3) have a lower increase of 6.2 % (red) and 2.4 % (blue), but are mainly influenced by the high increase of S_m during the first dissolution step. The comparison of two consecutive dissolution

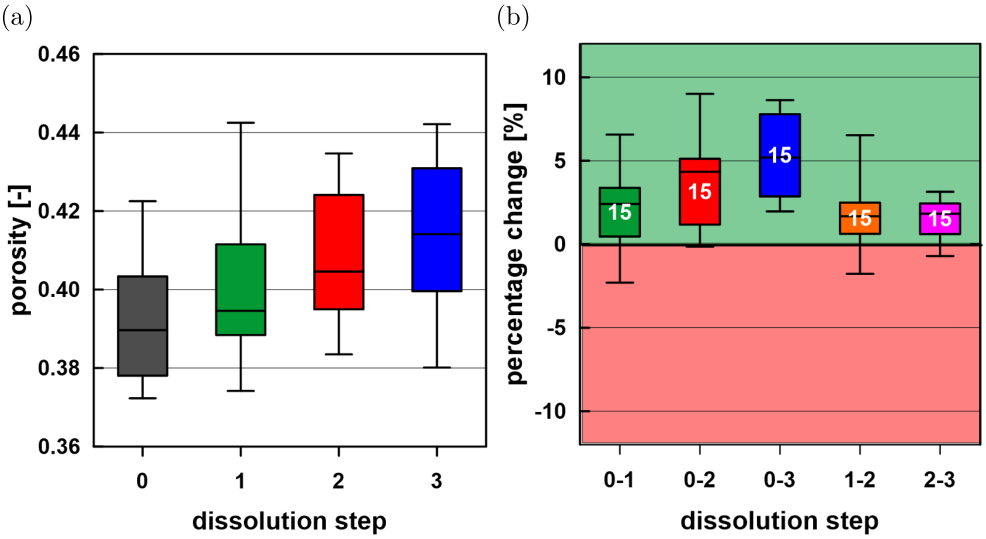

Figure 5.28: Results of porosity data of three dissolution steps are shown in box-and-whisker plots. a) Comparison of the absolute porosity including 15 samples. b) Comparison of the relative percentage change of the porosity between different dissolution steps. The white coloured number refers to the number of included samples.

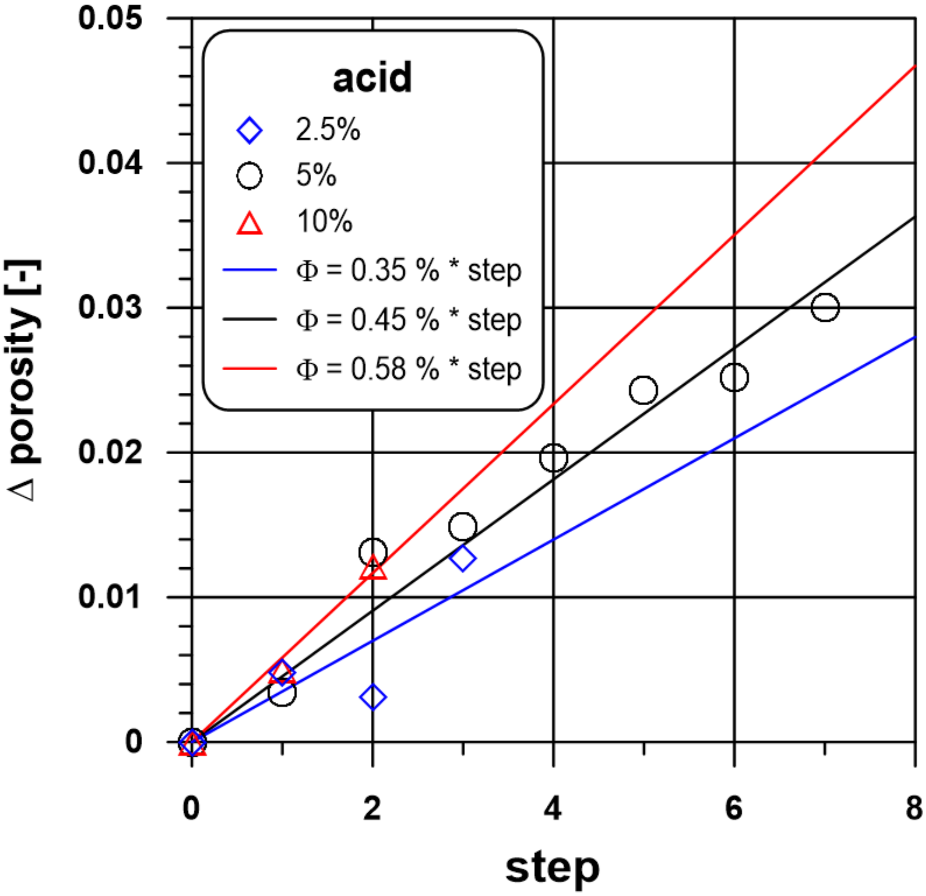

Figure 5.29: The absolute change of the porosity in relation to the dissolution step depending on the strength of the acid solution.

steps shows that the first dissolution causes an increase, whereas the following dissolution steps cause a decrease of S_{m} by 2 % (orange) and 6.8 % (pink).

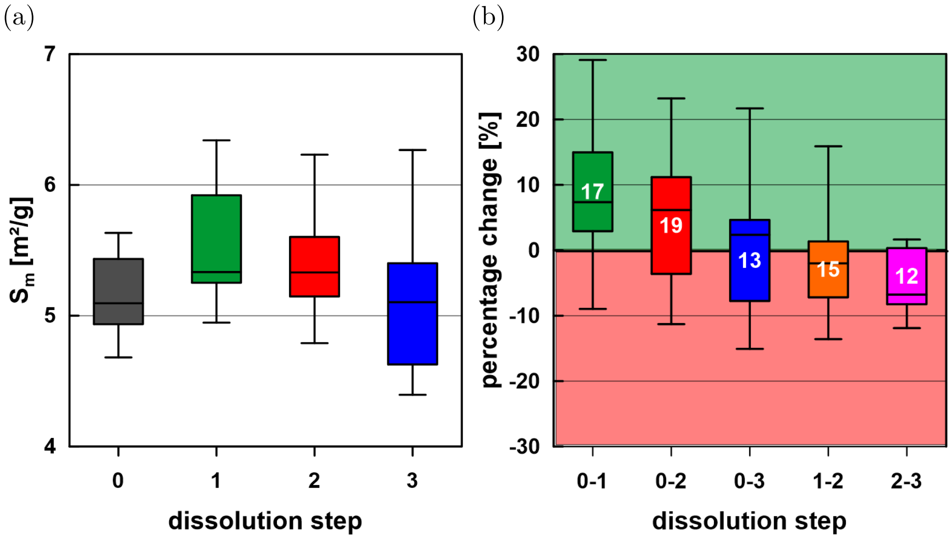

Figure 5.30: Results of the surface area related to the mass changes within three dissolution steps are shown in box-and-whisker plots. a) Comparison of the absolute S_{m} including 10 samples. b) Comparison of the relative percentage change of the S_{m} between different dissolution steps. The white coloured number refers to the number of included samples.

Surface related to pore volume Figure 5.31 a shows the changes of S_{por} for different dissolution steps including a set of 10 samples. The parameter S_{por} depends on density, porosity and S_{m}, and is calculated by using Equation 3.17. After the first dissolution, the median S_{por} value increases from $S_{\mathrm{por\,S0}} = 22.71$ to $S_{\mathrm{por\,S1}} = 23.33\,\mu\mathrm{m}^{-1}$. During the following dissolution steps, a decrease of S_{por} can be observed. The median S_{por} value decreases to $S_{\mathrm{por\,S2}} = 21.27\,\mu\mathrm{m}^{-1}$ at S2 and to $S_{\mathrm{por\,S3}} = 20.24\,\mu\mathrm{m}^{-1}$ at S3. The relative percentage change of S_{por} between different dissolution steps is displayed in Figure 5.31 b. A positive percentage change of the majority of the treated samples is only visible for the first dissolution (+3.6 %, green). Considering the first two (S0 - S2) and the first three dissolution steps (S0 - S3) a decrease of the median value of about 2 % (red) and 5.5 % (blue). The comparison of two consecutive dissolution steps shows that the first dissolution (S0 - S1) causes an increase, while the following steps cause a decrease of S_{por} by 5.4 % (S1 - S2, orange) and 4.1 % (S2 - S3, pink).

Table 5.7 summarises the variations of petrophysical parameters during dissolution as well as the changes of dominant pore radii and IP parameters.

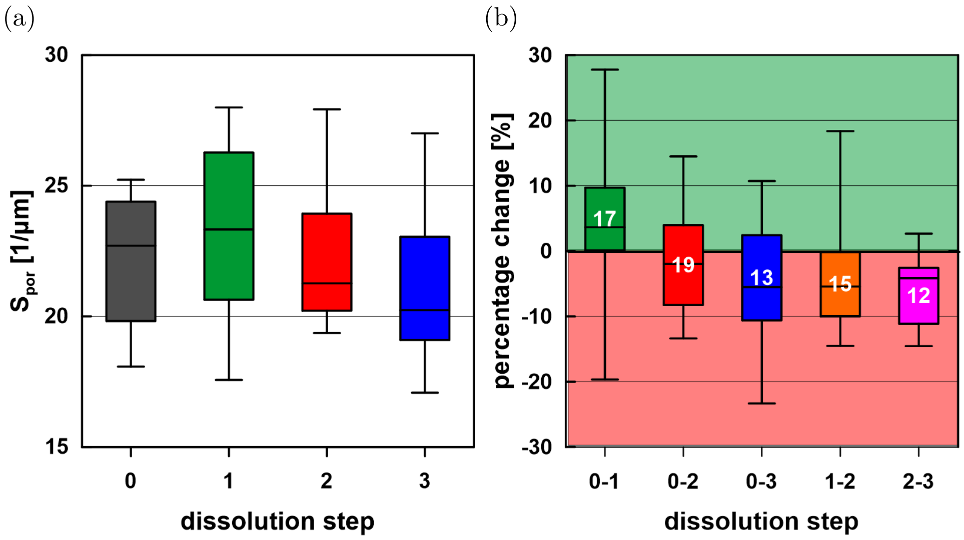

Figure 5.31: Results of the surface area related to the changing pore volume during three dissolution steps are shown in box-and-whisker plots. a) Comparison of the absolute S_{por} including 10 samples. b) Comparison of the relative percentage change of the S_{por} between different dissolution steps. The white coloured number refers to the number of included samples.

Pore radius

NMR NMR measurements were carried out for all treated samples (Fig. A.16). Figure 5.32 shows T_2 curves for three selected samples during dissolution. In general, the characteristic T_2 distribution of the EBK is a bimodal distribution. The dominant peak is around a T_2 decay time of 60 ms, whereas the second peak varies highly in its characteristic and occurs at higher T_2 decay times. Figure 5.32 a shows a shift of the dominant peak to smaller T_2 times after each of the five dissolution steps, but the amplitude does not change systematically. The minimum between the two peaks is also shifted to smaller pores and the amplitude decreases. These observations can be adopted for the other samples in Figure 5.32 b, c and d. The dominant peak is shifted towards smaller T_2 times with increasing dissolution steps. The shift is clearly identifiable for the whole sample set and controlled by the dissolution. The amplitude of the peak is unaffected or rather a systematic alteration is undetectable. Smaller T_2 times mean smaller pores. The second peak has a variable amplitude during the dissolution steps, but no systematic of increase or decrease is visible. The shift of the second peak shows no unique behaviour with increasing dissolution steps.

Figure 5.33 summarises the qualitative observation of the T_2 signal during two dissolution steps. The dominant peak of the T_2 is around 60 ms for an untreated sample (black) and is shifted to a smaller T_2 time of 50 ms for a sample with one dissolution step and is shifted further to 40 ms after two dissolution steps (red

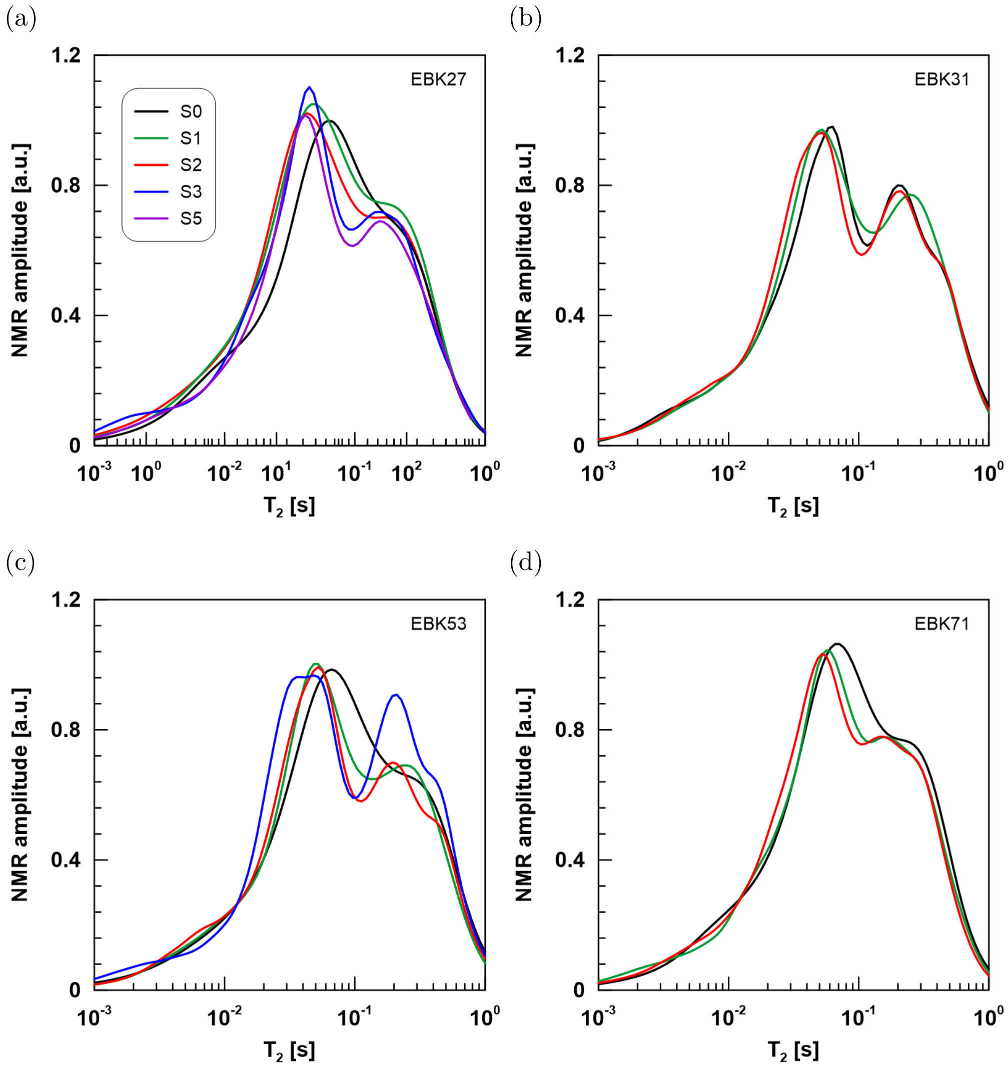

Figure 5.32: T_2 decay time spectra of four EBK samples during dissolution. a) Results of EBK27 for five dissolution steps. b) Results of EBK31 for three dissolution steps. c) Results of EBK53 for four dissolution steps. d) Results of EBK71 for three dissolution steps.

arrow). The purple circle shows the alteration of the second peak, which is not applicable for the whole sample set. However, the minimum between both peaks is also shifted towards smaller pores and the amplitude decreases. The assumed surface relaxivity of 100 μm·s^{-1} leads to a decrease of the pore radius of 12 μm to 8 μm.

MIP Figure 5.34 shows the pore throat radii distribution of EBK samples at different dissolution steps. Because MIP is an irreversible process, it is impossible to carry out MIP always for one sample after each dissolution step. Figure 5.34 a displays the MIP results of EBK17 after one dissolution step. A bimodal distribution is observed as for the untreated samples (Fig. 4.7). To simplify the reading comprehension in this section, the dominant peak is equivalent to mode 1 (r_1)

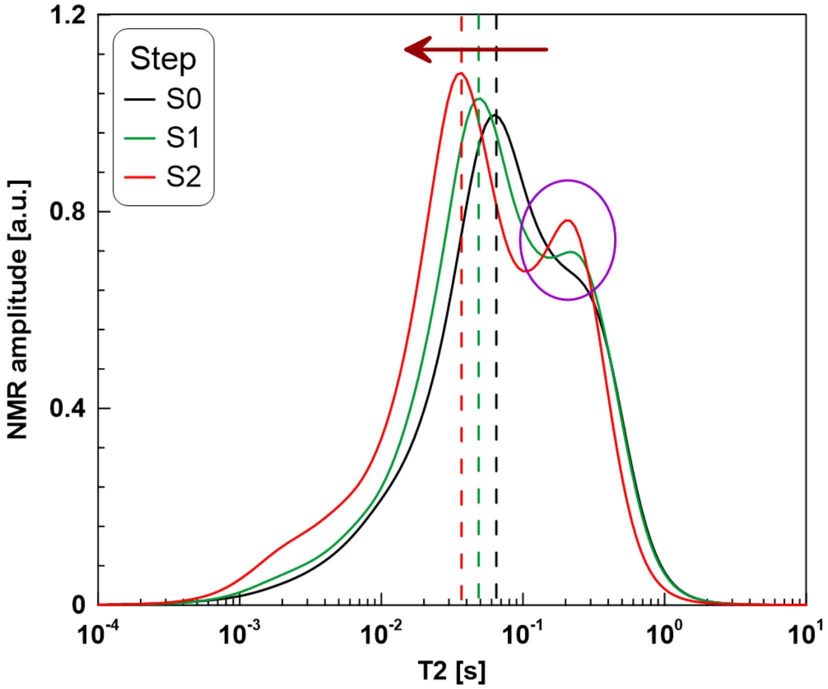

Figure 5.33: Qualitative T_2 decay time spectra of the EBK during dissolution.

and the second peak to mode 2 (r_2) The first mode is determined as $r_1 \approx 7\,\mu$m and the second mode is at $r_2 \approx 0.03\,\mu$m. The three curves correspond to the extraction point of the measured samples of EBK17: up (black), middle (red), and bottom (green). The differences in the amplitude between the curves result from the inhomogeneity of the sample itself. The porosity determined by MIP is $\Phi_{\text{up}} = 31.83\,\%$, $\Phi_{\text{middle}} = 38.28\,\%$, and $\Phi_{\text{bottom}} = 23.02\,\%$ which results in mean of $\Phi_{\text{mean}} = 31.04\,\%$. This mean is in good accordance to the porosity determined by TWM (30.39 %). The characteristic of the MIP curve is unaffected by inhomogeneity. Figure 5.34 b displays the MIP results of EBK16 after two dissolution steps. The observations made on EBK17 are transferable to EBK16. The first mode is determined as $r_1 \approx 8\,\mu$m and the second mode is at $r_2 \approx 0.03\,\mu$m. Figure 5.34 c displays the MIP results of EBK22 after two dissolution steps. The pore throat radii distribution is bimodal, as observed for all EBK samples. The first mode is determined by $r_1 \approx 8\,\mu$m and the second mode at $r_2 \approx 0.03\,\mu$m. A list of the pore throat radii is given in Table 5.6. The different values of one sample (up, middle, and bottom) regarding the pore throat distribution is similar to the variation caused by dissolution experiments. Thus, a general trend cannot be observed during acidification.

Figure 5.35 compares the representative pore throat distributions of the different dissolution steps. The first mode is in range of $6\,\mu$m to $8\,\mu$m, but no clear shift is

Table 5.6: Dominant pore throat radii of the bimodal distributions determined by MIP.

	EBK17	(S1)		EBK16	(S2)		EBK22	(S3)
r [μm]	up	middle	bottom	up	middle	bottom	up	bottom
(1)	7.34	6.56	7.34	7.34	8.21	8.21	8.24	8.22
(2)	0.033	0.030	0.019	0.042	0.030	0.030	0.030	0.030

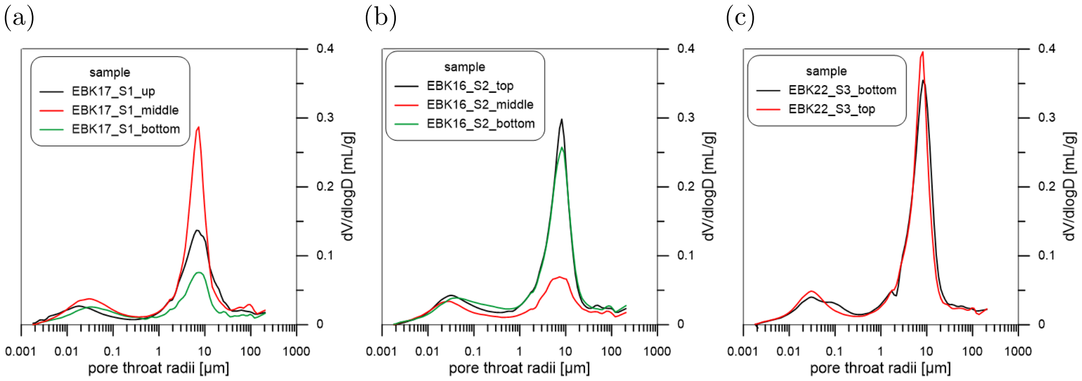

Figure 5.34: Pore throat radii distribution during dissolution determined by MIP. a) Results after one, b) two, and c) three dissolution steps.

detectable. The second mode of the bimodal distribution is between 0.02 μm and 0.07 μm. A comparison of the different dissolution steps shows a shift towards larger pore throat radii. The second mode of the untreated sample (black) is at $r_2 = 0.018\,\mu$m and increases to $r_2 = 0.030\,\mu$m for the samples after one (green), two (red), and three (blue) dissolution steps. The pore throat distributions of the first three dissolution steps are very similar to each other. A prove of the shift towards higher pore radii is obtained by one sample with eight dissolution steps (purple) and one sample with two dissolution steps using a 10 vol-% acid (orange). Both cases show a significant increase of the second mode to $r_2 = 0.074\,\mu$m (S8, purple) and $r_2 = 0.052\,\mu$m (10 vol-%, orange). Summing up, a clear change of the pore throat radius is observed in the small meso pore range (mode 2) and the number of small pores increases. The second mode increases in the meso pore range with progressive alteration process.

The observation of MIP results regarding the pore radii distribution at different dissolution steps can be confirmed and clarified by the MIP results of the systematic approach, as described in section 3.4. Figure 5.36 shows the pore radii distribution of the samples after different durations of dissolution. Mode 1 is slightly shifted towards larger pores and the pore volume increases with a longer duration of dissolution. A perfect chronological order is not achieved, but the general trend is clear. The second mode in the meso pore range is also shifted towards larger pores, as observed in Figure 5.35.

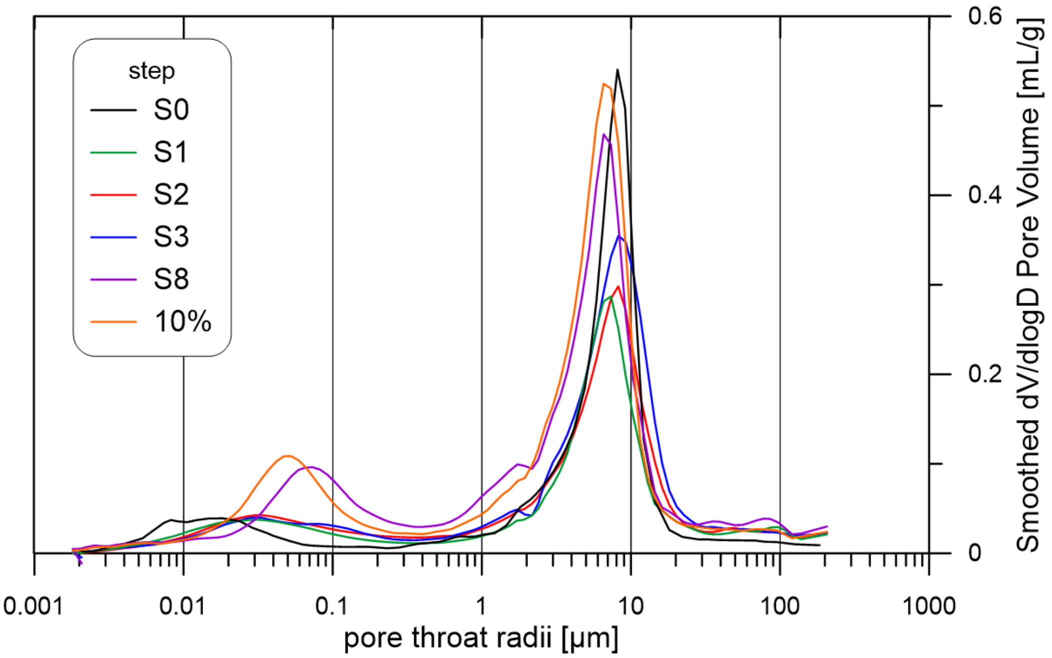

Figure 5.35: Pore throat radii distribution determined by MIP for dissolution step: S0 (black), S1 1 (green), S2 (red), S3 (blue), S8 (purple), and one sample at two dissolution steps using a stronger acid.

A better distinction between the dissolution durations provides the presentation in Figure 5.37, which displays the intrusion (solid line) and extrusion curves (dashed line) as cumulative pore volume depending on pressure respective pore radius. A general trend is observed: the pore volume increases with increasing duration of the dissolution. The comparability is given, since the measured material has the same initial sample weight for MIP.

μ-CT The analysis of the μ-CT data takes place on the specimens of the systematic approach, as described in section 3.4. Figure 5.38 shows the pore size distribution of the samples before and after the treatment. The number of points between the decades is 20 and the area below the curves corresponds to the porosity. The comparison of the untreated specimens explains the natural variation, which occurs within one sample (Fig. 5.38 a). The shape and the characteristics of the curves are similar, but the dominant pore radius varies slightly in the range of 45 μm to 63 μm. A significant change for the sample with 72 h dissolution can be observed due to the strong volume loss after dissolution (Fig. 5.38 b). Because of the strong volume loss, the representative elementary volume (REV) is too small for conclusive results. Hence, the result of the 72 h-sample will not be taken into account for further analysis. The comparison between untreated and treated samples suggests a slight shift of the dominant equivalent pore radii towards

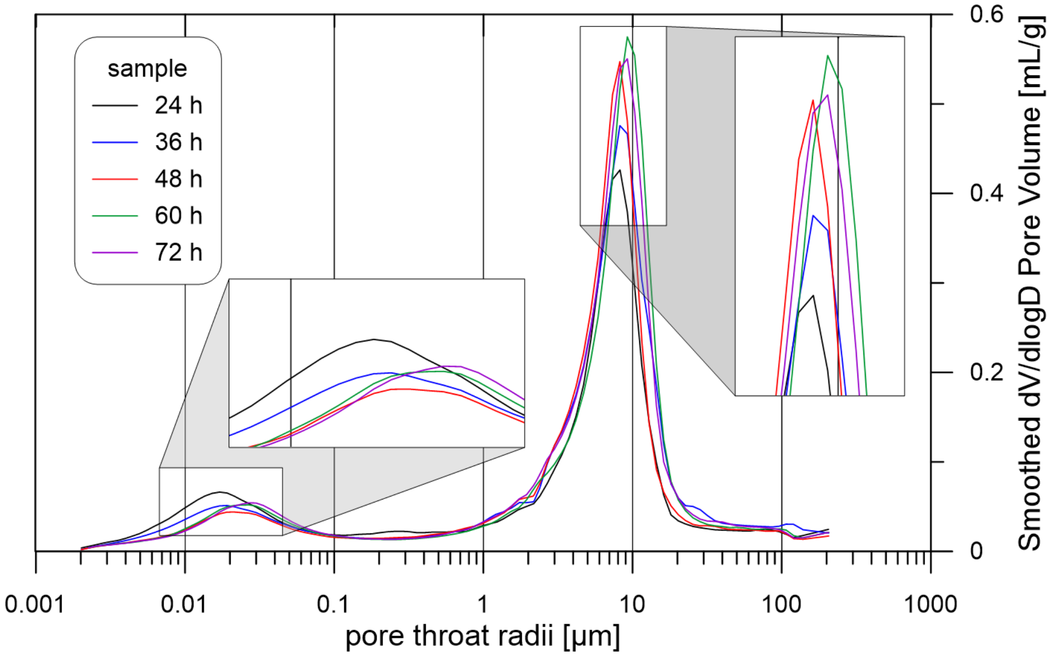

Figure 5.36: Pore throat radii distribution determined by MIP for different durations of dissolution: 24 h (black), 36 h (blue), 48 h (red), 60 h (green), and 72 h (purple). A zoom is inserted for a better interpretation of the two areas of interest.

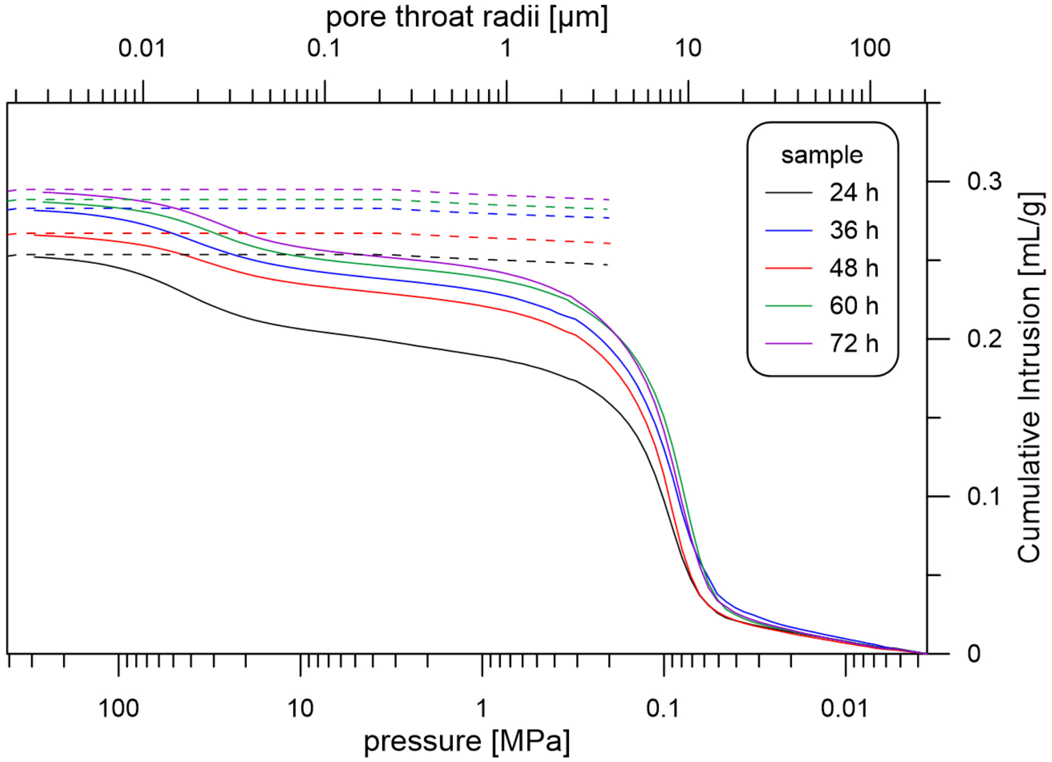

Figure 5.37: Pore throat radii distribution determined by MIP for different durations of dissolution: 24 h (black), 36 h (blue), 48 h (red), 60 h (green), and 72 h (purple). The solid lines display the intrusion curves referring to the pressure and pore radius. The dashed lines display the extrusion curves, which are referred to the pressure.

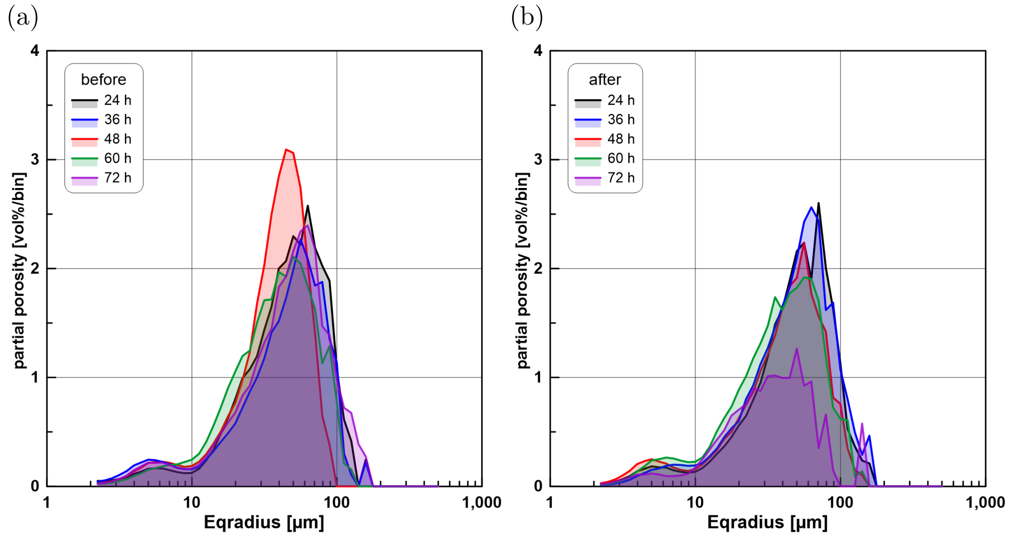

Figure 5.38: Equivalent pore radii distribution determined by μ-CT. a) Pore radii distribution of the five untreated specimens. b) Pore radii distribution of the five treated specimens for different dissolution durations: 24 h (black), 36 h (blue), 48 h (red), 60 h (green), and 72 h (purple).

higher radii. The comparison of the results of the single specimens before and after treatment is shown in (Fig. A.17). A list of the determined equivalent radii is compiled in Table B.18. For each sample the mean equivalent diameter increases after the dissolution process.

Figure 5.39 displays the percentage change of the pore volume between treated and untreated specimens. For comparison of the of the two μ-CT datasets, the values of the pore volume are standardised to the total volume. A decrease of the volume of the smallest pore can be observed for all four time-intervals as well as an increase of the volume of the largest pores. Because of the steep pore radii distribution, as shown in Figure 5.38, no significant change is visible in the range of 10 - 55 μm corresponding to the left slope of the dominant peak.

For a better comparison, three pore radii intervals are determined: 2 - 10 μm, which describes the range of the second dominant pore radius, 10 - 55 μm, which describes the left slope of the first dominant pore radius, and 55 - 128 μm, which describes the slope to the right of the first dominant pore radius. An approximation for all specimen is an average first dominant pore radius of 55 μm. The different pore sizes are evenly distributed in the sample and no clustering of the different pore radii segments can be observed (Fig. A.18). Hence, the representativeness of the samples is ensured. Figure 5.40 shows histograms for the different pore radii segments comparing the percentage of change for the pore volume at different

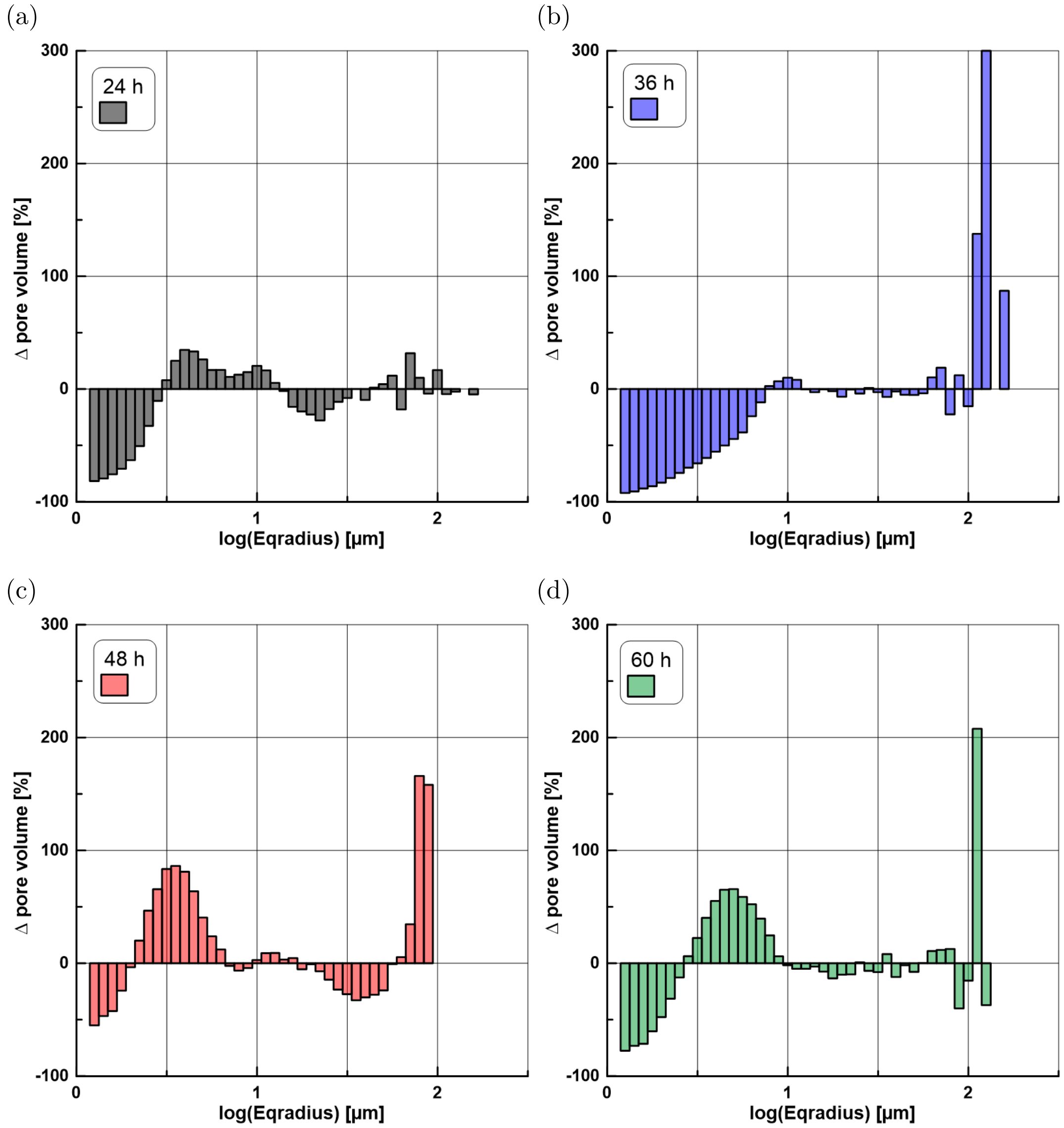

Figure 5.39: Relative pore volume change between one dissolution step for different durations. a) Pore volume change of the sample with 24 h dissolution. b) Pore volume change of the sample with 36 h dissolution. c) Pore volume change of the sample with 48 h dissolution. d) Pore volume change of the sample with 60 h dissolution.

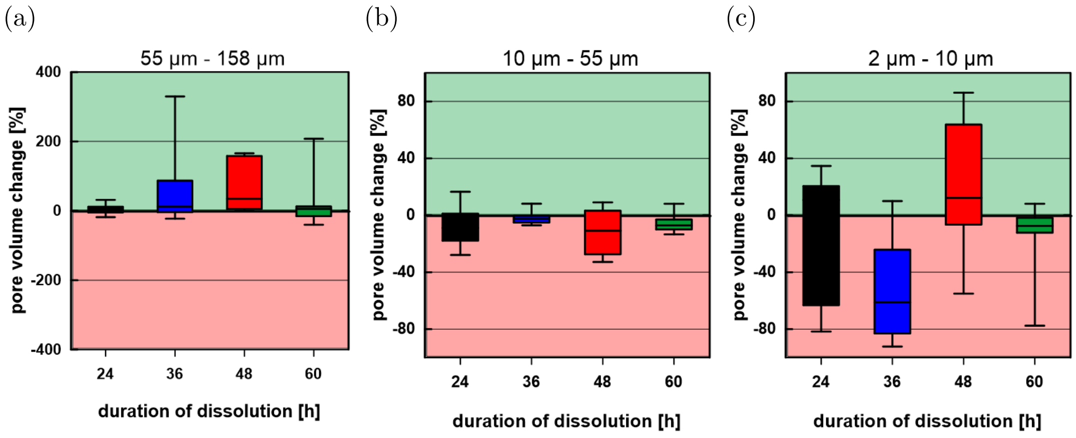

Figure 5.40: Relative pore volume change for a sample before and after dissolution for different duration of dissolution. a) Relative change for pore radii larger than 55 μm. b) Relative change for pore radii between 10 μm and 55 μm. c) Relative change for pore radii smaller than 10 μm.

dissolution times. For pores with a radius larger than 55 μm, the dissolution causes a significant increase of the pore volume until a dissolution duration of 48 h (Fig. 5.40 a). The median value increases from 2.4 % (24 h, black) to 12.1 % (36 h, blue) and to 34.6 % (48 h, red). The increase of the median value (+ 5.5 %) is significantly lower for the longest duration of dissolution (60 h, green) compared to 48 h of dissolution. The volume of the pores in the range of 10 - 55 μm decreases slightly (Fig. 5.40 b), which is caused by the shift of the dominant pore radius to larger pores radii, as shown in Figure A.17. Because of the steep distribution, no extensive change is expected. The maximum pore volume decrease is smaller than 40 % and the median value is between -2.5 % and 11 % for all durations of dissolution. For pores of the second peak, the relative change implies a decrease except for the specimen with a dissolution duration of 48 h (Fig. 5.40 c).

Table 5.7 summarises the variations of dominant pore radii during dissolution as well as the changes of petrophysical parameters and IP parameters.

Pore-shape analysis

A shape analysis of the pores for Feret caliper geometries is done, as described in Schmitt et al. (2016) and Halisch et al. (2016). The pore shape classification for rounded objects is based on Zingg (1935) and modified by Blott & Pye (2008), as shown in Figure 5.41 a. The pore type classification depends on the ratio of the longest (L), intermediate (l), and the shortest (S) pore dimension. The 'flatness' increases with smaller S/l (thickness) ratio as well as the length increases with decreasing l/L ratio (elongation). The results of the shape analysis of the untreated samples is given in Figure 5.41 b. The mean values of the ratio l/L

varies from 0.70 to 0.72 and the ratio S/l varies from 0.75 to 0.79. The values indicate slightly elongate and slightly flat pore shapes, which can be described as a sub-equant spheroid. After treatment the pores seem to be longer and thicker (Fig. 5.41 c).

For better analysability pore distributions are divided into small ($r < 10\,\mu$m) and large pores ($r > 10\,\mu$m). Figure 5.42 shows the pore-shape classification for the different durations of dissolution for the small and the large pores. For the durations of 24 h (Fig. 5.42 a), 36 h (Fig. 5.42 b) and 60 h (Fig. 5.42 d), a significant shift to longer and thicker pore shapes can be observed. The shape varies from a sub-equant spheroid to a prolate spheroid. The observation can be made for the small pores as well as for the large pores. For the small pores, the mean values of the l/L ratio decreases from ~ 0.72 to 0.64 and the mean values of the S/l ratio increases from ~ 0.79 to ~ 0.87. The mean values of the large pores shows similar values. The l/L ratio decreases from ~ 0.71 to $\sim$0.57 and the mean values of the S/l ratio increases from ~ 0.77 to ~ 0.88. It seems that the larger pores are slightly more influenced in their lengths as the small pores. Figure 5.42 c shows no significant change of the shape. The results of the pore shape analysis are discussed in section 6.2.2.

5.3.3 Complex electrical conductivity

In total, 24 samples, treated with 5 vol-% acid, were measured by using SIP: five samples with one dissolution step, seven samples with two dissolution steps, ten

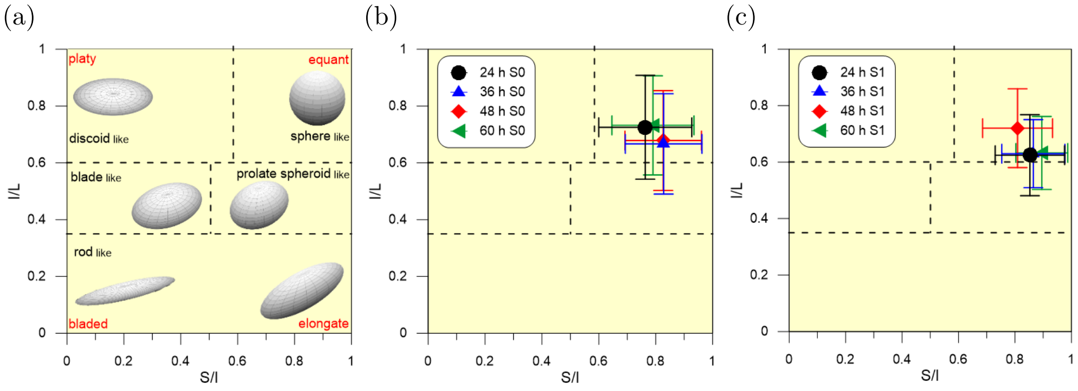

Figure 5.41: Pore type classification is based on the ratio of the longest (L), intermediate (l), and the shortest (S) pore dimensions. a) Principle pore types. b) Analysis results of the untreated specimens. The mean value of the respective specimen and the calculated standard deviation is plotted. b) Analysis results of the treated specimens. The mean value of the respective specimen and the calculated standard deviation is plotted.

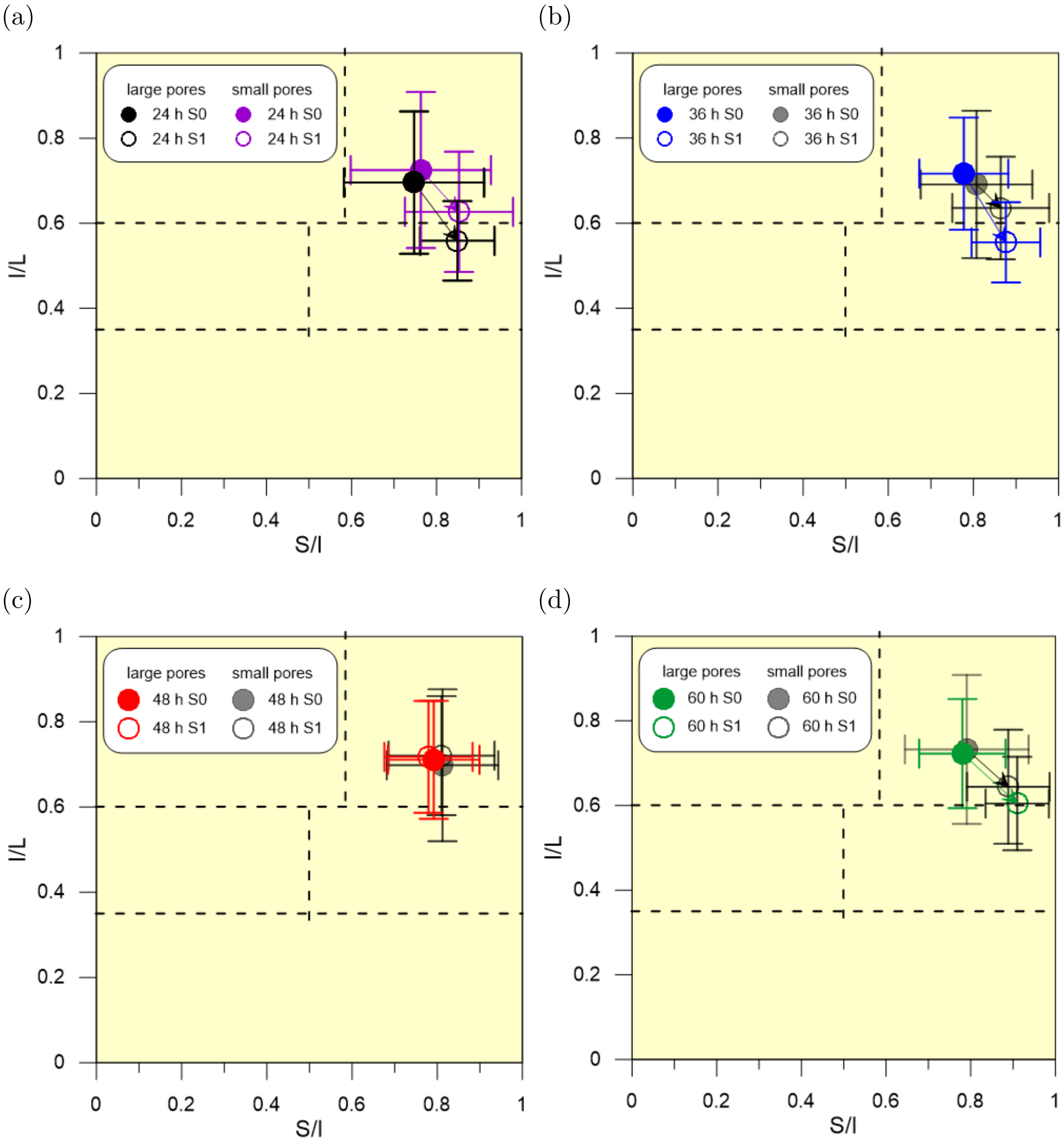

Figure 5.42: Pore type classification based on the ratio of the longest (L), intermediate (l), and the shortest (S) pore dimensions. The mean value of the respective specimen and the calculated standard deviation is plotted. The dataset is divided in small ($r < 10\,\mu$m) and large pores ($r > 10\,\mu$m). Pore-shape results of a) the24 h treated specimens, b) the 36 h treated specimens, c) the 48 h treated specimens, and d) the 60 h treated specimens.

samples with three dissolution steps and two samples with four dissolution steps. In addition, two special cases were investigated: one sample with eight dissolution steps using SIP at dissolution step S0, S4, and S8 and one sample, which was acidized with 10 vol-% acid.

IP spectra

Due to increasing porosity with successive dissolution steps, as seen in Figure 5.28, a higher real part of conductivity with successive dissolution steps is an obvious expectation of the SIP measurement. Considering the IP spectra relating to the real part of conductivity, the following observation can be made: an increasing real part of conductivity with successive dissolution steps can be observed for 11 samples. Six samples show increasing real parts of conductivity with increasing dissolution step including one outlier from the expected order. Two samples hardly show a change during dissolution and five samples do not fit the expected order of an increasing real part of conductivity with successive dissolution step. Considering the spectra of the single samples with only three or four dissolution steps, it is difficult to figure out a general trend. Figure 5.43 and Figure 5.44 display the IP spectra of both special cases to get information about the impact on IP-data with stronger and progressive dissolution. The sample EBK43 was acidized using an acid twice as strong as for the other samples, and it was measured at S0 (black) and S1 (green) using SIP. The spectrum of the real part of conductivity increases with successive dissolution (red arrow) (Fig. 5.43 a). Considering the imaginary part of conductivity, a typical peak behaviour of σ'' can be observed, which is typical for the EBK (Fig. 5.43 b). A comparison between the dissolution steps suggests a slight shift and decrease of the σ''-peak after dissolution. In addition, an overlap of the two spectra at the right side of the maximum and an associated increase of σ'' (red arrow) at higher frequencies (10 - 100 Hz) are observed. The same observations are made for the sample EBK28, which was acidized eight times during SIP measurements at S0 (black), S4 (green), and S8 (red) (Fig. 5.44). The real part of the conductivity increases with successive dissolution steps (red arrow). The maximum value and the peak frequency of σ''-peak stays constant during continuous dissolution. An overlap of the spectra can be observed at a frequency of 1 Hz and σ'' increases significant at higher frequencies, as shown for the sample EBK43.

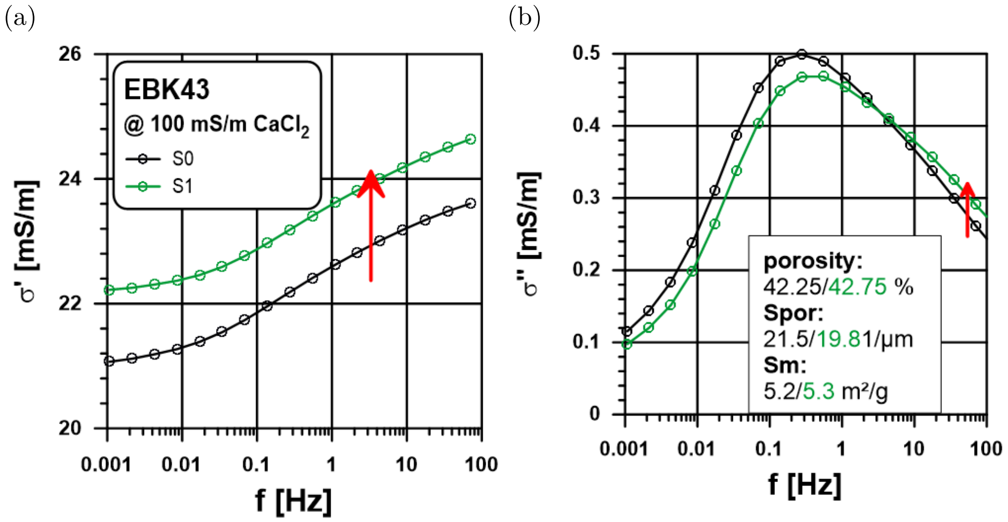

Figure 5.43: IP spectra of the EBK43 for S0 (black) and S1 (green). The sample was acidized with an acid of 10 vol-%. The red arrows indicate an increase with progressive dissolution. The box displays the color-coded petrophysical parameters during dissolution. a) Variation in the real part of conductivity spectra with progressive dissolution. b) Variation in quadrature conductivity spectra with progressive dissolution.

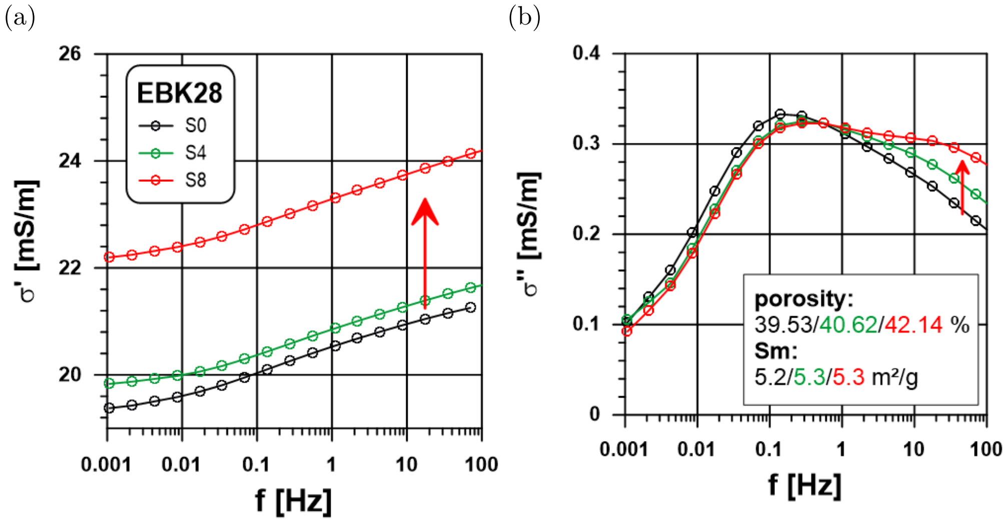

Figure 5.44: IP spectra of the EBK28 for S0 (black), S4 (green), and S8 (red). The red arrows indicate an increase with progressive dissolution. The box displays the colour-coded petrophysical parameters during different dissolution steps. a) Variation in the real part of conductivity spectra with progressive dissolution. b) Variation in quadrature conductivity spectra with progressive dissolution.

Box-and-whisker plots

The evaluation of single IP spectra is challenging. Therefore, it is realised using box-and-whisker plots. Each box-and-whisker plot includes only samples, which have three consecutive dissolution steps to ensure a better comparability. This condition is applied to 11 samples. Figures 5.45, 5.46, 5.47, 5.48, 5.49, and 5.50 display box-and-whisker plots for several IP parameters as real part of conductivity σ', imaginary part of conductivity σ'', phase shift φ, peak frequency f_{peak}, predicted formation factor F_{corr}, surface conductivity σ_{surf}, total chargeability m_{tot}, mean relaxation time τ_{mean}, and normalised chargeability m_{n}.

Real part of conductivity The real part of conductivity at a frequency of 1 Hz increases with successive dissolution steps (Fig. 5.45 a), as shown for the spectra of single samples. The median of $\sigma'(1\,\mathrm{Hz})$ increases from $\sigma'_{\mathrm{S0}} = 19.94\,\mathrm{mS{\cdot}m^{-1}}$ of the untreated samples (black) to $\sigma'_{\mathrm{S1}} = 20.36\,\mathrm{mS{\cdot}m^{-1}}$ (S1, green), to $\sigma'_{\mathrm{S2}} = 20.50\,\mathrm{mS{\cdot}m^{-1}}$ of (S2, red), and to $\sigma'_{\mathrm{S3}} = 21.38\,\mathrm{mS{\cdot}m^{-1}}$ (S3, blue). Three dissolution steps accumulate an increase of about $1.44\,\mathrm{mS{\cdot}m^{-1}}$. The relative percentage change of σ' between different dissolution steps is displayed in Figure 5.45 b. The majority of the sample set shows a positive percentage change of the porosity. The positive percentage change increases with each additional dissolution step: the increase of the median value is about 0.55 % from S0 to S1 (green), about 0.47 % from S0 to S2 (red), and about 1.7 % from S0 to S3 (red) including 11 samples. A comparison of the percentage change of two consecutive dissolution steps shows also an increase for σ': the first step triggers a median percentage change of 0.55 % and the following steps a median percentage change of 1.15 % (orange) and 0.38 % (pink).

Imaginary part of conductivity Figure 5.46 a shows the changes of the imaginary part of conductivity at a frequency of 1 Hz during continuous dissolution. No discernible trend could be observed for σ'' during dissolution. After the first dissolution, median σ'' increases from $\sigma''_{\mathrm{S0}} = 0.331\,\mathrm{mS{\cdot}m^{-1}}$ to $\sigma''_{\mathrm{S1}} = 0.334\,\mathrm{mS{\cdot}m^{-1}}$. In the following dissolution step, a decrease to $\sigma''_{\mathrm{S3}} = 0.329\,\mathrm{mS{\cdot}m^{-1}}$ can be observed. The imaginary part of conductivity is rather consistent. Considering the imaginary part of conductivity at the peak frequency, the same observation can be made as for σ'' at $f = 1\,\mathrm{Hz}$ (Fig. 5.46 b). The values are nearly constant during the dissolution. The median $\sigma''(\mathrm{f_{peak}})$ varies between $\sigma''_{\mathrm{S0}} = 0.357\,\mathrm{mS{\cdot}m^{-1}}$ of the untreated samples (black), $\sigma''_{\mathrm{S1}} = 0.365\,\mathrm{mS{\cdot}m^{-1}}$ (S1, green), $\sigma''_{\mathrm{S2}} = 0.358\,\mathrm{mS{\cdot}m^{-1}}$ of (S2, red), and $\sigma''_{\mathrm{S3}} = 0.370\,\mathrm{mS{\cdot}m^{-1}}$ (S3, blue). Figure 5.46 c validates the observation of an increase of σ'' at higher frequencies, as seen at the spectra of EBK43

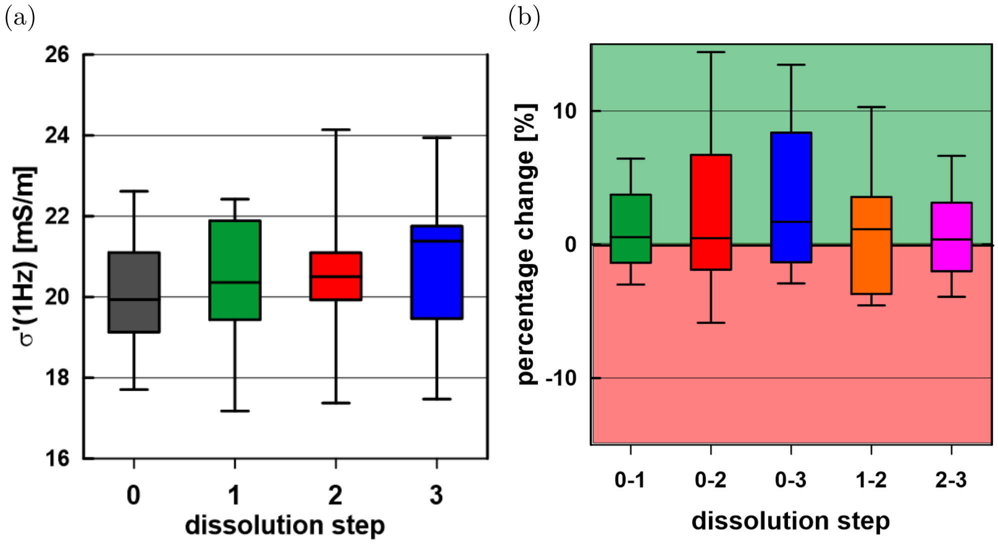

Figure 5.45: Variation of the real part of conductivity σ' at a frequency of 1 Hz during dissolution. a) Comparison of the absolute value of σ' including 11 samples. b) Comparison of the relative percentage change of σ' between different dissolution steps including 11 samples.

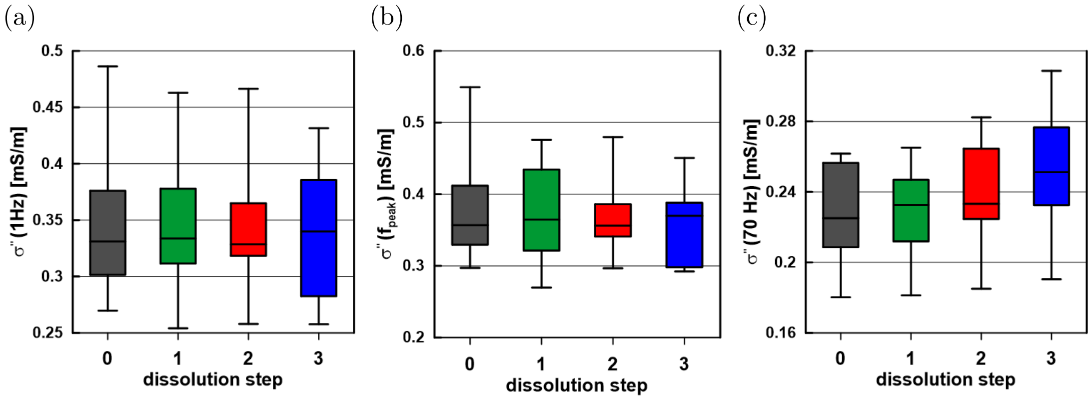

Figure 5.46: Variation of the imaginary part of conductivity at different frequencies for S0 (black), S1 (green), S2 (red), and S3 (blue). a) Variation of σ'' at a frequency of 1 Hz. b) Variation of σ'' at a the peak frequency. c) Variation of σ'' at a frequency of 70 Hz.

and EBK28 in Figure 5.43 and Figure 5.44. An increase of σ'' at 70 Hz is observed during dissolution and confirms the observation on the single sample for the whole sample set. The median σ''(70 Hz) increases from $\sigma''_{S0} = 0.225\,\mathrm{mS{\cdot}m^{-1}}$ (S0, black) to $\sigma''_{S3} = 0.251\,\mathrm{mS{\cdot}m^{-1}}$ (S3, blue). The comparison of the interquartile range of each dissolution step shows clearly the increase as well.

Phase shift Figures 5.47 a and b display the changes of the phase for the frequency of 1 Hz and the peak frequency during dissolution. A slight decrease of the phase shift can be observed for both frequencies. The median phase shift at a frequency of 1 Hz decreases from $\varphi_{S0} = 16.3$ mrad (S0) to $\varphi_{S3} = 15.9$ mrad (S3), which corresponds to a change of 0.4 mrad. The absolute change of the

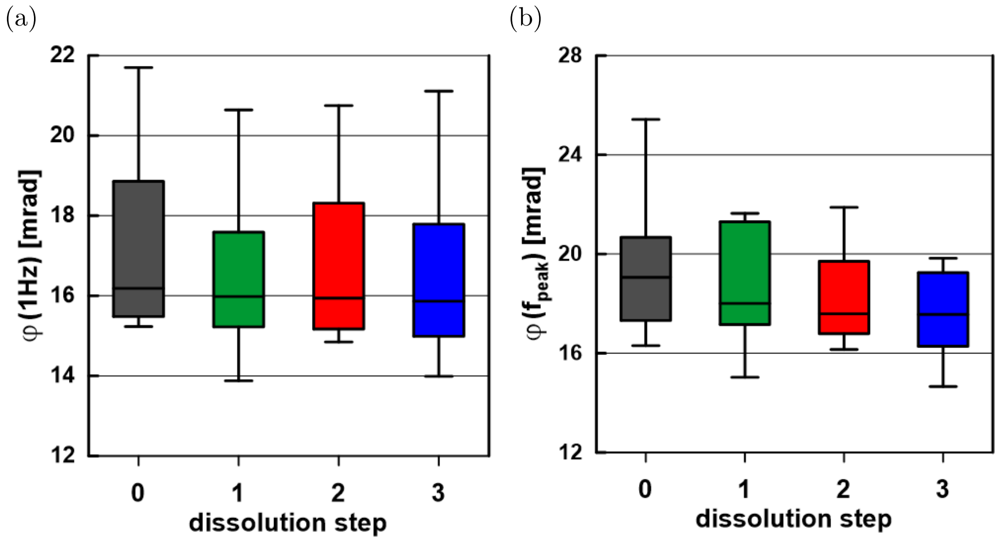

Figure 5.47: Variation of the phase shift at different frequencies for S0 (black), S1 (green), S2 (red), and S3 (blue). a) Variation of φ at a frequency of 1 Hz. b) Variation of φ at the peak frequency.

phase shift after three dissolution steps is very close to the resolution limit of the measurement device and is equivalent to the measuring inaccuracies because of new installation (geometry factor) and daily variances. The median phase shift at a peak frequency decreases from $\varphi_{\mathrm{S0}} = 19.1$ mrad (S0) to $\varphi_{\mathrm{S3}} = 17.6$ mrad (S3), but from the S2 to S3 the absolute change is smaller than 0.05 mrad.

Peak frequency The distribution of peak frequencies in phase spectra and spectra of the imaginary part of conductivity during dissolution is shown in Figures 5.48 a and b. Unfortunately, the information value is less, because of the regular wide frequency space of the SIP measurement. The histograms include only four different frequencies in a range of 0.07 to 0.55 Hz. It seems to be a slight shift of the peak towards higher frequencies, but the frequency grid is too coarse for a significant trend.

Formation factor & surface conductivity The formation factor is calculated by Equation 2.25 using the IP data and the factor l of the carbonates. Figure 5.49 a displays the formation factor derived by IP data for S0 to S3. A slight decrease can be observed during dissolution. The median of the formation factor decreases from $F_{\mathrm{S0}} = 14.9$ (S0) to $F_{\mathrm{S1}} = 14.5$ (S1), to $F_{\mathrm{S2}} = 14.2$ (S2), and to $F_{\mathrm{S3}} = 13.7$ (S3). The surface conductivity σ_{surf} is determined using the predicted formation factor in Equation 2.25. The calculated values during dissolution are summed up in a histogram (Fig. 5.49 b) The median decreases from $\sigma_{\mathrm{surf\,S0}} = 2.84\,\mathrm{mS\cdot m^{-1}}$ (S0) to $\sigma_{\mathrm{surf\,S1}} = 2.77\,\mathrm{mS\cdot m^{-1}}$ (S1), to $\sigma_{\mathrm{surf\,S2}} = 2.76\,\mathrm{mS\cdot m^{-1}}$

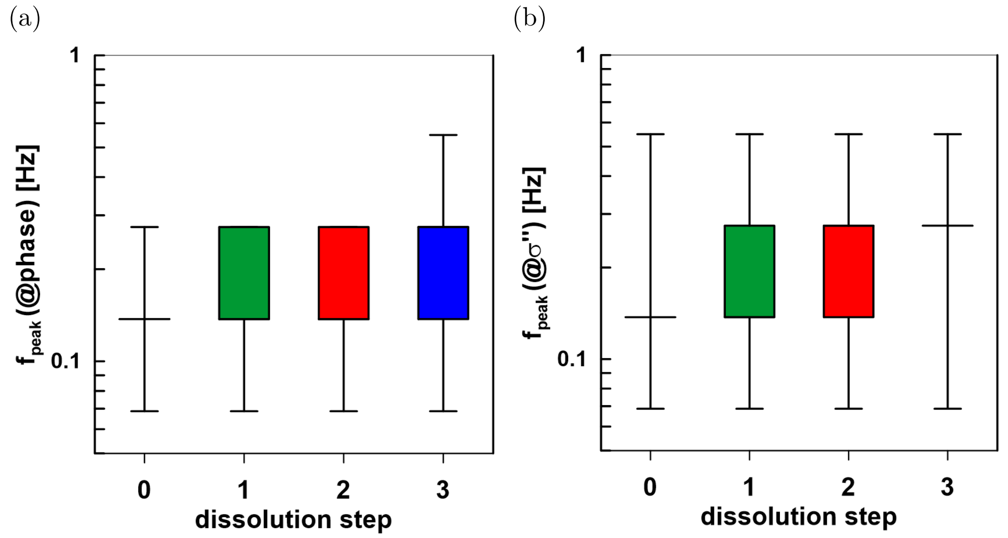

Figure 5.48: Histograms of the variation of peak frequency for S0 (black), S1 (green), S2 (red), and S3 (blue). a) Variation of the peak frequency of the phase spectra. b) Variation of the peak frequency of σ'' spectra.

(S2), and to $\sigma_{\mathrm{surf\,S3}} = 2.74\,\mathrm{mS{\cdot}m^{-1}}$ (S3). The changes in the median are very small and a comparison of the interquartile range of each dissolution step shows no trend.

Debye parameter Figures 5.50 a, b, and c display IP parameters derived by Debye decomposition. For the dependency of the chargeability from successive dissolution, no continuous increase or decrease can be observed (Fig. 5.50 a). The first two dissolution steps imply a decrease from $m_{\mathrm{DD_{S0}}} = 0.110$ (S0, black) to $m_{\mathrm{DD_{S2}}} = 0.105$ (S2, red), but after the third dissolution step m_{DD} increases to $m_{\mathrm{DD_{S3}}} = 0.110$. Thus, m_{DD} is constant during dissolution. Considering the normalised chargeability, the median m_{n} varies randomly and a general trend cannot be observed (Fig. 5.50 b). The variation of the relaxation time during the dissolution is shown in Figure 5.50 c. The median relaxation time decreases from $\tau_{\mathrm{S0}} = 0.16\,\mathrm{mS{\cdot}m^{-1}}$ (S0, black), to $\tau_{\mathrm{S1}} = 0.15\,\mathrm{mS{\cdot}m^{-1}}$ (S1, green), to $\tau_{\mathrm{S2}} = 0.13\,\mathrm{mS{\cdot}m^{-1}}$ (S2, red), and to $\tau_{\mathrm{S3}} = 0.13\,\mathrm{mS{\cdot}m^{-1}}$ (S3, blue). The decrease is also observed, while considering the interquartile range of different dissolution steps.

Table 5.7 summarises the variations of the IP parameter during dissolution as well as the changes of the petrophysical parameters and the dominant pore radii.

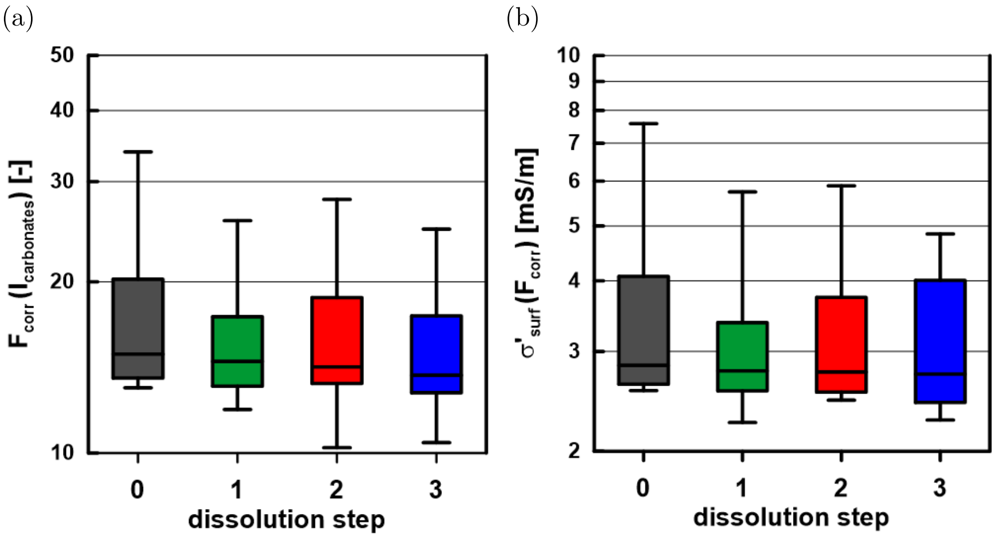

Figure 5.49: Variation of the formation factor and the surface conductivity for S0 (black), S1 (green), S2 (red), and S3 (blue). a) Variation of the formation factor F_{corr}. b) Variation of the surface conductivity σ'_{surf}.

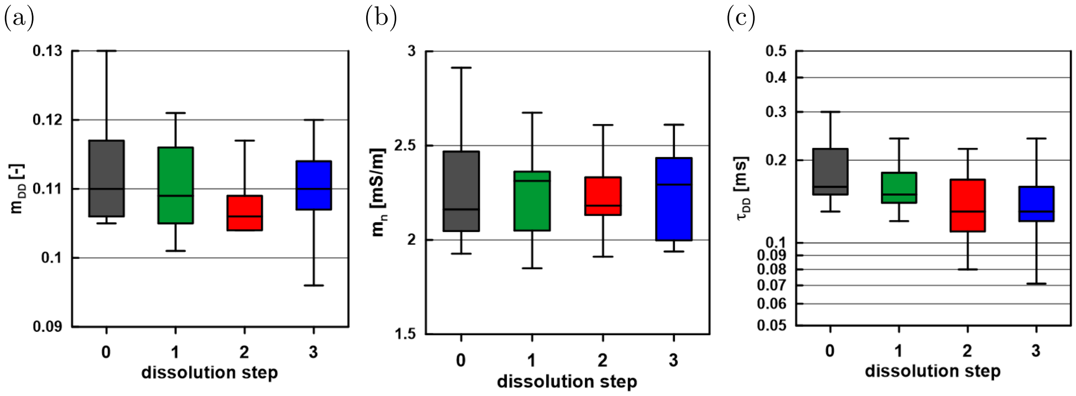

Figure 5.50: Variation of the Debye parameter for S0 (black), S1 (green), S2 (red), and S3 (blue). a) Variation of the chargeability m_{DD}. b) Variation of the normalised chargeability m_{n}. c) Variation of the relaxation time τ_{DD}.

Table 5.7: Variation of structural and IP parameters after dissolution. A big arrow represents significant changes, a small arrow indicates slight changes and an arrow in a bracket indicates minimal changes.

structural parameters

d_{gr}	Φ	S_{m}	S_{por}	r_{dom} (NMR)	r_{dom} (MIP)	r_{dom} (μ-CT)
↑	⇑	↑⇊	↑⇊	↓	↑	↑

IP parameters

σ'	σ'' (70 Hz)	φ	f_{peak}	F_{corr}	σ'_{surf}	m_{DD}	τ_{DD}
⇑	⇑	(↓)	(↑)	↓	↓	-	⇓

Cross plots

Besides spectra and histograms, cross plots of the porosity and the complex electrical conductivity are used to verify the observed behaviour of the IP parameters during dissolution. The porosity and the real part of conductivity are linked by Archie's Law (Eq. 2.11). Figure 5.51 a shows the relationship between porosity and the real part of conductivity ordered by samples. The connected points describe the behaviour of the porosity of one sample, while the arrows indicates continuing dissolution. The black solid line indicates the relation between porosity and real part of conductivity, which is given by all untreated EBK samples. The data points follow the general trend of untreated samples and an increase is visible. Data points of one sample do not show the same increase as the power law, because the measurement errors are too large in comparison to the occurring changes. Figure 5.51 b displays the relative changes of both parameters between different dissolution steps. The majority of the data points are in the first quadrant of the coordinate system implying an increase in porosity and the real part of conductivity.

Figure 5.52 shows the relationship between porosity and the imaginary part of conductivity. The relationship of all untreated samples is given by the black solid line (Fig. 5.52 a). It seems, that σ'' decreases with successive dissolution and the linear slope of the Φ - σ'' correlation is shifted to the right and down. Under the assumption that successive dissolution increases the porosity, this would

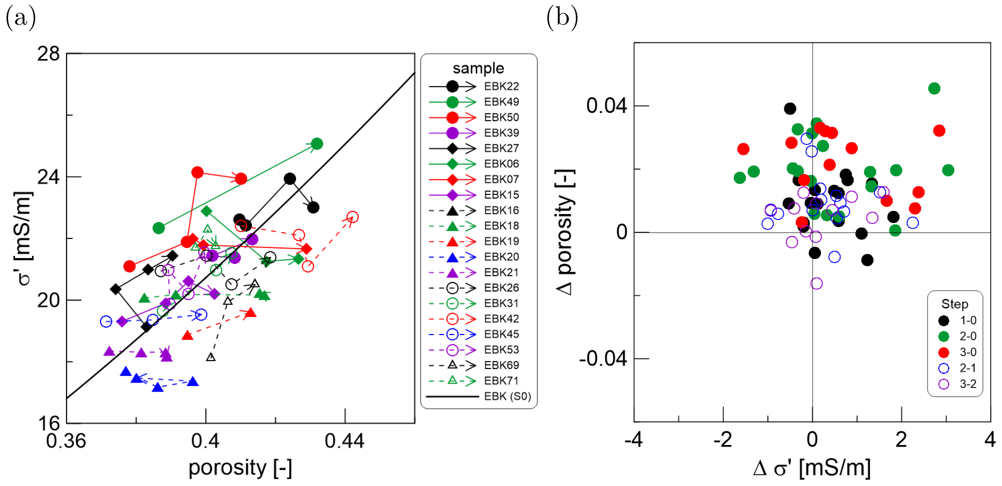

Figure 5.51: Relationships between porosity and real part of conductivity during dissolution. a) The connected points correspond to one sample, respectively and the arrow head points towards successive dissolution. The black solid line indicates the relationship between porosity and real part of conductivity for all untreated samples. b) Relative changes between the first (0-1, black), the first two (0-2, green), the first three (0-3, red), and two consecutive dissolution steps (1-2, blue; 2-3, purple).

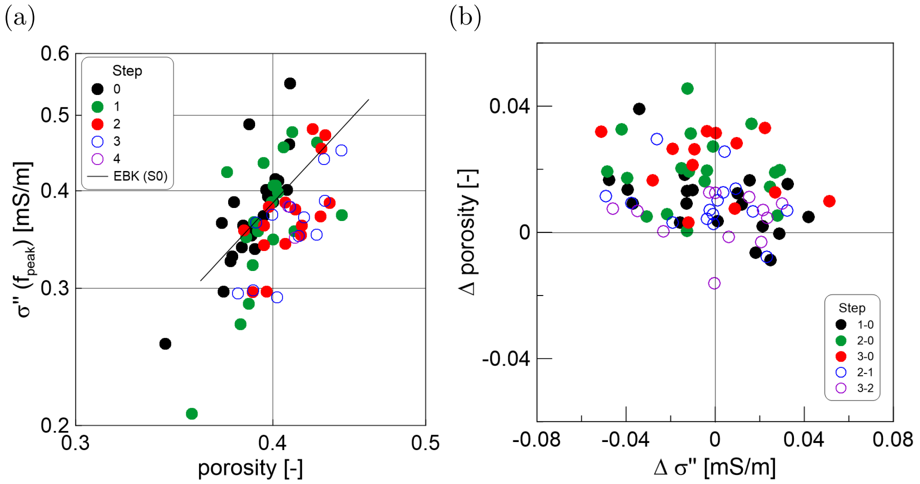

Figure 5.52: Relationships of porosity and imaginary part of conductivity during dissolution. a) The results of dissolution step 0 (black), step 1 (green), step 2 (red), step 3 (blue), and step 4 (purple). The black solid line indicates the relation between porosity and imaginary part of conductivity for all untreated samples. b) Relative changes between the first (0-1, black), the two first (0-2, green), the three first (0-3, red), and two consecutive dissolution steps (1-2, blue; 2-3, purple).

mean a decrease of σ'' with increasing porosity, in contrast to their relationship. Figure 5.52 b displays the relative changes of porosity and imaginary part of conductivity and does not confirm the previous observation. In case of a decrease of σ'' with increasing porosity, the data points should be located in the second quadrant of the coordinate system. Almost all data points are in the first or second quadrant, which indicates a clear increase of porosity. Between the first and the second quadrant the data points are distributed evenly and it is not possible to make a statement about the trend of σ''. Thus, the impact of dissolution on the imaginary part of conductivity is insignificant and the changes during dissolution are in the range of the measuring inaccuracy.

No correlation between porosity and phase shift can be observed, as shown in Figure 5.53 a. Figure 5.53 b shows the relationship of both parameters ordered by samples. The connected points describe the behaviour of one sample and the arrows show towards successive dissolution. A decrease of the phase shift with increasing porosity can be observed for each sample. The plot of the relative changes of porosity and phase shift confirms the observation (Fig. 5.53 c). The majority of the samples is located in the second quadrant of the coordinate system, which indicates an increase of porosity and a decrease of the phase shift.

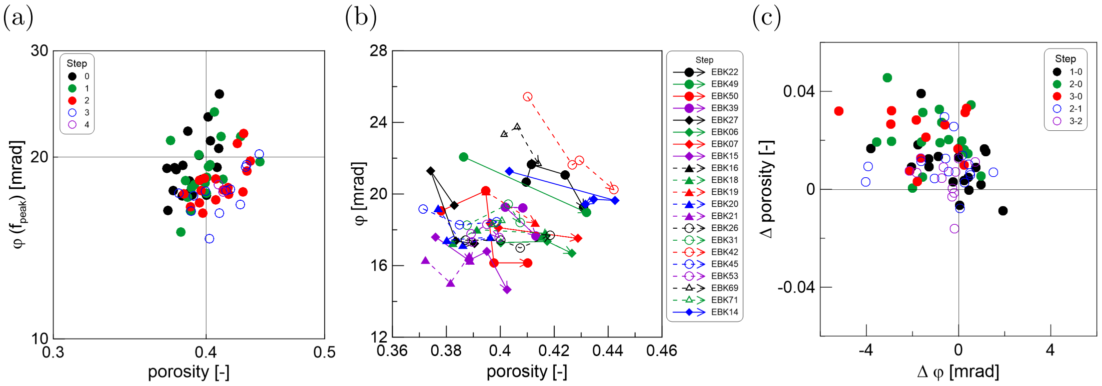

Figure 5.53: Relationships of porosity and phase shift of conductivity during successive dissolution. a) Results of S0 (black), S1 (green), S2 (red), S3 (blue), and S4 (purple). b) The connected points corresponds to one sample and the arrows show towards successive dissolution. c) Relative changes between the first (0-1, black), the two first (0-2, green), the three first (0-3, red), and two consecutive dissolution steps (1-2, blue; 2-3, purple).

6 Discussion

In the previous chapter, the main results of the methodical investigation of the complex electrical conductivity of carbonates, the dissolution experiments themselves and the changes of pore structure and IP behaviour during dissolution were presented. This chapter discusses the polarisation effects of carbonates as well as several approaches to explain the different phase behaviour. For the discussion, an additional dataset of Egypt carbonates (Tushka) of a previous study is added and a comparison of the findings with existing empirical relationships of sandstones is made. The final section discusses the dissolution experiments.

6.1 SIP on carbonates

A main finding of the first systematic SIP investigation on carbonate rocks is that carbonates clearly show polarisation effects. Four different types of polarisation curves were observed for the spectra of the imaginary part of conductivity and the phase shift. Each carbonate type can be assigned to a characteristic curve type. This observation is in contrast to the finding of a preliminary investigation on glauconite-rich, mollusc-rich chalky limestone samples from the Tushka area in Egypt (Halisch et al., 2014). The characteristic curve types occur randomly within the sample set and do not correlate with the three observed microfacies associations (MFA) of this study. One possible cause for this could be the high heterogeneity of the samples within one MFA, i.e. a lower comparability of the plugs of one MFA. A heterogeneous material is defined by the macroscopic properties of interest (e.g. porosity, permeability, electrical conductivity), which can differ from one sample to the next. For example, dead end pores caused by fossil shells, do not take part in current flow mechanisms (Revil & Cathles III, 1999). The three microfacies associations of the Tushka carbonates were characterised in a former study by El-Sayed et al. (2005) and were petrographically and petrophysically investigated by Öner et al. (2016). Two MFAs have a high amount of fossils (brachiopods, gastropods, echinoderms) up to a size of 2 mm and a sparry to micrite cemented matrix. The third MFA has a sparry to micrite cemented matrix with a high amount of secondary cementation and a lower amount of fossils. The heterogeneity affects also the results of the formation factor, which show a wide variation for MFA1 and MFA3. The four carbonate types of my study are less heterogeneous and each sample set has a sufficient number of identical or rather comparable samples. Hence, each polarisation behaviour can be assigned to a specific carbonate type and the result is reproducible for the whole sample set.

6.1.1 Investigations on peak behaviour

Different experiments were conducted to get more insight into the phase behaviour of the four investigated carbonate types. A phase peak would be expected, if a characteristic length scale exists that dominates the polarisation behaviour. It is known that a wide distribution of length scales results in flat phase spectra without distinct peaks. The EBK samples show a clear phase peak, whereas the other three carbonate types indicate phase spectra without a visible peak. The investigations in this chapter were designed to reveal the preconditions for the formation of a phase peak.

Prediction of peak frequency One explanation could be that the peaks are outside of the measured frequency spectra and therefore, no maximum is visible. The first approach deals with the prediction of these peak frequencies in order to verify if they are within measured spectrum of 2 mHz to 100 Hz. Revil & Florsch (2010) introduced a prediction of the Cole-Cole time constant from grain size and have transformed this equation in to a prediction from pore size by scaling from the point of view of dimensional analysis (Revil et al., 2012b):

$$\tau_{CC} \approx \frac{d^2}{8D_\mathrm{i}} \Rightarrow \tau_{CC} = \frac{\Lambda^2}{2D_\mathrm{i}}. \tag{6.1}$$

Therein, D_i represents the diffusion coefficient of the counterions in $[\mathrm{m}^2{\cdot}\mathrm{s}^{-1}]$ and the grain diameter d is replaced by the dynamic pore size Λ in $[\mu\mathrm{m}]$. On basis of Equation 6.1 and the calculation of the time constant by the peak frequency (Eq. 3.22), a prediction of the expected peak frequency can be expressed by:

$$f_\mathrm{peak} = \frac{1}{2\pi\tau_\mathrm{peak}} \text{ with } \tau_\mathrm{peak} = \frac{r_\mathrm{eff}^2}{2D_\mathrm{i}}\ , \tag{6.2}$$

assuming that the dynamic pore size corresponds to the effective hydraulic radius r_eff and $\tau_\mathrm{CC} = \tau_\mathrm{peak}$. The relation between τ_peak and r_eff is described in Weller et al. (2016) and has been validated for a set of sandstones. As D_i is unknown for specific carbonate types, a constant value of $3.8{\cdot}10^{-12}\,\mathrm{m}^2{\cdot}\mathrm{s}^{-1}$ is assumed, which has been proposed as diffusion coefficient for clayey sandstones by Revil (2013a).

A test with the EBK samples showed that this is an appropriate value. Rather than a constant D_i, an apparent diffusion coefficient is considered, as discussed for sandstones in Weller et al. (2016),

$$D_\mathrm{a} = 0.754 r_\mathrm{eff}^{1.72}. \tag{6.3}$$

Figure 6.1 shows the results of the predicted peak frequencies for the four carbonate types. Different radii derived by various methods are used for comparison. The effective pore radius is calculated by the formation factor derived by Archie's law (F_Arch) and the formation factor derived by IP data (F_corr) (Eq. 5.1). Additionally, radii from MIP (r_dom, r_{50}) and NMR (r_{50}) are used. The used surface relaxivities to calculate the pore radii of the T_2 distribution are listed in Table 5.1. The scale of the plotted frequency range is conform with the frequency spectra of the SIP measurement (1 mHz to 100 Hz).

The comparison of the expected peak frequencies with those measured for the EBK (red area) shows a slight underestimation using the pore radii r_eff determined by F_Arch and F_corr, as well as the radii determined by MIP (Fig. 6.1 a). In contrast, using the radii determined by NMR lead to an overestimation of the peak frequency, which could be an indicator of a incorrect surface relaxivity. The best results are achieved by the calculation with the apparent diffusion coefficient, since D_a was determined from f_max.

The comparison of f_peak of LK shows similar results, in a frequency range of 1 to 30 Hz, for the all radii with a constant diffusion coefficient (Fig.6.1 b). The expected peak frequencies calculated by D_a are one magnitude lower in a frequency range of 0.2 to 0.4 Hz, compared to the calculations with D_i. The results for ILS vary over several magnitudes (Fig.6.1 c). For r_eff (F_Arch, F_corr), f_peak is in the range of 0.02 to 0.04 Hz. The expected peak frequency derived by r_dom is one magnitude lower ($f_\mathrm{peak} = 0.003$), whereas f_peak derived by r_{50} (MIP, NMR) is significant higher ($f_\mathrm{peak} = 0.3$ - 5 Hz). The expected peak frequency derived by D_a is 0.1 Hz. The results of DOL vary in a frequency range of 0.01 to 0.2 Hz, except for f_peak calculated by r_dom (Fig. 6.1 d).

I summarise, all predicted peak frequencies are within the measured frequency range. Since I am looking for a frequency range and not an exact value, it is irrelevant which pore radius is used or if the diffusion coefficient varies. The comparison of the predicted with the measured peak frequency of the EBK shows a very good consistency. Hence, the prediction of the peak frequency is an

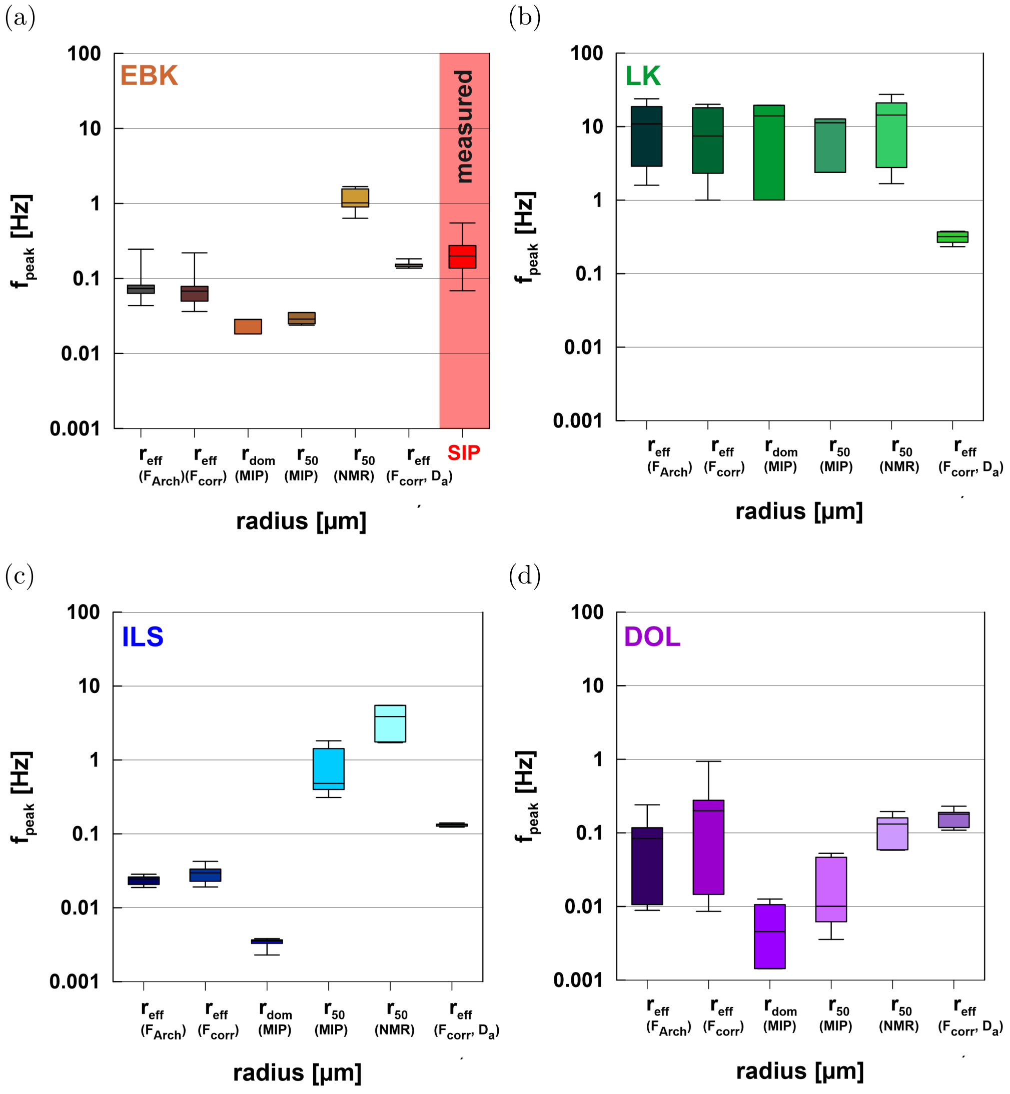

Figure 6.1: The results of the expected peak frequency using different radii. a) The results for EBK include the measured peak frequency (red area). b - d) The results for LK, ILS and DOL, respectively.

appropriate way to determine the expected peak frequency. The characteristic length scale of EBK is close to r_{eff}, whereas other carbonate types have a broader distribution of the characteristic length scale. A broader distribution leads to an overlap of possible peaks and thus to a flat distribution without peaks.

Reduction of fluid conductivity A further explanation of the missing phase peak could be a too low phase signal. The fluid conductivity has a great impact on the strength of the phase signal, as shown for the multi salinity measurement of EBK (Fig. 5.12). Therefore the second approach involves a significant reduction of the fluid conductivity to increase the phase signal for a better interpretation. Besides the standard fluid conductivity of 100 mS·m^{-1}, one sample of each carbonate type is measured with significantly-reduced fluid conductivity down to 6 mS·m^{-1}. Figure 6.2 shows the variation in phase spectra with fluid conductivity for LK, ILS, and DOL.

The characteristic phase behaviour of the LK is described by a combination of constant phase behaviour or slight slope at higher frequencies and a constant slope at lower frequencies without a visible phase peak at a fluid conductivity of 100 mS·m^{-1} (green) (Fig. 6.2 a). Reduction of the fluid conductivity leads to an increase of the phase signal and the curve is shifted to higher phase values. In contrast to the standard salinity, a phase peak is observed for a salinity of 12 mS·m^{-1} (blue) and 6 mS·m^{-1} (red). The peak frequency is at 1.5 Hz for $\sigma_{\mathrm{w}} = 12$ mS·m^{-1} and at 0.6 Hz for $\sigma_{\mathrm{w}} = 6$ mS·m^{-1}.

DOL shows a continuously increasing phase shift as characteristic behaviour at a fluid conductivity of 100 mS·m^{-1} (green) (Fig. 6.2 b). The phase shift increases

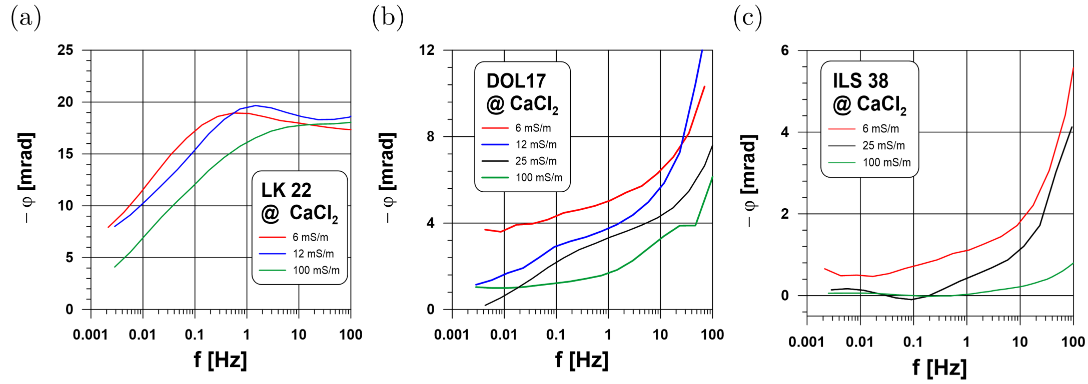

Figure 6.2: Variation in phase spectra for different salinities. a - c) Variation of LK, DOL and ILS, respectively, for fluid salinity of 100 mS·m^{-1} (green), 25 mS·m^{-1} (black), 12 mS·m^{-1} (blue), and 6 mS·m^{-1} (red), respectively.

with decreasing fluid conductivity. At a frequency of 1 Hz, the phase shift increases from $\varphi_{100} = 1.8$ mrad (green) to $\varphi_{25} = 3.3$ mrad (black), to $\varphi_{12} = 3.6$ mrad (blue), and to $\varphi_6 = 5{,}1$ mrad (red). Despite the increase of the phase shift, a phase peak is not formed.

Similar observation can be made for the ILS (Fig. 6.2 c). The characteristic phase behaviour of the ILS is a more or less constant phase shift at a fluid salinity of 100 mS·m^{-1} (black). With decreasing salinity, the phase shift increases from $\varphi_{100} = 0.03$ mrad (green) to $\varphi_{25} = 0.51$ mrad (black), and to $\varphi_6 = 1.12$ mrad (red) at a frequency of 1 Hz. However, a phase peak does not occur. The phase behaviour changes slightly from constant to a continuously increasing, which is significantly influenced by the high coupling effects.

Reducing the fluid conductivity leads to an increase of the phase signal and allows a better interpretation of the phase peak for the LK. However, the decrease of the fluid conductivity for the carbonates types ILS and DOL does not improve the interpretation and the phase peak cannot be detected. A reason for this could be that the IP signal is too low in general to allow a better interpretation despite strengthening of the phase signal. However, another possible conclusion might be that DOL and ILS have no peak behaviour in the IP spectra.

Influence of cation-exchange-capacity As a third approach, the cation-exchange-capacity (CEC) was regarded as a factor for the IP response (Fig. 6.3). Figure 6.3 a shows the imaginary part of conductivity as a function of CEC for carbonates. A relationship between σ'' and CEC is shown. The polarisation increases with higher CEC. The black dashed line describes the relationship by a power law and the red solid line indicates a quadratic relationship. In contrast, the model of Revil (2013a) suggests a linear relationship for sand and clayey material (Revil, 2013b). Considering the carbonate types separately, the general trend is obviously influenced by EBK. LK data have only one CEC value, but the small dataset follows the trend very well. DOL and ILS follow the trend partly: one half of the sample set complies with the correlation whereas the other half deviates significantly. The trend indicates that a higher CEC value causes a higher σ'', and thus a higher polarisability. Hence, the carbonates should posses a certain amount of clay, expressed as cation exchange capacity (CEC), to show significant polarisation effects. Nevertheless, for a CEC value of 400 C·kg^{-1} three different carbonate types exist, which differ more than an order of magnitude in the imaginary part of conductivity. Furthermore, it must be noted, that the smallest measured CEC

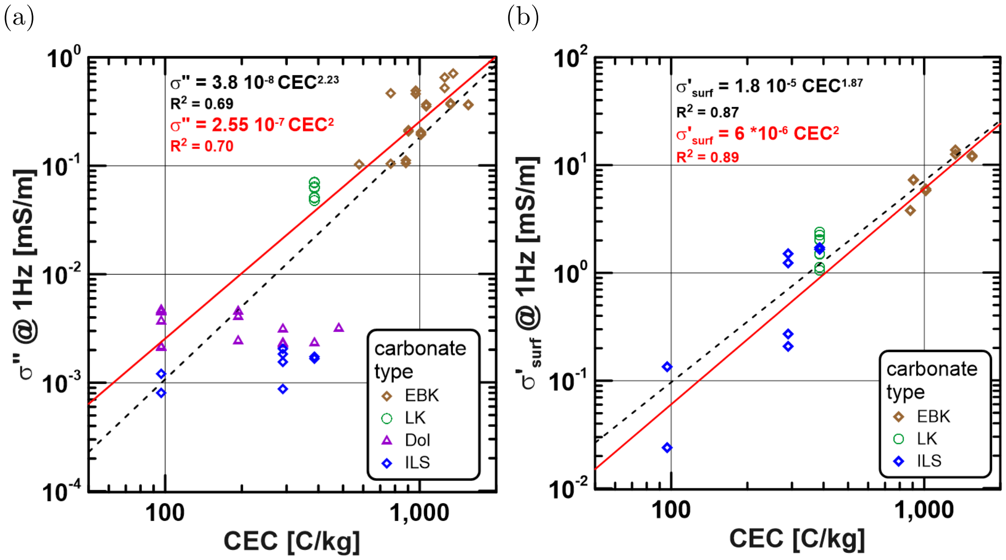

Figure 6.3: Relationship between CEC and a) imaginary part of conductivity and b) surface conductivity.

values of 100 C·kg^{-1} are at the detection limit of the Cu(II)-Triethylenetetramine technique. In total, the investigated samples have a comparably low amount of CEC, because of the very low proportion of clay in the carbonates of this study. The open question is: would the phase behaviour of EBK be the same, if it would contain a lower proportion of clay?

A second relationship between CEC and the surface conductivity was also detected (Fig. 6.3 b). This trend is also observed by Revil (2013b) and is consistent with the idea of a domination of the surface conductivity by the diffuse layer. The expression of the σ'', as a function of the specific surface, as discussed in Revil (2013b), is not relevant for the investigated carbonates. The Cu(II)-Triethylenetetramine-technique measures only the amount of clay, e.g. smectite. Hence, a lower amount of clay of the investigated carbonates leads to a distorted ratio of specific surface and CEC, and results in a guesstimate with no informative value.

Imaging procedures As a forth approach, imaging procedures like μ-CT and ESEM are used to create qualitative images of the carbonate samples and to investigate the pore space. μ-CT and ESEM imaging are useful tools to determine common features and differences between the carbonate types, with regards to e.g. connectivity, pore space and grain size (Tab. 5.2). The four carbonate types could be divided in two groups based on their phase behaviour: (1) EBK and LK with (nearly) phase peak behaviour and (2) ILS and DOL with a constant or continuous increase phase behaviour. My goal is to determine properties that can be assigned only to one group in order to be able to explain the different phase behaviour. One feature is the ratio of connected to non-connected pore space. The connected porosity of the carbonates determined by μ-CT data was introduced in chapter 5.1 *Combined rock evaluation.* A comparison of the connected porosity related to the total porosity shows that 93 % of the total pore volume of EBK and LK is connected. The percentage of connected pore space in DOL (73 %) and ILS (86 %) is significantly lower. Hence, the proportion of isolated pore space is higher for DOL and ILS. More dead ends imply more pores with no current flow, which affects the IP response. Dead ends can result from fossils (e.g. mollusc) or recrystallisation. The comparison of the pore-size distribution as second feature, as shown in Figure 5.4 c, leads to no clear assignment to the groups. EBK and DOL have a bimodal distribution and LK and ILS have an unimodal distribution, whereby LK is dominated by small pores and ILS by large pores. It has to be mentioned that the pore size distribution determined by μ-CT do not lead to a conclusive result, since the relevant lengths of the narrow pores are below the resolution of μ-CT data ($< 2\,\mu$m). The matrix of EBK and DOL commonly consists of idiomorphic crystals, but the size of these crystals differs more than five times (EBK < DOL). The grain-sizes of EBK and LK range from very fine to fine crystalline, whereas ILS and DOL have larger grain sizes from medium to coarse. Therefore, the grain size as feature can be attributed to one of the two groups. The comparison of the fossil content leads to no clear assignment to the groups. EBK and DOL have no fossils, whereas LK and ILS have fossils. All carbonate types show recrystallisation structures. As important properties, the connected pore space and a significant amount of small pores, regarding the equivalent pore radius distribution determined by μ-CT imaging, can be identified.

Mineralogy Considering the mineralogy of the carbonate types to distinguish by means of properties one group from the others, two characteristics can be identified: (1) EBK and LK have a significant higher amount of quartz (> 6 %) in comparison to ILS and DOL (< 1 %), and (2) the amount of clay is higher (1 % - 2 %) for EBK and LK compared to ILS and DOL (< 0.14 %) (Tab. 5.2). In contrast, a study of Müller-Huber et al. (2018) on mud-dominated and grain-dominated carbonate rocks found that phase peaks are not related to clay minerals, because a sample with high clay content shows no phase peak, whereas a sample with less clay amount exhibit a prominent peak. Nevertheless, EBK and LK belonging to clay-poor carbonates with respect to the investigated carbonates of Müller-Huber et al. (2018). Seemingly, no influence on peak behaviour is observable, whether the rock is dolomitic or not, because EBK as well as DOL are dolomites (Tab. 5.2).

6.1.2 Influence of fluid salinity

Mostly experiments for constant ionic composition of the pore fluid are reported in literature and the influence of σ_w on IP parameters has been neglected. In section 5.2.2, a salinity experiment was conducted on the EBK sample. The main observations have been summed up in Table 5.4. The discussion on the influence of fluid salinity on IP parameter is focussed on the comparison of the findings between sandstones and carbonates. Weller et al. (2011) and Weller & Slater (2012) have examined the salinity dependence on sandstones as well as on unconsolidated material.

First, I consider the dependence of conduction processes on fluid chemistry. The linear relationship between σ_w and σ' for sandstones (Rink & Schopper, 1974; Weller et al., 2011) can be observed for carbonates as well. Considering next the polarisation effects, the curve is characterised by a constant increase of σ'' at a frequency of 1 Hz. In contrast to sandstones, an asymptotic high-salinity value for σ'' is not observed, as predicted by the Diffuse layer polarisation model and Stern layer polarisation model (Lesmes & Frye, 2001; Weller et al., 2011; Weller & Slater, 2012). Weller et al. (2011) calculated that the saturation state of interfacial polarisation is reached when the product of surface charge density and ionic mobility reaches a maximum. Their observations show that the fluid salinity has to be increased to reach the saturation state, if S_por increases. Hence, the explanation could be that the high specific surface ($S_\mathrm{por} = 26\,\mu\mathrm{m}^{-1}$) of the sample and the non-asymptotic behaviour results from a not high enough fluid salinity range, i.e. salinities higher than $1600\,\mathrm{mS{\cdot}m}^{-1}$ are needed to reduce the slope. However, comparison with specific surfaces of sandstones shows that the non-asymptotic behaviour occurs for samples with $S_\mathrm{por} > 45\,\mu\mathrm{m}^{-1}$, whereas a sandstone with $S_\mathrm{por} = 30\,\mu\mathrm{m}^{-1}$ shows a reduction of the slope with increasing salinity. Both values are higher than those for carbonates. Another explanation for the non-asymptotic high-salinity value for σ'' could be the observation of a second phase peak in the σ'' spectra for salinities higher than $200\,\mathrm{mS{\cdot}m}^{-1}$. Comparing the exponent of the power law of the carbonate samples (0.1) with those of sandstones (0.1 - 0.59) in the study of Weller & Slater (2012), the exponent is at the lower limit of determined values, e.g. lower variations of σ'' with increasing salinity. Considering the chargeability, a decrease of m with increasing salinity is observed, which is in good agreement with the results from sandstones. Hence, the observations on the normalised chargeability are also transferable from sandstones to carbonates. As described in Weller et al. (2011), the power law dependences of σ'' and m_n can be used to correct IP parameter, which are used to correlate with petrophysical parameters.

The second peak in the σ'' spectra at high salinities is a behaviour that could be observed for sandstones as a change in the spectral shape for salinity experiments (Weller et al., 2015c) and for saturation experiments (Jougnot et al., 2010; Zhang et al., 2019). The assumption of an irreversible process due to a high salt concentration, by, e.g., change of pore-space geometry or dissolution/precipitation processes, was disproved. A repetition measurement with a fluid conductivity of $100\,\mathrm{mS{\cdot}m^{-1}}$ was carried out after the multi salinity measurements and the results perfectly matched (Fig. A.13). Therefore, it is concluded that the high salinities do not modify the sample irreversibly, but rather the process is reversible. Additionally, two other EBK samples were chosen for multi salinity experiments to verify this observation. The same behaviour is observed for the phase spectra at conductivities above $200\,\mathrm{mS{\cdot}m^{-1}}$.

6.1.3 Empirical relationships in comparison to sandstones

The database of sandstones contains a sufficient amount of widely diversified samples, resulting in empirical relationships between petrophysical and IP parameters. The results of this study are extended by the data of the Tushka carbonates (El-Sayed et al., 2005; Halisch et al., 2014; Öner et al., 2016) and compared with the known relationships of sandstones for discussion purposes.

Porosity & permeability Figure 6.4 shows the relationship between porosity and real part of conductivity of the investigated carbonates of this study, including the Tushka carbonates. The conductivity increases with increasing porosity of the carbonates. This results from the fact that with increasing porosity, the amount of pore fluid increases as does as the conductivity. The porosity of the Tushka carbonates is less than 10 % and enlarges the porosity range from 2 % to 45 %. The correlation of the carbonates of this study (red) changes slightly, it the Tushka carbonates (black) are added. The correlation can be described by $\sigma' = 5.8 \cdot 10^{-2}\Phi^{1.53}, R^2 = 0.86$, which was introduced as Archie's Law in Equation 2.11. The exponent describes the parameter m, which is 1.93 for the carbonates of this study and 1.53 for the Tushka carbonates. The exponent m determined by the IP measurements corresponds to the exponent m determined by the Φ - F relation. The exponent m of the studied carbonates varies from 1.97 to 2.5 (Φ - F), whereas the exponent m of the Tushka carbonates is significantly smaller ($m = 1.4$; Φ - F). The significantly smaller m of the Tushka carbonates explains the decrease of the correlation exponent of the relationship between σ'

and Φ after adding the Tushka carbonates.

Due to the correlation between porosity and σ' as well as between porosity and permeability, a dependence of σ' on permeability is observed, especially for EBK and LK. These two carbonate types, with higher polarisation effects (EBK/LK), show a strong relationship between permeability and quadrature conductivity. This relationship contradicts theory. EBK and LK show also a relationship between porosity and σ''. An explanation for the dependence of σ'' on porosity and permeability is given by Figure 6.5. A clear correlation between σ' and σ'' is observed for EBK, LK and the Tushka carbonates, which is unknown for sandstones. The good correlation means that the real and imaginary part of conductivity have the same informative value. Hence, the relationships between imaginary part of conductivity and porosity and permeability can be derived from the correlations between the real part of conductivity and porosity and permeability.

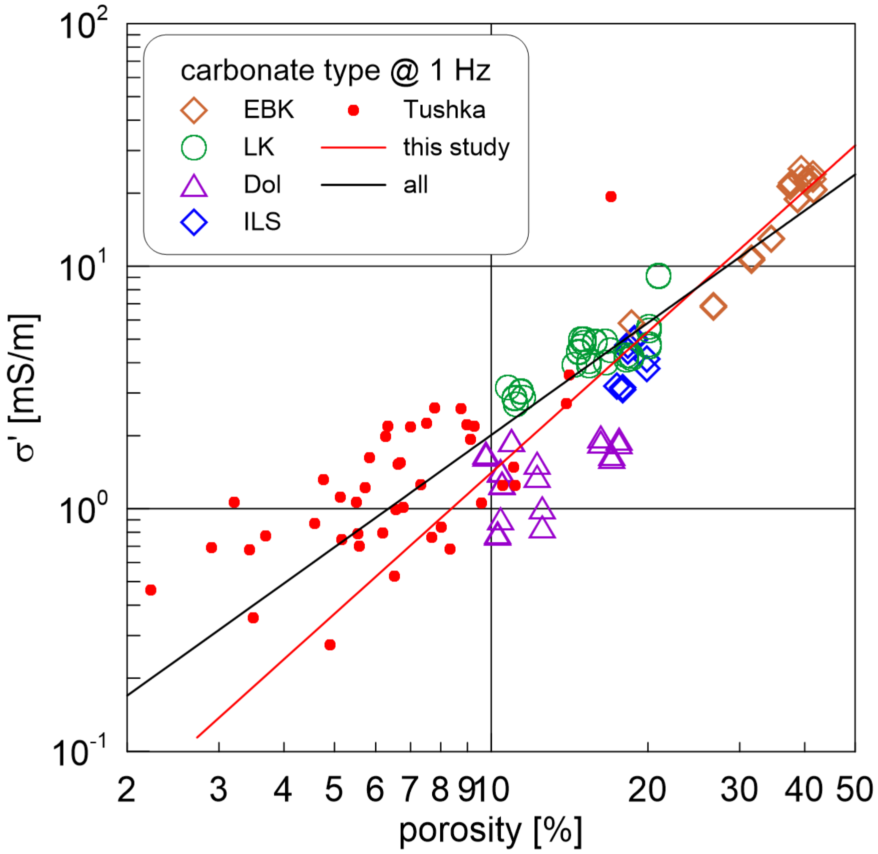

Figure 6.4: Variation of σ' (with a constant fluid conductivity of 100 mS/m) with porosity. Red solid line displays the data fit of this study (112 data points) and the black solid line shows the data fit of all carbonates (149 data points).

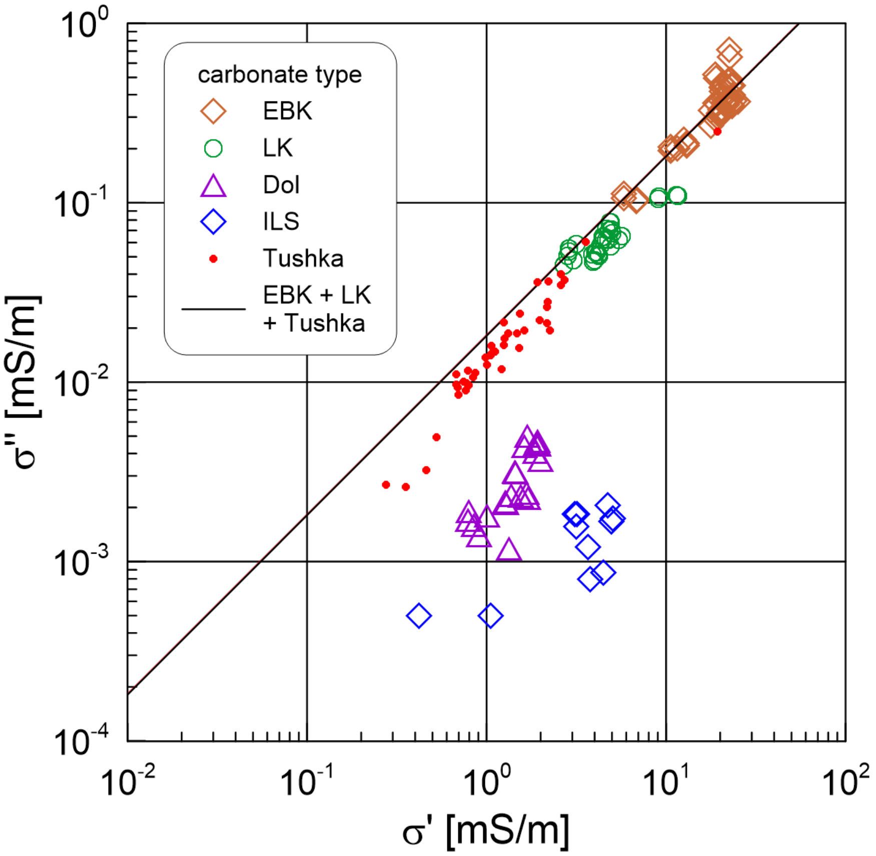

Figure 6.5: Relationship between σ' and σ''. The black solid line displays the best data fit of EBK, LK and the Tushka carbonates.

Specific surface The specific surface has an important role in controlling the magnitude of the IP effect, as shown in several studies (Börner, 1992; Börner et al., 1996; Weller & Slater, 2012; Weller et al., 2015b). The results of the four carbonate types show no clear relationship between S_{por} and σ'' (Fig. 6.6 a). A weak linear relationship is given by $\sigma'' = 0.007 \cdot S_{\mathrm{por}}$, $R^2 = 0.41$ (red solid line). Adding the Tushka carbonates (red points) does not improve the correlation. Öner et al. (2016) pointed out the high amount of iron oxides as an explanation. The iron oxides, with their large specific surface, have a significant effect on the S_{por} values, compared to petrophysical parameters. The carbonates of this study have no comparable features, which can explain the scattering of the data. A comparison with the well-established correlation of sandstones (Weller & Slater, 2012) shows good consistency for the two carbonate types with higher polarisation effect (EBK/LK), whereas the two carbonate types with lower polarisation effects (ILS/DOL) exhibit larger variations with regard to the sandstone correlation.

The POLARIS model developed by Revil (2012) implies S_{m} as the controlling textural factor. Revil (2012) showed with a dataset of Börner (1992) a higher correlation of S_{m} and σ'' than between S_{por} and σ''. The correlation of Revil (2012) is shown in Figure 6.6 b (black solid line), including the carbonate dataset of this study and the Tushka carbonates. Since EBK and LK fit well the trend of Revil (2012) and provide the majority of the data points (72), a comparison with

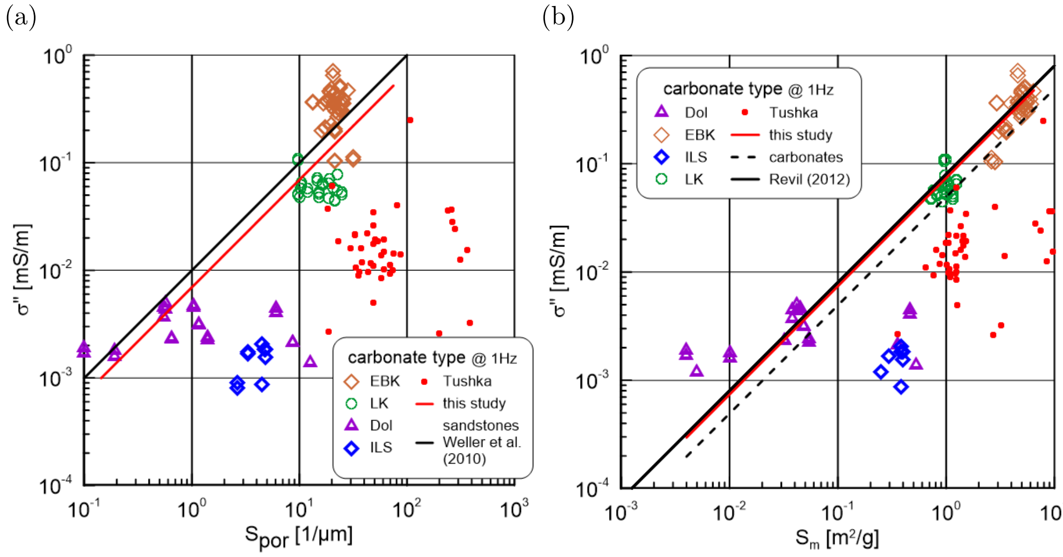

Figure 6.6: Imaginary part of conductivity versus a) specific surface related to the pore volume and b) the specific surface related to the mass. The red solid lines correspond to the linear relationships of the data of this study (101 data points). The black solid lines correspond to the linear relationships of sandstones. The black dashed line includes all carbonate samples (143 data points).

the correlation of this study (red solid line) are in very good accordance. Adding the Tushka carbonates (red points) leads to a shift of the carbonate correlation (black dashed line), due to the high amount of iron oxide as already explained. The correlation for carbonates between σ'' and S_{m} (this study: $R^2 = 0.92$, all carbonates: $R^2 = 0.64$) is much better than the one with S_{por} (this study: $R^2 = 0.41$, all carbonates: $R^2 = 0.04$).

Weller & Slater (2012) proposed a linear relationship of σ'' to the textural parameter $S_{\mathrm{por}} \cdot F^{-1}$, which is based on experimental data as well as on the Diffuse layer (Rink & Schopper, 1974) and Stern layer polarisation models (Leroy et al., 2008). This relationship is also consistent with an equation developed by Revil (2012). Revil (2013a) demonstrated correction of S_{m} by tortuosity ($T = F \cdot \Phi$) for low porosity material. Niu et al. (2016) confirmed $S_{\mathrm{por}} \cdot F^{-1}$ as well as $S_{\mathrm{m}} \cdot F^{-1}\Phi^{-1}$ as textural parameters controlling σ'', over a broad range of porous media (borosilicate beads, sandstones, and low-porosity clayey samples). A correction of the specific surface by the formation factor or tortuosity of carbonates could be more important than for sandstones, because of the higher amount of non-connected pore space. Figure 6.7 shows the relationship between σ'' and the corrected specific surfaces. It is notable that the Tushka carbonates are significantly shifted towards the correlation of carbonates. The relationship between σ'' and the textural parameter $S_{\mathrm{por}} \cdot F^{-1}$ provides a R^2 of 0.68 (Fig. 6.7 a). The determination coefficient of the linear regression of σ'' and the textural parameter $S_{\mathrm{m}} \cdot F^{-1}\Phi^{-1}$ is $R^2 = 0.78$

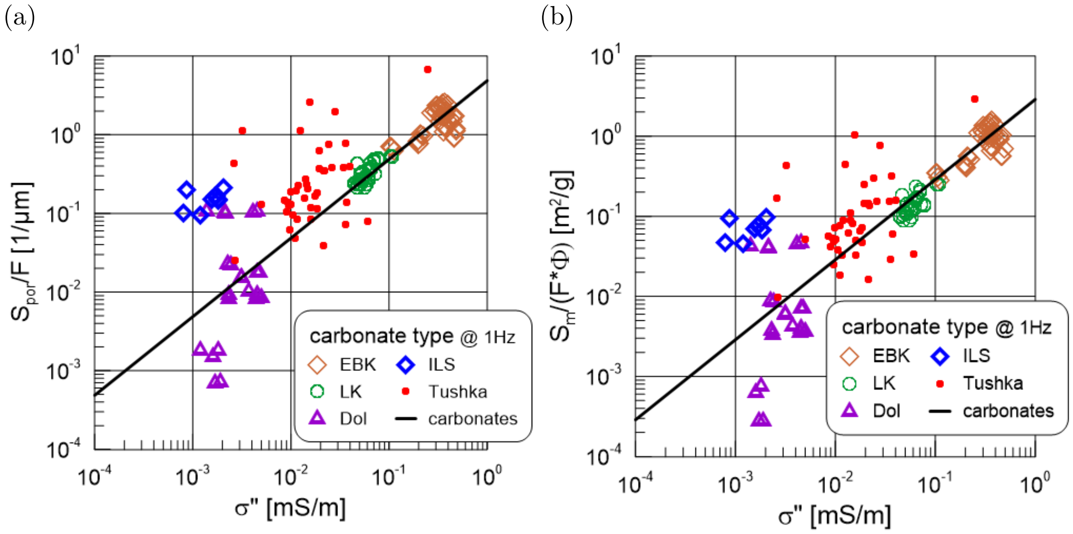

Figure 6.7: The relation between imaginary part of conductivity and a) $S_{\mathrm{por}} \cdot F^{-1}$ and b) $S_{\mathrm{m}} \cdot F^{-1}\Phi^{-1}$. The solid line is the best linear fit to the carbonate samples.

(Fig. 6.7 b). Both linear regressions have a higher determination coefficient after correction of the specific surface by the formation factor or tortuosity.

Pore radius The EBK is the only investigated carbonate type of this study with a maximum type in the phase or σ''-spectra that results from a characteristic length scale. Considering the relationship between r_{dom} and τ_{peak} for sandstones, the EBK corresponds well to the correlation of Kruschwitz et al. (2010) (Fig. 6.8). Figure 6.9 shows a combined interpretation of MIP, NMR, μ-CT and SIP data for one EBK sample. The relative position of the pore radius axis and the frequency axis was determined using the fit of Kruschwitz et al. (2010). The MIP curve corresponds to the pore throats, whereas the μ-CT curve correlates to the pore body radius. The two relaxation peaks of the NMR measurement ($\rho_S = 100\,\mu\mathrm{ms}^{-1}$) correspond to either pore throats or pore bodies. The IP-spectra can be attributed to pore throats of the MIP curve, as assumed by Figure 6.8. The characteristic length scale of the polarisation maximum of EBK is the dominant pore throat size determined by MIP. For carbonates no general statement can be given, since only EBK has a τ_{peak} and can be added to the cross plot using the correlation of Kruschwitz et al. (2010).

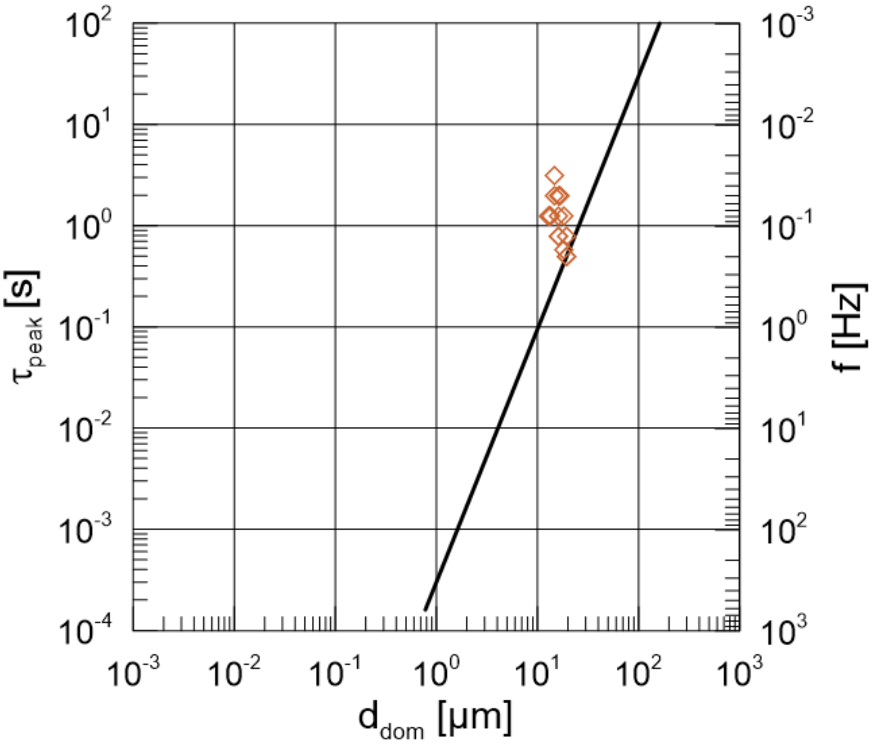

Figure 6.8: Variation of the relaxation time τ_{peak} ($= (2\pi f_{\mathrm{peak}})^{-1}$) with dominant pore throat diameter d_{dom} for EBK. The power law fit $\tau \propto d_{\mathrm{dom}}^{2.97}$ of Kruschwitz et al. (2010) is shown.

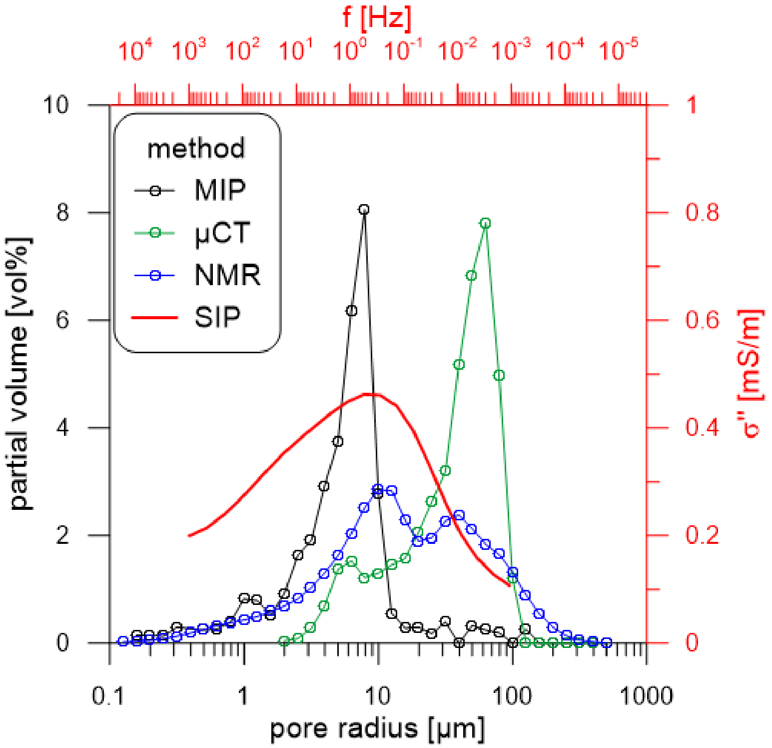

Figure 6.9: Pore volume distribution measured with MIP (black), NMR (blue) and μ-CT (green) (bottom and left axis). The imaginary part of conductivity σ'' measured by SIP is plotted as a function of the frequency (red) (top and right axis).

Formation factor prediction The relationship between σ_{surf} and σ'' is basis for a reliable prediction of formation factors of carbonate rocks, as described in section 5.2.2 (Fig. 6.10). The studied carbonate dataset is extended by the Tushka carbonates. The results of the Tushka carbonates support the correlation of the carbonates of this study very well. The factor l for all carbonates is 0.025 with a R-squared of 0.93, including 78 data points. The surface and the quadrature conductivity appear to correlate in a way that is consistent with sandstones ($l = 0.042$, $R^2 = 0.91$, (Weller et al., 2013) or $l = 0.037$, $R^2 = 0.79$, (Revil et al., 2015)). The determined l offers the opportunity to calculate F_{corr} for the whole sample set. The good consistency between measured and predicted formation factor was shown in Figure 5.20 ($d = 0.096$). Hence, each SIP measurement of a carbonate sample provides a reliable formation factor, which characterises the topology of the pore space.

Permeability predication The permeability predictions that were carried out for the carbonates of this study, were based on (1) F alone and based on (2) F and σ'', as described in section 5.2.2. For discussion purposes, the studied carbonate dataset is extended by the Tushka carbonates and the permeability predictions are repeated. Due to the Tushka carbonates, the permeability range is

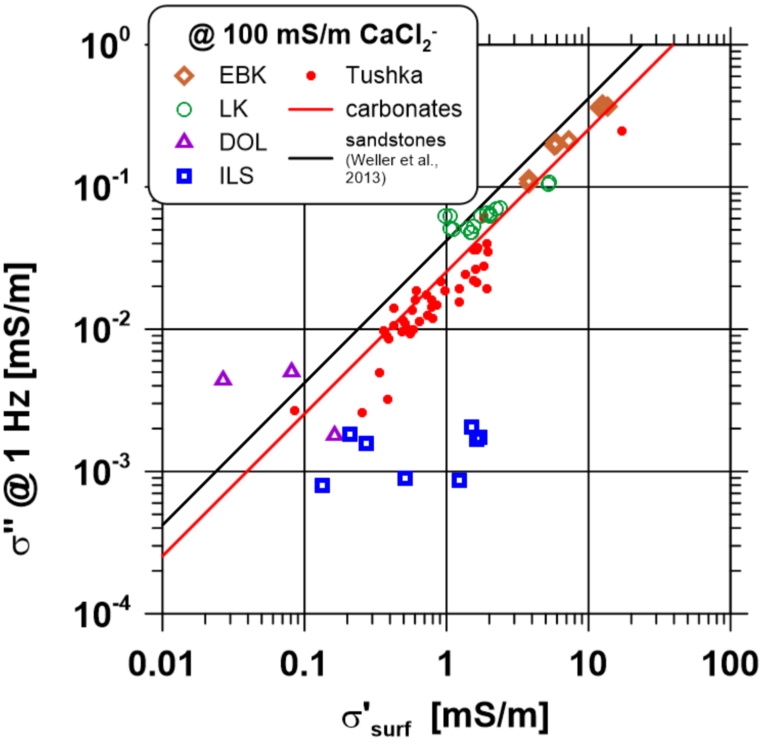

Figure 6.10: Crossplot between σ'' (at ~1 Hz) and σ'_{surf} for the investigated samples and the Tushka carbonates. The red solid line displays the data fit including 78 samples. The black line displays the relationship for sandstones.

extended by six orders of magnitude. To compare the predictive capabilities of the resulting equations for permeability prediction, the average absolute logarithmic deviation between predicted and measured permeability was determined. Table 6.1 summarises the number of used data points and the average logarithmic deviation, as well as the resulting parameters and their variances. The predicted permeability k_{F} is based on formation factor alone and $k_{\text{F}\sigma''}$ is determined by the formation factor and the imaginary part of conductivity. Comparing the resulting average absolute logarithmic deviation of both predictions, d is always lower for $k_{\text{F}\sigma''}$. Hence, the IP parameter improves the permeability prediction for carbonates and can be integrated into models of permeability prediction as shown for sandstones (Weller et al., 2015a; Robinson et al., 2018). Considering the exponent as a weighting term, the formation factor F is more important for permeability prediction than σ''. Small errors in the IP parameter have a lower impact as small errors in the formation factor, which will result in large errors in permeability prediction. The formation factor is a limiting factor of the predication of the permeability according to Equation 5.5. In the field, F is not measured directly from borehole electrical logging. On a laboratory scale, F is not available for all datasets, as it requires additional measurement. Therefore, the estimation of the formation factor based on IP data is used to extend the data base significantly (Tab. 6.1).

The comparison between the average logarithmic deviation between predicted and measured permeability shows a better prediction for the studied carbonates using F_{corr}, whereas d is lower for the prediction of all carbonates using F_{M}. This is due to the fact that the prediction of permeability of the Tushka carbonates is significantly better using F_{M} (Fig. 6.11 a and Fig. 6.11 b), which accounts for the majority of the used dataset. A larger dataset leads to better correlation, noticeable by decreasing variances of the parameters a, b and c, as shown in Table 6.1. Using the sandstone correlation to predict the permeabilities of the carbonate dataset yields a distinct underestimation of several orders of magnitudes of the permeabilities, as shown in Figure 6.11 c. The average logarithmic deviation is $d = 3.1$. This result points out the need of an own correlation for carbonates. In general, the approach of permeability prediction using IP data works well for sandstones and carbonates, but the models for permeability prediction vary considerably between sandstones and carbonates. Hence, a fitting should be made with separated datasets.

This study demonstrates that it is not possible at this time to formulate an universal model of permeability prediction that includes both sandstones and carbonates.

Table 6.1: A table including number of datapoints, average logarithmic deviation d, resulting parameters (a, b, c of Equation 5.5) and their variances of the permeability prediction using F_{corr} and F_{M} as formation factor. The studied carbonates and the additional Tushka carbonates are shown separately, as well as the parameters of the permeability prediction of sandstones reported by Robinson et al. (2018).

	F_{corr}		F_{M}		sandstones
	this study	+ Tushka	this study	+ Tushka	(Robinson et al., 2018)
datapoints	106	148	39	81	58
d of					
k_{m} & k_{F}	0.71	0.82	0.98	0.85	
k_{m} & $k_{\mathrm{F}\sigma''}$	0.63	0.74	0.75	0.68	0.77
parameter					
a	$3.2{\cdot}10^{-7}$	$9.4{\cdot}10^{-8}$	$6.4{\cdot}10^{-8}$	$4.0{\cdot}10^{-7}$	$2.66{\cdot}10^{-7}$
b	3.5	2.9	3.2	3.6	5.35
c	0.72	0.46	0.87	0.75	0.66
variance of					
a	0.29	0.19	0.63	0.29	
b	0.23	0.12	0.47	0.16	
c	0.09	0.09	0.14	0.12	

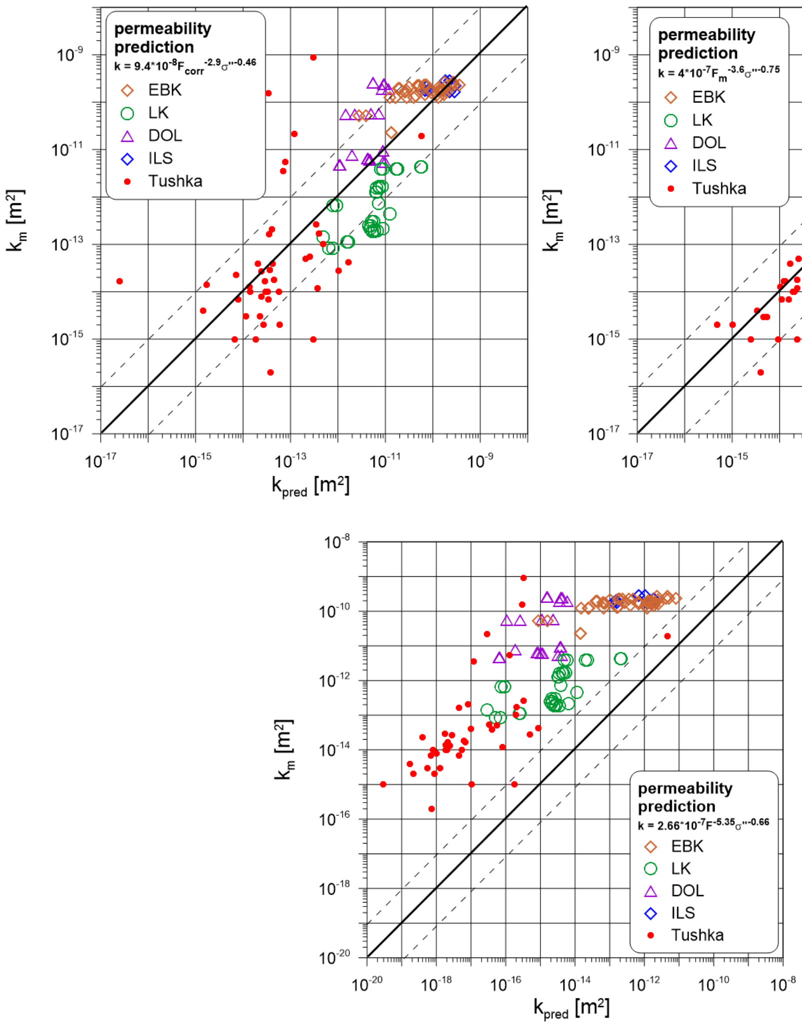

Figure 6.11: Comparison of the predicted and the measured permeability using the correlation a) based on F_{corr}, b) based on F_{M}, and c) based on an equation derived for sandstones (Robinson et al., 2018). The dashed lines correspond to plus or minus of an order magnitude for prediction of the permeability.

6.2 Dissolution experiment

In this chapter, the results of the dissolution experiments are discussed in three parts. The first part focusses on the experimental procedure itself regarding functionality and quality assessment of the acid dissolution. The second part discusses the structural changes of the rock samples triggered by the acid solution. The last part deals with the influence on the IP parameter by dissolution processes. My major interest is to understand and quantify how the pore space and structure is modified and how this influences the geophysical response of the carbonate.

6.2.1 Experimental procedure and acid

The results of the monitoring of the in- and outflowing fluids during acidifying and flushing phases prove the functionality of the experimental setup (Fig. 5.23). Both the acidifying and the flushing phase lead to an exchange of the pore fluid from acid to water and vice versa, which can observed in the electrical fluid conductivity measurements. The difference between in- and outflow conductivities of the acid indicates that a slight reaction between acid solution and sample took place during the acidification procedure. Since the acid is activated by temperature, the acid was cooled down from approximately 20 °C to 5 °C before use, to reduce this effect.

Orientation analysis An orientation analysis includes a number of qualitative and quantitative specifications, which provide an overview about the quality and composition of the mixture. The analytical results of the orientation analysis indicate that no chemical precipitation of formates takes place during the dissolution (Fig. A.14). All dissolved ingredients of the acid, which flowed through the sample, were flushed out of the sample. This information is important for the interpretation of the structural changes caused by dissolution.

Acid Acidgen$^{\mathrm{TM}}$FG3 was used as an acid to obtain a homogeneous and heat activated dissolution of the EBK. The images of the treated samples show a significant mass loss for some dissolution steps (Fig. 5.24 b). The high mass loss during one dissolution step can be explained by the length of endurance of the acid-water-mixture. The endurance describes the time after mixing the water with Acidgen$^{\mathrm{TM}}$FG3 (Stage 1, Eq. 3.26). The experience of the performance of several dissolution procedures leads to the implication that a longer endurance of the acid-water-mixture (after stage 1), causes a higher strength of the acid solution. Furthermore, the temperature activation as a controlling factor, seems to be negligible. Hence, the reaction between acid solution and carbonate takes place immediately after the contact. This conclusion was taken into account before further procedure within this study. The study of Kjøller et al. (2016) uses a similar acid (Acidgen$^{\text{TM}}$) for the dissolution of chalk specimens and reported no comparable observations. The desired homogeneous dissolution of the carbonates is proven by the image analysis of ESEM images. Kjøller et al. (2016) also used ESEM and μ-CT images to evaluate dissolution of rock samples by acetic acid and Acidgen$^{\text{TM}}$. In contrast to acetic acid, the Acidgen$^{\text{TM}}$ creates a homogeneous dissolution. The ESEM images show that the acid leads to a dissolution, but causes no permanent changes of the rock micro structure due to welding, as described by Vanorio et al. (2011). Vanorio et al. (2011) injected CO_2-rich water under constant confining and fluid pressure for carbonate dissolution and observed the loss of granular micro structure, probably due to pressure effects.

6.2.2 Structural changes

Petrophysics

The results of the petrophysical measurements lead to the following statements regarding density, porosity, and specific surface areas ($S_{\mathrm{m}}, S_{\mathrm{por}}$):

(1) density increases with increasing dissolution steps,

(2) porosity increases with increasing dissolution steps, and

(3) the specific surface area increases after the first dissolution step and decreases during the following dissolution steps.

Density and porosity The increasing density can be explained by the analysis of the ESEM images (Fig. 5.25). The carbonate cement is preferably dissolved in comparison to the crystals, which consist primary of dolomite. A similar observation was made by Vanorio et al. (2011) and Grombacher et al. (2012), who showed ESEM images in which the micrite phase is preferentially dissolved in carbonates and the grains are exposed in the rock microstructure after micrite dissolution. The carbonate cement has a density of about $2.72\,\mathrm{g{\cdot}cm^{-3}}$, which is lower than the dolomite with a density of $2.90\,\mathrm{g{\cdot}cm^{-3}}$. Due to the different densities and the preferred dissolution of pure $CaCO_3$, the increase of the density with each dissolution step is logical. The expected increasing porosity is simply a result of dissolved material. At the same time, no precipitation took place, which is proven by the orientation analysis and by the high solubility of calcium formate, as reported by the patent of the Acidgen FG (Harris & Holdsworth, 2016). Enhancement of pore space is the typical result of dissolution processes and a dissolution-induced compaction may occur during injection under pressure (Grombacher et al., 2012). A linear porosity increase, depending on the acid concentration, as observed in Fig. 5.29, is as well described by Kjøller et al. (2016). The comparison of the absolute change in porosity after six dissolution steps with a 5 % acid shows similar values for both studies, despite different carbonate types: $\Delta\Phi \approx 3\,\%$ (Kjøller et al., 2016) and $\Delta\Phi = 2.7\,\%$ (this study).

Both parameter, density (Eq. 3.5) and porosity (Eq. 3.4), are determined by the triple weighing method, as explained in section 3.1.1. The assumption of a systematic error of the balance of $\Delta m = 0.01\,\mathrm{g}$, results in a mean error of 0.05 % for the porosity value and a mean error of $0.0004\,\mathrm{g} \cdot \mathrm{cm}^{-3}$ for the density value. Both errors are significantly below the changes of porosity and density triggered by the dissolution. However, the accuracy error which depends on repeatability of the individual weighings increases. Although a mean value of three measurements was calculated, the values of the individual weighings differ, especially the weight of the saturated sample (m_{sat}). The removal of the excess water leads to substantial variations in the weight and is challenging to reproduce, because the method of rolling the sample on a towel is unique and can result in a very slightly loss of mass. Additionally, the sample loses its perfect cylindrical shape during the dissolution process, which affects the removal of the excess water at the ends of the cylinder. For a quantification of the resulting error, the TWM was conducted at the beginning and at the end of the workflow during one dissolution step, keeping in mind that the repeated saturating and drying affects the sample weights. Nevertheless, the resulting density and porosity values should be unaffected and comparable. In total, 15 samples were used to determine an average deviation of the density and the porosity values: $\Delta d_{\mathrm{gr}} = \pm 0.012\,\mathrm{g} \cdot \mathrm{cm}^{-3}$ and $\Delta\Phi = \pm 0.27\,\%$, which is equal to a relative deviation of $\frac{\Delta d_{\mathrm{gr}}}{d_{\mathrm{gr}}} = \pm 0.43\,\%$ and $\frac{\Delta\Phi}{\Phi} = \pm 0.67\,\%$. The smaller percentage of the density values results from the fact that only two weighings (m_{dry}, m_{im}) are necessary. A comparison between the average deviation and the absolute change during three dissolution steps indicates similar values for the density $\Delta d_{\mathrm{gr}} = \pm 0.012\,\mathrm{g} \cdot \mathrm{cm}^{-3}$ and $d_{\mathrm{grS3}} - d_{\mathrm{grS0}} = 0.035\,\mathrm{g} \cdot \mathrm{cm}^{-3}$ and larger difference for the porosity $\Delta\Phi = \pm 0.27\,\%$ and $\Phi_{\mathrm{S3}} - \Phi_{\mathrm{S0}} = 2.5\,\%$. On average, the relative change of each dissolution step is always higher than the average relative deviation for a single measurement. Nevertheless, despite the similar values of relative density change and the average relative deviation of the density, the trend is clear due to combined interpretation of all datasets in histograms. Because of the large dataset, the error of a single sample is of less importance.

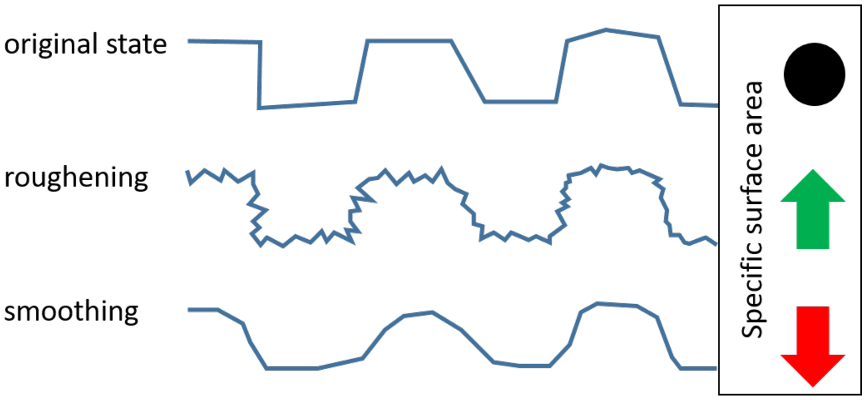

Figure 6.12: A simplified model of roughening and smoothing of the pore surface during dissolution. The pore space is roughened by dissolution leading to an increase of the surface area (green arrow) and subsequently the pore space is smoothed by dissolution, which causes a decrease of the surface area (red arrow).

Specific surface area A reason for the different behaviour of increasing and decreasing S_{m} and S_{por} might be the preferable dissolution of the carbonate cement in the first dissolution step. The carbonate cement smooths the surface and covers the rough areas beneath. Thus, the surface increases after the first dissolution step. During subsequent dissolution steps, the process of smoothing the surface is more dominant compared to abrading the surface and therefore S_{m} and S_{por} decrease in total. Another explanation is given by a highly simplified model showing a scenario of surface changes during dissolution (Fig. 6.12). The pore space is roughened by dissolution leading to an increased surface area. Subsequent dissolution processes are smoothing the pore suface and reducing the specific surface area. The two processes occur simultaneously, whereby the roughening dominates the first dissolution steps resulting in an increased surface area. At a later stage smoothing dominates, which is evident by the decrease of the surface area.

The calculated values of S_{por} depend on porosity, density and S_{m} (Eq. 3.17) and are affected by the uncertainties of all the parameters. Since the determination of S_{m} has less input parameters, S_{m} is more reliable.

Pore radius

An important aspect is the changing pore space, especially the impact on the pore radii distribution, after the dissolution. On the basis of the increasing porosity, it is assumed that the dominant pore radius would be increase as well during dissolution. For this reason the results of NMR, MIP and μ-CT are jointly interpreted and discussed regarding pore radii distributions. The observations of the results of the dominant pore radii of the particular methods lead to the following statements:

(1) r_{dom} derived by NMR decreases with increasing dissolution steps, and

(2) r_{dom} derived by MIP and μ-CT increases with increasing dissolution steps.

NMR A possible explanation of the opposite behaviour of r_{dom} derived by NMR is that the assumption of a constant surface relaxivity does not occur in reality. To achieve a shift of r_{dom} to higher pore radii, as observed by MIP and μ-CT, the surface relaxivity has to increase. In comparison to MIP and μ-CT, the pore radii distributions of NMR measurements have a higher uncertainty because of the challenging determination of the surface relaxivity. In this work, the surface relaxivity of EBK was derived from pore radii distributions of μ-CT data and NMR results, as seen in Figure 4.8. The NMR curve was shifted along the axis of pore radii until a good agreement between μ-CT and NMR curves is reached. This method provides the correct order of magnitude of the surface relaxivity, but not a precise value. The uncertainties can be explained among other things by the fact that NMR data are measured across the whole cylindrical sample, whereas the μ-CT data measures a significantly smaller fragment of the sample. The untreated sample EBK27 has a surface relaxivity of $100\,\mu\mathrm{m}\cdot\mathrm{s}^{-1}$ and a r_{dom} of $12.5\,\mu\mathrm{m}$. I consider how the surface relaxivity could change over several dissolution steps. For convenience, r_{dom} is assumed to be constant for all dissolution steps, since the possible increase of r_{dom} is unknown. The surface relaxivity has to be increased to $125\,\mu\mathrm{m}\cdot\mathrm{s}^{-1}$ (S1), $146\,\mu\mathrm{m}\cdot\mathrm{s}^{-1}$ (S2), $141\,\mu\mathrm{m}\cdot\mathrm{s}^{-1}$ (S3), and $152\,\mu\mathrm{m}\cdot\mathrm{s}^{-1}$ (S4) for congruent T_2 time distributions. The surface relaxivity is influenced by the roughness and the magnetic properties of the sample. Although the macroscopic magnetic properties are unaffected, the microscopic magnetic properties could be affected by the dissolution process. As concluded from the ESEM images, the calcite cement is preferably dissolved and, at a later time, the dolomite is dissolved by the formic acid, which may also affect the surface relaxivity. In total, the shifts of the maxima of the T_2 distributions are small and probably close to the error range. Since all samples show the same shift, the general trend towards smaller T_2 times is most likely a real effect. Grombacher et al. (2012) investigated the change of microstructure of carbonate rocks by the injection of CO_2-rich water using NMR measurements among others. The NMR T_2 distributions of Grombacher et al. (2012) showed a minimal change in pore geometry and slight shifts to shorter or longer T_2 times (depending on enlargement of pore space or dissolution-induced compaction). They concluded that NMR T_2 measurement is useful as an indicator of pore-geometry changes, but it is often difficult to interpret.

MIP and μ-CT For MIP and μ-CT results, the shift of r_{dom} towards higher pore radii is also small and near the limit of resolution. For both methods, it is valid that the general trend is clear, despite slight changes during dissolution. The μ-CT curve corresponds to the pore bodies, whereas the MIP curve correlates to the pore throats radius. The dominant pore body radii ($r_1 = 55\ \mu$m), as well as the dominant pore throat radii ($r_1 = 8\,\mu$m) of mode 1, increase. Mode 1 is related to large pores, whereas the dominant pore body radius of mode 2 ($r_2 = 5\,\mu$m) is related to the voids of the crystals, according to small pores. It should be mentioned that MIP cannot detect the whole pore space, because of *shielded pore spaces*, as discussed in Kruschwitz et al. (2016).

With MIP data, it is possible to detect changes caused by different duration of dissolution of the systematic investigation, whereas the results of the μ-CT data detect primarily differences between untreated and treated samples, while differences between the dissolution durations cannot be observed. The changes in the μ-CT data by dissolution processes are very small, with the consequence that the samples of the systematic investigation cannot be distinguished. Noticeable is the discrepancy of the sample with 48 h acidification duration against the other samples in the MIP data, as well as in μ-CT data. The pore radius distributions derived by μ-CT data of the untreated samples explain this behaviour (Fig. 5.38 a). Whereas the remaining samples show very similar pore size distribution with a dominant pore body radius of 55 μm, the 48 h sample has a significant shift to a smaller dominant pore body radius of 40 μm and a higher amplitude of the peak. Hence, the slice of the 48 h sample differs slightly from the others, already before the treatment, which leads to discrepancy from the other results in MIP and μ-CT after dissolution.

The data of the systematic investigation has more importance for the resulting statements, since the MIP and μ-CT data of the regular acidification procedures is only able to consider qualitatively-comparable samples.

Pore-shape analysis

Additionally to pore radii, the pore-shape analysis considers pore length. The results of the pore-shape analysis (section 5.3.2) based on μ-CT imaging can be explained by simplified models. The EBK consists of idiomorphic rhombohedral shaped crystals (r = 5 μm - 10 μm) including voids. The pore space inside the crystals can be assigned to the range of the small pores (r < 10 μm). Figure 6.13 shows a simplified model, which explains the change of the pore shape for small pores. The acid moves into the hollowed crystals via holes at the edges and further enlarges the voids. The cavities become longer and thicker, as shown by the pore-shape analysis.

A typical pore segmentation of the large pores ($r = 10\,\mu m - 200\,\mu m.$) is shown in Figure 6.14. The blue-coloured pore space (Fig. 6.14) is transversely separated at pore constrictions or separation points (white circle) using the watershed algorithm. The dissolution leads to an increase of the surface by roughing and subsequent smoothing of the pathways, as explained before. In addition, the pore volume increases. After the dissolution, the watershed algorithm separates the pores differently because former separations points (white circles) have been dissolved. Hence, the pore shapes of the large pores become longer and thicker during dissolution.

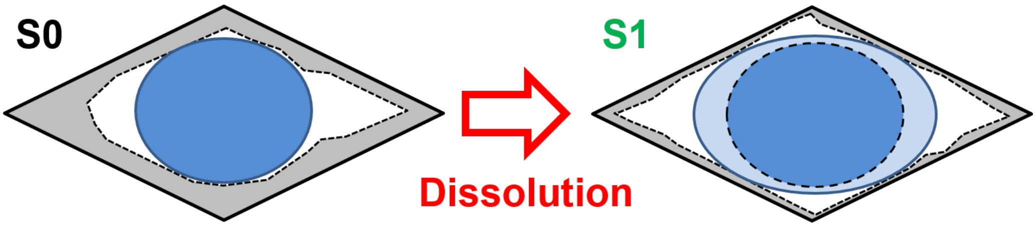

Figure 6.13: Simplified 2D model of the dissolution process in the crystals for the range of the small pores. On the left is the untreated crystal and on the right is the treated crystal. The blue ellipsoid describes the calculated pore shape of the untreated crystal. The light blue ellipsoid describes the pore shape of the treated crystal.

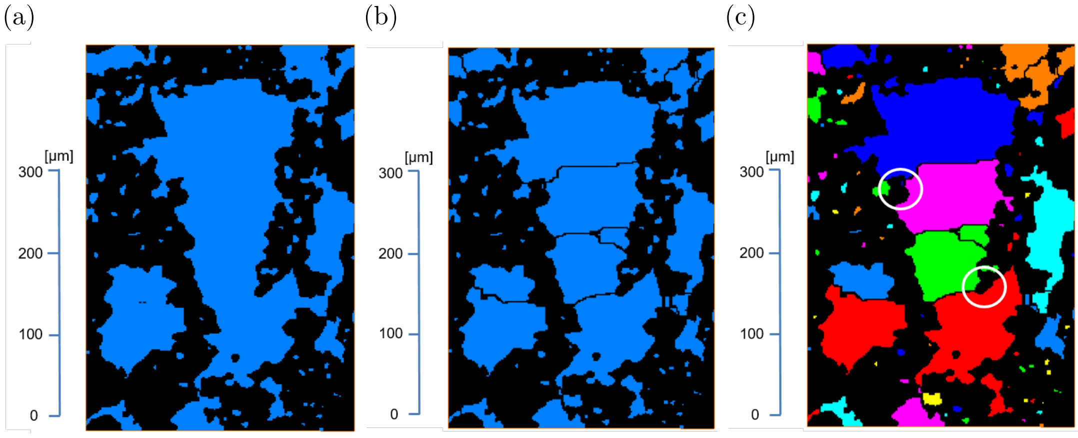

Figure 6.14: 2D slices during post-processing of a large pore. a) Blue-colored pore space. b) Pore segmentation. c) Pore separation after labelling. The white circles mark exemplified separation points of the algorithm.

6.2.3 IP data

MIP, μ-CT, and BET provide important information about pore-space characterisation and alteration of carbonates after the dissolution procedure, but can be only applied in a laboratory. In contrast, SIP is able to conduct fundamental research on laboratory scale, as well as on field scale. Since, SIP has rarely been used on carbonates up to now, the carbonate dissolution processes and associated changes were not yet investigated in combination with IP measurements.

The change of the IP parameters by dissolution processes is shown in Table 5.7. The slight parameter changes make the interpretation challenging. Additionally the IP data quality will be discussed for a better assessment of the parameter changes. In general, it is challenging to obtain an accurate and repeatable data set, especially for SIP (Kemna et al., 2012). The most important factors are:

(1) The measuring accuracy of the SIP-Quad is reported to be ~0.01 % for measured quantities impedance amplitude and phase shift.

(2) The temperature dependence of SIP measurements leads to deviations of 2% to 2.5 % per 1 K for σ' and 1% to 3 % per 1 K for σ'', after Bairlein (2017). It is impossible to measure the temperature of the pore fluid directly, but the fluid within the tanks of the core holder indicates a temperature variations of 0.1 K to 0.3 K for most conducted SIP measurements of this work. In total, a variation of ~0.5 % is assumed for both parameters. Every measurement is repeated at least three times on different days to reduce temperature effects (daily variance).

(3) A major factor is the installation of the sample within the core holder and the related determination of the geometric factor of the core holder by measuring the distance between the two potential electrodes. Typically, the influence of several new installations is 0.2 $\mathrm{mS \cdot m^{-1}}$ (~1 %) for σ' and 0.003 $\mathrm{mS \cdot m^{-1}}$ (~1.3 %) for σ''. Outliers of single measurements show deviations of up to 3 $\mathrm{mS \cdot m^{-1}}$ (~10 %) for σ' and 0.02 $\mathrm{mS \cdot m^{-1}}$ (~8 %) for σ'' at frequencies higher than 0.1 Hz. Every sample, on each dissolution step, is installed at least three times in the core holder to reduce the uncertainties of new installation and the geometry factor, compared to the other dissolution steps.

(4) Some samples have significant mass loss after dissolution, which leads to a bumpy cross-sectional area of the cylindrical sample (Fig. 5.24 b). This can affect the field lines of the external electrical field and thus the measured

parameters. This effect is assumed to be of minor importance, since the potential ring electrodes are not placed directly at the edges of the sample.

In total, an error of ±1.5 % is assumed for σ' and an error of ±2 % for σ''. However, it is possible that errors can increase for single measurements. The average change per dissolution step is $\sigma'_{\Delta\mathrm{S}}$ =2.4 % and $\sigma''_{\Delta\mathrm{S}}$ =3.9 % at a frequency of 70 Hz or $\sigma''_{\Delta\mathrm{S}}$ =1 % at f_{peak}. The changes per dissolution step are higher than the errors. Therefore, the reported changes in IP parameters do not result from the errors only, but are rather the result of the dissolution process. An appropriate number of repeated measurements and extreme care when performing the defined SIP measurement protocol is required to ensure and enhance the reliability of the IP data.

In the following, the IP parameters changes during the dissolution process are discussed and the validity of the first Archie's Law (Eq. 2.11) is verified. The low-frequency conductivity, σ_0, is usually taken at f = 0.01 mHz. In this part, $\sigma'(1\,\mathrm{Hz})$ is used as σ_0, which never leads to differences of the qualitative statements regarding increase or decrease during dissolution. The porosity, the real part of conductivity and the formation factor are linked by Archie's Law. The rock conductivity is sensitive to changes in porosity and both parameter are directly proportional to each other. Both parameters, porosity (Fig. 5.28) and σ' (Fig. 5.45), increase during dissolution and their relationship is shown by a cross plot in Figure 5.51 a. An increased porosity leads to a decrease of the formation factor. A comparison of both parameters during dissolution shows the increase of the porosity (Fig. 5.28), while F_{corr} (Fig. 5.49 a) decreases slightly. The relation between the real part of the conductivity and the formation factor can also be considered. Since σ_{w} is assumed to be constant, despite temperature dependence, a slight decrease of F_{corr} (Fig. 5.49 a) causes an increase of σ' (Fig. 5.45). However, the temperature dependence of σ_{w} can influence this relationship, if the changes of F and σ' are small, compared to the error range of σ_{w}.

A simple conceptional model of a pore before and after dissolution is shown in Figure 6.15. A pore, with a fluid conductivity σ_{w} and a surface conductivity σ_{surf}, has a complex electrical conductivity of $\sigma^* = \sigma_0 + \sigma^*_{\mathrm{surf}}$ (Rink & Schopper, 1974; Vinegar & Waxman, 1984). After dissolution the pore widens, which leads to an increasing σ_0 and a decreasing σ^*_{surf}, assuming that the volume tortuosity decreases and the surface tortuosity increases. σ_0 is influenced strongly by the formation factor and thus the porosity, as shown before. The formation factor can be related to the tortuosity ($F = T \cdot \Phi^{-1}$). The dissolution of the cement leads

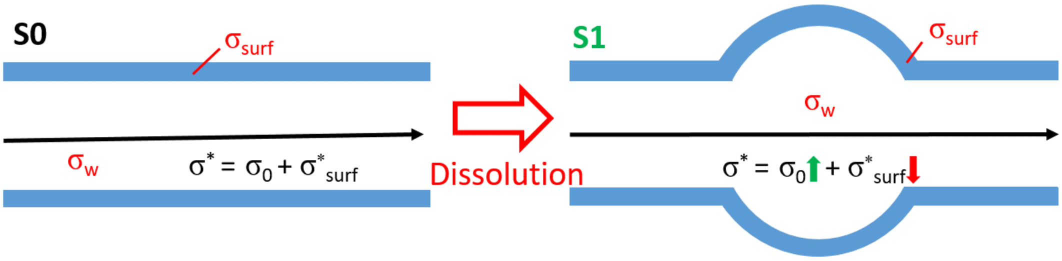

Figure 6.15: A simplified model the pore with a pore fluid conductivity σ_w and a surface conductivity σ_surf before (S0) and after (S1) dissolution and the resulting complex electrical conductivity σ^*. The expansion of the pore space leads to increasing σ_0 and decreasing σ^*_surf.

to a better connectivity of the pore channels and consequently to a decrease in the volume tortuosity. Hence, the decrease of the volume tortuosity leads to the significant increase of $\sigma'(1\,\mathrm{Hz})$, as observed in Figure 5.45.

At the same time, the surface tortuosity increases by the dissolution process, which causes a decrease of the imaginary part of conductivity. That could not be observed in Figure 5.46, which means that the model cannot be confirmed. An increase of σ^*_surf can be explained by a decreased volume tortuosity and/or a decreased surface tortuosity resulting from smoothing of the surface as shown in the model of Figure 6.12.

In literature, σ'' is related directly to S_por (Weller et al., 2010a, 2015b). Since the surface area increases and decreases during dissolution (Fig. 5.31), this behaviour should be transferable to σ''. The study of Wu et al. (2010) investigated the IP of calcite precipitation (the reverse process of dissolution). They observed that σ'' increases with increasing S_por. Therefore, in case of dissolution and the decreased surface area, σ'' is expected to decrease. The observation of σ'' during dissolution (Fig. 5.46) demonstrates that this is not the case. The imaginary part of conductivity varies slightly during dissolution, exhibiting no clear trend ($\sigma''(1\,\mathrm{Hz}, f_\mathrm{peak})$) or increases ($\sigma''(70\,\mathrm{Hz})$).

Two findings about carbonates arise from this work in section 6.1: (1) the correction of the specific surface using the formation factor for carbonates is more important than for sandstones and improves the coefficient of determination (Fig. 6.7), and (2) the correlation between σ' and σ'' (Fig. 6.5). Due to the correction of S_por by F, σ'' is also affected by F during dissolution. Therefore, the behaviour of S_por during dissolution cannot directly be related to σ''. The increased σ'' at higher frequencies can be explained by the decreasing formation factor, despite a decrease in surface area. Another explanation for the behaviour of σ'' is σ'. Obviously, σ'' and σ' have a similar dependence on F and T, respectively. A decreased T and a potentially decreased surface tortuosity resulting from smoothing, enable an increased σ'' despite decreased S_{por}. The volume conductivity increases more strongly than the surface conductivity, because of the influence of the decreased surface area.

The calcite precipitation experiment of Wu et al. (2010) showed a decreasing peak frequency of the σ''-spectra during precipitation. However, the dissolution experiment of this study indicates a nearly constant f_{peak}, with a tendency to higher frequencies during dissolution. The minor changes in peak frequency are caused by minimal variations of characteristic length scale during dissolution. The characteristic length scale of the EBK is the dominant pore throat size determined by MIP, as discussed in section 6.1.3. The systematic investigation of r_{dom} showed a slight shift towards higher radii, as discussed in section 6.2.2. The relationship observed by Kruschwitz et al. (2016) indicates a decreased f_{peak} with increasing r_{dom}. Because of the minimal variations of f_{peak} during dissolution and the coarse frequency grid of the SIP measurement, a clear trend cannot be detected, which is caused by increasing r_{dom}. The significant increase of σ'' at a frequency of 70 Hz (Fig. 5.46 c) and the overlapping of the σ''-spectra at higher frequencies (Fig. 5.43 and Fig. 5.44) during dissolution indicate significant modification in the range of smaller pores ($< r_{\mathrm{dom}}$). The change of the curve shape of the σ''-spectra at higher frequencies affects the relaxation time τ_{DD}, which decreases (Fig. 5.50). It can be concluded that the change of τ does not indicate the increase of r_{dom}, but instead the formation of many small pores.

This work shows the potential of SIP to characterise dynamic processes. However, variations of SIP parameter during dissolution are small and challenging to interpret, but seem to be reliable, as the overall trend matches those of single samples throughout the whole set. The upscaling from laboratory to field scale will lead to complications regarding the interpretation of the results, because the data error increases significantly (Orozco et al., 2012; Slater & Binley, 2006). It is possible that the higher error level would mask the observed parameter changes due to dissolution. For example, electromagnetic coupling can represent a significant problem at frequencies > 10 Hz (Zimmermann et al., 2008a; Radic, 2004; Kemna et al., 1999; Ghorbani et al., 2009). This frequency range corresponds to the area of interest, in which σ'' increases significantly. Furthermore, the dissolution process is much more complicated on the field scale and more investigations are necessary to extrapolate the laboratory findings towards the field scale. A better understanding of structural pore changes resulting from dissolution at the pore scale is essential for the prediction of reactive processes in carbonates, as well as in potential areas of subrosion. Imaging provides information about dissolution processes, in particular where they occur and which rock component, grains, matrix, and/or cement, is involved in the process. Precise knowledge about this process is fundamental for using laboratory data to model the geophysical response of a carbonate reservoir with regards to dissolution processes. A better understanding of the pore growth and structural changes caused by dissolution would provide the basics for numerical modelling in rock mechanics. Within the junior research group, it was planned to use the major findings of this laboratory study to simulate dissolution processes during carbonate failure on the field scale for a better understanding of subrogation processes.

7 Summary and Conclusion

Systematic laboratory measurements on carbonates were conducted to investigate carbonate rock characteristics and their influence on IP responses as methodical research and associated with dissolution processes. It could be shown that in a laboratory environment SIP is a suitable tool to obtain detailed information about rock properties and to characterise the pore space.

Systematic study on complex electrical conductivity of carbonates

This work is the first systematic study about SIP on carbonates and therefore, represents a huge improvement of the carbonate data base related to SIP. Carbonate sample sets from different type locations with a large and broad range of petrophysical parameters are investigated.

I have shown that carbonate rocks indicate polarisation effects, as it was already described for sandstones. With respect to the frequency dependence, four different types of polarisation behaviour were observed in the spectra of the phase shift as well as of the quadrature conductivity: a constant phase angle (ILS), a continuous increase (DOL), a combination of both (LK), and a maximum type (EBK). Each behaviour can be assigned to the specific carbonate type and can be reproduced for the whole sample set.

Different experiments are conducted to get more insight into the phase behaviour of the four carbonate types and to investigate the preconditions for the formation of a phase peak. The characteristic length scale of EBK is close to r_{eff}, which results from the observed peak frequency, whereas other carbonate types have a broader distribution of the characteristic length scale and thus no peak behaviour. The empirical relationship between τ_{peak} and r_{dom} indicates the dominant pore size derived by MIP as characteristic length of the polarisation maximum of EBK. Reducing the fluid conductivity leads to an increase of the phase signal and allows a better interpretation of the phase peak for the LK. However, no phase peak could be detected for the carbonate types DOL and ILS. Multi salinity measurements were conducted on EBK to analyse the influence of σ_{w} on IP parameters compared with the findings of sandstones. The observations of the salinity dependence on IP parameters are transferable from sandstones to carbonates.

A comparison between SIP data and petrophysical parameters of the carbonate sample sets shows that it is more challenging to find a clear correlation between them, especially compared to sandstones. Carbonates with higher polarisation effects ($\sigma'' > 10^{-2}\,\mathrm{mS{\cdot}m^{-1}}$) fit the existing relationships for sandstones much better than types with lower polarisation effects. Imaging procedures and mineralogical investigations are used to identify common characteristics and differences between the carbonate types (e.g. pore size distribution, connected pore space, mineral content). One objective was to explain the different amplitudes of the polarisation effects by empirical relationships developed for sandstones.

The relationship between the specific surface and the quadrature conductivity is improved by a correction of the specific surface using the formation factor or the tortuosity. This correction is for carbonates more important than for sandstones, because of the higher amount of non-connected pore space. Dependencies of the cation-exchange-capacity on σ'_{surf} and σ'' were detected, as well. Furthermore, a single linear relationship $\sigma'' = l \cdot \sigma'_{\mathrm{surf}}$ with $l = 0.029$ is observed. The estimation of the factor l helps to improve petrophysical interpretation regarding resistivity and IP measurements. The factor l enables a more reliable prediction of formation factors for carbonate rocks as shown by a comparison with four other approaches for a formation factor estimation. This prediction is useful for applications in well logging and hydrogeophysics.

A special characteristic of the carbonates types EBK, LK, and Tushka is the direct proportionality of σ' and σ''. This behaviour is unknown for sandstones and is not in accordance to commonly used physical laws in petrophysics.

The carbonate data set was also used to improve the SIP data processing for a better correlation and prediction of permeability. This study demonstrates that it is not possible at this time to formulate an universal model of permeability prediction, which includes sandstones and carbonates. But, it is possible to transfer empirical relationships and model assumptions from sandstones to carbonates.

Induced dissolution experiments

This work demonstrates the importance and motivation for systematic dissolution experiments on carbonates. For this purpose, an experimental setup for systematic dissolution under monitoring conditions and an individually adopted measuring concept were successfully developed. The replacement of the fluid within the sample (acidifying and flushing) worked well and can be verified by the monitored quantities (electrical conductivity and pH-value) of the inflowing and outflowing fluid. Furthermore, the effect and application of the chosen acid has been analysed and evaluated. It is important to produce the acid-water mixture as close as possible to the start of the dissolution experiment and to ensure a temperature of 5 ° C, since dissolution process is unwanted before temperate activation. Due to the small changes of the recorded parameters during one dissolution step it is proposed to repeat the dissolution procedure four times before beginning the petrophysical and SIP measurements. The strength of the acid (5 vol-%), as well as temperature (50 ° C) and duration (24 h) of the temperature activation for the induced dissolution process were carefully selected and turned out to be well suited for the dissolution procedure. The knowledge gained during performance and interpretation of the dissolution experiment are the base for further development and optimisation of the specially designed device, the joint methodical work flow and the handling of the acid.

Analysis of ESEM images is a strong tool to demonstrate the homogeneous dissolution process of the sample and to figure out which part of the rock component is preferentially dissolved. In case of the EBK, the carbonate cement is preferably dissolved compared to the dolomitic crystals. The induced dissolution processes affect several petrophysical parameters with different sensitivity. Grain density and porosity increase, whereas the specific surface increases firstly and afterwards decreases depending on different scenarios of specific surface changes at the pore scale. Since the MIP and μ-CT data of the regular dissolution procedures enables only a qualitative comparison of samples, the data of the systematic investigation has more importance for the resulting statements. The pore radii distributions of MIP and μ-CT data, obtained by the systematic investigation of the dissolution process, indicate an enlargement of the dominant pore radii with increasing dissolution. Additionally, the pore-shape analysis, based on μ-CT imaging, gave an idea of the modification of the pores to longer and thicker pore shapes, which can be explained by a simplified model. A better understanding of pore enlargement resulting from dissolution processes and knowledge about preferentially dissolved rock components is essential for the prediction of subrosion processes in carbonates.

The changes within the sample material during dissolution can be partially resolved by SIP measurements. The real part of the conductivity, which increases continuously, shows a high sensitivity to the dissolution process. The increase of σ' results from an increased porosity, a decreased formation factor, and a decreased volume tortuosity of the sample. The quadrature conductivity increases slightly at higher frequencies ($f = 70\,\mathrm{Hz}$), whereas a rather constant behaviour appears below 10 Hz. Despite σ'' is controlled by the surface area, the expected trend of σ'' during dissolution depends on the surface tortuosity, which is influenced by the process of roughing or smoothing of the surface. Roughing of the pore causes an increased surface tortuosity, leading to a decreasing of σ''. In contrast, smoothing causes a decreased surface tortuosity, which can explain in combination with the decreased volume tortuosity the increased σ'' during dissolution. Both processes occur simultaneously during dissolution and are not separable. In total, the volume conductivity increases more strongly than the surface conductivity.

A change of the shape of the σ''-spectra with increasing dissolution can be noticed and results in increasing σ''-values at higher frequencies. The increased σ''-values at higher frequencies causes decreased mean relaxation times indicating the formation of smaller pores. It can be concluded that the slight increase of r_{dom} has no impact on the relaxation time.

This work demonstrates the importance of fundamental research to obtain new insights in process characterisation as well as for understanding subrosion processes. A quantification of the alteration of the sample material in 4D has been successfully carried out. The potential of SIP to characterise dynamic processes - especially subrosion - has been shown. This dissolution process is much more complicated on the field scale and more investigations are required to validate whether the findings of the laboratory study can be applied on the field scale. The upscaling of laboratory IP data to the field scale will lead to challenges regarding the interpretation of the results, because the data error increases significantly. At this time the relative change of the parameter caused by dissolution is close to the resolution limits of the methods, which challenges interpretation. Hence, ongoing research and improvement of the dissolution procedure is essential.

Outlook

SIP on carbonates The presented work provides a starting point for further investigations of SIP on carbonates. Even for sandstones polarisation phenomena and the question which parameters and length scales control σ'' are not yet fully understood after more than 20 years of research. This systematic study was focused on almost pure calcite or dolomitic carbonates ($CaCO_3$,$CaMg(CO_3)_2 > 90\,\%$) with low clay content. Ongoing research should include more carbonate types in order to extent the carbonate data base. An increasing number of carbonate types would expand the present knowledge and allow a verification of the empirical relationships for carbonates of this work. A larger data base could also solve the issue of carbonates, which fit into known sandstone correlations, and carbonates, which do not fit into these correlations. Future research should focus on the direct proportionality of σ' and σ'' for three carbonate types. Additional measurements and samples are required to figure out which properties of the carbonates lead to this direct proportionality.

Dissolution experiment The development and improvement of the experimental setup, as well as the combination of dissolution procedures and SIP measurements is part of ongoing research. So far the experiments have been conducted only on one carbonate type. Future dissolution experiments should also focus on different carbonates types to consequently increase the data set and to validate the observations of this work. Additional systematic investigations are required with, for example, an increased number of dissolution steps to obtain larger pore space changes. In addition to the improved dissolution procedures, distinct improvements for the accuracy of SIP measurements is substantial to derive clear correlations. The impact of dissolution processes on NMR measurements should be considered more in detail to investigate possible changes of the surface relaxivity during dissolution. Future laboratory work should regard other types of acids to simulate subrosion processes. The dissolution procedures should be repeated until rock failure occurs to implement recorded petrophysical parameters a into numerical modelling of subrosion processes. The knowledge of the fundamental research on dissolution processes is the base to develop a reliable sinkhole monitoring and forecasting system in combination with the results of an integrated geophysical approach.

References

Al-Halbouni, D., Holohan, E. P., Saberi, L., Alrshdan, H., Sawarieh, A., Closson, D., Walter, T. R., & Dahm, T. (2017). Sinkholes, subsidence and subrosion on the eastern shore of the dead sea as revealed by a close-range photogrammetric survey. *Geomorphology*, *285*, 305–324.

Al-Halbouni, D., Holohan, E. P., Taheri, A., Schöpfer, M. P., Emam, S., & Dahm, T. (2018). Geomechanical modelling of sinkhole development using distinct elements: model verification for a single void space and application to the dead sea area. *Solid Earth*, *9*, 1341–1373.

Alexander, S. C., Rahimi, M., Larson, E., Bomberger, C., Greenwaldt, B., & Alexander Jr, C. (2013). Combining LiDAR, aerial photography, and Pictometry® tools for karst features database management. In *Applied Karst Geology: Proceedings of the Fourth Multidisciplinary Conference on Sinkholes and the Engineering and Environmental Impacts of Karst (pp. 63-72).*

Archie, G. (1942). The electrical resistivity log as an aid in determing some reservoir characteristics. *Trans. Am. Inst.Min.*, *146*, 54–62.

Atekwana, E. A., & Slater, L. D. (2009). Biogeophysics: A new frontier in Earth science research. *Reviews of Geophysics*, *47*.

Atzori, S., Baer, G., Antonioli, A., & Salvi, S. (2015). InSAR-based modeling and analysis of sinkholes along the Dead Sea coastline. *Geophysical Research Letters*, *42*, 8383–8390.

Augarde, C. E., Lyamin, A. V., & Sloan, S. W. (2003). Prediction of undrained sinkhole collapse. *Journal of Geotechnical and Geoenvironmental Engineering*, *129*, 197–205.

Bairlein, K. (2017). *Die Temperaturabhängigkeit der spektralen induzierten Polarisation.* Ph.D. thesis TU Braunschweig.

Bairlein, K., Bücker, M., Hördt, A., & Hinze, B. (2016). Temperature dependence of spectral induced polarization data: experimental results and membrane polarization theory. *Geophysical Supplements to the Monthly Notices of the Royal Astronomical Society*, *205*, 440–453.

Benito-Calvo, A., Gutiérrez, F., Martínez-Fernández, A., Carbonel, D., Karampaglidis, T., Desir, G., Sevil, J., Guerrero, J., Fabregat, I., & García-Arnay, Á. (2018). 4D monitoring of active sinkholes with a Terrestrial Laser Scanner (TLS): A case study in the evaporite karst of the Ebro Valley, NE Spain. *Remote Sensing*, *10*, 571.

Bezuidenhout, C., & Enslin, J. (1970). Surface subsidence and sinkholes in the dolomitic areas of the Far West Rand, Transvaal, Republic of South Africa.

Binley, A., Kruschwitz, S., Lesmes, D., & Kettridge, N. (2010). Exploiting the temperature effects on low frequency electrical spectra of sandstone: A comparison of effective diffusion path lengths. *Geophysics*, *75*, A43–A46.

Binley, A., Slater, L. D., Fukes, M., & Cassiani, G. (2005). Relationship between spectral induced polarization and hydraulic properties of saturated and unsaturated sandstone. *Water resources research*, *41*.

Blaschek, R., & Hördt, A. (2009). Numerical modelling of the IP effect at the pore scale. *Near Surface Geophysics*, *7*, 579–588.

Bleil, D. F. (1953). Induced polarization: a method of geophysical prospecting. *Geophysics*, *18*, 636–661.

Blott, S. J., & Pye, K. (2008). Particle shape: a review and new methods of characterization and classification. *Sedimentology*, *55*, 31–63.

Börner, F. (1992). Complex conductivity measurements of reservoir properties. *Advances in Core Evaluation III (Reservoir Management). Gordon and Breach Science Publishers, London*, .

Börner, F., Gruhne, M., & Schön, J. (1993). Contamination indications derived from electrical properties in the low frequency range. *Geophysical Prospecting*, *41*, 83–98.

Börner, F., Schopper, J., & Weller, A. (1996). Evaluation of transport and storage properties in the soil and groundwater zone from induced polarization measurements. *Geophysical Prospecting*, *44*, 583–601.

Bragg, W. H., & Bragg, W. L. (1913). The reflection of X-rays by crystals. *Proceedings of the Royal Society of London. Series A, Containing Papers of a Mathematical and Physical Character*, *88*, 428–438.

Breede, K., Kemna, A., Esser, O., Zimmermann, E., Vereecken, H., & Huisman, J. (2012). Spectral induced polarization measurements on variably saturated sand-clay mixtures. *Near Surface Geophysics*, *10*, 479–490.

Brinkmann, R., Parise, M., & Dye, D. (2008). Sinkhole distribution in a rapidly developing urban environment: Hillsborough County, Tampa Bay area, Florida. *Engineering Geology*, *99*, 169–184.

Brownstein, K. R., & Tarr, C. (1979). Importance of classical diffusion in NMR studies of water in biological cells. *Physical review A*, *19*, 2446.

Bruggeman, V. D. (1935). Berechnung verschiedener physikalischer Konstanten von heterogenen Substanzen. I. Dielektrizitätskonstanten und Leitfähigkeiten der Mischkörper aus isotropen Substanzen. *Annalen der Physik*, *416*, 636–664.

Brunauer, S., Emmett, P. H., & Teller, E. (1938). Adsorption of gases in multimolecular layers. *J. Am. Chem. Soc*, *60*, 309–319.

Buades, A., Coll, B., & Morel, J.-M. (2005). A review of image denoising algorithms, with a new one. *Multiscale Modeling & Simulation*, *4*, 490–530.

Bücker, M., & Hördt, A. (2013a). Analytical modelling of membrane polarization with explicit parametrization of pore radii and the electrical double layer. *Geophysical Journal International*, *194*, 804–813.

Bücker, M., & Hördt, A. (2013b). Long and short narrow pore models for membrane polarization. *Geophysics*, *78*, E299–E314.

Carbonel, D., Rodríguez, V., Gutiérrez, F., McCalpin, J. P., Linares, R., Roqué, C., Zarroca, M., Guerrero, J., & Sasowsky, I. (2014). Evaluation of trenching, ground penetrating radar (GPR) and electrical resistivity tomography (ERT) for sinkhole characterization. *Earth Surface Processes and Landforms*, *39*, 214–227.

Carman, P. (1938). Determination of the specific surface of powders I. Transactions. *J. Soc. Chemical Industries.*, *57*, 225–234.

Carr, D. D., Felli, J., French, R. R., Hatfield, C., Howard, J., Votaw, R., & Potter, P. E. (1966). Cross-bedding in the Salem Limestone of Central Indiana. *Sedimentology*, *6*, 95–114.

Cassiani, G., Kemna, A., Villa, A., & Zimmermann, E. (2009). Spectral induced polarization for the characterization of free-phase hydrocarbon contamination of sediments with low clay content. *Near Surface Geophysics*, *7*, 547–562.

Cole, K. S., & Cole, R. H. (1941). Dispersion and Absorption in Dielectrics I. Alternating Current Characteristics. *The Journal of Chemical Physics*, *9*, 341–351.

Cooper, A. H., & Waltham, A. C. (1999). Subsidence caused by gypsum dissolution at Ripon, North Yorkshire. *Quarterly Journal of Engineering Geology and Hydrogeology*, *32*, 305–310.

Darcy, H. P. G. (1856). *Les Fontaines publiques de la ville de Dijon.*. Dalmont.

Davidson, D., & Cole, R. (1950). Dielectric relaxation in glycerine. *The Journal of Chemical Physics*, *18*, 1417–1417.

Debye, P. J. W. (1929). *Polar molecules*. Chemical Catalog Company, Incorporated.

Desir, G., Gutiérrez, F., Merino, J., Carbonel, D., Benito-Calvo, A., Guerrero, J., & Fabregat, I. (2018). Rapid subsidence in damaging sinkholes: Measurement by high-precision leveling and the role of salt dissolution. *Geomorphology*, *303*, 393–409.

Dias, C. A. (2000). Developments in a model to describe low-frequency electrical polarization of rocks. *Geophysics*, *65*, 437–451.

Dou, J., Li, X., Yunus, A. P., Paudel, U., Chang, K.-T., Zhu, Z., & Pourghasemi, H. R. (2015). Automatic detection of sinkhole collapses at finer resolutions using a multi-component remote sensing approach. *Natural Hazards*, *78*, 1021–1044.

Dukhin, S. S. (1991). Electrokinetic phenomena of the second kind and their applications. *Advances in colloid and interface science*, *35*, 173–196.

Dunn, K.-J., Bergman, D. J., & LaTorraca, G. A. (2002). *Nuclear magnetic resonance: Petrophysical and logging applications* volume 32. Elsevier.

El-Sayed, A., Kassab, M., El Safori, Y., & Abass, A. (2005). Carbonate facies and its reservoir properties, west Tushka, South Western Desert, Egypt. In *First International Conference on the Geology of the Tethys, Cairo University* (pp. 267–278).

Festa, V., Fiore, A., Parise, M., & Siniscalchi, A. (2012). Sinkhole evolution in the Apulian karst of southern Italy: a case study, with some considerations on sinkhole hazards. *Journal of Cave and Karst Studies*, *74*, 137–147.

Florsch, N., Revil, A., & Camerlynck, C. (2014). Inversion of generalized relaxation time distributions with optimized damping parameter. *Journal of Applied Geophysics*, *109*, 119–132.

Folk, R. L. (1962). Spectral subdivision of limestone types. *American Association of Petroleum Geologists Special Volumes*, (pp. 62–84).

Ford, D., & Williams, P. D. (2013). *Karst hydrogeology and geomorphology*. John Wiley & Sons.

Frumkin, A., Ezersky, M., Al-Zoubi, A., Akkawi, E., & Abueladas, A.-R. (2011). The Dead Sea sinkhole hazard: Geophysical assessment of salt dissolution and collapse. *Geomorphology*, *134*, 102–117.

Galloway, D., Jones, D. R., & Ingebritsen, S. (1999). Land subsidence in the United States: US Geological Survey Circular 1182. *US Geological Survey: Reston, Virginia, VA, USA*, (p. 177).

Ghorbani, A., Camerlynck, C., & Florsch, N. (2009). Cr1dinv: A matlab program to invert 1d spectral induced polarization data for the cole–cole model including electromagnetic effects. *Computers & Geosciences*, *35*, 255–266.

Glover, P. (2015). Geophysical properties of the near surface Earth: Electrical properties. *Geophysics*, *11*, 89–137.

Gómez-Ortiz, D., & Martín-Crespo, T. (2012). Assessing the risk of subsidence of a sinkhole collapse using ground penetrating radar and electrical resistivity tomography. *Engineering Geology*, *149*, 1–12.

Grahame, D. C. (1947). The electrical double layer and the theory of electrocapillarity. *Chemical reviews*, *41*, 441–501.

Grombacher, D., Vanorio, T., & Ebert, Y. (2012). Time-lapse acoustic, transport, and NMR measurements to characterize microstructural changes of carbonate rocks during injection of CO_2-rich water. *Geophysics*, *77*, WA169–WA179.

Guéguen, Y., & Palciauskas, V. (1994). *Introduction to the physics of rocks*. Princeton University Press.

Gutiérrez, F. (2016). Sinkhole hazards. *Oxford Research Encyclopedia of Natural Hazard Science. Oxford University Press, Oxford*, (pp. 1–88).

Gutiérrez, F., Galve, J., Lucha, P., Bonachea, J., Jordá, L., & Jordá, R. (2009). Investigation of a large collapse sinkhole affecting a multi-storey building by means of geophysics and the trenching technique (Zaragoza city, NE Spain). *Environmental Geology*, *58*, 1107–1122.

Gutiérrez, F., Guerrero, J., & Lucha, P. (2008). A genetic classification of sinkholes illustrated from evaporite paleokarst exposures in Spain. *Environmental Geology*, *53*, 993–1006.

Gutiérrez, F., Parise, M., De Waele, J., & Jourde, H. (2014). A review on natural and human-induced geohazards and impacts in karst. *Earth-Science Reviews*, *138*, 61–88.

Halisch, M. (2013). *Application and Assessment of the Lattice Boltzmann Method for Fluid Flow Modeling in Porous Rocks*. Ph.D. thesis TU Berlin.

Halisch, M., Grelle, T., Hupfer, S., Blanke, J.-T., & Lehne, C. (2017). A new and modular laboratory core holder for high-precision measurements with low frequency impedance spectroscopy on natural rocks. In *Society of Core Analysts Annual Symposium, Proceedings, Vienna, 2017, SCA2017-069*.

Halisch, M., Schmitt, M., & Fernandes, C. P. (2016). Pore Shapes and Pore Geometry of Reservoirs Rocks from μ-CT Imaging and Digital Image Analysis. In *Proceedings of the Annual Symposium of the SCA*.

Halisch, M., Weller, A., & Kassab, M. A. (2014). Impedance spectroscopy on carbonates. In *Proceeding of the annual symposium of the Society of Core Analysis*. volume 36.

Hanai, T. (1960). Theory of the dielectric dispersion due to the interfacial polarization and its application to emulsions. *Kolloid-Zeitschrift*, *171*, 23–31.

Harris, R. E., & Holdsworth, D. (2016). Process for acidizing. US Patent App. 15/111,030.

Heard, H. C., & Griggs, D. T. (1972). *Flow and fracture of rocks*. American Geophysical Union.

Higuera-Díaz, I. C., Carpenter, P. J., & Thompson, M. D. (2007). Identification of buried sinkholes using refraction tomography at Ft. Campbell Army Airfield, Kentucky. *Environmental Geology*, *53*, 805–812.

Hördt, A., Bairlein, K., Bielefeld, A., Bücker, M., Kuhn, E., Nordsiek, S., & Stebner, H. (2016). The dependence of induced polarization on fluid salinity and pH, studied with an extended model of membrane polarization. *Journal of Applied Geophysics*, *135*, 408–417.

Hördt, A., Bairlein, K., Bücker, M., & Stebner, H. (2017). Geometrical constraints for membrane polarization. *Near Surface Geophysics*, *15*, 579–592.

Intrieri, E., Gigli, G., Nocentini, M., Lombardi, L., Mugnai, F., Fidolini, F., & Casagli, N. (2015). Sinkhole monitoring and early warning: An experimental and successful GB-InSAR application. *Geomorphology*, *241*, 304–314.

ISO9227 (2010). *Determination of the Specific Surface are of Solids by Gas Adsorption Using the BET Method*.

Ji, Y., Baud, P., Vajdova, V., & Wong, T.-F. (2012). Characterization of pore geometry of Indiana limestone in relation to mechanical compaction. *Oil & Gas Science and Technology–Revue d'IFP Energies nouvelles*, *67*, 753–775.

Johansson, S., Sparrenbom, C., Fiandaca, G., Lindskog, A., Olsson, P.-I., Dahlin, T., & Rosqvist, H. (2016). Investigations of a cretaceous limestone with spectral induced polarization and scanning electron microscopy. *Geophysical Journal International*, *208*, 954–972.

Jougnot, D., Ghorbani, A., Revil, A., Leroy, P., & Cosenza, P. (2010). Spectral induced polarization of partially saturated clay-rocks: A mechanistic approach. *Geophysical Journal International*, *180*, 210–224.

Kaufmann, G. (2014). Geophysical mapping of solution and collapse sinkholes. *Journal of Applied Geophysics*, *111*, 271–288.

Kaufmann, G., Romanov, D., Tippelt, T., Vienken, T., Werban, U., Dietrich, P., Mai, F., & Börner, F. (2018). Mapping and modelling of collapse sinkholes in soluble rock: The Münsterdorf site, northern Germany. *Journal of Applied Geophysics*, *154*, 64–80.

Kemna, A., Binley, A., Cassiani, G., Niederleithinger, E., Revil, A., Slater, L., Williams, K. H., Orozco, A. F., Haegel, F.-H., Hoerdt, A. et al. (2012). An overview of the spectral induced polarization method for near-surface applications. *Near Surface Geophysics*, *10*, 453–468.

Kemna, A., Räkers, E., & Dresen, L. (1999). Field applications of complex resistivity tomography. In *SEG Technical Program Expanded Abstracts 1999* (pp. 331–334). Society of Exploration Geophysicists.

Kjøller, C., Sigalas, L., Christensen, H. F., & Minde, M. (2016). A fast method for homogeneous dissolution of chalk specimens for laboratory experiments - documentation by X-ray CT-scanning and scanning electron microscopy. In

Society of Core Analysts Annual Symposium, Proceedings, Snowmass (Colorado), 2016.

Klinkenberg, L. et al. (1941). The permeability of porous media to liquids and gases. In *Drilling and production practice*. American Petroleum Institute.

Knödel, K., Krummel, H., & Lange, G. (2013). *Handbuch zur Erkundung des Untergrundes von Deponien und Altlasten: Band 3: Geophysik*. Springer-Verlag.

Kobe, M., Gabriel, G., Weise, A., & Vogel, D. (2019). Time-lapse gravity and levelling surveys reveal mass loss and ongoing subsidence in the urban subrosion-prone area of bad frankenhausen, germany. *Solid Earth*, *10*, 599–619.

Kozeny, J. (1927). Über kapillare Leitung des Wassers im Boden. *Royal Academy of Science, Vienna, Proc. Class I*, *136*, 271–306.

Kruschwitz, S., Binley, A., Lesmes, D., & Elshenawy, A. (2010). Textural controls on low-frequency electrical spectra of porous media. *Geophysics*, *75*, WA113–WA123.

Kruschwitz, S., Prinz, C., & Zimathies, A. (2016). Study into the correlation of dominant pore throat size and SIP relaxation frequency. *Journal of Applied Geophysics*, *135*, 375–386.

Langmuir, I. (1916). Adsorption of gases by solids. *J. Am. Chem. Soc*, *38*, 2267.

Lei, M., Gao, Y., Jiang, X., & Guan, Z. (2013). Emergency investigation of extremely large sinkholes, Maohe, Guangxi, China, .

Leroy, P., Devau, N., Revil, A., & Bizi, M. (2013). Influence of surface conductivity on the apparent zeta potential of amorphous silica nanoparticles. *Journal of colloid and interface science*, *410*, 81–93.

Leroy, P., Revil, A., Altmann, S., & Tournassat, C. (2007). Modeling the composition of the pore water in a clay-rock geological formation (Callovo-Oxfordian, France). *Geochimica et cosmochimica acta*, *71*, 1087–1097.

Leroy, P., Revil, A., Kemna, A., Cosenza, P., & Ghorbani, A. (2008). Complex conductivity of water-saturated packs of glass beads. *Journal of Colloid and Interface Science*, *321*, 103–117.

Lesmes, D., & Frye, K. (2001). Influence of pore fluid chemistry on the complex conductivity and induced polarization responses of Berea sandstone. *Journal of Geophysical Research*, *106*, 4079–4090.

Lowrie, W. (2007). *Fundamentals of geophysics.* Cambridge university press.

Maclay, R. W., & Small, T. A. (1984). *Carbonate geology and hydrology of the Edwards aquifer in the San Antonio area, Texas.* Technical Report US Geological Survey.

Markl, G. (2008). *Minerale und Gesteine: Mineralogie–Petrologie–Geochemie.* Springer-Verlag.

Marshall, D., & Madden, T. (1959). Induced polarisation, a study of its causes. *Geophysics*, *24*, 790–816.

Martinez, F. J., Batzle, M. L., & Revil, A. (2012). Influence of temperature on seismic velocities and complex conductivity of heavy oil-bearing sands. *Geophysics*, *77*, WA19–WA34.

Martinez, J. D., Johnson, K. S., & Neal, J. T. (1998). Sinkholes in evaporite rocks: surface subsidence can develop within a matter of days when highly soluble rocks dissolve because of either natural or human causes. *American Scientist*, *86*, 38–51.

Maxwell, J. C. (1865). A dynamical theory of the electromagnetic field. *Philosophical transactions of the Royal Society of London*, *155*, 459–512.

McDonnell, A., Loucks, R. G., & Dooley, T. (2007). Quantifying the origin and geometry of circular sag structures in northern Fort Worth Basin, Texas: Paleocave collapse, pull-apart fault systems, or hydrothermal alteration? *AAPG bulletin*, *91*, 1295–1318.

Meier, L. P., & Kahr, G. (1999). Determination of the cation exchange capacity (CEC) of clay minerals using the complexes of copper (II) ion with triethylenetetramine and tetraethylenepentamine. *Clays Clay Miner*, *47*, 386–388.

Miao, X., Qiu, X., Wu, S.-S., Luo, J., Gouzie, D. R., & Xie, H. (2013). Developing efficient procedures for automated sinkhole extraction from Lidar DEMs. *Photogrammetric Engineering & Remote Sensing*, *79*, 545–554.

Miensopust, M. P., Igel, J., Günther, T., Dlugosch, R., & Hupfer, S. (2015). Electric and Electromagnetic Investigation of a Karst System. In *Near Surface Geoscience 2015-21st European Meeting of Environmental and Engineering Geophysics.*

Mikulic, D. G., Kluessendorf, J. et al. (1999). *The classic Silurian reefs of the Chicago area.* Champaign, IL: Illinois State Geological Survey.

Militzer, H., & Weber, F. (1985). *Angewandte Geophysik: Band 2: Geoelektrik-Geothermik-Radiometrie-Aerogeophysik* volume 2. Springer.

Müller-Huber, E., Börner, F., Börner, J. H., & Kulke, D. (2018). Combined interpretation of NMR, MICP, and SIP measurements on mud-dominated and grain-dominated carbonate rocks. *Journal of Applied Geophysics*, *159*, 228–240.

Nabighian, M. N. (1988). *Electromagnetic methods in applied geophysics–Theory* volume 1. Society of Exploration Geophysicists, Tulsa, OK.

Niu, Q., Prasad, M., Revil, A., & Saidian, M. (2016). Textural control on the quadrature conductivity of porous media. *Geophysics*, *81*, E297–E309.

Norbisrath, J. H., Weger, R. J., & Eberli, G. P. (2017). Complex resistivity spectra and pore geometry for predictions of reservoir properties in carbonate rocks. *Journal of Petroleum Science and Engineering*, *151*, 455–467.

Nordsiek, S., & Weller, A. (2008). A new approach to fitting induced-polarization spectra. *Geophysics*, *73*, F235–F245.

Ohser, J., & Schladitz, K. (2009). *3D images of materials structures: processing and analysis*. John Wiley & Sons.

Öner, Ü., Weller, A., Sattler, C.-D., & Kassab, M. A. (2016). Petrographic and petrophysical investigation on carbonate samples (Upper Cretaceous) from the Tushka Area (Egypt) with special focus on the effective pore radius. *Arabian Journal of Geosciences*, *9*, 229.

Orozco, A. F., Kemna, A., & Zimmermann, E. (2012). Data error quantification in spectral induced polarization imaging. *Geophysics*, *77*, E227–E237.

Pape, H., Riepe, L., & Schopper, J. R. (1987). Theory of self-similar network structures in sedimentary and igneous rocks and their investigation with microscopical and physical methods. *Journal of Microscopy*, *148*, 121–147.

Patterson, D., Davey, J., Cooper, A., & Ferris, J. (1995). The application of microgravity geophysics in a phased investigation of dissolution subsidence at Ripon, Yorkshire. *Quarterly Journal of Engineering Geology*, *28*, 83–94.

Pelton, W., Ward, S., Hallof, P., Sill, W., & Nelson, P. (1978). Mineral discrimination and removal of inductive coupling with multifrequency IP. *Geophysics*, *43*, 588–609.

Radic, T. (2004). Elimination of cable effects while multi-channel SIP measurements. In *Near Surface 2004 - 10th European Meeting of Environmental and EngineeringGeophysics*. Utrecht, Niederlande.

Radic, T., & Halisch, M. (2017). Apparatur zur synchronen Messung der elektrischen Impedanz von 4 Gesteinsproben im Frequenzbereich 100 μHz - 250 kHz. In *77. Jahrestagung der Deutschen Geophysikalischen Gesellschaft*.

Radon, J. (1917). Über die Bestimmung von Funktionen durch ihre Integralwerte längs gewisser Mannigfaltigkeiten. *Akademie der Wissenschaften Leipzig*, *69*, 262.

Rawal, K., Wang, Z.-M., & Hu, L.-B. (2015). Exploring the Geomechanics of Sinkholes: A Numerical Simulation Approach. In *Geo-Chicago 2016* (pp. 372–381).

Revil, A. (2012). Spectral induced polarization of shaly sands: Influence of the electrical double layer. *Water Resources Research*, *48*.

Revil, A. (2013a). Effective conductivity and permittivity of unsaturated porous materials in the frequency range 1 mHz - 1 GHz. *Water Resources Research*, *49*, 1–22.

Revil, A. (2013b). On charge accumulation in heterogeneous porous rocks under the influence of an external electric field. *Geophysics*, *78*, D271–D291.

Revil, A. (2014). Comment on ”On the relationship between induced polarization and surface conductivity: Implications for petrophysical interpretation of electrical measurements” (Weller, A. and Slater, L. and Nordsiek, S., 2014, Geophysics, 78, no. 5, D315–D325). *Geophysics*, *79*, X1–X5.

Revil, A., Binley, A., Mejus, L., & Kessouri, P. (2015). Predicting permeability from the characteristic relaxation time and intrinsic formation factor of complex conductivity spectra. *Water Resources Research*, *51*, 6672–6700.

Revil, A., & Cathles III, L. (1999). Permeability of shaly sands. *Water Resources Research*, *35*, 651–662.

Revil, A., & Florsch, N. (2010). Determination of permeability from spectral induced polarization in granular media. *Geophysical Journal International*, *181*, 1480–1498.

Revil, A., Florsch, N., & Camerlynck, C. (2014). Spectral induced polarization porosimetry. *Geophysical Journal International*, *198*, 1016–1033.

Revil, A., & Glover, P. (1997). Theory of ionic-surface electrical conduction in porous media. *Physical Review B*, *55*, 1757.

Revil, A., Karaoulis, M., Johnson, T., & Kemna, A. (2012a). Some low-frequency electrical methods for subsurface characterization and monitoring in hydrogeology. *Hydrogeology Journal*, *20*, 617–658.

Revil, A., Koch, K., & Holliger, K. (2012b). Is it the grain size or the characteristic pore size that controls the induced polarization relaxation time of clean sands and sandstones? *Water Resources Research*, *48*, W05602.

Revil, A., Schmutz, M., & Batzle, M. L. (2011). Influence of oil wettability upon spectral induced polarization of oil-bearing sands. *Geophysics*, *76*, A31–A36.

Rink, M., & Schopper, J. (1974). Interface conductivity and its implications to electric logging. In *SPWLA 15th Annual Logging Symposium*. Society of Petrophysicists and Well-Log Analysts.

Robinson, J., Slater, L., Weller, A., Keating, K., Robinson, T., Rose, C., & Parker, B. (2018). On permeability prediction from complex conductivity measurements using polarization magnitude and relaxation time. *Water Resources Research*, *54*, 3436–3452.

Rodriguez, V., Gutiérrez, F., Green, A., Carbonel, D., Horstmeyer, H., & Schmelzbach, C. (2014). Characterizing sagging and collapse sinkholes in a mantled karst by means of ground penetrating radar (GPR). *Environmental & engineering geoscience*, *20*, 109–132.

RP40, A. P. I. (1998). *Recommended practices for core analysis*. API Publishing Services. Second edition.

Rubin, Y., & Hubbard, S. S. (2006). *Hydrogeophysics* volume 50. Springer Science & Business Media.

Rybakov, M., Rotstein, Y., Shirman, B., & Al-Zoubi, A. (2005). Cave detection near the Dead SeaŮa micromagnetic feasibility study. *The Leading Edge*, *24*, 585–590.

Sahu, P., & Lokhande, R. D. (2015). An investigation of sinkhole subsidence and its preventive measures in underground coal mining. *Procedia Earth and Planetary Science*, *11*, 63–75.

Sargent, C., & Goulty, N. (2009). Seismic reflection survey for investigation of gypsum dissolution and subsidence at Hell Kettles, Darlington, UK. *Quarterly journal of engineering geology and hydrogeology.*, *42*, 31–38.

Schmitt, M., Halisch, M., Müller, C., & Fernandes, C. P. (2016). Classification and quantification of pore shapes in sandstone reservoir rocks with 3-D X-ray micro-computed tomography. *Solid Earth*, *7*, 285–300.

Schmutz, M., Revil, A., Vaudelet, P., Batzle, M., Viñao, P. F., & Werkema, D. (2010). Influence of oil saturation upon spectral induced polarization of oil-bearing sands. *Geophysical Journal International*, *183*, 211–224.

Schön, J. (2004). *Physical Properties of Rocks - Fundamentals and Principles of Petrophysics* volume 18. Elsevier.

Schwarz, G. (1962). A theory of the low-frequency dielectric dispersion of colloidal particles in electrolyte solution. *J. Phys. Chem.*, *66*, 2636–2642.

Scott, J., & Barker, R. (2003). Determining pore-throat size in Permo-Triassic sandstones from low-frequency electrical spectroscopy. *Geophysical Research Letters*, *30*, 1450.

Scott, J., & Barker, R. (2005). Characterization of sandstone by electrical spectroscopy for stratigraphical and hydrogeological investigations. *Quarterly Journal of Engineering Geology and Hydrogeology*, *38*, 143–154.

Seigel, H., Nabighian, M., Parasnis, D., & Vozoff, K. (2007). The early history of the induced polarization method. *The Leading Edge*, *26*, 312–321.

Siever, R., Press, F., Grotzinger, J., & Jordan, T. H. (2004). *Understanding Earth.* WH Freeman.

Sing, K. (2001). The use of nitrogen adsorption for the characterisation of porous materials. *Colloids and Surfaces A: Physicochemical and Engineering Aspects*, *187*, 3–9.

Skold, M., Revil, A., & Vaudelet, P. (2011). The pH dependence of spectral induced polarization of silica sands: Experiment and modeling. *Geophysical Research Letters*, *38*, L12304.

Slater, L. (2007). Near surface electrical characterization of hydraulic conductivity: From petrophysical properties to aquifer geometries-A review. *Surveys in Geophysics*, *28*, 169–197.

Slater, L., & Binley, A. (2006). Synthetic and field-based electrical imaging of a zerovalent iron barrier: Implications for monitoring long-term barrier performance. *Geophysics*, *71*, B129–B137.

Slater, L., & Glaser, D. (2003). Controls on induced polarization in sandy unconsolidated sediments and application to aquifer characterization. *Geophysics*, *68*, 1547–1558.

Slater, L., & Lesmes, D. (2002). IP interpretation in environmental investigations. *Geophysics*, *67*, 77–88.

Slater, L. D., Choi, J., & Wu, Y. (2005). Electrical properties of iron-sand columns: Implications for induced polarization investigation and performance monitoring of iron-wall barriers. *Geophysics*, *70*, G87–G94.

Smyth, C. H. (1913). The relative solubilities of the chemical constituents of rocks. *The Journal of Geology*, *21*, 105–120.

Song, K.-I., Cho, G.-C., & Chang, S.-B. (2012). Identification, remediation, and analysis of karst sinkholes in the longest railroad tunnel in South Korea. *Engineering Geology*, *135*, 92–105.

Stebner, H., Halisch, M., & Hördt, A. (2017). Simulation of membrane polarization of porous media with impedance networks. *Near Surface Geophysics*, *15*, 563–578.

Stern, O. (1924). Zur Theorie der elektrolytischen Doppelschicht. *Zeitschrift für Elektrochemie und angewandte physikalische Chemie*, *30*, 508–516.

Telford, W. M., Telford, W., Geldart, L., & Sheriff, R. E. (1990). *Applied geophysics* volume 1. Cambridge university press.

Teufel, L. W., & Clark, J. A. (1981). *Hydraulic-fracture propagation in layered rock: experimental studies of fracture containment*. Technical Report Sandia National Labs., Albuquerque, NM (USA).

Tiab, D., & Donaldson, E. C. (2012). *Petrophysics: Theory and Practice of Measuring Reservoir Rock and Fluid Transport Properties*. Gulf professional publishing.

Tihansky, A. B. (1999). Sinkholes, west-central florida. *Land subsidence in the United States: US geological survey circular*, *1182*, 121–140.

Tipler, P. A., & Mosca, G. (2007). *Physics for scientists and engineers*. Macmillan.

Titov, K., Komarov, V., Tarasov, V., & Levitski, A. (2002). Theoretical and experimental study of time domain-induced polarization in water-saturated sands. *Journal of Applied Geophysics*, *50*, 417–433.

Titov, K., Tarasov, A., Ilyin, Y., Seleznev, N., & Boyd, A. (2010). Relationships between induced polarization relaxation time and hydraulic properties of sandstone. *Geophysical Journal International*, *180*, 1095–1106.

Tucker, M. E., & Wright, V. P. (1990). *Carbonate sedimentology.* John Wiley & Sons.

Tuckwell, G., Grossey, T., Owen, S., & Stearns, P. (2008). The use of microgravity to detect small distributed voids and low-density ground. *Quarterly Journal of Engineering Geology and Hydrogeology*, *41*, 371–380.

Ullrich, C., & Slater, L. (2004). Induced polarization measurements on unsaturated, unconsolidated sand. *Geophysics*, *69*, 762–771.

Van Voorhis, G., Nelson, P., & Drake, T. (1973). Complex resistivity spectra of porphyry copper mineralization. *Geophysics*, *38*, 49–60.

Vanhala, H., & Peltoniemi, M. (1992). Spectral IP studies of Finnish ore prospects. *Geophysics*, *57*, 1545–1555.

Vanorio, T., Nur, A., & Ebert, Y. (2011). Rock physics analysis and time-lapse rock imaging of geochemical effects due to the injection of co_2 into reservoir rocks. *Geophysics*, *76*, O23–O33.

Vaudelet, P., Revil, A., Schmutz, M., Franceschi, M., & Bégassat, P. (2011). Induced polarization signatures of cations exhibiting differential sorption behaviors in saturated sands. *Water Resources Research*, *47*.

Vinegar, H., & Waxman, M. (1984). Induced polarization of shaly sands. *Geophysics*, *49*, 1267–1287.

Volkmann, J., & Klitzsch, N. (2010). Frequency-dependent electric properties of microscale rock models for frequencies from one millihertz to ten kilohertz. *Vadose Zone Journal*, *9*, 858–870.

Volkmann, J., & Klitzsch, N. (2016). Evaluation of low frequency polarization models using well characterized sintered porous glass samples. *Journal of Applied Geophysics*, *124*, 39–53.

Wadas, S. H., Polom, U., & Krawczyk, C. M. (2016). High-resolution shear-wave seismic reflection as a tool to image near-surface subrosion structures-a case study in Bad Frankenhausen, Germany. *Solid Earth*, *7*, 1491.

Wadas, S. H., Tanner, D. C., Polom, U., & Krawczyk, C. M. (2017). Structural analysis of S-wave seismics around an urban sinkhole: evidence of enhanced dissolution in a strike-slip fault zone. *Natural Hazards and Earth System Sciences*, *17*, 2335.

Wagner, K. W. (1914). Erklärung der dielektrischen nachwirkungsvorgänge auf grund maxwellscher vorstellungen. *Electrical Engineering (Archiv für Elektrotechnik)*, *2*, 371–387.

Waltham, T. (2002). The engineering classification of karst with respect to the role and influence of caves. *International Journal of Speleology*, *31*, 2.

Waltham, T., Waltham, A. C., Bell, F. G., & Culshaw, M. G. (2005). *Sinkholes and subsidence: karst and cavernous rocks in engineering and construction*. Springer Science & Business Media.

Warburg, E. (1899). Über das Verhalten sogenannter unpolarisierbarer Elektroden gegen Wechselstrom. *Annalen der Physik*, *303*, 493–499.

Ward, S. H. (1990). Resistivity and induced polarization methods. In *Geotechnical an Environmental Geophysics: Volume I: Review and Tutorial* (pp. 147–190). Society of Exploration Geophysicists.

Washburn, E. W. (1921). The dynamics of capillary flow. *Physical review*, *17*, 273.

Waxman, M., & Smits, L. (1968). Electrical Conductivities in Oil-Bearing Shaly Sands. *Society of Petroleum Engineers Journal*, (pp. 107–122).

Weller, A., Breede, K., Slater, L., & Nordsiek, S. (2011). Effect of changing water salinity on complex conductivity spectra of sandstones. *Geophysics*, *76*, F315–F327.

Weller, A., Nordsiek, S., & Debschütz, W. (2010a). Estimating permeability of sandstone samples by nuclear magentic resonance and spectral-induced polarization. *Geophysics*, *75*, E215–E226.

Weller, A., & Slater, L. (2012). Salinity dependence of complex conductivity of unconsolidated and consolidated materials: Comparisons with electrical double layer models. *Geophysics*, *77*, D185–D198.

Weller, A., & Slater, L. (2015). Induced polarization dependence on pore space geometry: Empirical observations and mechanistic predictions. *Journal of Applied Geophysics*, *123*, 310–315.

Weller, A., Slater, L., Binley, A., Nordsiek, S., & Xu, S. (2015a). Permeability prediction based on induced polarization: Insights from measurements on sandstone and unconsolidated samples spanning a wide permeability range. *Geophysics*, *80*, D161–D173.

Weller, A., Slater, L., Huisman, J. A., Esser, O., & Haegel, F.-H. (2015b). On the specific polarizability of sands and sand-clay mixtures. *Geophysics*, *80*, A57–A61.

Weller, A., Slater, L., & Nordsiek, S. (2013). On the relationship between induced polarization and surface conductivity: Implications for petrophysical interpretation of electrical measurements. *Geophysics*, *78*, D315–D325.

Weller, A., Slater, L., & Nordsiek, S. (2014). Reply on comment on ”On the relationship between induced polarization and surface conductivity: Implications for petrophysical interpretation of electrical measurements” (Weller, A. and Slater, L. and Nordsiek, S., 2014, Geophysics, 78, no. 5, D315–D325). *Geophysics*, *79*, X5–X10.

Weller, A., Slater, L., Nordsiek, S., & Ntarlagiannis, D. (2010b). On the estimation of specific surface per unit pore volume from induced polarisation: A robust empirical relation fits muliple datasets. *Geophysics*, *75*, WA105–WA112.

Weller, A., Zhang, Z., & Slater, L. (2015c). High-salinity polarization of sandstones. *Geophysics*, *80*, D309–D318.

Weller, A., Zhang, Z., Slater, L., Kruschwitz, S., & Halisch, M. (2016). Induced polarization and pore radius – A discussion. *Geophysics*, *81*, D519–D526.

Willman, H. B. (1973). *Rock stratigraphy of the Silurian System in northeastern and northwestern Illinois*. Urbana, Illinois State Geological Survey.

Wong, J. (1979). An electrochemical model of the induced-polarization phenomenon in disseminated sulfides ores. *Geophysics*, *44*, 1245–1265.

Wu, Y., Hubbard, S., Williams, K. H., & Ajo-Franklin, J. (2010). On the complex conductivity signatures of calcite precipitation. *Journal of Geophysical Research: Biogeosciences*, *115*.

Yechieli, Y., Abelson, M., Wachs, D., Shtivelman, V., Crouvi, O., & Baer, G. (2003). Formation of sinkholes along the shore of the dead sea-preliminary investigation. In *Sinkholes and the Engineering and Environmental Impacts of Karst* (pp. 184–194).

Zhang, Z., Weller, A., & Kruschwitz, S. (2017). Pore radius distribution and fractal dimension derived from spectral induced polarisation. *Near Surface Geophysics*, *15*, 625–632.

Zhang, Z., Weller, A., Kruschwitz, S., & Nordsiek, S. (2019). Effect of evaporative drying on complex conductivity spectra of sandstones. *Geophysics*, *84*, MR61–MR72.

Zimmermann, E., Kemna, A., Berwix, J., Glaas, W., & H.Vereecken (2008a). EIT measurement system with high phase accuracy for the imaging of spectral induced polarization properties of soil and sediments. *Measurement Science and Technology*, *19*.

Zimmermann, E., Kemna, A., Berwix, J., Glaas, W., Münch, H., & Huisman, J. (2008b). A high-accuracy impedance spectrometer for measuring sediments with low polarizability. *Measurement Science and Technology*, *19*.

Zingg, T. (1935). *Beitrag zur Schotteranalyse.* Ph.D. thesis ETH Zurich.

Zisser, N., Kemna, A., & Nover, G. (2010). Relationship between low-frequency electrical properties and hydraulic permeability of low-permeability sandstones. *Geophysics*, *75*, E131–E141.

Zisser, N., & Nover, G. (2009). Anisotropy of permeability and complex resistivity of tight sandstones subjected to hydrostatic pressure. *Journal of Applied Geophysics*, *68*, 356–370.

List of Symbols

Symbol	Meaning	Dimension
A	cross section	m^2
$\mathbf{B}$	magnetic field	T
c	BET parameter	none
c_0	ion strength	mol·m^{-3}
d	(a) grain density (d_{gr}) derived by TWM (d_{a}) and derived by pycnometry (d_{p})	g·cm^{-3}
	(b) diameter	m
D	diffusion coefficient	m^2·s^{-1}
$\mathbf{D}$	electric displacement field	C·m^{-2}
e	elementary charge ($e = 1.602 \cdot 10^{-19}$)	C
$\mathbf{E}$	electric field intensity	V·m^{-1}
f	technical frequency	Hz
F	formation factor	none
$\mathbf{H}$	magnetic field intensity	A·m^{-1}
I	electric current	A
$\mathbf{J}$	current density	A·m^{-2}
k	permeability	m^2 or mD
k_{B}	Boltzmann constant $k_{\mathrm{B}} = 1.38064852 \cdot 10^{-23}$	kg·m^2·s^{-2}·K^{-1}
K_n	Knudsen number	none
l	length	m
m	(a) mass	g
	(b) chargeabiliy	none
	(c) cementation exponent	none
n	(a) amount of substance	mol
	(b) capacity	mol·g^{-1}
N_{A}	Avogadro-constant ($\mathrm{N_A} = 6.022 \cdot 10^{23}$)	mol^{-1}
p	pressure	Pa or N·cm^{-2}
Q	flow rate	m^3·s^{-1}
r	radius	m

R	(a) gas constant ($k_B N_A = R = 8.31541$)	J·K^{-1}·mol^{-1}
	(b) resistance	Ω
S_{m}	surface area per mass	m$^2 \cdot g^{-1}$
S_{por}	surface area related to pore volume	μm^{-1}
S_{w}	water saturation	none
T	(a) (absolute) temperature	(K) or °C
	(b) period	s
	(c) NMR relaxation time	s
U	electric voltage	V
V	volume	m^3
Z	electrical impedance	Ω
α	Klinkenberg-factor	
γ	surface tension	N·m^{-1}
ϵ	dielectric permittivity	A·s·V^{-1}·m^{-1}
ϵ_{r}	dielectric constant	none
ϵ_0	permittivity of free space/vacuum	A·s·V^{-1}·m^{-1}
	$\epsilon_0 = 8.85 \cdot 10^{-12}$	
η	viscosity	Pa·s
θ	wetting angle of contact	°
	incident angle	°
λ	wavelength	m
μ	ion mobility	m^2·V^{-1}·s^{-1}
ρ	electrical resistivity	Ωm
ρ_{S}	surface relaxivity	μm·s^{-1}
σ	electrical conductivity	S·m^{-1}
σ_{surf}	electrical surface conductivity	S·m^{-1}
σ_{w}	electrical fluid conductivity	S·m^{-1}
Φ	porosity	% or none
φ	phase shift	mrad
τ	relaxation time	s
ω	angular frequency	rad·s^{-1}

List of Figures

List of Tables

Acknowledgements

While completing this PhD thesis, I was supported by many people, who I want to thank at this point.

First of all, want to thank my colleague and supervisor Matthias Halisch for his valuable scientific guidance, many useful hints, comments, discussions and help during this thesis and my time at LIAG. I was able to benefit and learn from his expertise. Thanks for your trust in my skills and for keeping me on track. Special thanks to my doctoral supervisor Andreas Weller for many fruitful discussions, his input, his patience while explaining advanced SIP theory and for pushing my thesis straight forward to the finishing line. I thank Sabine Kruschwitz for taking up the position as second reviewer and for all the scientific discussions during my thesis.

I also want to thank the other members of the junior research group ‘Subrosion’, especially Sonja Wadas and Martin Kobe for their hard work while proofreading the manuscript. Further thanks goes to all my colleagues at LIAG and in section S5. Special thanks to the Calisthenics group for our regular Tuesday lunch breaks together, with their strenuous and challenging exercises. Keep it up! I thank Thomas Burschil for his special ability to convince me to do many activities at times where I was actually quite busy.

I would like to thank Stephan Kaufhold and Maria Sitnikova (both Federal Institute for Geosciences and Natural Resources, BGR) for their support with the ESEM-imaging. Additionally, I would like to thank the company Cleansorb (Guildford, UK) for providing the Acidgen$^{\text{TM}}$FG3 that has been used for this study. I thank Hans-Peter Plumhoff of Westphal Precision technology for the realisation of our idea of an experimental setup for systematic dissolution experiments.

Finally, I would like to thank my family, especially Mathias Ronczka, for their help, support and motivational words.

A Figures

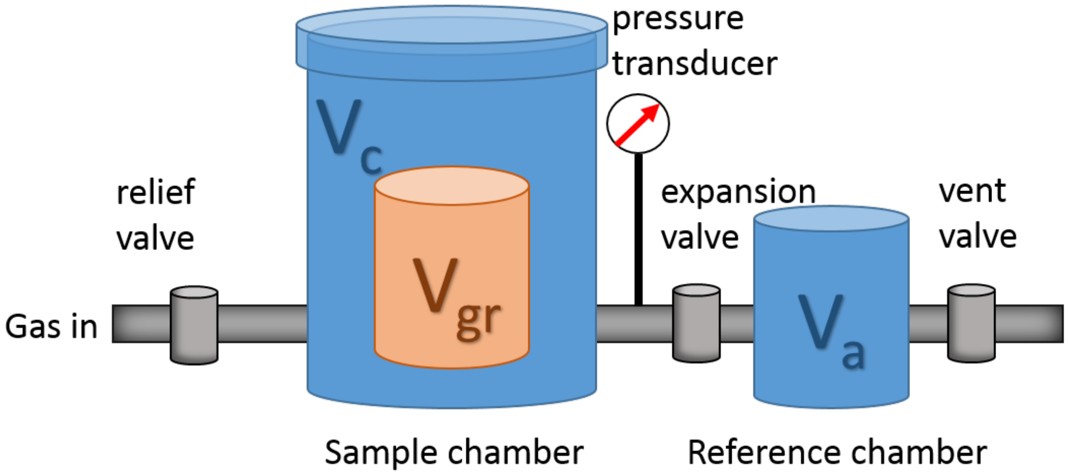

Figure A.1: Schematic view of the principles operations of the pycnometer. This two-chamber system (V_c, V_a) provide the grain volume V_gr after measuring the pressure on two conditions.

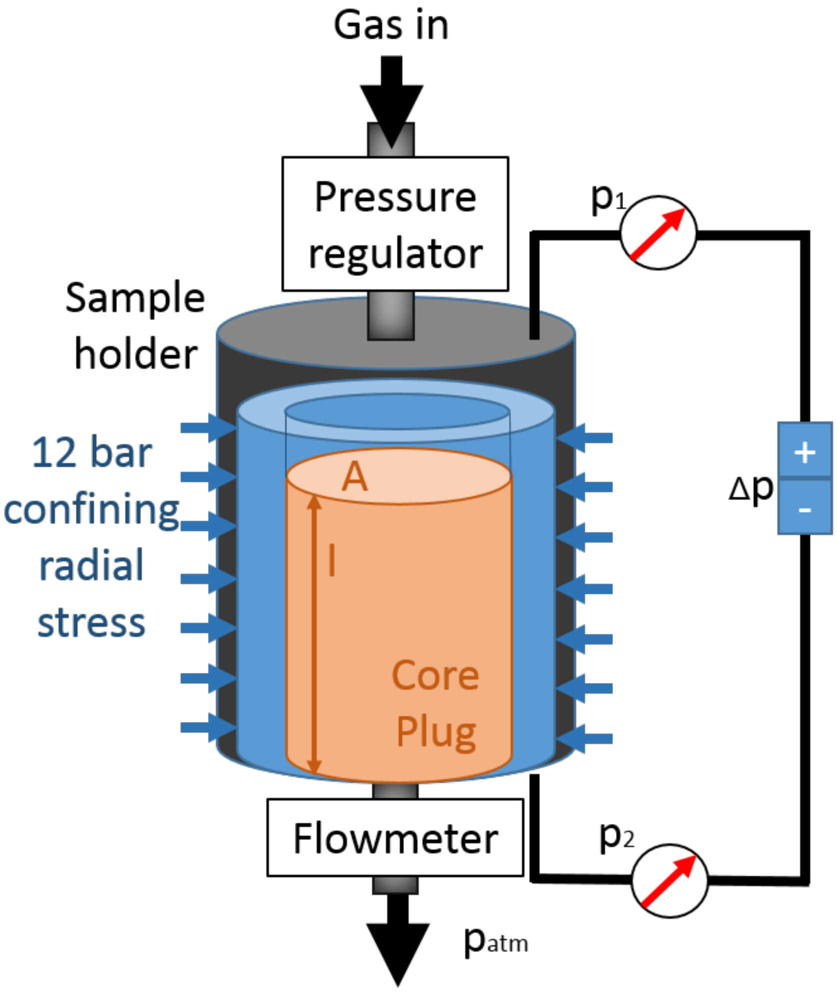

Figure A.2: Schematic view of the principles operation of the permeameter.

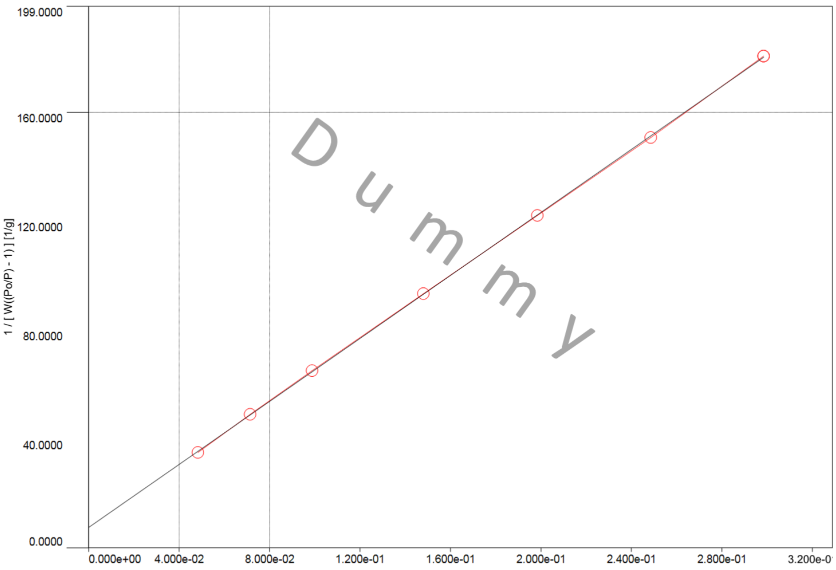

Figure A.3: Screenshot of an exemplified graphic of a seven point BET-measurement. It shows the relative pressure versus the left part of Eq. 3.13 and the calculated linear regression $y = a \cdot x + b$ (Eq. 3.14, 3.15).

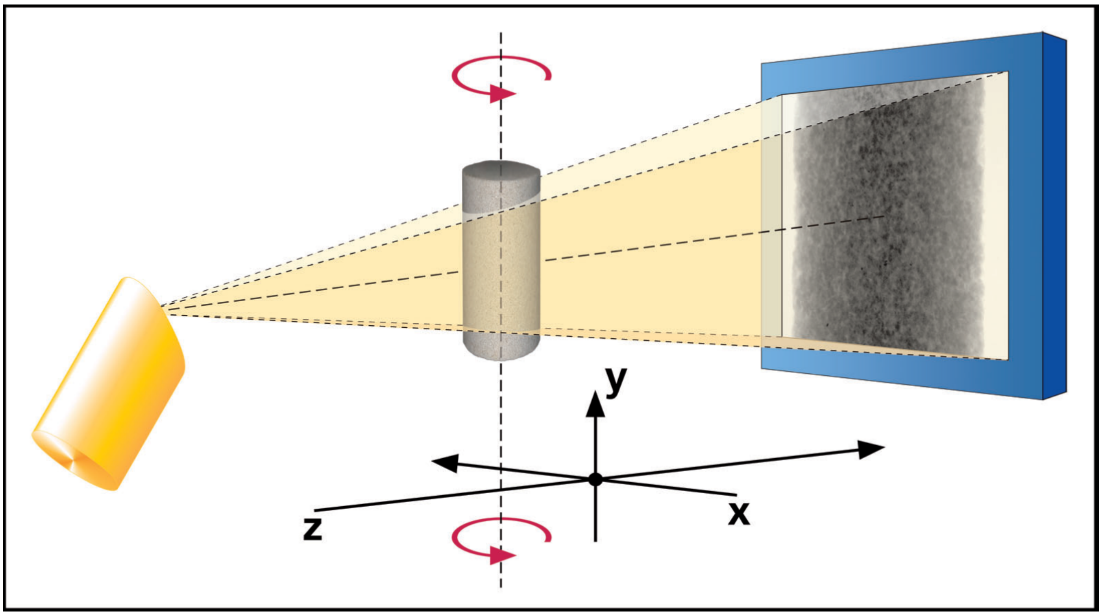

Figure A.4: Schematic view of the basic setup of a μ-CT scanner. The three main components are X-ray-source (left), the computerised numerical control unit with the sample (middle) and the special detector unit (right) (Halisch, 2013).

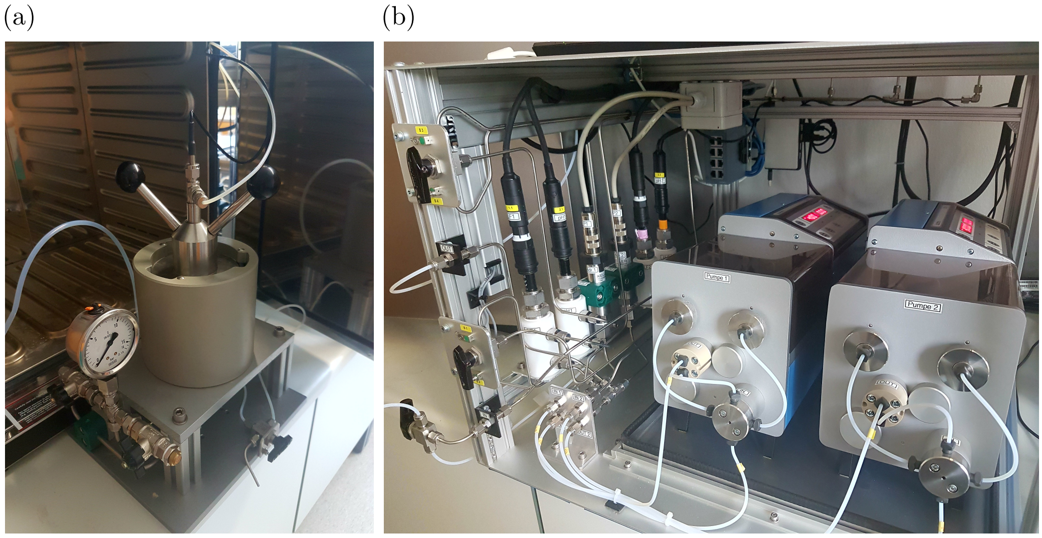

Figure A.5: Experimental setup of the acidification treatment procedure without reservoir tanks. a) Core holder with temperature sensor inside a furnace for sample saturation and cleaning. b) High precision piston pumps for each fluid, including pressure measurement between core holder inflow and piston pumps and pH-value and fluid conductivity monitoring at both, inflow and outflow side.

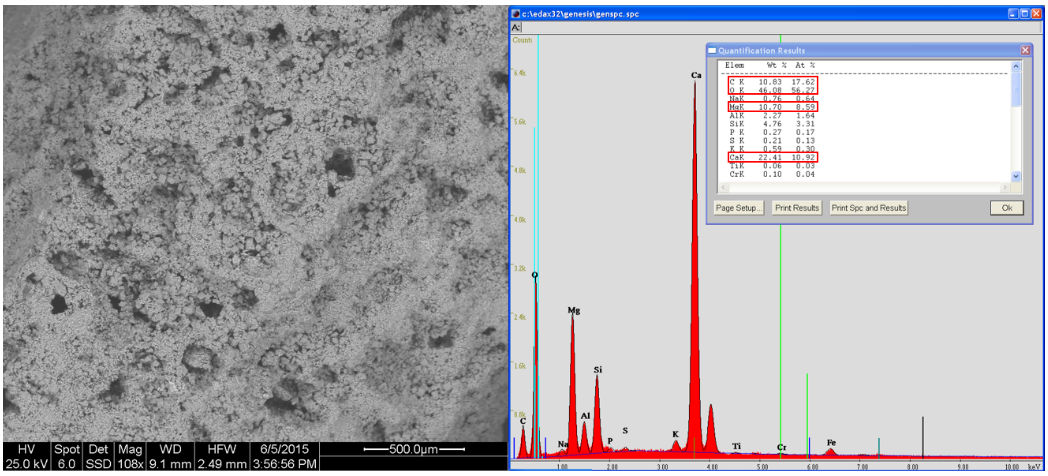

```
 Elem      Wt %   At %
---------------------------------------------------------
 C K      10.83   17.62
 O K      46.08   56.27
 NaK       0.76    0.64
 MgK      10.70    8.59
 AlK       2.27    1.64
 SiK       4.76    3.31
 P K       0.27    0.17
 S K       0.21    0.13
 K K       0.59    0.30
 CaK      22.41   10.92
 TiK       0.06    0.03
 CrK       0.10    0.04
```

Figure A.6: The ESEM-image of the EBK (left) is basis for EDX spectrum and the resulting quantification (right). The detected major elements (red boxes) are carbon (C), oxygen (O), calcium (Ca) and magnesium (Mg). Dolomite ($MgCa(CO_3)_2$) represents an amount of 90 wt% of the total.

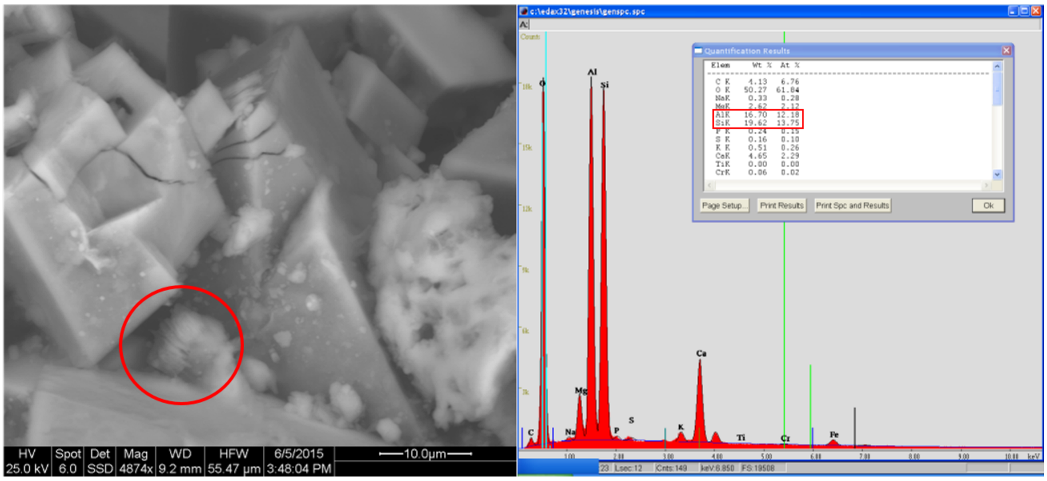

```
 Elem      Wt %   At %
-----------------------------------------------------------
  C K     4.13   6.76
  O K    50.27  61.84
  NaK     0.33   0.28
  MgK     2.62   2.12
  AlK    16.70  12.18
  SiK    19.62  13.75
  P K     0.24   0.15
  S K     0.16   0.10
  K K     0.51   0.26
  CaK     4.65   2.29
  TiK     0.00   0.00
  CrK     0.06   0.02
```

Figure A.7: The red marked part of the ESEM-image of the EBK (left) is basis for the EDX spectrum and the resulting quantification (right). The high content of Aluminium (Al) and silicon (Si) (red boxes) leads to the conclusion of the occurrence of kaolinite. Hence, the layered material in the red circle is a clay mineral.

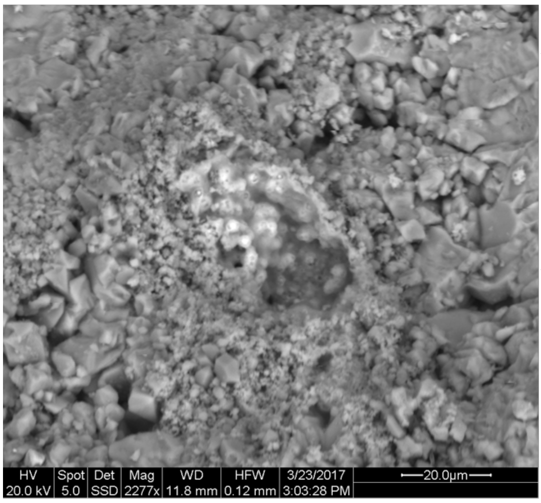

Label :
Acquisition Time : 14:56:36 Date:23-Mar-2017
kV : 20.00 Tilt: 0.00 Take-off:36.11 AmpT : 1.60
Detector Type: SDD Apollo XL Resolution:139.33 Lsec 10

Element	Wt %	At %
C K	15.04	25.67
O K	37.52	48.07
NaK	0.78	0.69
MgK	1.61	1.36
AlK	1.10	0.83
SiK	3.64	2.66
P K	0.68	0.45
S K	0.60	0.38
ClK	0.47	0.27
K K	0.47	0.25
CaK	37.18	19.01
TiK	0.35	0.15
FeK	0.56	0.21
Total	100.00	100.00

Figure A.8: The ESEM-image of the LK (left) is basis for EDX spectrum and the resulting quantification (right). The detected major elements are carbon (C), oxygen (O_2) and calcium (Ca). Calcium carbonate ($CaCO_3$) represents an amount of 90 wt% of the total.

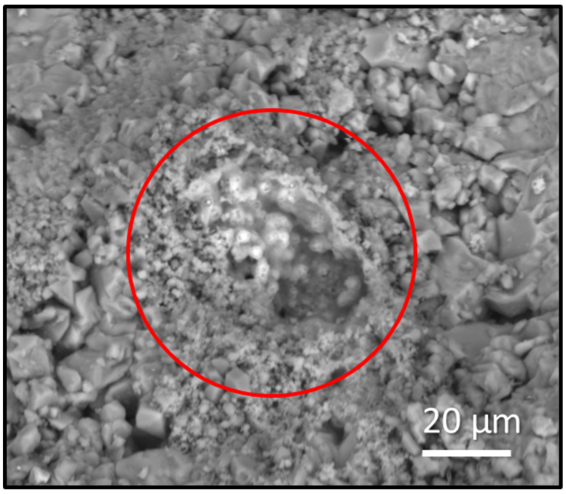

Label :
Acquisition Time : 15:09:12 Date:23-Mar-2017
kV : 20.00 Tilt: 0.00 Take-off:36.05 AmpT : 1.60
Detector Type: SDD Apollo XL Resolution:139.33
Lsec 5

Element	**Wt %**	**At %**
C K	7.26	13.03
O K	**43.78**	**58.97**
NaK	0.38	0.36
MgK	**1.41**	**1.25**
AlK	**5.69**	**4.54**
SiK	**11.51**	**8.83**
P K	0.09	0.07
S K	0.20	0.14
ClK	0.04	0.02
K K	**1.10**	**0.61**
CaK	**7.80**	**4.19**
TiK	0.22	0.10
FeK	**20.09**	**7.75**
ZnK	0.42	0.14
Total	**100.00**	**100.00**

Figure A.9: The red marked part of the ESEM-image of the LK (left) is basis for the EDX spectrum and the resulting quantification (right). The high content of iron (Fe) and oxygen (O_2) (red boxes) leads to the conclusion of the occurrence of iron oxide. The high amount of aluminium (Al) and silicon (Si) provide the assumption of the presence of a clay mineral.

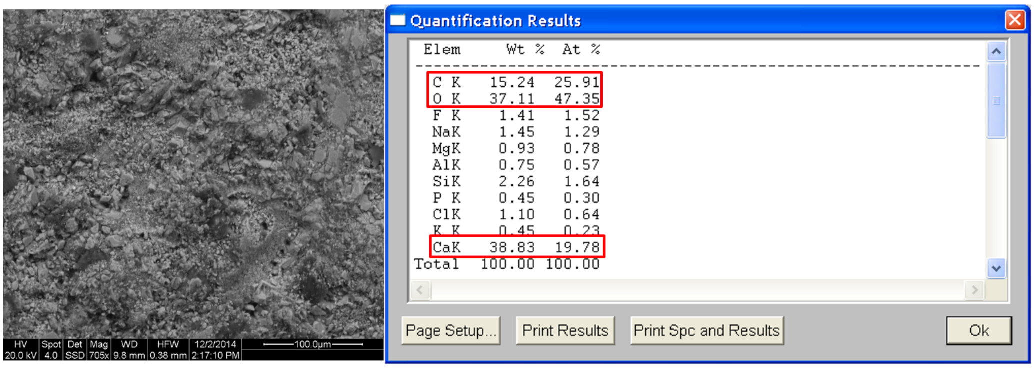

```
Elem      Wt %   At %
-------------------------------------------------------------
  C K    15.24  25.91
  O K    37.11  47.35
  F K     1.41   1.52
  NaK     1.45   1.29
  MgK     0.93   0.78
  AlK     0.75   0.57
  SiK     2.26   1.64
  P K     0.45   0.30
  ClK     1.10   0.64
  K K     0.45   0.23
  CaK    38.83  19.78
Total   100.00 100.00
```

Figure A.10: The ESEM-image of the ILS (left) is basis for EDX spectrum and the resulting quantification (right). The detected major elements (red boxes) are carbon (C), oxygen (O), calcium (Ca): Calcium carbonate ($CaCO_3$) represents an amount of 91 wt% of the total.

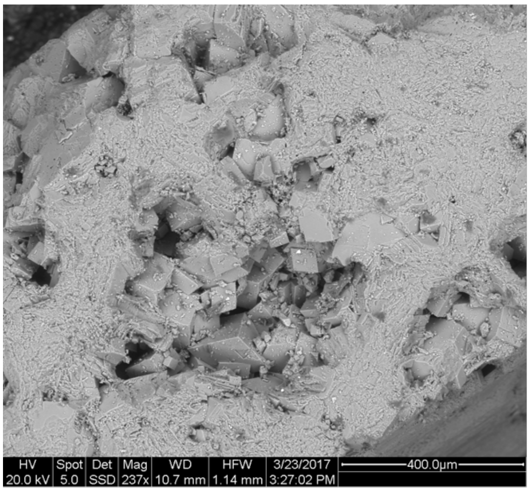

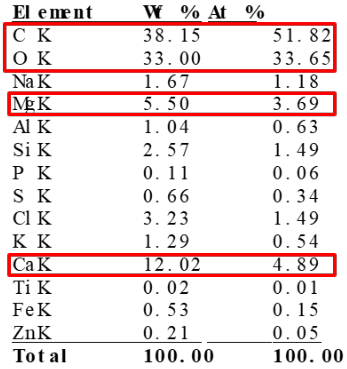

Element	Wt %	At %
C K	38.15	51.82
O K	33.00	33.65
NaK	1.67	1.18
MgK	5.50	3.69
Al K	1.04	0.63
Si K	2.57	1.49
P K	0.11	0.06
S K	0.66	0.34
Cl K	3.23	1.49
K K	1.29	0.54
CaK	12.02	4.89
Ti K	0.02	0.01
FeK	0.53	0.15
ZnK	0.21	0.05
Total	**100.00**	**100.00**

Figure A.11: The ESEM-image of the DOL (left) is basis for EDX spectrum and the resulting quantification (right). The detected major elements (red boxes) are carbon (C), oxygen (O), calcium (Ca) and magnesium (Mg): Dolomite ($MgCa(CO_3)_2$) represents an amount of 88.5 wt% of the total.

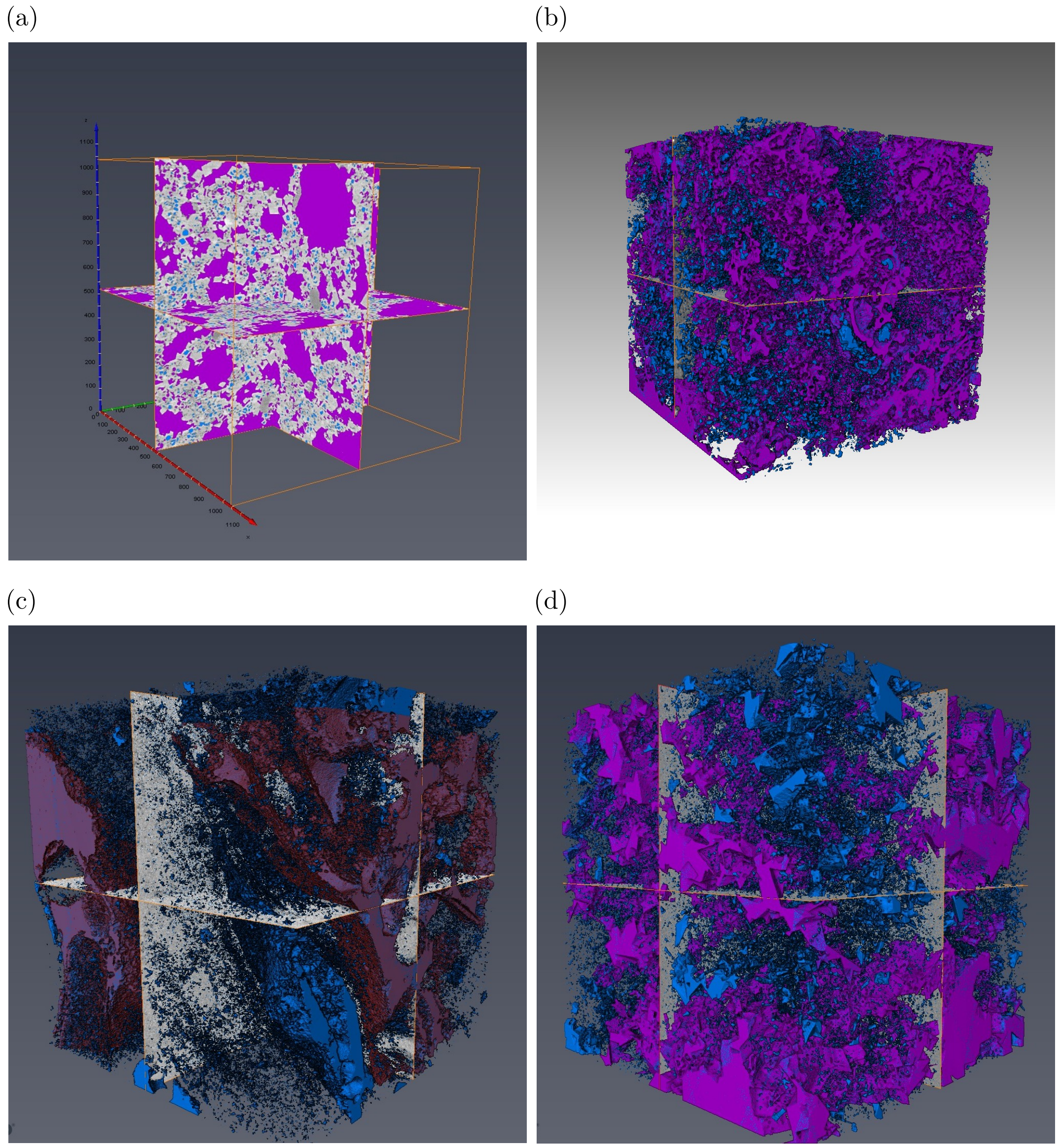

Figure A.12: Visualisation of the connected (purple) and unconnected pore space (blue) after the generalised workflow of pore network extraction of a μ-CT measurement.
a) Slices in x,y and z direction of pore network generated of 3D μ-CT data for the EBK sample. The connected porosity is 40.8 % compared to the total porosity of 43.6 %. b) 3D pore network visualisation generated of 3D μ-CT data for the LK sample. The connected porosity is 19.9% compared to the total porosity of 21.3 %. c) 3D pore network visualisation generated of 3D μ-CT data for the ILS sample. The connected porosity is 8.06 % compared to the total porosity of 11.1 %. d) 3D pore network visualisation generated of 3D μ-CT data for the DOL sample. The connected porosity is 15.2 % compared to the total porosity of 13.8 %.

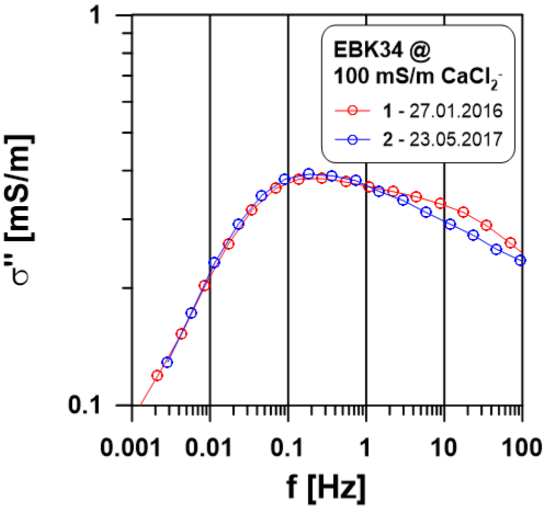

Figure A.13: Comparison of two SIP measurements at a fluid conductivity 100 mS/m. The red curve belongs to measurement during the multi salinity experiment and the blue line represent a repeat measurement after the comleted experiment. Both curves are nearly identical. Therefore, it is concluded that the high salinities do not modify the sample irreversibly.

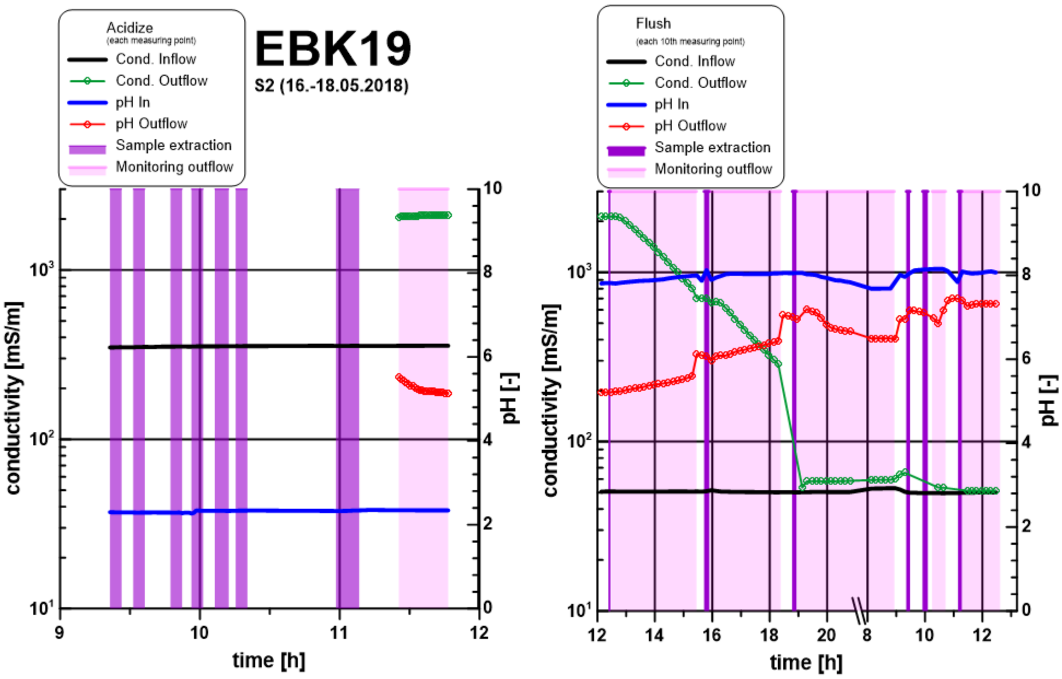

Figure A.14: Monitoring of the conductivity and pH value at inflow and outflow during the sample extraction for the orientation analysis.

(a)

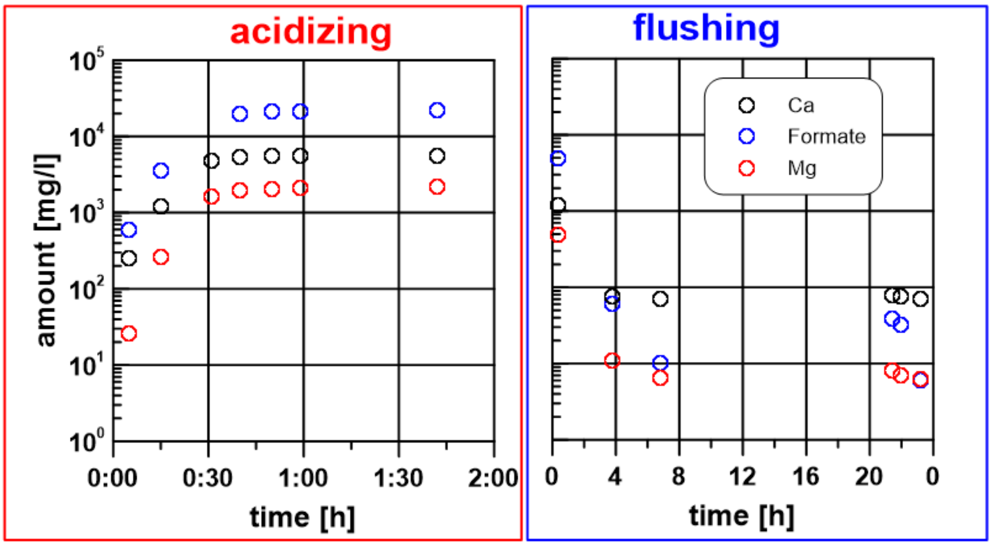

(b)

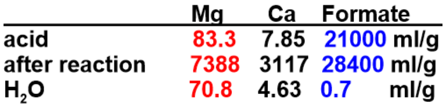

	Mg	Ca	Formate	
acid	83.3	7.85	21000	ml/g
after reaction	7388	3117	28400	ml/g
H_2O	70.8	4.63	0.7	ml/g

Figure A.15: Results of the orientation analysis. a) Amount of calcium, magnesium, and formate during acidifying and flushing. b) Amount of calcium, magnesium, and formate of the acid, the acid after reaction, and the tap water.

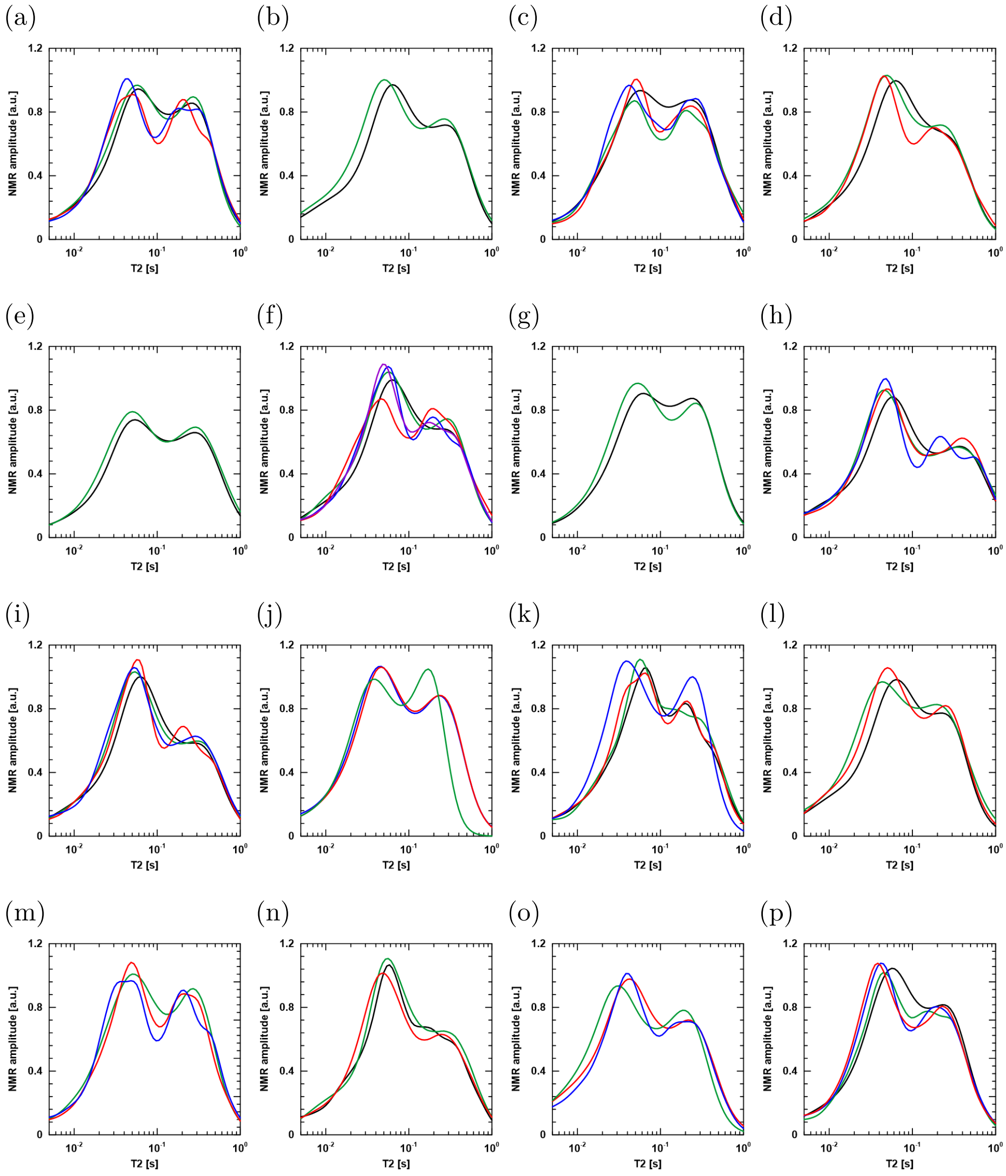

Figure A.16: T_2 distribution of the EBK samples for dissolution step: S0 (black), S1 (green), S2 (red), and S3 (blue).
a) EBK06. b) EBK07. c) EBK14. d) EBK15. e) EBK16. f) EBK18. g) EBK19. h) EBK20. i) EBK21. j) EBK22. k) EBK26. l) EBK39. m) EBK42. n) EBK45. o) EBK50. p) EBK69.

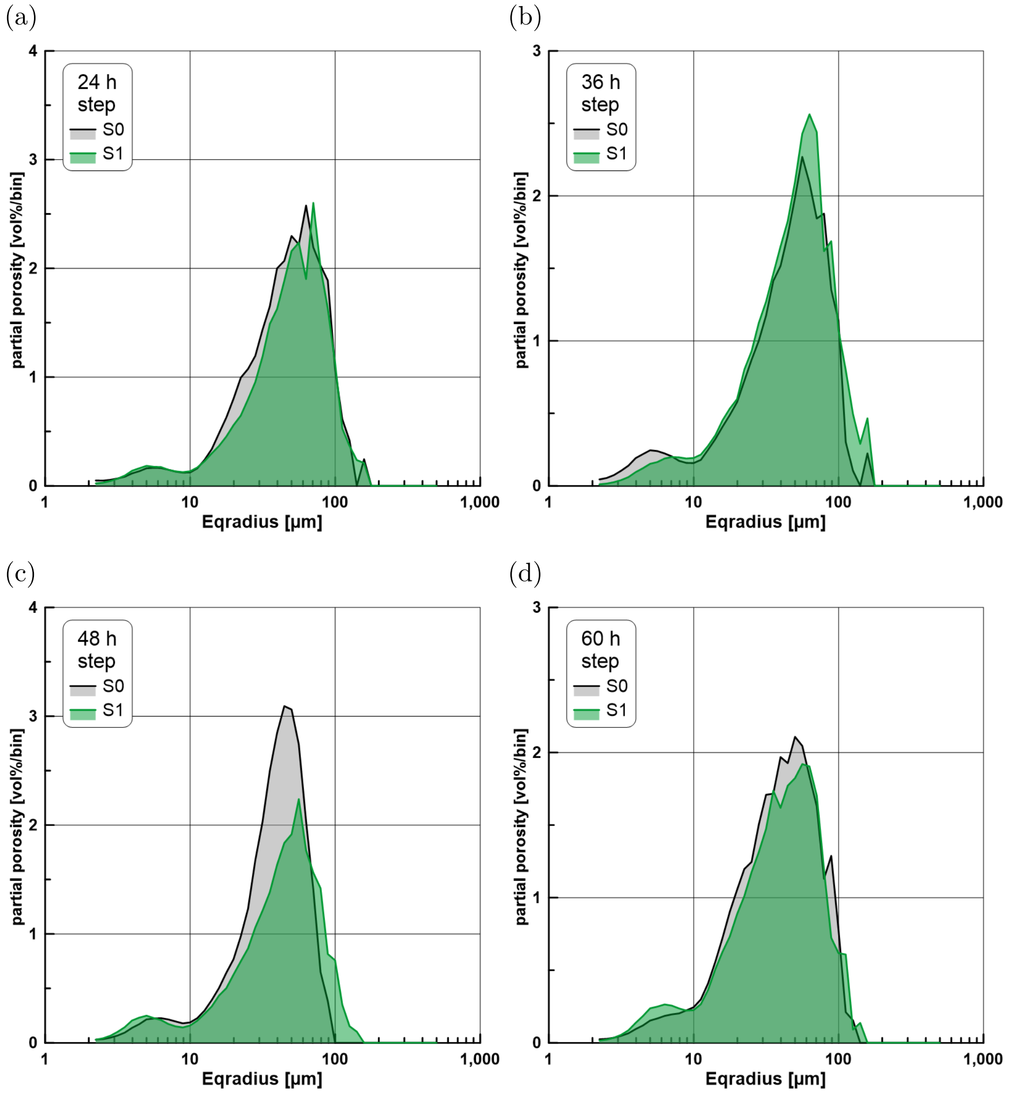

Figure A.17: Pore radii distribution determined by μ-CT.
Comparison of the pore radii distribution a) between untreated and 24 h treated sample, b) between untreated and 36 h treated sample, c) between untreated and 48 h treated sample, and d) between untreated and 60 h treated sample.

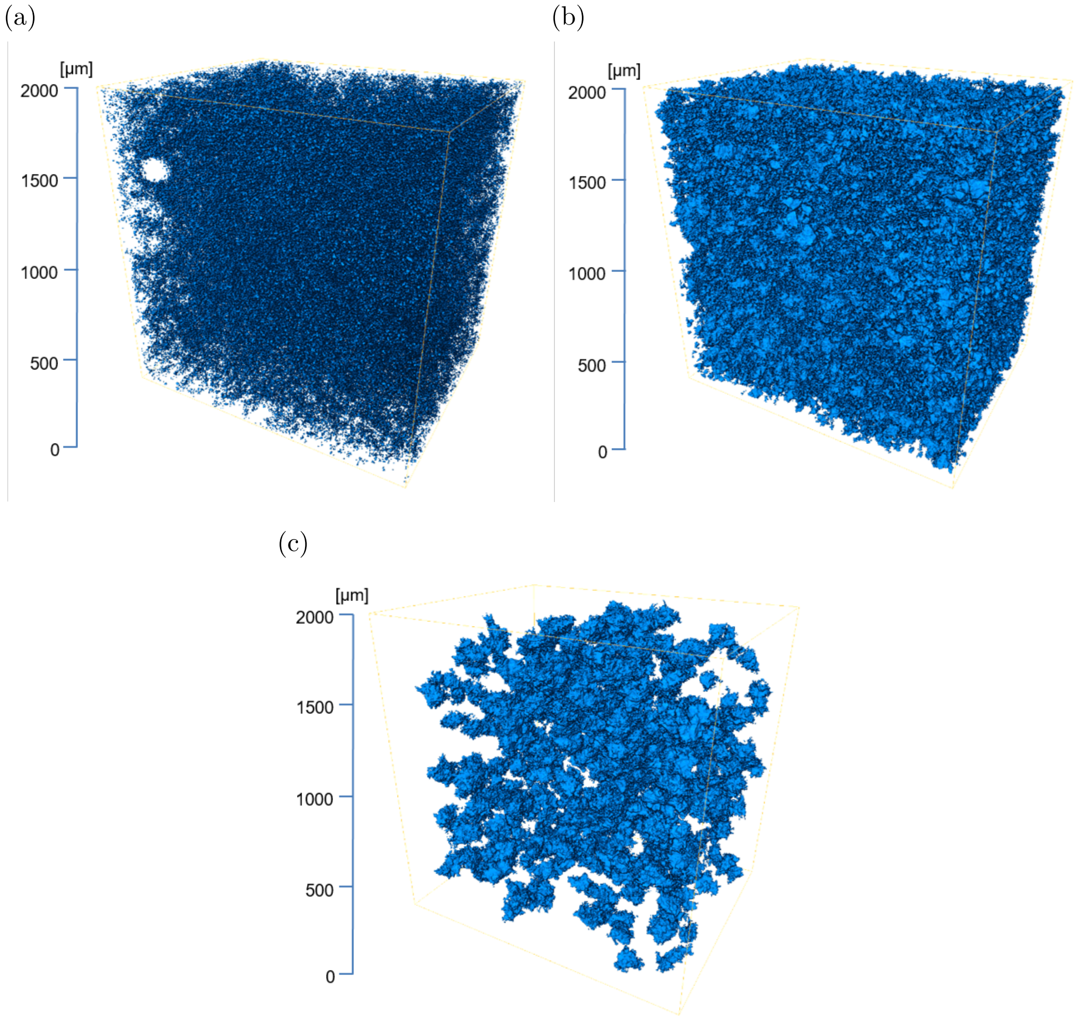

Figure A.18: 3D cube of the pore network of the EBK using equivalent pore radii a) smaller than 10 μm, b) from 10 μm to 55 μm, and c) larger than 55 μm.

B Tables

Table B.1: Complete list of EBK samples with TWM data and the resulting porosity (Φ) and density values (d_a) as well as the density values derived by pycnometry (d_p) with the standard deviation of the measurement (Δd_a). Assuming an error of $\Delta m = 0.01\,\mathrm{g}$ for the TWM method, the error of the porosity has a mean value of 0.05 % and the error of the density has a mean value of $0.0004\,\mathrm{g} \cdot \mathrm{cm}^{-3}$.

sample	m_{dry} [g]	m_{sat} [g]	m_{im} [g]	Φ [%]	d_a [$\frac{g}{cm^3}$]	d_p [$\frac{g}{cm^3}$]	Δd_p [$\frac{g}{cm^3}$]
EBK01	44.47	55.39	28.36	40.39	2.75	2.87	0.0271
EBK02	43.60	54.68	27.78	41.19	2.75	2.90	0.0012
EBK03	44.99	55.66	28.73	39.62	2.76	2.90	0.0176
EBK04	51.22	59.70	32.74	31.46	2.77	2.88	0.0003
EBK05	43.20	53.92	27.62	40.77	2.77	2.90	0.0103
EBK06	44.22	54.87	28.26	40.04	2.77	2.90	0.0013
EBK07	45.08	55.74	28.84	39.63	2.77	2.92	0.0032
EBK08	43.59	54.71	27.77	41.27	2.75	2.89	0.0180
EBK09	45.63	55.96	29.25	38.68	2.78	2.92	0.0295
EBK10	44.73	55.19	28.64	39.40	2.77	2.89	0.0023
EBK11	44.66	55.67	28.46	40.46	2.75	2.87	0.0296
EBK12	55.03	62.30	35.08	26.72	2.75	2.86	0.0149
EBK13	43.78	55.07	27.95	41.64	2.76	2.89	0.0248
EBK14	44.42	55.29	28.34	40.35	2.76	2.86	0.0465
EBK15	46.41	56.46	29.73	37.60	2.78	2.89	0.0034
EBK16	49.09	58.34	31.30	34.20	2.75	2.89	0.0028
EBK17	50.39	59.23	32.11	32.59	2.75	2.86	0.0102
EBK18	45.43	55.58	29.04	38.26	2.77	2.91	0.0051
EBK19	44.96	55.59	28.66	39.49	2.75	2.88	0.0008
EBK20	45.01	54.88	28.70	37.71	2.75	2.90	0.0035
EBK21	45.92	55.73	29.38	37.22	2.77	2.89	0.0255
EBK22	43.94	55.02	27.97	40.95	2.75	2.85	0.0223
EBK23	47.13	56.86	29.98	36.21	2.74	2.87	0.0034
EBK24	51.92	60.29	33.10	30.78	2.75	2.86	0.0036
EBK25	43.69	54.83	27.85	41.29	2.75	2.87	0.0201
EBK26	45.92	56.37	29.38	38.71	2.77	2.94	0.0009
EBK27	46.94	56.86	29.99	36.91	2.76	2.88	0.0010
EBK28	46.91	57.21	29.94	37.78	2.76	2.87	0.0117
EBK29	48.55	57.81	30.93	34.46	2.75	2.87	0.0144
EBK30	46.01	56.14	29.32	37.76	2.75	2.88	0.0169
EBK31	45.09	53.41	28.79	33.79	2.76	2.88	0.0121
EBK32	45.26	55.79	28.89	39.14	2.76	2.86	0.0117
EBK33	60.92	66.00	38.67	18.60	2.73	2.82	0.0153
EBK34	46.27	56.30	29.52	37.46	2.76	2.88	0.0176
EBK35	46.49	56.39	29.61	36.95	2.75	2.87	0.0027
EBK36	53.35	61.15	33.97	28.70	2.75	2.86	0.0033
EBK37	53.70	61.47	34.20	28.48	2.75	2.86	0.0033
EBK38	44.13	55.05	28.04	40.44	2.74	2.86	0.0140
EBK39	44.55	55.04	28.44	39.44	2.76	2.88	0.0162
EBK40	48.70	58.16	31.06	34.88	2.75	2.88	0.0215
EBK41	47.27	57.14	30.16	36.59	2.76	2.87	0.0262
EBK42	43.84	54.96	27.85	41.04	2.74	2.86	0.0226
EBK43	44.68	55.51	28.36	39.91	2.73	2.85	0.0112
EBK44	43.59	54.75	27.84	41.45	2.76	2.89	0.0131
EBK45	46.84	56.85	29.90	37.14	2.76	2.86	0.0018
EBK46	45.07	55.74	28.60	39.31	2.73	2.83	0.1158
EBK47	44.52	55.23	28.35	39.85	2.75	2.85	0.1547
EBK48	51.17	59.77	32.56	31.61	2.74	2.85	0.0014
EBK49	45.85	56.38	29.13	38.63	2.74	2.85	0.0021
EBK50	46.40	56.63	29.57	37.80	2.75	2.88	0.0021

Table B.2: Complete list of LK samples with TWM data and the resulting porosity (Φ) and density values (d_a) as well as the density values derived by pycnometry (d_p) with the standard deviation of the measurement (Δd_a). Assuming an error of $\Delta m = 0.01\,\mathrm{g}$ for the TWM method, the error of the porosity has a mean value of 0.05 % and the error of the density has a mean value of $0.0004\,\mathrm{g} \cdot \mathrm{cm}^{-3}$.

sample	m_{dry} [g]	m_{sat} [g]	m_{im} [g]	Φ [%]	d_a [$\frac{g}{cm^3}$]	d_p [$\frac{g}{cm^3}$]	Δd_p [$\frac{g}{cm^3}$]
LK01	61.42	66.05	38.68	16.91	2.70	2.78	0.035
LK02	62.45	66.62	39.33	15.29	2.70	2.78	0.053
LK03	62.78	66.94	39.54	15.17	2.70	2.77	0.017
LK04	63.45	67.48	40.00	14.65	2.70	2.78	0.029
LK05	61.98	66.20	39.06	15.55	2.70	2.78	0.020
LK06	65.60	68.76	41.32	11.52	2.70	2.78	0.003
LK07	62.38	66.58	39.29	15.38	2.70	2.79	0.002
LK08	61.47	66.00	38.74	16.63	2.70	2.79	0.015
LK09	60.42	65.38	38.08	18.18	2.70	2.80	0.004
LK10	62.82	67.25	39.75	16.12	2.72	2.77	0.016
LK11	62.94	66.94	39.62	14.64	2.69	2.79	0.004
LK12	63.18	67.17	39.77	14.55	2.69	2.79	0.007
LK13	65.63	68.68	41.36	11.14	2.70	2.77	0.011
LK14	62.09	66.49	39.08	16.04	2.69	2.79	0.025
LK15	62.86	66.93	39.51	14.86	2.69	2.78	0.014
LK16	63.76	67.71	40.14	14.34	2.69	2.78	0.001
LK17	62.83	66.99	39.57	15.16	2.70	2.77	0.077
LK18	61.39	65.88	38.66	16.50	2.70	2.78	0.052
LK19	59.24	64.76	37.34	20.15	2.70	2.78	0.036
LK20	61.85	66.28	38.97	16.23	2.70	2.79	0.018
LK21	65.49	68.58	41.29	11.32	2.70	2.77	0.004
LK22	65.97	68.91	41.59	10.76	2.70	2.77	0.023
LK23	62.93	67.22	39.59	15.50	2.69	2.78	0.016
LK24	61.68	66.29	38.86	16.81	2.70	2.78	0.029
LK25	61.85	66.30	38.95	16.26	2.70	2.78	0.030
LK26	62.69	66.75	39.44	14.85	2.69	2.77	0.003
LK27	62.21	66.63	39.17	16.08	2.69	2.78	0.005
LK28	62.94	67.19	39.65	15.42	2.70	2.76	0.038
LK29	61.66	66.21	38.85	16.64	2.70	2.79	0.034
LK30	62.89	66.92	39.56	14.74	2.69	2.77	0.027
LK31	62.87	66.88	39.57	14.68	2.69	2.77	0.002
LK32	65.69	68.83	41.32	11.40	2.69	2.75	0.040
LK33	60.48	65.27	38.02	17.59	2.69	2.78	0.029
LK34	65.10	68.28	40.98	11.65	2.69	2.77	0.019
LK35	62.12	66.24	39.09	15.16	2.69	2.74	0.020
LK36	63.67	67.66	40.06	14.46	2.69	2.78	0.002
LK37	60.76	65.65	38.18	17.79	2.69	2.78	0.024
LK38	61.82	65.89	38.89	15.07	2.69	2.77	0.031
LK39	63.80	67.72	40.10	14.22	2.69	2.77	0.042
LK40	65.67	68.70	41.39	11.08	2.70	2.76	0.023
LK41	61.51	66.04	38.67	16.56	2.69	2.74	0.004
LK42	59.60	64.65	37.47	18.59	2.69	2.77	0.001
LK43	61.49	66.00	38.67	16.50	2.69	2.76	0.022
LK44	64.25	68.11	40.41	13.94	2.69	2.76	0.041
LK45	62.61	66.63	39.40	14.76	2.69	2.76	0.022
LK46	61.56	66.09	38.72	16.56	2.69	2.76	0.029
LK47	59.41	64.94	37.38	20.07	2.69	2.77	0.121
LK48	61.84	66.29	38.90	16.27	2.69	2.75	0.065
LK49	61.77	66.06	38.91	15.81	2.70	2.77	0.024
LK50	58.94	64.72	37.09	20.93	2.69	2.77	0.033

Table B.3: Complete list of ILS samples with TWM data and the resulting porosity (Φ) and density values (d_a) as well as the density values derived by pycnometry (d_p) with the standard deviation of the measurement (Δd_a). Assuming an error of $\Delta m = 0.01\,\mathrm{g}$ for the TWM method, the error of the porosity has a mean value of 0.05 % and the error of the density has a mean value of $0.0004\,\mathrm{g} \cdot \mathrm{cm}^{-3}$.

sample	m_{dry} [g]	m_{sat} [g]	m_{im} [g]	Φ [%]	d_a $[\frac{g}{cm^3}]$	d_p $[\frac{g}{cm^3}]$	Δd_p $[\frac{g}{cm^3}]$
ILS02	60.65	65.58	38.07	17.91	2.68	2.71	0.039
ILS03	60.34	65.36	37.85	18.27	2.68	2.71	0.005
ILS04	59.88	64.92	37.57	18.42	2.68	2.71	0.003
ILS05	60.06	65.07	37.71	18.30	2.68	2.71	0.004
ILS06	60.74	65.37	38.12	17.01	2.68	2.71	0.005
ILS07	60.44	65.26	37.93	17.62	2.68	2.72	0.005
ILS08	59.76	64.71	37.48	18.19	2.68	2.71	0.020
ILS09	60.02	64.96	37.65	18.10	2.68	2.71	0.003
ILS10	60.95	65.70	38.26	17.32	2.68	2.72	0.001
ILS11	60.84	65.51	38.17	17.09	2.68	2.70	0.003
ILS12	59.77	64.81	37.49	18.45	2.68	2.71	0.002
ILS13	60.38	65.22	37.88	17.72	2.68	2.71	0.017
ILS14	59.66	64.74	37.45	18.63	2.68	2.71	0.019
ILS15	59.92	65.08	37.61	18.79	2.68	2.71	0.007
ILS16	61.01	65.81	38.29	17.44	2.68	2.71	0.014
ILS17	59.54	64.54	37.38	18.41	2.68	2.71	0.002
ILS18	59.73	64.69	37.50	18.24	2.68	2.72	0.004
ILS19	59.60	64.67	37.40	18.59	2.68	2.68	0.009
ILS20	61.87	66.25	38.74	15.93	2.67	2.67	0.009
ILS21	59.63	64.82	37.38	18.93	2.68	2.69	0.005
ILS22	58.66	64.09	36.82	19.91	2.68	2.71	0.024
ILS23	58.83	64.18	36.93	19.61	2.68	2.70	0.024
ILS24	61.60	66.08	38.55	16.25	2.67	2.68	0.001
ILS25	59.86	64.88	37.55	18.36	2.68	2.71	0.003
ILS26	59.92	64.90	37.59	18.25	2.68	2.70	0.006
ILS27	59.22	64.42	37.15	19.07	2.68	2.70	0.016
ILS28	59.96	64.90	37.62	18.11	2.68	2.70	0.007
ILS29	60.15	65.04	37.69	17.88	2.67	2.70	0.028
ILS30	59.34	64.54	37.22	19.02	2.68	2.70	0.018
ILS31	59.66	64.60	37.44	18.21	2.68	2.72	0.032
ILS32	60.15	65.24	37.75	18.52	2.68	2.70	0.004
ILS33	59.14	64.45	37.07	19.37	2.67	2.71	0.003
ILS34	60.62	65.45	38.09	17.66	2.68	2.70	0.009
ILS35	60.98	65.67	38.23	17.10	2.68	2.69	0.005
ILS36	60.74	65.66	38.10	17.84	2.68	2.70	0.001
ILS37	59.95	64.93	37.61	18.20	2.68	2.70	0.012
ILS38	61.48	65.29	38.46	14.18	2.67	2.69	0.010
ILS39	61.11	65.64	38.26	16.54	2.67	2.69	0.020
ILS40	59.72	64.73	37.45	18.38	2.68	2.72	0.005
ILS41	59.78	64.86	37.51	18.56	2.68	2.71	0.001
ILS42	61.39	65.81	38.42	16.11	2.67	2.69	0.003
ILS43	59.77	64.96	37.50	18.88	2.68	2.71	0.000
ILS44	59.10	64.20	37.00	18.74	2.67	2.71	0.009
ILS45	58.96	64.09	36.95	18.90	2.67	2.70	0.008
ILS46	59.84	64.78	37.47	18.10	2.67	2.70	0.005
ILS47	59.68	64.57	37.37	17.98	2.67	2.70	0.010
ILS48	59.32	64.39	37.15	18.60	2.67	2.70	0.018
ILS49	60.48	65.38	37.86	17.80	2.67	2.70	0.011
ILS50	59.31	64.44	37.19	18.82	2.68	2.70	0.020

Table B.4: Complete list of DOL samples with TWM data and the resulting porosity (Φ) and density values (d_a) as well as the density values derived by pycnometry (d_p) with the standard deviation of the measurement (Δd_a). Assuming an error of $\Delta m = 0.01\,\mathrm{g}$ for the TWM method, the error of the porosity has a mean value of 0.05 % and the error of the density has a mean value of $0.0004\,\mathrm{g} \cdot \mathrm{cm}^{-3}$.

sample	m_{dry} [g]	m_{sat} [g]	m_{im} [g]	Φ [%]	d_a [$\frac{g}{cm^3}$]	d_p [$\frac{g}{cm^3}$]	Δd_p [$\frac{g}{cm^3}$]
DOL01	66.73	70.44	42.99	13.49	2.80	2.86	0.0021
DOL02	69.30	72.29	44.82	10.88	2.82	2.87	0.0277
DOL03	65.52	69.59	42.15	14.83	2.80	2.83	0.0026
DOL04	63.30	68.10	40.75	17.56	2.80	2.85	0.0224
DOL05	64.30	68.75	41.39	16.25	2.80	2.85	0.0258
DOL06	63.51	68.27	40.88	17.38	2.80	2.85	0.0041
DOL07	63.99	68.53	41.13	16.58	2.79	2.84	0.0037
DOL08	71.45	73.67	46.07	8.05	2.81	2.83	0.0055
DOL09	70.17	72.83	45.29	9.65	2.81	2.84	0.0016
DOL10	68.74	71.86	44.32	11.32	2.81	2.82	0.0027
DOL11	70.42	73.03	45.46	9.47	2.82	2.82	0.0024
DOL12	71.60	73.76	46.21	7.85	2.81	2.83	0.0024
DOL13	64.93	69.10	41.83	15.30	2.81	2.82	0.0195
DOL14	69.23	72.20	44.66	10.77	2.81	2.81	0.0036
DOL15	69.56	72.38	44.86	10.27	2.81	2.80	0.0045
DOL16	70.42	73.00	45.46	9.37	2.82	2.82	0.0054
DOL17	67.58	71.03	43.52	12.55	2.80	2.81	0.0067
DOL18	69.39	72.27	44.74	10.46	2.81	2.81	0.0038
DOL19	64.78	69.15	41.77	15.96	2.81	2.86	0.0523
DOL20	68.32	71.45	44.04	11.42	2.81	2.81	0.0051
DOL21	63.88	68.61	41.16	17.21	2.81	2.83	0.0176
DOL22	68.84	71.88	44.39	11.06	2.81	2.81	0.0046
DOL23	68.34	71.37	44.18	11.16	2.82	2.84	0.0141
DOL24	67.95	71.35	43.78	12.33	2.81	2.81	0.0053
DOL25	69.74	72.41	45.02	9.77	2.82	2.83	0.0051
DOL26	69.24	72.17	44.67	10.64	2.81	2.87	0.0028
DOL27	63.31	68.27	40.85	18.08	2.81	2.85	0.0028
DOL28	71.80	74.06	46.43	8.19	2.82	2.84	0.0031
DOL29	70.83	73.33	45.75	9.07	2.82	2.85	0.0017
DOL30	72.91	74.77	47.16	6.75	2.83	2.82	0.0287
DOL31	65.12	69.45	42.06	15.81	2.82	2.85	0.0275
DOL32	70.86	73.33	45.78	8.97	2.82	2.84	0.0046
DOL33	68.63	71.85	44.26	11.69	2.81	2.83	0.0200
DOL34	64.08	68.62	41.31	16.65	2.81	2.84	0.0107
DOL35	65.39	69.69	42.26	15.67	2.82	2.85	0.0160
DOL36	68.28	71.61	44.08	12.08	2.82	2.84	0.0050
DOL37	69.70	72.53	45.02	10.29	2.82	2.84	0.0056
DOL38	71.35	73.69	46.13	8.51	2.82	2.85	0.0012
DOL39	68.05	71.40	43.84	12.16	2.81	2.84	0.0023
DOL40	63.98	68.56	41.20	16.75	2.80	2.84	0.0216
DOL41	69.43	72.31	44.81	10.48	2.81	2.84	0.0024
DOL42	63.69	68.35	41.02	17.05	2.80	2.84	0.0049
DOL43	64.39	68.83	41.45	16.22	2.80	2.83	0.0219
DOL44	69.55	72.42	44.87	10.42	2.81	2.83	0.0076
DOL45	67.87	71.25	43.67	12.25	2.80	2.83	0.0040
DOL46	70.16	72.85	45.29	9.76	2.82	2.83	0.0030
DOL47	68.89	71.89	44.45	10.94	2.81	2.84	0.0051
DOL48	69.41	72.27	44.77	10.42	2.81	2.83	0.0033
DOL49	68.78	71.78	44.30	10.93	2.80	2.83	0.0043
DOL50	63.35	68.18	40.78	17.62	2.80	2.83	0.0037

Table B.5: The complete list of major and trace elements for the Edwards Brown carbonate determined by XRF.

	SiO2 [%]	TiO2 [%]	Al2O3 [%]	Fe2O3 [%]	MnO [%]	MgO [%]	CaO [%]	Na2O [%]	K2O [%]	P2O5 [%]	SO3 [%]	Cl [%]	F [%]	LOI [%]	**Sum_RF [%]**
EBK-29	3.7	0.043	0.80	0.37	0.040	15.93	34.4	0.04	0.104	0.024	0.23	0.003	<0.05	44.2	**99.94**
EBK-46	6.1	0.067	1.26	0.53	0.040	16.76	31.5	0.04	0.161	0.030	0.24	0.002	<0.05	43.3	**99.94**
EBK-30	5.6	0.063	1.29	0.52	0.041	17.44	31.0	0.07	0.189	0.032	0.27	0.004	<0.05	43.4	**99.93**
EBK-33	3.2	0.038	0.73	0.32	0.034	11.36	40.2	0.02	0.086	0.020	0.17	0.004	<0.05	43.8	**99.95**
EBK-44	5.3	0.060	1.15	0.52	0.041	17.48	31.2	0.05	0.165	0.031	0.26	0.004	<0.05	43.6	**99.94**
EBK-48	4.3	0.051	0.93	0.42	0.038	14.04	36.1	0.05	0.130	0.023	0.21	0.003	<0.05	43.7	**99.95**
EBK-09	5.6	0.058	1.16	0.49	0.039	17.17	31.1	0.02	0.120	0.030	0.24	<0.002	<0.05	43.9	**99.89**
EBK-10	4.9	0.052	1.08	0.49	0.041	17.85	31.0	0.04	0.122	0.030	0.24	<0.002	<0.05	44.1	**99.91**
EBK-11	6.2	0.069	1.32	0.55	0.041	17.69	30.5	0.07	0.213	0.031	0.25	<0.002	<0.05	43.0	**99.90**
EBK-12	4.3	0.047	0.93	0.43	0.038	14.86	35.7	0.02	0.098	0.024	0.23	<0.002	<0.05	43.3	**99.89**
EBK-13	6.8	0.073	1.42	0.56	0.041	17.53	30.2	0.05	0.183	0.031	0.25	<0.002	<0.05	42.9	**99.88**
Mean	**5.1**	**0.06**	**1.10**	**0.47**	**0.04**	**16.19**	**33.0**	**0.04**	**0.14**	**0.03**	**0.24**	**0.00**	**<0.05**	**43.6**	
	(As)_SI [mg/kg]	Ba_SI [mg/kg]	Bi_SI [mg/kg]	Ce_SI [mg/kg]	Co_SI [mg/kg]	Cr_SI [mg/kg]	Cs_SI [mg/kg]	Cu_SI [mg/kg]	Ga_SI [mg/kg]	Hf_SI [mg/kg]	La_SI [mg/kg]	Mo_SI [mg/kg]	Nb_SI [mg/kg]	Nd_SI [mg/kg]	Ni_SI [mg/kg]
EBK-29	<3	<70	<6	<57	<6	<11	<76	22	<4	<17	<45	<7	<2	<38	<6
EBK-46	<3	<69	<6	<55	<6	<11	<74	24	<4	<16	<44	<7	<2	<37	<6
EBK-30	<3	<70	<6	<56	<6	32	<75	22	<4	<17	<44	<7	3	<38	<6
EBK-33	<3	<74	<6	<59	<7	<12	<80	20	<5	<18	<47	<7	3	<40	<6
EBK-44	<3	<70	<6	<57	<6	<11	<75	22	<4	<17	<45	<7	3	<38	<6
EBK-48	<3	<72	<6	<58	<6	<12	<78	26	<5	<17	<46	<7	3	<39	<6
EBK-09	<3	<68	<5	<54	<6	<11	<74	26	<4	<16	<43	<6	<6	<36	<6
EBK-10	<3	<68	<5	<54	<6	<11	<73	46	<4	<16	<43	<6	<6	<37	8
EBK-11	<3	<68	<5	<54	<6	<11	<73	21	<4	<16	<43	<6	<6	<37	<6
EBK-12	<3	<71	<6	61	<6	<11	<76	46	<4	<17	<45	<7	<6	<38	<6
EBK-13	<3	<68	<5	<54	<6	<11	<74	49	<4	<16	<43	<6	<5	<37	<6
	Pb_SI [mg/kg]	Rb_SI [mg/kg]	Sb_SI [mg/kg]	Sc_SI [mg/kg]	Sm_SI [mg/kg]	Sn_SI [mg/kg]	Sr_SI [mg/kg]	Ta_SI [mg/kg]	Th_SI [mg/kg]	U_SI [mg/kg]	V_SI [mg/kg]	W_SI [mg/kg]	Y_SI [mg/kg]	Zn_SI [mg/kg]	Zr_SI [mg/kg]
EBK-29	10	7	<99	<28	<39	<36	248	<11	11	<9	18	<11	25	22	27
EBK-46	7	13	<98	<27	<38	<35	252	<11	11	<9	17	<10	28	10	39
EBK-30	17	14	<98	<27	<39	<35	253	<11	15	<9	<17	<11	28	33	44
EBK-33	10	11	<104	<29	<41	<36	267	<11	10	<9	<17	<11	23	15	21
EBK-44	19	14	<99	<27	<39	<36	256	<11	12	<9	<17	<11	28	62	36
EBK-48	12	9	<102	<28	<40	<36	245	<11	<8	<9	19	<11	25	25	23
EBK-09	11	9	<97	<26	<38	<35	242	<11	7	<8	<16	<10	23	17	34
EBK-10	9	9	<96	<26	<37	<34	239	<11	7	<8	18	<10	26	15	33
EBK-11	10	14	<96	<26	<38	<34	248	<11	<6	<8	25	<10	25	17	36
EBK-12	8	6	<99	<27	<39	<35	249	<11	<6	<8	20	<10	24	14	24
EBK-13	10	11	<97	<26	<38	<34	255	<11	<6	<8	<16	<10	24	21	37

Table B.6: The complete list of major and trace elements for the Indiana Limestone determined by XRF.

sample	SiO2 [%]	TiO2 [%]	Al2O3 [%]	Fe2O3 [%]	MnO [%]	MgO [%]	CaO [%]	Na2O [%]	K2O [%]	P2O5 [%]	SO3 [%]	Cl [%]	F [%]	LOI [%]	**Sum_RF [%]**
ILS-01	0.4	<0.001	0.05	0.15	0.007	0.62	54.9	0.01	0.005	0.008	0.09	0.003	<0.05	43.7	**99.98**
ILS-02	0.3	<0.001	0.05	0.17	0.006	0.60	55.0	0.01	0.005	0.007	0.09	0.003	<0.05	43.7	**99.96**
ILS-03	0.4	<0.001	0.05	0.17	0.005	0.60	55.1	0.01	0.005	0.008	0.09	0.002	<0.05	43.6	**99.97**
ILS-50	0.5	<0.001	0.07	0.14	0.008	0.60	54.9	0.01	0.005	0.007	0.09	0.004	<0.05	43.6	**99.96**
Mean	**0.4**	**<0.001**	**0.06**	**0.16**	**0.01**	**0.60**	**55.0**	**<0.01**	**<0.005**	**0.01**	**0.09**	**0.00**	**<0.05**	**43.6**	
	(As)_SI [mg/kg]	Ba_SI [mg/kg]	Bi_SI [mg/kg]	Ce_SI [mg/kg]	Co_SI [mg/kg]	Cr_SI [mg/kg]	Cs_SI [mg/kg]	Cu_SI [mg/kg]	Ga_SI [mg/kg]	Hf_SI [mg/kg]	La_SI [mg/kg]	Mo_SI [mg/kg]	Nb_SI [mg/kg]	Nd_SI [mg/kg]	Ni_SI [mg/kg]
ILS-01	11	7	<111	<31	<43	<38	225	<12	<9	<10	<18	<12	<9	53	<9
ILS-02	<8	6	<114	<33	<45	<39	228	<13	<10	<10	<19	<13	<9	22	<9
ILS-03	<8	6	<114	<32	<44	<39	227	<12	<10	<10	<19	<12	<9	21	<9
ILS-50	<8	7	<114	<32	<45	<39	226	<13	<10	<10	<19	<12	<9	21	<9
	Pb_SI [mg/kg]	Rb_SI [mg/kg]	Sb_SI [mg/kg]	Sc_SI [mg/kg]	Sm_SI [mg/kg]	Sn_SI [mg/kg]	Sr_SI [mg/kg]	Ta_SI [mg/kg]	Th_SI [mg/kg]	U_SI [mg/kg]	V_SI [mg/kg]	W_SI [mg/kg]	Y_SI [mg/kg]	Zn_SI [mg/kg]	Zr_SI [mg/kg]
ILS-01	<3	<78	<6	<62	<7	<12	<85	30	<5	<19	<50	<7	<2	<42	<7
ILS-02	<4	<82	<7	<64	<7	<13	<89	21	<5	<20	<52	<8	<3	<44	<7
ILS-03	<4	<81	<7	<64	<7	<13	<87	18	<5	<19	<51	<8	<3	<43	<7
ILS-50	<4	<82	<7	<64	<7	<13	<88	19	<5	<19	<51	<8	<3	<43	<7

Table B.7: The complete list of major and trace elements for the Lueders carbonate determined by XRF.

	SiO2	TiO2	Al2O3	Fe2O3	MnO	MgO	CaO	Na2O	K2O	P2O5	SO3	Cl	F	LOI	**Sum_RF**
	[%]	[%]	[%]	[%]	[%]	[%]	[%]	[%]	[%]	[%]	[%]	[%]	[%]	[%]	[%]
LK-7	5.1	0.030	0.72	0.53	0.040	0.80	51.3	0.02	0.032	0.037	0.16	<0.002	<0.05	41.2	**99.97**
LK-30	5.1	0.027	0.72	0.59	0.039	0.78	51.4	0.04	0.050	0.043	0.18	<0.002	<0.05	41.0	**99.92**
LK-32	3.9	0.022	0.62	0.54	0.039	0.79	52.2	0.03	0.040	0.037	0.17	0.002	<0.05	41.6	**99.95**
LK-38	5.8	0.032	0.78	0.66	0.038	0.79	50.9	0.04	0.059	0.046	0.18	0.003	<0.05	40.6	**99.93**
LK-42	3.6	0.015	0.44	0.44	0.044	0.71	52.7	0.03	0.020	0.031	0.14	0.002	<0.05	41.8	**99.96**
Mean	**4.7**	**0.02**	**0.61**	**0.55**	**0.04**	**0.75**	**51.8**	**<0.01**	**<0.005**	**0.04**	**0.16**	**0.00**	**<0.05**	**41.2**	
	(As)_SI	Ba_SI	Bi_SI	Ce_SI	Co_SI	Cr_SI	Cs_SI	Cu_SI	Ga_SI	Hf_SI	La_SI	Mo_SI	Nb_SI	Nd_SI	Ni_SI
	[mg/kg]	[mg/kg]	[mg/kg]	[mg/kg]	[mg/kg]	[mg/kg]	[mg/kg]	[mg/kg]	[mg/kg]	[mg/kg]	[mg/kg]	[mg/kg]	[mg/kg]	[mg/kg]	[mg/kg]
	4	<80	<7	<64	<7	<13	<87	23	<5	<19	<51	<8	<2	<43	<7
LK-7	4	<80	<7	<64	<7	<13	<87	23	<5	<19	<51	<8	<2	<43	<7
LK-30	4	<81	<7	<64	<7	<13	<87	22	<5	<19	<51	<8	3	<43	<7
LK-32	<4	<81	<7	<65	<7	<13	<86	26	<5	<20	<51	<8	5	<43	<7
LK-38	<4	<80	<7	<64	<7	<13	<86	18	<5	<19	<51	<8	<2	<43	<7
LK-42	Pb_SI	Rb_SI	Sb_SI	Sc_SI	Sm_SI	Sn_SI	Sr_SI	Ta_SI	Th_SI	U_SI	V_SI	W_SI	Y_SI	Zn_SI	Zr_SI
	[mg/kg]	[mg/kg]	[mg/kg]	[mg/kg]	[mg/kg]	[mg/kg]	[mg/kg]	[mg/kg]	[mg/kg]	[mg/kg]	[mg/kg]	[mg/kg]	[mg/kg]	[mg/kg]	[mg/kg]
LK-7	17	11	<112	<32	<44	<39	218	<12	<9	<10	<19	<13	<9	57	<9
LK-30	17	11	<112	<32	<44	<39	218	<12	<9	<10	<19	<13	<9	57	<9
LK-32	14	<6	<113	<32	<44	<39	207	<12	<9	<10	<19	<12	9	51	<9
LK-38	21	11	<113	<32	<45	<39	223	<12	<10	<10	<19	<12	<9	58	<9
LK-42	8	6	<113	<32	<44	<39	194	<12	10	<10	<19	<12	<9	51	<9

Table B.8: The complete list of major and trace elements for the Silurian Dolomite determined by XRF.

	SiO2 [%]	TiO2 [%]	Al2O3 [%]	Fe2O3 [%]	MnO [%]	MgO [%]	CaO [%]	Na2O [%]	K2O [%]	P2O5 [%]	SO3 [%]	Cl [%]	F [%]	LOI [%]	**Sum_RF** **[%]**
DOL-41	0.3	<0.001	0.05	0.26	0.021	21.83	30.4	0.01	0.005	<0.001	0.07	0.016	<0.05	47.1	**99.96**
DOL-43	0.1	0.003	0.06	0.14	0.013	21.96	30.4	0.01	0.005	<0.001	0.01	0.025	<0.05	47.3	**99.95**
DOL-44	0.2	<0.001	0.05	0.27	0.021	21.83	30.3	0.01	0.005	<0.001	0.09	0.013	<0.05	47.2	**99.96**
DOL-45	0.3	<0.001	0.05	0.24	0.020	21.86	30.3	0.01	0.005	<0.001	0.07	0.016	<0.05	47.2	**99.96**
DOL-46	0.2	<0.001	0.05	0.27	0.021	21.91	30.4	0.01	0.005	0.002	0.08	0.015	<0.05	47.0	**99.96**
DOL-49	0.1	<0.001	0.08	0.15	0.014	22.00	30.5	0.01	0.005	<0.001	0.01	0.020	<0.05	47.1	**99.97**
DOL-50	0.1	0.003	0.07	0.15	0.015	21.96	30.4	0.01	0.005	<0.001	0.02	0.024	<0.05	47.2	**99.97**
Mean	**0.1**	**0.00**	**0.08**	**0.15**	**0.01**	**21.98**	**30.4**	**<0.01**	**<0.005**	**<0.001**	**0.02**	**0.02**	**<0.05**	**47.2**	
	(As)_SI [mg/kg]	Ba_SI [mg/kg]	Bi_SI [mg/kg]	Ce_SI [mg/kg]	Co_SI [mg/kg]	Cr_SI [mg/kg]	Cs_SI [mg/kg]	Cu_SI [mg/kg]	Ga_SI [mg/kg]	Hf_SI [mg/kg]	La_SI [mg/kg]	Mo_SI [mg/kg]	Nb_SI [mg/kg]	Nd_SI [mg/kg]	Ni_SI [mg/kg]
DOL-41	<3	<67	<5	<53	<6	<11	<72	33	<4	<15	<43	<6	<5	<36	6
DOL-43	<3	<67	<5	<53	<6	<11	<72	35	<4	<15	<42	<6	<5	<36	<5
DOL-44	<3	<67	<5	<53	<6	<11	<72	32	<4	<16	<43	<6	<5	<36	<5
DOL-45	<3	<67	<5	<53	<6	<11	<71	35	<4	<16	<43	<6	<5	<36	<5
DOL-46	<3	<67	<5	<53	<6	<11	<72	35	<4	<16	<43	<6	<5	<36	<5
DOL-49	<3	<67	<5	<53	<6	<11	<72	27	<4	<15	<42	<6	<5	<36	<5
DOL-50	<3	<67	<5	<53	<6	<11	<72	32	<4	<15	<43	<6	<5	<36	<5
	Pb_SI [mg/kg]	Rb_SI [mg/kg]	Sb_SI [mg/kg]	Sc_SI [mg/kg]	Sm_SI [mg/kg]	Sn_SI [mg/kg]	Sr_SI [mg/kg]	Ta_SI [mg/kg]	Th_SI [mg/kg]	U_SI [mg/kg]	V_SI [mg/kg]	W_SI [mg/kg]	Y_SI [mg/kg]	Zn_SI [mg/kg]	Zr_SI [mg/kg]
DOL-41	<7	<5	<94	<26	<37	<34	51	<11	<6	<8	<16	<10	<7	<4	<7
DOL-43	<7	5	<94	<26	<37	<34	44	<11	<6	<8	<16	<10	8	<4	<7
DOL-44	<7	<5	<95	<26	<37	<34	49	<11	<6	<8	<16	<10	<7	5	<7
DOL-45	<7	<5	<95	<26	<37	<34	51	<11	<6	<8	<16	<10	<7	<4	<7
DOL-46	<7	<5	<95	<25	<37	<34	51	<11	<6	<8	<16	<10	7	<4	<7
DOL-49	<6	<4	<94	<26	<37	<34	42	<11	<6	<8	<16	<10	8	<4	<7
DOL-50	<7	<4	<95	<26	<37	<34	44	<11	<6	<8	<16	<10	8	<4	<7

Table B.9: The list of major and trace elements for the EBK, LK, ILS and DOL determined by XRD and the results of the carbon and sulfur analysis (CO).

	RD analysis		**CO analysis**			
sample	Major/Minor components	Traces	Cges %	Corg %	Ccarb %	Sges %
EBK-09	ankerite	quartz, calcite				
EBK-10	ankerite	quartz, calcite				
EBK-11	ankerite	quartz, calcite				
EBK-12	ankerite, calcite	quartz				
EBK-13	ankerite	quartz, ±calcite				
EBK-29	dolomite, calcite	quartz	12	0.05	11.95	0.05
EBK-30	dolomite	quartz, calcite, ±kaolinite	11.6	0.07	11.53	0.07
EBK-33	dolomite, calcite	quartz	11.9	0.09	11.81	0.04
EBK-44	dolomite	quartz, calcite, ±kaolinite	11.7	0.1	11.6	0.08
EBK-48	dolomite, calcite	quartz	11.8	0.05	11.75	0.07
EBK-46	ankerite	calcite, quartz	11.5	0.06	11.44	0.06
LK-07	calcite	quartz				
LK-30	calcite	quartz	11.2	0.06	11.14	0.07
LK-32	calcite	quartz	11.3	0.05	11.25	0.04
LK-38	calcite	quartz	11.1	0.05	11.05	0.06
LK-42	calcite	quartz	11.5	0.04	11.46	0.05
ILS-01	calcite		12	0.04	11.96	0.04
ILS-02	calcite	quartz	12.1	0.05	12.05	0.02
ILS-03	calcite	quartz	12.1	0.04	12.06	0.04
ILS-50	calcite	quartz	11.9	0.05	11.85	0.02
DOL-41	dolomite					
DOL-43	dolomite					
DOL-44	dolomite		12.7	0.02	12.68	< 0.03
DOL-45	dolomite		12.7	< 0.02	12.7	-
DOL-46	dolomite					
DOL-49	dolomite		12.5	< 0.02	12.5	-
DOL-50	dolomite					

Table B.10: Petrophysical properties of EBK samples: porosity Φ, permeability k, specific surface related to pore volume S_{por} and related to mass S_{m}. IP parameter of the EBK samples: peak frequency f_{peak}, real part of conductivity $\sigma'(1\mathrm{Hz})$, imaginary part of conductivity $\sigma''(1\mathrm{Hz})$ and $\sigma''(f_{\mathrm{peak}})$, total chargeability m_{DD}, and mean relaxation time τ_{DD}.

Sample	Φ [%]	k [mD]	S_{por} [μm^{-1}]	S_{m} [m^2g^{-1}]	f_{peak} [Hz]	$\sigma'(1\mathrm{Hz})$ [mS·m^{-1}]	$\sigma''(1\mathrm{Hz})$ [mS·m^{-1}]	$\sigma''(f_{\mathrm{peak}})$ [mS·m^{-1}]	m_{DD} [-]	τ_{DD} [s]
EBK01	40.4	168.7	21.2	5.2	0.18	22.2	0.482	0.517	0.12	0.30
EBK02	41.2	216.77	20.0	5.1	0.18	22.1	0.426	0.501	0.12	0.28
EBK06	40.0	235.6	21.6	5.2	0.14	23.4	0.347	0.393	0.10	3.80
EBK07	39.6	208.0	19.4	4.6	0.27	22.0	0.380	0.392	0.10	0.25
EBK09	38.7	190.7	23.7	5.4	0.20	18.9	0.494	0.514	0.15	0.27
EBK09	38.7	190.7	23.7	5.4	0.20	18.7	0.518	0.541	0.14	0.27
EBK10	39.4	235.7	20.8	4.9	0.32	25.2	0.367	0.371	0.09	0.34
EBK10	39.4	235.7	20.8	4.9	0.20	23.1	0.352	0.359	0.09	0.31
EBK11	40.5	200.5	20.6	4.6	0.13	22.8	0.651	0.719	0.17	0.39
EBK11	40.5	200.5	20.6	4.6	0.13	22.5	0.712	0.783	0.16	0.42
EBK12	26.7	23.1	21.2	2.8	0.50	6.9	0.104	0.105	0.09	0.23
EBK12	26.7	23.1	21.2	2.8	0.32	6.8	0.102	0.103	0.09	0.22
EBK13	41.6	199.0	19.1	4.9	0.20	20.8	0.464	0.494	0.13	0.29
EBK14	40.3	232.2	18.1	5.4	0.14	19.9	0.376	0.412	0.12	0.19
EBK15	37.6	185.1	21.6	4.7	0.14	19.3	0.302	0.325	0.11	0.15
EBK16	34.2	178.6	16.0	3.0	0.14	11.6	0.200	0.200	0.10	0.26
EBK17	32.6	126.3	19.9	3.5	0.14	12.5	0.225	0.237	0.11	0.34
EBK18	38.2	181.4	20.1	4.5	0.14	20.1	0.332	0.365	0.11	0.16
EBK19	39.5	230.9	16.7	4.0	0.27	18.8	0.359	0.371	0.11	0.27
EBK20	37.7	126.6	22.4	4.9	0.07	17.7	0.270	0.330	0.12	0.30
EBK21	37.2	179.5	23.1	4.9	0.55	18.9	0.291	0.297	0.11	0.16
EBK22	41.0	231.6	19.6	4.9	0.14	22.9	0.448	0.456	0.11	0.27
EBK26	38.7	222.0	23.5	5.4	0.27	21.0	0.324	0.342	0.11	0.14
EBK27	38.3	145.7	24.4	5.2	0.14	19.1	0.352	0.383	0.11	0.13
EBK28	39.5	165.5	23.6	5.2	0.14	20.5	0.311	0.331	0.10	0.34
EBK29	34.5	224.8	17.4	3.3	0.32	13.1	0.214	0.215	0.10	0.28
EBK29	34.5	224.8	17.4	3.3	0.32	13.0	0.208	0.209	0.10	0.25
EBK30	37.8	182.4	13.4	3.0	0.20	21.7	0.360	0.378	0.10	0.22
EBK30	37.8	182.4	13.4	3.0	0.20	22.1	0.369	0.392	0.10	0.25
EBK31	38.8	182.6	24.5	5.6	0.14	19.6	0.314	0.350	0.10	0.28
EBK33	18.6	52.4	31.6	2.6	0.20	5.8	0.106	0.109	0.13	0.06
EBK33	18.6	52.4	31.6	2.6	0.20	5.8	0.113	0.115	0.12	0.07
EBK34	37.5	161.8	25.7	5.6	0.32	21.3	0.388	0.410	0.10	0.24
EBK39	40.8	179.3	25.0	5.9	0.14	23.5	0.399	0.439	0.10	0.30
EBK42	41.0	211.5	19.8	5.0	0.27	22.4	0.486	0.551	0.13	0.22
EBK43	42.3	190.8	21.5	5.2	0.27	23.5	0.449	0.463	0.12	0.31
EBK44	41.5	273.8	18.1	4.6	0.20	24.0	0.370	0.403	0.09	0.28
EBK45	37.1	178.0	22.8	4.9	0.27	17.8	0.328	0.336	0.10	0.31
EBK48	31.6	125.6	21.3	3.6	0.08	10.6	0.194	0.216	0.12	0.36
EBK48	31.6	125.6	21.3	3.6	0.13	10.8	0.199	0.226	0.12	0.37
EBK48	31.6	125.6	21.3	3.6	0.08	10.7	0.205	0.222	0.12	0.38
EBK49	38.6	128.2	28.0	6.4	0.27	22.3	0.471	0.487	0.11	0.26
EBK50	37.8	146.5	25.2	5.6	0.14	21.1	0.362	0.387	0.12	0.15
EBK53	39.0	147.0	24.7	5.6	0.14	19.9	0.305	0.337	0.11	0.15
EBK69	40.1	138.3	23.0	5.5	0.14	20.5	0.416	0.455	0.12	0.26
EBK71	39.7	176.8	25.9	6.1	0.27	21.8	0.354	0.377	0.10	0.22

Table B.11: Petrophysical properties of LK samples: porosity Φ, permeability k, specific surface related to pore volume S_{por} and related to mass S_{m}. IP parameter of the LK samples: peak frequency f_{peak}, real part of conductivity $\sigma'(1\mathrm{Hz})$, imaginary part of conductivity $\sigma''(1\mathrm{Hz})$ and $\sigma''(f_{\mathrm{peak}})$, total chargeability m_{DD}, and mean relaxation time τ_{DD}

Sample	Φ [%]	k [mD]	S_{por} [μm^{-1}]	S_{m} [m^2g^{-1}]	$\sigma'(1\mathrm{Hz})$ [mS·m^{-1}]	$\sigma''(1\mathrm{Hz})$ [mS·m^{-1}]	m_{DD} [-]	τ_{DD} [s]
LK03	12.2	0.20	18.8	1.25	4.5	0.064	0.091	0.130
LK08	16.6	0.73	10.0	0.74	4.0	0.048	0.091	0.058
LK09	18.2	1.26	11.9	0.98	4.3	0.057	0.080	0.078
LK09	18.2	1.26	11.9	0.98	4.1	0.053	0.078	0.077
LK13	11.1	0.09	21.5	1.00	11.6	0.109	0.063	0.130
LK13	11.1	0.09	21.5	1.00	11.4	0.110	0.063	0.130
LK22	10.8	0.66	20.6	0.92	2.7	0.045	0.092	0.083
LK22	10.8	0.66	20.6	0.92	2.7	0.045	0.078	0.057
LK15	14.9	0.22	14.7	0.96	5.0	0.067	0.087	0.099
LK28	15.4	0.31	15.1	1.02	3.9	0.051	0.109	0.140
LK30	14.7	0.19	16.3	1.05	4.4	0.064	0.091	0.089
LK30	14.7	0.19	16.3	1.05	4.4	0.062	0.090	0.100
LK32	11.4	0.11	15.2	0.73	3.0	0.048	0.100	0.120
LK32	11.4	0.11	15.2	0.73	3.1	0.048	0.099	0.120
LK36	14.5	0.19	18.6	1.17	3.9	0.047	0.083	0.092
LK38	15.1	1.59	19.0	1.25	4.8	0.070	0.084	0.065
LK38	15.1	1.59	19.0	1.25	5.0	0.071	0.089	0.087
LK40	11.1	0.08	24.8	1.14	2.9	0.053	0.110	0.110
LK40	11.1	0.08	24.8	1.14	2.8	0.050	0.113	0.130
LK42	18.6	1.68	9.7	0.82	4.2	0.052	0.075	0.068
LK42	18.6	1.68	9.7	0.82	4.2	0.051	0.075	7.100
LK49	15.8	0.25	22.7	0.98	4.9	0.078	0.093	0.083
LK46	16.6	0.45	10.3	0.76	4.9	0.057	0.056	0.016
LK47	20.1	3.87	10.5	0.98	4.8	0.062	0.080	0.097
LK47	20.1	3.87	10.5	0.98	4.7	0.062	0.081	0.100
LK50	20.9	4.41	9.7	0.95	9.1	0.105	0.068	0.067
LK50	20.9	4.41	9.7	0.95	9.2	0.108	0.072	0.100

Table B.12: Petrophysical properties of ILS samples: porosity Φ, permeability k, specific surface related to pore volume S_{por} and related to mass S_{m}. IP parameter of the LK samples: peak frequency f_{peak}, real part of conductivity $\sigma'(1\mathrm{Hz})$, imaginary part of conductivity $\sigma''(1\mathrm{Hz})$ and $\sigma''(f_{\mathrm{peak}})$, total chargeability m_{DD}, and mean relaxation time τ_{DD}

Sample	Φ [%]	k [mD]	S_{por} [μm^{-1}]	S_{m} [m^2g^{-1}]	$\sigma'(1\mathrm{Hz})$ [mS·m^{-1}]	$\sigma''(1\mathrm{Hz})$ [mS·m^{-1}]	m_{DD} [-]	τ_{DD} [s]
ILS01	17.4	209.9	4.8	0.4	3.2	0.0018	0.003	0.031
ILS02	17.9	178.9	4.8	0.4	3.1	0.0018	0.003	0.014
ILS02	17.9	178.9	4.8	0.4	3.2	0.0016	0.001	0.022
ILS03	18.3	168.4	4.5	0.4	4.5	0.0009	0.003	0.056
ILS03	18.3	168.4	4.5	0.4	4.7	0.0021	0.003	0.047
ILS38	14.2	151.5	4.5	0.3	3.2	0.0001	0.003	0.036
ILS22	19.9	290.2	2.7	0.3	3.7	0.0012	0.002	0.170
ILS50	18.8	228.7	3.3	0.3	5.0	0.0017	0.003	0.054

Table B.13: Petrophysical properties of DOL samples: porosity Φ, permeability k, specific surface related to pore volume S_{por} and related to mass S_{m}. IP parameter of the LK samples: peak frequency f_{peak}, real part of conductivity $\sigma'(1\text{Hz})$, imaginary part of conductivity $\sigma''(1\text{Hz})$ and $\sigma''(f_{\text{peak}})$, total chargeability m_{DD}, and mean relaxation time τ_{DD}

Sample	Φ	k	S_{por}	S_{m}	$\sigma'(1\text{Hz})$	$\sigma''(1\text{Hz})$	m_{DD}	τ_{DD}
	[%]	[mD]	[μm^{-1}]	[m^2g^{-1}]	[mS·m^{-1}]	[mS·m^{-1}]	[-]	[s]
DOL15	10.27	4.79	0.10	0.004	0.79	0.0017	0.013	0.019
DOL15	10.27	4.79	0.10	0.004	0.80	0.0019	0.014	0.022
DOL17	12.55	56.43	0.19	0.010	1.01	0.0018	0.017	0.053
DOL17	12.55	56.43	0.19	0.010	0.85	0.0016		
DOL32	8.97	2.10	0.14	0.005	1.33	0.0012	0.007	0.040
DOL41	10.48	6.63	8.58	0.357	1.28	0.0021	0.016	0.052
DOL41	10.48	6.63	8.58	0.357	1.27	0.0021	0.013	0.023
DOL42	17.04	260.58	0.57	0.042	1.63	0.0044	0.017	0.044
DOL42	17.04	260.58	0.57	0.042	1.68	0.0050	0.017	0.039
DOL43	16.22	193.75	0.55	0.038	1.99	0.0037	0.018	0.052
DOL43	16.22	193.75	0.55	0.038	1.89	0.0045	0.022	0.054
DOL44	10.42	6.12	1.16	0.048	1.43	0.0032	0.013	0.024
DOL44	10.42	6.12	1.16	0.048	1.45	0.0031	0.014	3.200
DOL45	12.25	58.15	0.64	0.032	1.55	0.0023	0.013	0.038
DOL45	12.25	58.15	0.64	0.032	1.37	0.0023	0.016	0.087
DOL46	9.76	5.46	1.41	0.054	1.71	0.0023		
DOL46	9.76	5.46	1.41	0.054	1.66	0.0024	0.011	0.038
DOL48	10.42	7.75	12.68	0.525	0.91	0.0014		
DOL49	10.93	9.61	1.03	0.045	1.91	0.0046	0.019	0.058
DOL49	10.93	9.61	1.03	0.045	1.92	0.0047	0.017	0.034
DOL50	17.62	244.94	6.08	0.464	1.87	0.0041	0.017	0.018
DOL50	17.62	244.94	6.08	0.464	1.94	0.0045	0.017	0.023

Table B.14: Parameters for description of the influence of pore fluid conductivity of the sample EBK34.

pore fluid conductivity [mS/m]	f_{peak} [Hz]	σ' at f_{peak} [mS/m]	σ'' at f_{peak} [mS/m]	σ' at 1 Hz [mS/m]	σ'' at 1 Hz [mS/m]
25	0.183	12.7	0.354	13.1	0.301
50	0.183	17.2	0.388	17.7	0.339
100	0.183	20.8	0.387	21.3	0.355
200	0.183	31.8	0.428	32.1	0.410
400	0.366	50.9	0.439	51.3	0.421
800	11.719	99.5	0.381	98.9	0.419
1600	8.789	175.4	0.440	174.7	0.470

Table B.15: IP parameters chargeability and relaxation time for description of the influence of pore fluid conductivity of the sample EBK34.

	at $\mathbf{f_{peak}}$		**DD**				**CC**			
σ_{w} [mS/m]	τ_{peak} [s]	τ_{n} [ms/Ωm]	m_{DD} [-]	m_n [mS/m]	τ_{DD} [s]	τ_{n} [ms/Ωm]	m_{CC} [-]	m_n [mS/m]	τ_{CC} [s]	τ_{n} [ms/Ωm]
25	0.8692	10.4	0.054	0.742	0.21	2.5	0.062	0.646	0.49	5.9
50	0.8692	14.3	0.044	0.840	0.19	3.1	0.051	0.725	0.40	6.6
100	0.8692	17.3	0.039	1.078	0.16	3.2	0.054	0.778	0.83	16.6
200	0.8692	26.8	0.031	1.297	0.15	4.6	0.042	0.957	0.81	25.0
400	0.4356	21.6	0.021	1.444	0.12	6.0	0.029	1.045	0.41	20.4
800	0.0136	1.2	0.010	1.367	0.09	9.2	0.014	0.977	0.01	1.4
1600	0.0181	3.1	0.008	1.704	0.14	23.9	0.010	1.363	0.01	2.4

Table B.16: Formation factor of EBK and LK obtained by different methods.

sample	F_{Arch}	F_{M}	F_{corr}	sample	F_{Arch}	F_{M}	F_{corr}
EBK01	10	10	18	LK01	33	-	-
EBK02	9	-	16	LK02	40	-	-
EBK03	10	-	-	LK03	41	40	44
EBK04	18	-	-	LK04	44	-	-
EBK05	9	-	-	LK05	39	-	-
EBK06	10	-	9	LK06	71	-	105
EBK07	10	-	11	LK07	40	-	-
EBK08	9	-	-	LK08	34	-	43
EBK09	11	-	52	LK09	29	-	43
EBK10	10	-	9	LK10	36	-	-
EBK11	10	-	-	LK11	44	-	-
EBK12	27	-	30	LK12	45	-	-
EBK13	9	-	21	LK13	75	72	13
EBK14	10	-	14	LK14	37	-	-
EBK15	12	-	11	LK15	43	-	46
EBK16	15	-	21	LK16	46	-	-
EBK17	16	-	21	LK17	41	-	-
EBK18	11	-	11	LK18	35	-	-
EBK19	10	-	16	LK19	23	-	-
EBK20	11	-	12	LK20	36	-	-
EBK21	12	-	11	LK21	73	-	-
EBK22	9	-	13	LK22	81	-	87
EBK23	13	-	-	LK23	39	-	-
EBK24	19	22	-	LK24	34	37	-
EBK25	9	-	-	LK25	36	-	-
EBK26	11	-	10	LK26	43	-	-
EBK27	12	-	14	LK27	37	-	-
EBK28	11	-	10	LK28	40	40	47
EBK29	14	17	17	LK29	34	-	-
EBK30	11	10	11	LK30	43	42	44
EBK31	15	-	11	LK31	44	-	-
EBK32	10	11	-	LK32	72	65	71
EBK33	67	49	51	LK33	31	-	-
EBK34	12	13	-	LK34	69	-	-
EBK35	12	11	-	LK35	41	-	-
EBK36	23	-	-	LK36	45	-	43
EBK37	23	23	-	LK37	30	-	-
EBK38	10	-	-	LK38	42	39	39
EBK39	10	-	10	LK39	47	41	-
EBK40	14	13	-	LK40	76	65	90
EBK41	12	-	-	LK41	35	-	-
EBK42	9	-	18	LK42	28	32	40
EBK43	10	-	12	LK43	35	-	-
EBK44	9	10	10	LK44	48	-	-
EBK45	12	-	15	LK45	43	-	-
EBK46	10	-	-	LK46	35	-	34
EBK47	10	11	-	LK47	24	27	29
EBK48	18	21	25	LK48	36	-	-
EBK49	11	-	16	LK49	38	-	45
EBK50	11	-	12	LK50	22	26	18

Table B.17: Formation factor of ILS and DOL obtained by different methods.

sample	F_{Arch}	F_{M}	F_{corr}	sample	F_{Arch}	F_{M}	F_{corr}
ILS01	35	-	32	DOL01	115	-	-
ILS02	33	35	33	DOL02	192	-	-
ILS03	32	31	23	DOL03	92	-	-
ILS04	32	-	-	DOL04	62	-	-
ILS05	32	-	-	DOL05	74	-	-
ILS06	37	-	-	DOL06	63	-	-
ILS07	35	-	-	DOL07	71	-	-
ILS08	32	-	-	DOL08	391	-	-
ILS09	33	-	-	DOL09	255	-	-
ILS10	36	-	-	DOL10	175	-	-
ILS11	37	-	-	DOL11	267	-	-
ILS12	31	-	-	DOL12	416	-	-
ILS13	34	-	-	DOL13	86	-	-
ILS14	31	-	-	DOL14	196	-	-
ILS15	30	-	-	DOL15	220	-	137
ILS16	35	-	-	DOL16	274	247	-
ILS17	32	-	-	DOL17	137	118	126
ILS18	32	-	-	DOL18	211	-	-
ILS19	31	-	-	DOL19	77	-	-
ILS20	42	-	-	DOL20	171	-	-
ILS21	30	-	-	DOL21	65	-	-
ILS22	27	28	28	DOL22	185	-	-
ILS23	28	-	-	DOL23	181	-	-
ILS24	41	-	-	DOL24	143	-	-
ILS25	32	-	-	DOL25	248	-	-
ILS26	32	-	-	DOL26	202	235	-
ILS27	29	-	-	DOL27	58	-	-
ILS28	33	30	-	DOL28	376	-	-
ILS29	34	-	-	DOL29	296	-	-
ILS30	30	-	-	DOL30	596	-	-
ILS31	32	-	-	DOL31	79	-	-
ILS32	31	-	-	DOL32	304	-	78
ILS33	28	-	-	DOL33	162	-	-
ILS34	34	-	-	DOL34	70	-	-
ILS35	37	-	-	DOL35	81	-	-
ILS36	34	-	-	DOL36	150	-	-
ILS37	32	-	-	DOL37	219	250	-
ILS38	54	-	31	DOL38	343	-	-
ILS39	39	-	-	DOL39	148	-	-
ILS40	32	-	-	DOL40	69	-	-
ILS41	31	32	-	DOL41	210	-	83
ILS42	41	-	-	DOL42	66	63	66
ILS43	30	-	-	DOL43	75	-	58
ILS44	30	30	-	DOL44	213	-	76
ILS45	30	-	-	DOL45	145	-	78
ILS46	33	-	-	DOL46	248	-	63
ILS47	33	-	-	DOL47	189	-	-
ILS48	31	-	-	DOL48	213	-	116
ILS49	34	-	-	DOL49	190	-	56
ILS50	30	30	20	DOL50	61	-	58

Table B.18: Summarising the obtained μ-CT data of the side track induced dissolution experiment of the EBK sample.

Sample		Voxel	reconstructed	interested	number	area			volume			Eqdiameter		
		resolution [μm]	Volume (Pixel)	Volume (Pixel)	of pores	Mean	Min	Max	Mean	Min	Max	Mean	Min	Max
24 h	S0	1.75	2284x2284x2304	1400x1400x1400	2128920	530.8	9.2	1404920	2084	5.4	17645500	4.91	2.2	323
24 h	S1	1.75	2284x2284x2304	1365x1172x1240	622868	872.1	9.2	890214	4660	5.4	22340700	7.686	2.2	349
36 h	S0	1.75	2284x2284x2304	1400x1400x1141	1142550	528.1	9.2	921462	2114	5.4	19716000	6.002	2.2	335
36 h	S1	1.75	2284x2284x2304	1300x1300x1300	316857	1404	9.2	1093960	8499	5.4	23243100	10.37	2.2	354
48 h	S0	1.75	2284x2284x2304	1200x1200x1200	1051820	806.9	9.2	384425	3358	5.4	4157970	6.772	2.2	200
48 h	S1	1.75	2284x2284x2304	1200x1200x1200	853172	699.6	9.2	603729	3354	5.4	11999300	7.825	2.2	284
60 h	S0	1,75	2284x2284x2304	1300x1300x1300	964491	872	9.2	857836	3440	5.4	9626940	6.566	2.2	264
60 h	S1	1.75	2284x2284x2304	1200x1200x1200	474801	1128	9.5	629785	5156	5.4	12687700	9.525	2.2	289
72 h	S0	1,75	2284x2284x2304	1400x1400x1400	940430	914.3	9.2	1081560	4520	5.4	20567300	7.848	2.2	340
72 h	S1	1.75	2284x2284x2304	800x800x800	127894	765.1	9.2	734487	3346	5.4	15821400	7.959	2.2	311

Sarah Hupfer

Persönliche Daten

Name	Sarah Hupfer
Geburtsdatum	20.12.1988
Geburtsort	Leipzig

Beruflicher Werdegang

08/2014 - 12/2018 **Wiss. Mitarbeiterin**, Leibniz-Institut für Angewandte Geophysik, Sektion 5 - Gesteinsphysik und Bohrlochgeophysik, Hannover.

Projekt: Nachwuchsgruppe Subrosion - Untersuchung der komplexen elektrischen Eigenschaften zur Charakterisierung von Karbonatgestein.
Promotionsarbeit: "Spectral Induced Polarization for an enhanced pore space characterization and analysis of solution processes of carbonate rocks" (Monographie in Vorbereitung)

Tätigkeiten:

- Durchführung von Labormessungen (Petrophysik, NMR, SIP)
- Datenbearbeitung, -auswertung und -interpretation
- Entwicklung SIP-Messzelle & Lösungsmessplatz
- Präsentation auf nationalen und internationalen Konferenzen und Veröffentlichung in wiss. Fachzeitschriften.

Ausbildung

2011 - 2014 **Master of Science**, *(1,8)*, Universität Potsdam, Geowissenschaften, Vertiefungsrichtung Geophysik.

Masterarbeit: "Systematische Untersuchungen zum komplexen elektrischen Widerstand an Mineral Quarzsand-Gemischen" (Note: 1,2)

2008 - 2011 **Bachelor of Science**, *(1,9)*, Universität Potsdam, Geowissenschaften.

Bachelorarbeit: "Coulomb-Spannungsänderungen durch das Tohoku-oki-Erdbeben" (Note: 1,7)

2008 **Allgemeine Hochschulreife (Abitur)**, *(1,5)*, Carl-Bechstein-Gymnasium, Erkner.

Leistungskurse: Mathematik, Physik
Sprachkenntnisse: Englisch (9 Jahre), Französisch (4), Latein (5)

Praktika/Studentische Hilfstätigkeiten

18.02. - 28.03.2013 **Projektpraktikum**, Leibniz-Institut für Angewandte Geophysik, Hannover.

Sektion 2 "Geoelektrik und Elektromagnetik"

24.09. - 06.10.2012 **Studentische Hilfskraft**, Deutsches Geoforschungszentrum, Potsdam.

Zentrum für CO2-Speicherung, 3D-seismische Messungen in Ketzin

21.02. - 01.04.2011 **Projektpraktikum**, Deutsches Geoforschungszentrum, Potsdam.
Sektion 2.1 "Erdbebenrisko und Frühwarnung"

15.09. - 26.09.2008 **Freies Praktikum**, Deutsches Geoforschungszentrum, Potsdam.
ehemalige Sektion 5.1. "Umwelttechnik"

Kenntnisse/Fähigkeiten

Sprachen Englisch: sehr gute Kenntnisse in Wort und Schrift
Französisch: Grundkenntnisse
Schwedisch: Grundkenntnisse
Latein: Großes Latinum
Deutsch: Muttersprache

EDV Office-Anwendungen, $\LaTeX$, Python, Grapher, Petrel, ArcGIS

Führerschein Klasse B

Weiterbildung

11/2016	Erste Hilfe, Johanniter, 1 Tag
09/2016	Kommunizieren und Kooperieren, Spirit Training & Consulting GmbH, 3,5 Tage
11/2015	Kreativitätstraining, Deutsche Gesellschaft für Personalwesen e. V., 1,5 Tage
11/2015	Konzentrations- und Gedächtnistraining, 1 Tag
02/2015	Python 3 für Programmierer und Wissenschaftler, Python Academy, 5 Tage

Fachliche Interessen

Gesteinsphysik, Karst, Reservoircharakterisierung, Lösungsprozesse, Labormessung, poröse Medien, komplexe elektrische Eigenschaften

Publikationen

peer reviewed **Hupfer**, Martin, Weller, Günther, Kuhn, Nguimeya & Noell (**2015**). *Polarization effects of unconsolidated sulphide-sand-mixtures.* Journal of applied geophysics, 135, 456-465.

Sonstiges Halisch, **Hupfer**, Weller, Dlugosch & Plumhoff (**2018**). *An experimental setup for the assessment of effects of carbonate rock dissolution in complex electrical conductivity spectra.* Society of Core Analyst Annual Symposium, Proceedings, Trondheim, SCA2018-040.

Hupfer, Halisch & Weller (**2017**). *Using low frequency electrical impedance spectroscopy for an enhanced pore space characterization and assessment of carbonates.* Society of Core Analyst Annual Symposium, Proceedings, Wien, SCA2017-115.

Halisch, Grelle, **Hupfer**, Blanke & Lehne (**2017**). *A new and modular laboratory core holder for high-precision measurements with low frequency impedance spectroscopy on natural rocks.* Society of Core Analyst Annual Symposium, Proceedings, Wien, SCA2017-021.

Wadas, **Hupfer**, Kobe, Miensopust & Schneider-Löbens (**2017**). Georisiko Erdfall: Und plötzlich war da ein Loch - Die Nachwuchsgruppe Subrosion des LIAG stellt sich vor. Mitteilungen der Deutschen Geophysikalischen Gesellschaft, 1, 17-33.

Präsentationen auf Fachtagungen

2017	Säuerungsexperiment & SIP an Karbonaten: Erste Ergebnisse. (Nationaler IP-Workshop, Aachen)
	Using low frequency electrical impedance spectroscopy for an enhanced pore space characterization and assessment of carbonates. (SCA, Wien)
	Characterization of carbonates by Spectral Induced Polarization. (EGU, Wien)
	Untersuchungen an Karbonatgesteinen mittels Spektraler Induzierter Polarisation. (DGG, Münster)
2016	SIP-Messungen an Karbonaten. (Bucha-Seminar, Leipzig)
2015	Charakterisierung von Karbonatgestein. (Nationaler IP-Workshop, Berlin)
2014	Laboratory SIP - investigation on unconsolidated mineral-sand-mixtures. (Internationaler IP-Workshop, Ile d'Oleron)
	Laboruntersuchungen zur komplexen Leitfähigkeit an Metall-Quarzsand-Gemischen. (DGG, Karlsruhe)
2012	Tohoku-oki earthquake - Stress transfer to neighbouring faults. (DGG, Hamburg)